NASA TECHNICAL MEMORANDUM

NASA TM X-2947

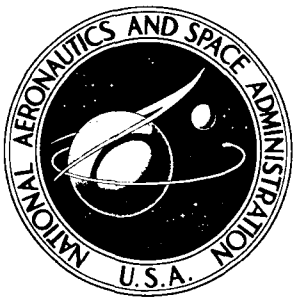

NASA TM X-2947

EXHAUST-NOZZLE CHARACTERISTICS FOR A TWIN-JET VARIABLE-WING-SWEEP FIGHTER AIRPLANE MODEL AT MACH NUMBERS TO 2.2

by David E. Reubush and Charles E. Mercer

Langley Research Center
Hampton, Va. 23665

NATIONAL AERONAUTICS AND SPACE ADMINISTRATION • WASHINGTON, D. C. • JUNE 1974

1. Report No.	2. Government Accession No.	3. Recipient's Catalog No.
NASA TM X-2947		

4. Title and Subtitle	5. Report Date
EXHAUST-NOZZLE CHARACTERISTICS FOR A TWIN-JET VARIABLE-WING-SWEEP FIGHTER AIRPLANE MODEL AT MACH NUMBERS TO 2.2	June 1974
	6. Performing Organization Code

7. Author(s)	8. Performing Organization Report No.
David E. Reubush and Charles E. Mercer	L-9273
	10. Work Unit No.
9. Performing Organization Name and Address	760-17-01-11
NASA Langley Research Center Hampton, Va. 23665	11. Contract or Grant No.
	13. Type of Report and Period Covered
12. Sponsoring Agency Name and Address	Technical Memorandum
National Aeronautics and Space Administration Washington, D.C. 20546	14. Sponsoring Agency Code

15. Supplementary Notes

16. Abstract

A wind-tunnel investigation has been conducted to determine the exhaust-nozzle aerodynamic and propulsive characteristics for a twin-jet variable-wing-sweep fighter airplane model. The powered model was tested in the Langley 16-foot transonic tunnel and in the Langley 4-foot supersonic pressure tunnel at Mach numbers to 2.2 and at angles of attack from about -2° to 6°. Compressed air was used to simulate the nozzle exhaust flow at values of jet total-pressure ratio from approximately 1 (jet off) to about 21. Effects of configuration variables such as speed-brake deflection, store installation, and boundary-layer thickness on the nozzle characteristics were also investigated.

17. Key Words (Suggested by Author(s))	18. Distribution Statement
Jet engine exhaust nozzles Jet effects Airplane aerodynamics Boattail drag	Unclassified – Unlimited STAR Category 02

19. Security Classif. (of this report)	20. Security Classif. (of this page)	21. No. of Pages	22. Price*
Unclassified	Unclassified	135	$4.75

*For sale by the National Technical Information Service, Springfield, Virginia 22151

EXHAUST-NOZZLE CHARACTERISTICS FOR A TWIN-JET VARIABLE-WING-SWEEP FIGHTER AIRPLANE MODEL AT MACH NUMBERS TO 2.2

By David E. Reubush and Charles E. Mercer
Langley Research Center

SUMMARY

A wind-tunnel investigation has been conducted to determine the exhaust-nozzle aerodynamic and propulsive characteristics for a twin-jet variable-wing-sweep fighter airplane model. The powered model was tested in the Langley 16-foot transonic tunnel and in the Langley 4-foot supersonic pressure tunnel at Mach numbers to 2.2 and at angles of attack from about -2° to 6°. Compressed air was used to simulate the nozzle exhaust flow at values of jet total-pressure ratio from approximately 1 (jet off) to about 21. Effects of configuration variables such as speed-brake deflection, store installation, and boundary-layer thickness on the nozzle characteristics were also investigated.

The results of this investigation show that at subsonic speeds nozzle drag is reduced when the jet is first turned on, but further moderate increases in jet total-pressure ratio have only small effects on the drag. At supersonic speeds nozzle drag was reduced as jet total-pressure ratio was increased. At all speeds jet operation had only minor effects on either nozzle lift or pitching moment. Deflection of the speed brakes generally resulted in increased nozzle drag (up to 500 percent), but had no consistent effects on either nozzle lift or pitching moment. All nozzles had asymmetric pressure distributions at all test conditions, but the load asymmetry was judged not to be of significant concern regarding possible distortion of the nozzles.

INTRODUCTION

In an effort to improve airplane performance through reduced weight and improved static balance the engine exhaust nozzles of modern fighter airplanes are made as light as possible. With the conventional twin-jet configuration which has side-by-side engines buried in the fuselage with variable exhaust nozzles at the rear, control surfaces such as vertical and horizontal tails, ventral fins, and speed brakes in the immediate vicinity of the nozzles create aerodynamic interference. The nearness to the nozzles of these sources of interference and the wide variety of flight conditions which the airplane will

encounter give rise to concern about the asymmetric loadings which occur on the external surface of the nozzles at the various operating conditions. It is possible that the asymmetric loading could cause either mechanical failure of the nozzle structure or might distort the nozzle to the point that its actuating mechanism would not function. Aerodynamic data for these fighter airplanes are obtained from sting mounted wind-tunnel force and moment models that simulate neither the correct nozzle-afterbody geometries nor the correct engine-operating values of jet total-pressure ratio, reference 1. Therefore, powered models which do simulate the correct nozzle-afterbody geometries and provide a means of simulating the jet exhaust must be investigated to assess the effects of jet operation on the characteristics of the airplane and of the exhaust nozzles, references 2 to 6.

The purpose of this investigation was to determine the nozzle aerodynamic and propulsive characteristics: drag, lift, pitching moment, and external pressure distributions, for two different types of exhaust nozzles, convergent-divergent iris and convergent-divergent balance beam, which were installed on a twin-jet variable-wing-sweep fighter airplane model. The primary objective of the investigation was to determine the combined effects of jet operation and airplane configuration changes on the aerodynamic characteristics of the exhaust nozzles. The configuration changes included speed-brake deflection, addition of external stores, and variation of fuselage boundary-layer thickness. Additional data on some of these nozzles and others investigated after the model geometry had been slightly modified can be found in reference 2.

The model used in this investigation had provisions for two fixed wing-sweep positions: 22° for subsonic speeds, and 68° for supersonic speeds. Exhaust nozzles representative of those for cruise, partial afterburning, and maximum afterburning power settings for two different engines were utilized. Nozzle exhaust flow was simulated by use of high pressure air at about room temperature.

This investigation was conducted in the Langley 16-foot transonic tunnel at static conditions and at Mach numbers from 0.6 to 1.3, and in the Langley 4-foot supersonic pressure tunnel at a Mach number of 2.2. Angle of attack was varied from -2° to 6° in the 16-foot tunnel and was held constant at 0° in the 4-foot tunnel. Jet total-pressure ratio was varied from approximately 1 (jet off) to 21, depending on Mach number. Included in the appendix are static thrust and mass flow characteristics for the nozzles used in this investigation obtained through use of the test vehicle and procedure discussed in reference 7.

SYMBOLS

All stability-axis coefficients are based on the geometry of the model having a wing leading-edge sweep of 20°.

A cross-sectional area, m^2

A_{cc} cross-sectional area at fuselage-nozzle juncture (customer connect station), m^2

A_e nozzle exit area, m^2

A_t nozzle throat area, m^2

$C_{D,n}$ nozzle pressure-drag coefficient, $\frac{\text{Drag of two nozzles}}{q_\infty S}$

$C_{L,n}$ nozzle lift coefficient, $\frac{\text{Lift of two nozzles}}{q_\infty S}$

$C_{m,n}$ nozzle pitching-moment coefficient, $\frac{\text{Pitching moment of two nozzles}}{q_\infty S\bar{c}}$

$C_{p,\beta}$ local boattail pressure coefficient, $\frac{p_l - p_\infty}{q_\infty}$

$\bar{c}$ mean aerodynamic chord of wing, m

d_{cc} diameter of engine nacelle at customer connect station, m

F nozzle gross thrust, N

F_i ideal isentropic gross thrust, $\dot{m}\sqrt{\frac{2\gamma}{\gamma - 1} RT_{t,j}\left[1 - \left(\frac{p_\infty}{p_{t,j}}\right)^{\frac{\gamma-1}{\gamma}}\right]}$, N

l reference length from airplane nose to tip of horizontal tail, m

M free-stream Mach number

$\dot{m}$ actual mass flow rate through nozzle, kg/s

$\dot{m}_i$ ideal mass flow rate: $A_t p_{t,j}\sqrt{\frac{\gamma}{RT_{t,j}}\left(\frac{2}{\gamma + 1}\right)^{\frac{\gamma+1}{\gamma-1}}}$ for choked flow;

$A_t p_{t,j}\left(\frac{p_\infty}{p_{t,j}}\right)^{1/\gamma}\sqrt{\frac{2\gamma}{(\gamma - 1)RT_{t,j}}\left[1 - \left(\frac{p_\infty}{p_{t,j}}\right)^{\frac{\gamma-1}{\gamma}}\right]}$ for unchoked flow, kg/s

p_l	local boattail static pressure, N/m^2
$p_{t,j}$	jet total pressure, N/m^2
$p_{t,l}$	local total pressure, N/m^2
$p_{t,\infty}$	free-stream total pressure, N/m^2
p_∞	free-stream static pressure, N/m^2
q_∞	free-stream dynamic pressure, N/m^2
R	gas constant, 287.3 N-m/kg-K
S	reference wing area, m^2
$T_{t,j}$	jet total temperature, K
x	longitudinal distance from model nose (station 0), positive rearward, m
y	height of boundary-layer probe above and normal to model surface, m
α	angle of attack, deg
γ	ratio of specific heats
δ_{SB}	speed-brake deflection, deg
θ	angle of radius from nozzle center line to nozzle surface pressure orifice, clockwise positive for left nozzle, counterclockwise positive for right nozzle; facing upstream 0^o is at top of nacelle, deg
Λ	wing sweep angle, deg

ABBREVIATIONS

BL	buttock line, spanwise distance from vertical plane of symmetry

WL water line, vertical distance from reference horizontal plane

FS fuselage station, axial distance from reference station zero (for this investigation, from model nose)

APPARATUS AND PROCEDURE

Wind Tunnels

This investigation was conducted in the Langley 16-foot transonic tunnel and in the Langley 4-foot supersonic pressure tunnel. The Langley 16-foot transonic tunnel is a single-return, continuous-flow, atmospheric wind tunnel with a slotted octagonal test section. Test section airspeed is continuously variable between Mach numbers of 0.20 and 1.30. The Langley 4-foot supersonic pressure tunnel is a single-return, continuous-flow wind tunnel with a stagnation-pressure range of 27.58 kN/m^2 to 206.84 kN/m^2 (0.27 atm to 2.04 atm), and a stagnation-temperature range of 309 K to 322.2 K. By use of interchangeable nozzle blocks, the Mach number can be varied from 1.25 to 2.20.

Model

Photographs of the model mounted in the Langley 16-foot transonic tunnel and in the Langley 4-foot supersonic pressure tunnel are shown in figure 1. A sketch of the model showing principal dimensions is shown in figure 2(a). The model was supported in the 16-foot transonic tunnel by a thin sweptback strut attached to the bottom of the fuselage just aft of the nose, as shown in figure 2(b). The strut blended into a sting which had a constant cross section beginning at the intersection with the strut trailing edge and extending downstream to a station well aft of the model. Model details and dimensions are presented in figure 3.

The model was tested with two wing sweep positions: 22° sweep for subsonic speeds with extendable glove vanes retracted and horizontal tails set at 0°; and with 68° sweep for transonic and supersonic speeds with glove vanes extended and horizontal tails set at -2°. The model also had provisions for varying the speed-brake deflection from 0° to 40°, figures 1(d) and 3(h), for the addition of missiles and fuel tanks, figure 1(e), and for the addition of a "fence" of varying height around the fuselage near the inlet lip, figures 1(g) and 3(i), to thicken artificially the model boundary layer.

Two different sets of exhaust nozzles representing various power settings of two different nozzle types were investigated. One set represented various power settings of a convergent-divergent iris-type nozzle (type A) and the second set represented various

power settings of a convergent-divergent balance-beam type of nozzle (type B). Photographs and geometric details of these nozzles are shown in figures 1(a), 1(d), 1(e), 1(f), 1(g), and 4. The nozzle exhaust flow was simulated by use of a high pressure compressed air system similar to that described in reference 8. Configurations 1 and 2 have been reported in reference 2. The nozzles have been given configuration numbers as follows:

3 – Nozzle type A, cruise power setting, $A_e/A_t = 1.05$

4 – Nozzle type A, modified cruise power setting, $A_e/A_t = 1.02$

5 – Nozzle type A, low partial afterburning power setting, $A_e/A_t = 1.11$

6 – Nozzle type A, high partial afterburning power setting, $A_e/A_t = 1.15$

7 – Nozzle type A, maximum afterburning power setting, $A_e/A_t = 1.21$

8 – Nozzle type A, modified maximum afterburning power setting, $A_e/A_t = 1.20$

9 – Nozzle type B, cruise power setting, $A_e/A_t = 1.02$

10 – Nozzle type B, sea-level maximum afterburning power setting, $A_e/A_t = 1.19$

11 – Nozzle type B, transonic maximum afterburning power setting, $A_e/A_t = 1.37$

Although this model is the same as that used for the work reported in reference 3 the model lines were very slightly modified prior to this investigation. Also for this test the inlets were smoothly faired as opposed to blocked inlets as in reference 2; and, at $M = 2.2$ some of the current configurations were tested with flow-through inlets.

Instrumentation and Tests

The various exhaust nozzle configurations were equipped with external static pressure orifices as indicated in table I. The total pressure and temperature of the jet simulation air were measured in each tail pipe by use of a total-pressure probe and a stagnation thermocouple. Also, the right nozzle of configuration 5 (nozzle type A, low partial afterburning power setting) was equipped with three boundary-layer rakes ($\theta = 35^\circ$, 225°, and 315° – see fig. 1(f)) at station 141.499 (customer-connect station).

Data were obtained for Mach numbers from 0.6 to 1.3 at angles of attack from -2° to 6° and for a Mach number of 2.2 at 0°. In the 16-foot transonic tunnel the model angle of attack was set remotely and was corrected for support deflection due to loads and tunnel upflow. The average Reynolds number per meter varied from 1.00×10^7 at $M = 0.6$ to 1.19×10^7 at $M = 2.2$. Jet total-pressure ratio was varied from jet off to about 21, depending on Mach number.

Boundary-layer transition was fixed on the model by means of 3.2-mm-wide strips of No. 120 carborundum grains. The transition strips (or boundary-layer trips) were

located downstream of the leading edges of the ventral fins and horizontal- and vertical-tail surfaces at a distance of 5.08 mm measured normal to the leading edge. The transition strips on the wing were located as shown by figure 5, and a 3.2-mm-wide ring of carborundum grains also was located 13.5 mm aft of the nose of the fuselage.

Static internal performance of the various nozzles was obtained through use of the nacelle model and procedure described in reference 7. These data are presented in the appendix.

Data Reduction

Model and wind-tunnel data recorded on magnetic tape were used to compute standard force and pressure coefficients by use of an electronic computer. All nozzle force and moment data are referenced to the stability axes through the airplane center of gravity. Nozzle drag, lift, and pitching moment were obtained by assigning the appropriate projected area to each orifice and summing the incremental forces. No correction was made for strut interference, but data from references 4 and 5 indicate that the effect is small for a similar model and support system.

PRESENTATION OF RESULTS

The results of this investigation are presented in the following figures:

DISCUSSION OF RESULTS

Pressure-Coefficient Distributions

Typical circumferential distributions of pressure coefficient for the various configurations are shown in figure 6. All measurements are indicated to be located on the left nozzle, however a few were actually obtained on the right nozzle for some configurations (see table I). At all conditions there are large variations in the pressure coefficients around the nozzles for both nozzle types indicating that the interference surfaces (vertical and horizontal tails, ventral fins, interfairing, etc.) are causing definite asymmetric loadings on the nozzles. Especially noticeable is the depression in pressure for the first circumferential row (x/l = 0.909 or 0.919) near the top of the nozzle (θ values of about 340° to 20°) probably caused by interference from the vertical tails (for example, see fig. 6(a)). Although this large variation in pressure level is present for all configurations it does not cause great concern because it occurs on a fixed part of the nozzle structure, which is stronger than the nozzle regions that incorporate variable geometry.

Basic Aerodynamic Characteristics

The variation of the nozzle aerodynamic forces and moments with jet total-pressure ratio is presented in figures 7 to 15 for the various Mach numbers and angles of attack. Data are presented for the two different sets of exhaust nozzles (nozzle types A and B). All configurations exhibit similar trends with jet total-pressure ratio and angle of attack. For all subsonic Mach numbers when the jets are operated the nozzle drag is initially reduced at the low values of pressure ratio $\left(p_{t,j}/p_{\infty} \approx 1.2\right)$, but further increases in pressure ratio have only a relatively small effect on nozzle drag when compared with the initial drag reduction from the jet-off condition (see also ref. 2 and fig. 35). The trend is for the drag level to increase slightly, but to remain below the jet-off value as the pressure ratio is increased to $p_{t,j}/p_{\infty} \approx 3$, at which point the drag begins gradually to decrease. At the supersonic Mach numbers the nozzle drag coefficients generally decrease in level with increasing jet total-pressure ratio. Changes in angle of attack generally had small effect on the nozzle drag coefficients at all values of Mach number.

Variation of either jet total-pressure ratio or angle of attack had little to no effect on the nozzle lift and pitching moment coefficients at most subsonic Mach numbers for all configurations. At supersonic Mach numbers an increase in model angle of attack generally resulted in an increase in nozzle lift coefficient and correspondingly in a decrease of nozzle pitching-moment coefficient. . The variation of jet total-pressure ratio had almost no effect on this phenomenon at supersonic speeds, and the increment in either nozzle lift or pitching-moment coefficient between two angles of attack for a given configuration was generally about the same regardless of the value of jet pressure ratio (see fig. 9(c)).

Typical schedules of engine operating pressure ratio for each of the two exhaust nozzle types are presented in figure 16. All comparisons made at a constant value of Mach number will be made at a value of jet total-pressure ratio corresponding to these operating schedules.

Variation of nozzle drag coefficient with Mach number is presented in figure 17 for the two nozzle types. The nozzles which have the greater boattail projected area have the higher drag. The decrease in nozzle projected area which is related mechanically to the change from cruise power to maximum afterburning power, always resulted in a decreased level of drag coefficient. A further comparison that also illustrates this drag reduction is shown in figure 18, which presents nozzle drag-coefficient variation with the ratio of nozzle throat area to nacelle cross-sectional area at the customer-connect station for various Mach numbers. Here again the data show that the smaller the area ratio (greater closure or boattail angle), the higher the nozzle drag.

Effect of Speed-Brake Deflection

The effects of speed-brake deflection on the nozzle pressure distributions and on the related aerodynamic force and moment coefficients are presented in figures 19 to 26. The deflection of the speed brakes to 14° at $M = 1.2$ for configuration 3, a practical operation condition only in the case of engine flame-out, results only in a slightly higher drag coefficient at jet-off conditions. No effect on either nozzle lift or pitching-moment coefficient was observed for these conditions. In figure 20 the distributions of pressure coefficient at jet-off conditions, where highest pressure differential results in maximum loads on the nozzle, show mixed effects of the speed-brake deflection; some pressure coefficients were more positive while others were more negative. However, in no case was the magnitude of the pressure variation great enough to cause concern with regard to excessive loads on the nozzle structure. When the type A nozzle is being operated in the maximum afterburner setting, configuration 7, at a Mach number of 2.2, it is shown in figure 21 that a deflection of the speed brakes to 40° results in a decrease in nozzle drag coefficient, a very slight increase in nozzle lift coefficient, and a correspondingly small decrease in nozzle pitching-moment coefficient for all values of pressure ratio. The distributions of pressure coefficient for the afterburning nozzle, figure 22, also show that, as with the cruise nozzles, deflection of the speed brakes has a mixed effect. However, the region of greatly increased pressure near the beginning of the nozzle boattail ($x/l = 0.909$) results in the drag decrease shown in figure 21. A comment similar to that made concerning the pressure variations near the upstream end of the nozzle boattail would also apply here, that this part of the nozzle remains mechanically fixed and so is structurally stronger than those portions which must be actuated to vary the nozzle geometry.

Data are presented for the type B nozzles, cruise, configuration 9, in figure 23, and for the transonic maximum afterburning nozzle, configuration 11, in figure 25. These results indicate a large increase in nozzle drag with increasing speed-brake deflection for all values of jet total-pressure ratio and angles of attack, at subsonic Mach numbers. Typically $C_{D,max}$ at $\delta_{SB} = 40^{o}$ is 3 to 5 times larger than $C_{D,max}$ at $\delta_{SB} = 0^{o}$. Also under those same test conditions speed-brake deflection generally decreased nozzle lift coefficient by a small amount and increased nozzle pitching-moment coefficient slightly. The corresponding pressure distributions, figures 24 and 26, show that, except for the first row of orifices at $x/l = 0.909$, and at 0.919, for configurations 9 and 11, respectively, the shapes of the pressure distribution curves are similar but the level is successively depressed with each increment in speed-brake deflection. Although these reduced pressures would increase the axial loading on the nozzles, the fact that the distribution of load remained essentially the same over the mechanically variable portion of the nozzle would tend to preclude radial distortion of the nozzle. Distortion and mechanical failure are avoided also because the pressure difference across the nozzle did not increase to a value beyond that which the structure will withstand.

At supersonic speeds (M = 1.2) the drag of the transonic maximum afterburning nozzles, configuration 11, was generally slightly less with the speed brakes deployed than with brakes retracted; however, no consistent pattern existed. The same inconsistency and relatively small effects were observed for nozzle lift and pitching moment. Similarly the effect of speed-brake deployment, as shown in figure 26(b), was erratic distribution of nozzle surface pressures. Again there is little concern over these varying pressure levels because the large variations in pressure occur only on the fixed portion of the nozzle ($x/l = 0.919$), and the increased asymmetry of the pressure distributions therefore should not cause distortion of the rigid upstream portion of the nozzle, nor cause binding of the downstream actuated portion.

Effect of Store Installation

The type A maximum afterburning nozzles, configuration 7, were tested at subsonic and low supersonic speeds in combination with four missiles and two fuel tanks installed on the model forward of the nozzles as shown in figure 1(e), and the results are presented in figure 27. For all Mach numbers installation of these stores resulted in reduced nozzle drag (up to 20 percent less for some conditions) and had only minor effects on nozzle lift and pitching-moment coefficients. The pressure-coefficient distributions presented in figure 28 show that the nozzle pressures are generally slightly higher when the stores are installed than when the airplane is "clean." The pressure distributions show also that in addition to causing a small decrease in the axial loading on the nozzles, the addition of the stores improved slightly the symmetry of the loading, especially at station $x/l = 0.940$, as shown in figure 28(b).

Effect of Boundary-Layer Modification

In an effort to gain some insight into the possible effects of a variation in Reynolds number on the nozzle aerodynamic characteristics a short investigation was made in which the model boundary layer was artificially thickened by use of a "fence" around the model near the inlets to simulate two lower values of Reynolds number. The fence installation is shown in figures 1(g) and 3(i). Obviously it would have been more desirable to simulate increased rather than decreased values of Reynolds number; however, this was hardly possible in the Langley 16-foot transonic tunnel which operates at atmospheric stagnation pressure. It was felt that perhaps this method would give some idea of the effect of Reynolds number. For this investigation the type A low partial afterburning nozzles, configuration 5, were tested at Mach numbers of 0.7 and 0.8 at $\alpha = 4.3^{\circ}$ with three different boundary-layer thicknesses: clean model; "fence" with 3 wires; and "fence" with 7 wires. The 3-wire "fence" configuration consisted of the bottom 3 wires of those shown in figure 3(i).

Figure 29 presents the data showing the effects of these variations in boundary-layer thickness on the exhaust-nozzle aerodynamic characteristics. At $M = 0.7$ the increase in boundary-layer thickness caused by the 3-wire "fence" resulted in almost no change in nozzle drag, a slight decrease in nozzle lift, and a slight increase in nozzle pitching moment. The additional boundary-layer thickness due to the 7-wire "fence" resulted in a reduction of nozzle drag when compared with either the no "fence" configuration or the 3-wire "fence" configuration (C_D difference ≈ 0.0005 for the pressure ratio range), a further reduction in nozzle lift, and a further increase in nozzle pitching moment. At $M = 0.8$ the nozzle drag generally decreased with increasing boundary-layer thickness (fence height). Also at this Mach number the nozzle lift was slightly decreased and the nozzle pitching moment slightly increased for the 3-wire "fence" configuration, while the increase in boundary-layer height due to the 7-wire "fence" had almost no further effect on either lift or pitching moment. The corresponding pressure distributions, presented in figure 30, show that thickening the boundary layer generally increased the pressures slightly in the expansion region of the boattail at stations $x/l = 0.909$ and 0.934, and generally decreased the pressures by a very small amount in the separated region, at stations $x/l = 0.946$ and 0.957. These results tend to agree with those presented in reference 9 concerning Reynolds number effects on the drag of aft-mounted exhaust nozzles; that is, a decrease in Reynolds number will yield a decrease in drag due to a "softened" expansion around the nozzle boattail shoulder even though there may occur some loss of total pressure in the external flow.

To evaluate the effect of the "fences" on the external flow adjacent to the model, measurements of the boundary-layer total pressure were obtained on the right nozzle at the customer-connect station for three circumferential locations, $\theta = 35^{\circ}$, 225°, and 315°.

A photograph of the boundary-layer rake installation is presented in figure 1(f). The boundary-layer profiles are presented in figure 31 for the "fence" off configuration, in figure 32 for the 3-wire "fence," and in figure 33 for the 7-wire "fence." Typical comparisons of the distributions of total pressure in the boundary layers for the foregoing conditions are shown in figure 34. These comparisons illustrate that the "fences" caused a significant reduction in boundary-layer momentum without significantly altering the shape of the profile at any station. The effects of the progressively increased thickness of the airframe boundary layer on the nozzle aerodynamic characteristics are regarded as indicating at least a qualitative trend of the data with progressively reduced values of Reynolds number.

Comparisons With Other Data

Comparisons of nozzle drag coefficients from this investigation with those from reference 2 are shown in figure 35 to assess the effects of the minor model modifications mentioned under model description. For the type A cruise nozzles (configuration 3), the type B sea level, maximum afterburning nozzles (configuration 10), and the transonic maximum afterburning nozzles (configuration 11) the agreement is generally good. For the type A maximum afterburning nozzles, configuration 7, and the type B cruise nozzles, configuration 9, the agreement is rather poor. This inconsistency may be due to the fact that the aerodynamics of configurations 7 and 9 which are on the borderline of having separated flow are sensitive to changes in body contours, as is illustrated by the pressure distributions of figures 6(e) and 6(g). On the other hand configurations 10 and 11 are not so sensitive, and the external flow over configuration 3 is already substantially separated as indicated in figure 6(a), regardless of the upstream conditions. However, even for the configurations where the absolute agreement is not good, the magnitude of the effects of jet operation on the nozzle aerodynamic characteristics is generally the same for both investigations.

CONCLUDING REMARKS

An investigation has been conducted in the Langley 16-foot transonic tunnel and in the 4-foot supersonic pressure tunnel at Mach numbers to 2.2 to determine the effect of jet operation on the exhaust nozzle aerodynamic characteristics for a twin-jet variable-wing-sweep fighter model. The results of this investigation indicate several things. At subsonic speeds nozzle drag is reduced when the jet is initially turned on, but further increases in jet total-pressure ratio to realistic jet engine operating values have only small effects on the drag. At supersonic speeds nozzle drag was reduced as jet total-pressure ratio was increased. At all speeds jet operation generally had only small

effects on nozzle lift and pitching moment for most nozzles. Also for most nozzles at all speeds angle-of-attack variation generally resulted in only small variations in nozzle aerodynamic characteristics. Deflection of the speed brakes at subsonic speeds generally resulted in increased nozzle drag (as much as 500 percent for some configurations), generally reduced nozzle drag at supersonic speeds, and had no large effects on either nozzle lift or pitching moment in any speed range. Installation of stores generally reduced the nozzle drag for the type A maximum afterburning nozzles (up to 20 percent) but had only minor effects on nozzle lift and pitching moment. Artificial thickening of the model boundary layer to simulate lower Reynolds numbers generally reduced the nozzle drag for the type A low partial afterburning nozzles and caused a small decrease in nozzle lift and a small increase in nozzle pitching moment. All nozzles exhibited asymmetric pressure distributions for all conditions tested; however, the most unsymmetrical loading occurred for both nozzle types on the fixed part of the nozzle where the boattail shoulder structure is relatively rigid, and as a result of this circumstance the possibility of nozzle distortion due to the asymmetric loading is minimized.

Langley Research Center,
National Aeronautics and Space Administration,
Hampton, Va., February 25, 1974.

APPENDIX

STATIC THRUST AND MASS FLOW RATIOS

The static thrust and mass flow ratios for the various nozzle configurations of this investigation were obtained through use of the model and procedure discussed in reference 7 and are presented in figure 36. Two different runs are shown for each configuration to indicate data repeatability.

The type A cruise and partial afterburning nozzles exhibited static thrust ratio performance which peaked at about 0.985, while the maximum afterburning nozzles peaked at a slightly lower value of about 0.975. The values of mass flow ratio above choke for the cruise and partial afterburning nozzles remained relatively constant at about 0.980, while those for the maximum afterburning nozzles were slightly higher at about 0.985. Although the performance of these nozzles was relatively good, performance might have been improved by lengthening the nozzles to reduce the internal angles before and after the throat. The increased length would correspondingly increase weight, however, which would have to be traded off against the improved performance.

The three type B nozzles exhibited thrust ratios which peaked at values from about 0.975 to about 0.990 and mass flow ratios which ranged from about 0.955 to about 0.985. In addition to lengthening these nozzles to improve their performance it is believed that rounding the present sharp throat would also improve their performance.

REFERENCES

1. Henderson, William P.; and Dollyhigh, Samuel M.: Stability and Control Characteristics of a Variable-Sweep Fighter Configuration With a Supercritical Airfoil Section. NASA TM X-2032, 1970.

2. Mercer, Charles E.; and Reubush, David E.: Sting and Jet Interference Effects on Longitudinal Aerodynamic Characteristics of a Twin-Jet, Variable-Wing-Sweep Fighter Model at Mach Numbers to 2.2. NASA TM X-2825, 1973.

3. Maiden, Donald L.; and Berrier, Bobby L.: Effects of Afterbody Closure and Sting Interference on the Longitudinal Aerodynamic Characteristics of a Fixed-Wing, Twin-Jet Fighter Airplane Model. NASA TM X-2415, 1971.

4. Re, Richard J.; Wilmoth, Richard G.; and Runckel, Jack F.: Investigation of Effects of Afterbody Closure and Jet Interference on the Drag of a Twin-Engine Tactical Fighter. NASA TM X-1382, 1967.

5. Runckel, Jack F.; Lee, Edwin E., Jr.; and Simonson, Albert J.: Sting and Jet Interference Effects on the Afterbody Drag of a Twin-Engine Variable-Sweep Fighter Model at Transonic Speeds. NASA TM X-755, 1963.

6. Berrier, Bobby L.; and Maiden, Donald L.: Effect of Nozzle-Exhaust Flow on the Longitudinal Aerodynamic Characteristics of a Fixed-Wing, Twin-Jet Fighter Airplane Model. NASA TM X-2389, 1971.

7. Reubush, David E.: Effects of Fineness and Closure Ratios on Boattail Drag of Circular-Arc Afterbody Models With Jet Exhaust at Mach Numbers up to 1.30. NASA TN D-7163, 1973.

8. Mercer, Charles E.; and Berrier, Bobby L.: Effect of Afterbody Shape, Nozzle Type, and Engine Lateral Spacing on the Installed Performance of a Twin-Jet Afterbody Model. NASA TM X-1855, 1969.

9. Chamberlin, Roger; and Blaha, Bernard J.: Flight and Wind Tunnel Investigation of the Effects of Reynolds Number on Installed Boattail Drag at Subsonic Speeds. NASA TM X-68162, [1973].

TABLE I.- NOZZLE ORIFICE COORDINATE VALUES OF θ AND x/l

Nozzle type A – left nozzle							Nozzle type B – left nozzle				Nozzle type B – right nozzle			
θ, deg	x/l for configuration –						θ, deg	x/l for configuration –			θ, deg	x/l for configuration –		
	3	4	5	6	7	8		9	10	11		9	10	11
0	0.935	0.935	0.934	0.933	0.932	0.932	12	0.909	0.919	0.919	36	0.909		
20	.909	.909	.909	.909	.909	.909	12	.948	.937	.937	36	.936		
35	.935	.935	.934	.933	.932	.932	12	.970	.955	.956	36	.948		
35	.950	.948	.946	.944	.940	.937	60	.909	.919	.919	36	.970		
35	.963	.961	.957	.954	.947	.943	60	.936	.937	.937	84	.909	0.927	0.927
50	.909	.909	.909	.909	.909	.909	60	.948	.943	.943	84	.948	.943	.943
75	.950	.948	.946	.944	.940	.937	60	.957	.955	.956	84	.970	.974	.976
75	.963	.961	.957	.954	.947	.943	60	.970	.974	.976	156	.909		
95	.935	.935	.934	.933	.932	.932	108	.909	.919	.919	156	.948		
135	.909	.909	.909	.909	.909	.909	108	.948	.937	.937	156	.957		
135	.935	.935	.934	.933	.932	.932	108	.957	.943	.943	156	.970		
135	.950	.948	.946	.944	.940	.937	108	.970	.974	.976	204	.909		
180	.909	.909	.909	.909	.909	.909	180	.909	.919	.919	204	.970		
180	.963	.961	.957	.954	.947	.943	180	.936	.937	.937	252		.943	.943
225	.909	.909	.909	.909	.909	.909	180	.948	.943	.943	252	.970	.974	.976
225	.935	.935	.934	.933	.932	.932	180	.957	.955	.956	264	.909	.909	.909
225	.950	.948	.946	.944	.940	.937	180	.970	.974	.976	264	.927	.927	.927
264	.909	.909	.909	.909	.909	.909	228	.909	.919	.919	276	.948		
264	.922	.922	.922	.922	.922	.922	228	.948	.937	.937	276	.957		
264	.945	.943	.943	.939	.937	.935	228	.970	.955	.956	276	.970		
275	.963	.961	.957	.954	.947	.943	276	.957	.955	.956	290	.909	.909	.909
287	.909	.909	.909	.909	.909	.909	290	.927	.927	.927	300	.948	.943	.943
287	.922	.922	.922	.922	.922	.922	324	.909	.919	.919	300	.970	.974	.976
287	.945	.943	.943	.939	.937	.935	324	.936	.937	.937	348	.909		
315	.935	.935	.934	.933	.932	.932	324	.948	.943	.943	348	.948		
315	.950	.948	.946	.944	.940	.937	324	.957	.955	.956	348	.957		
315	.963	.961	.957	.954	.947	.943	324	.970	.974	.976	348	.970		
350	.909	.909	.909	.909	.909	.909	348	.909	.919	.919				

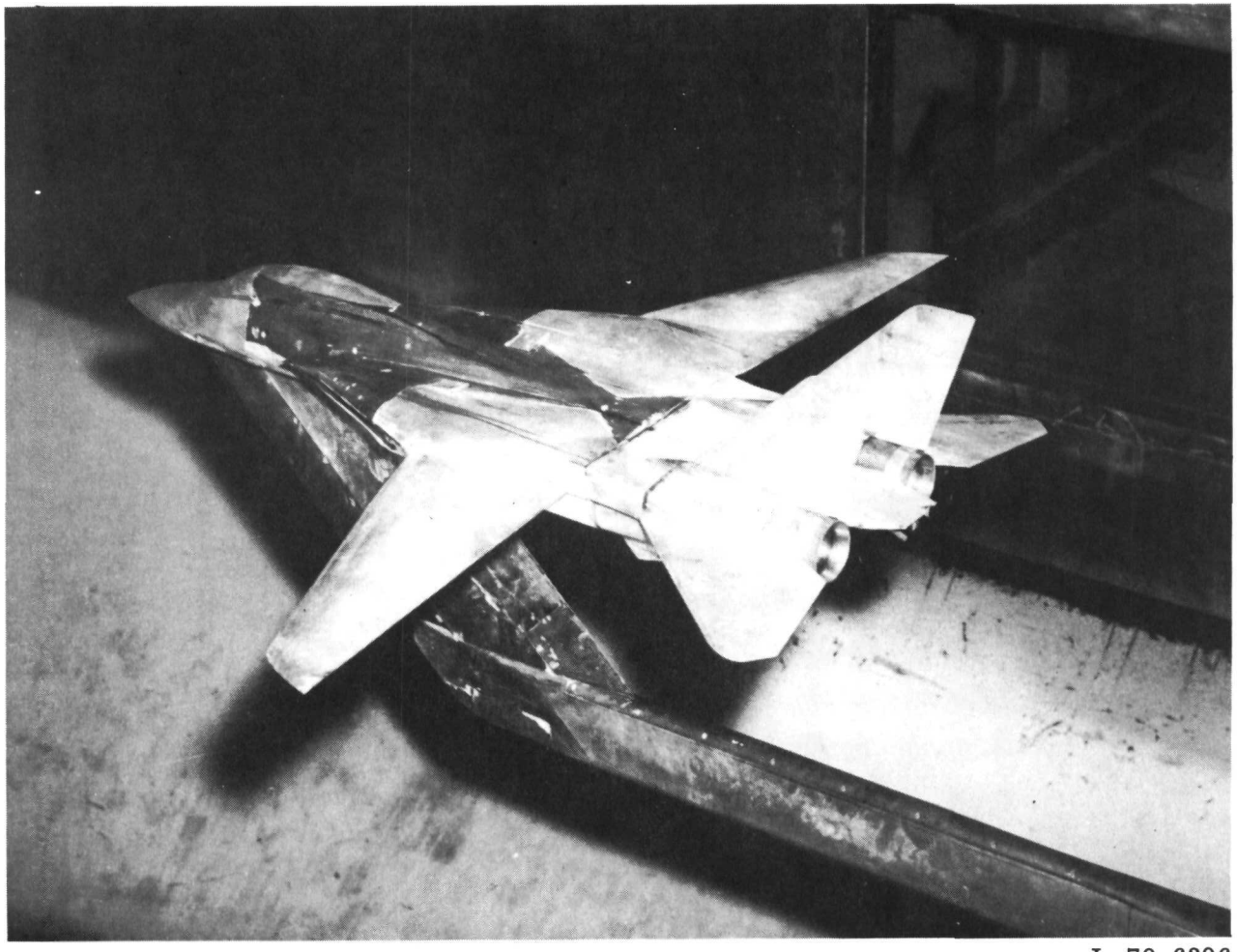

L-70-6396

(a) Configuration 7 (maximum afterburning power setting, nozzle type A) in the Langley 16-foot transonic tunnel.

Figure 1.- Photographs of model installed in the Langley 16-foot transonic tunnel and 4-foot supersonic pressure tunnel.

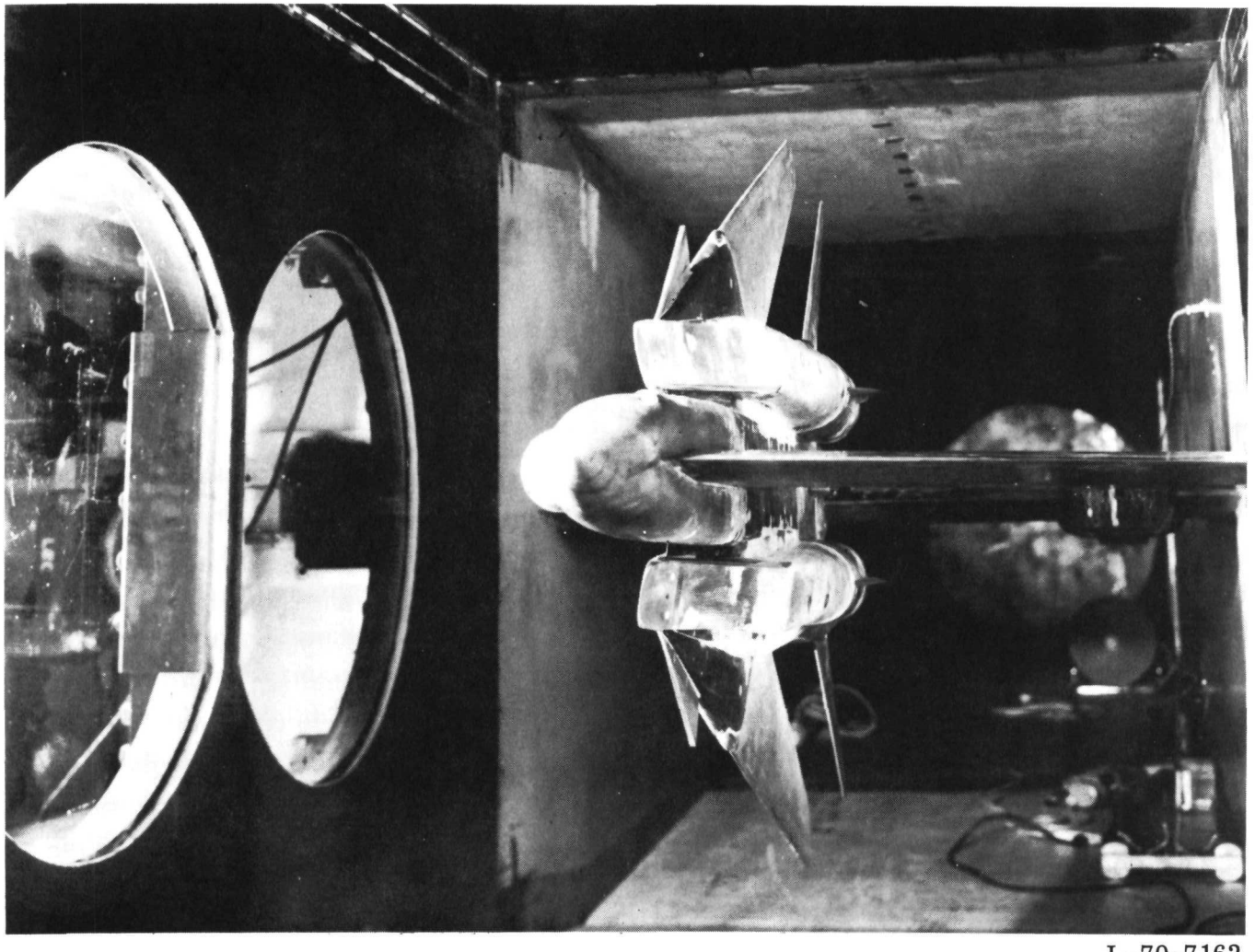

L-70-7162

(b) Front view of model in the Langley 4-foot supersonic pressure tunnel showing faired inlets.

Figure 1.- Continued.

L-70-7840

(c) Front view of model in the Langley 4-foot supersonic pressure tunnel showing flow-through inlet configuration.

Figure 1.- Continued.

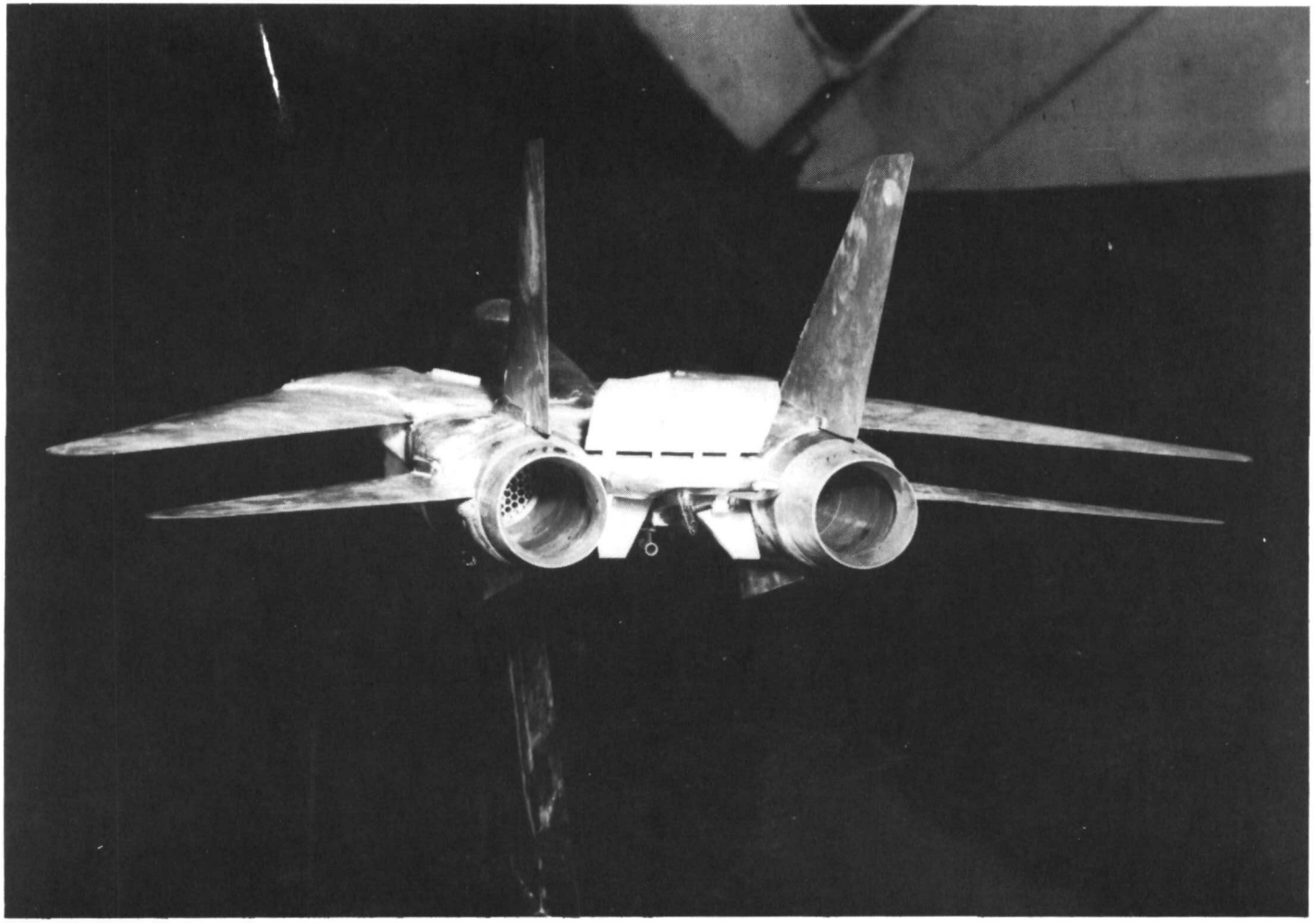

L-70-5434

(d) Configuration 11 (transonic maximum afterburning power setting, nozzle type B) with speed brakes deflected 40^{o} (16-foot transonic tunnel).

Figure 1.- Continued.

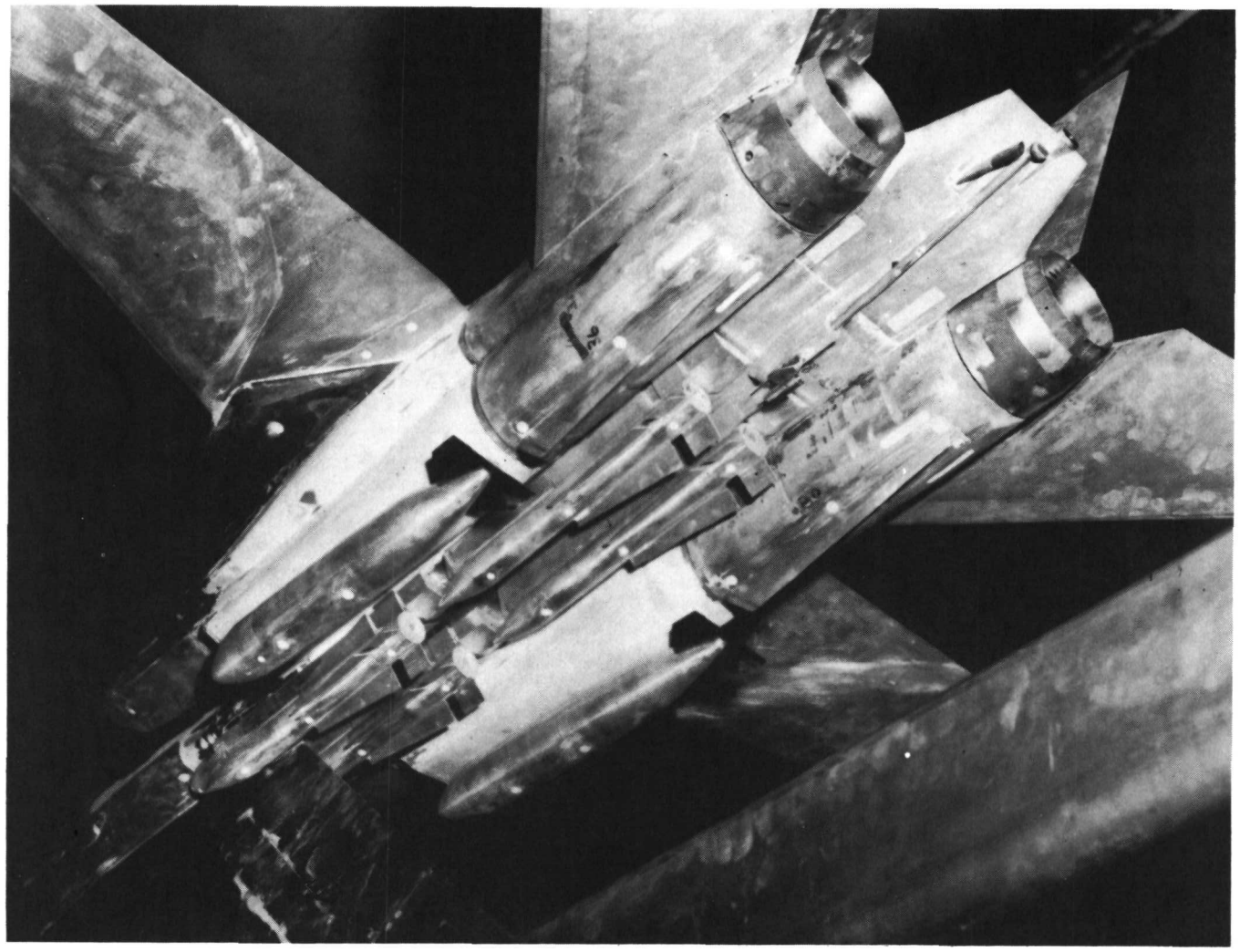

L-70-6045

(e) Configuration 7 (maximum afterburning power setting, nozzle type A) with stores and fuel tanks installed (16-foot transonic tunnel).

Figure 1.- Continued.

L-70-5499

(f) Configuration 5 (low partial afterburning power setting, nozzle type A) with boundary-layer rakes installed (16-foot transonic tunnel).

Figure 1.- Continued.

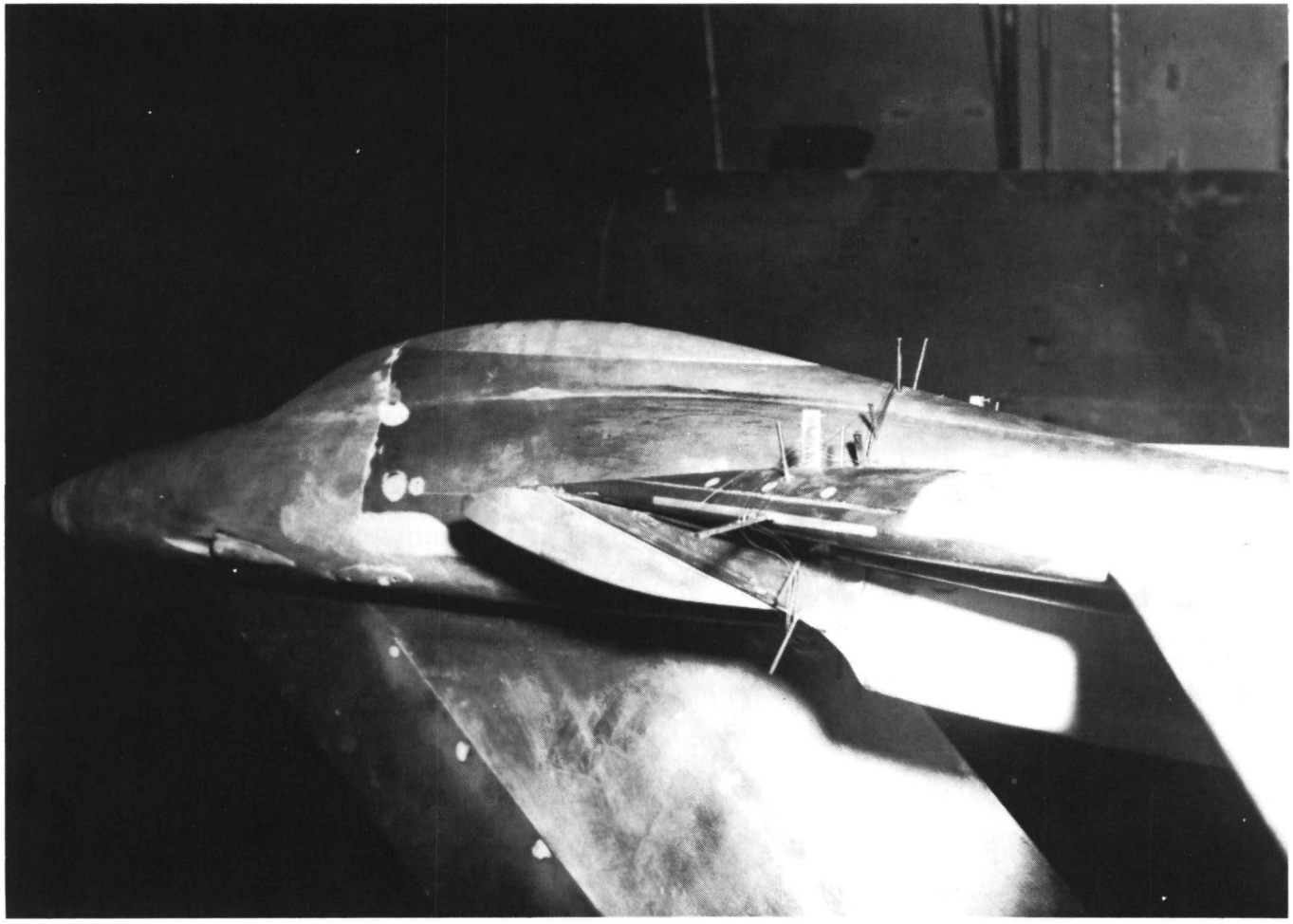

L-70-5498

(g) Boundary-layer "fence" (16-foot transonic tunnel).

Figure 1.- Concluded.

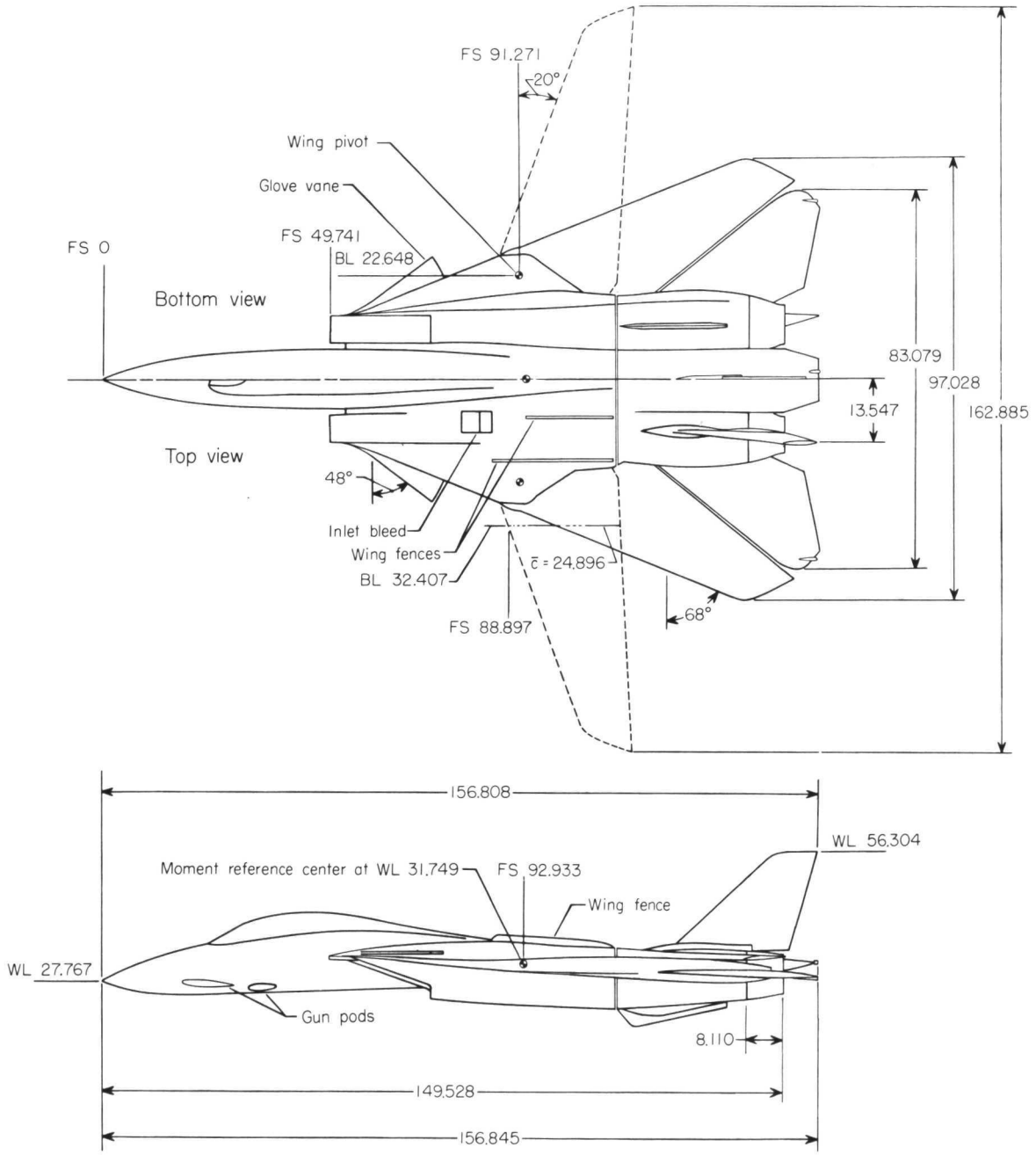

(a) Real afterbody with maximum afterburning nozzles.

Figure 2.- Sketch of model and geometric details of model support. All dimensions are in centimeters unless otherwise specified.

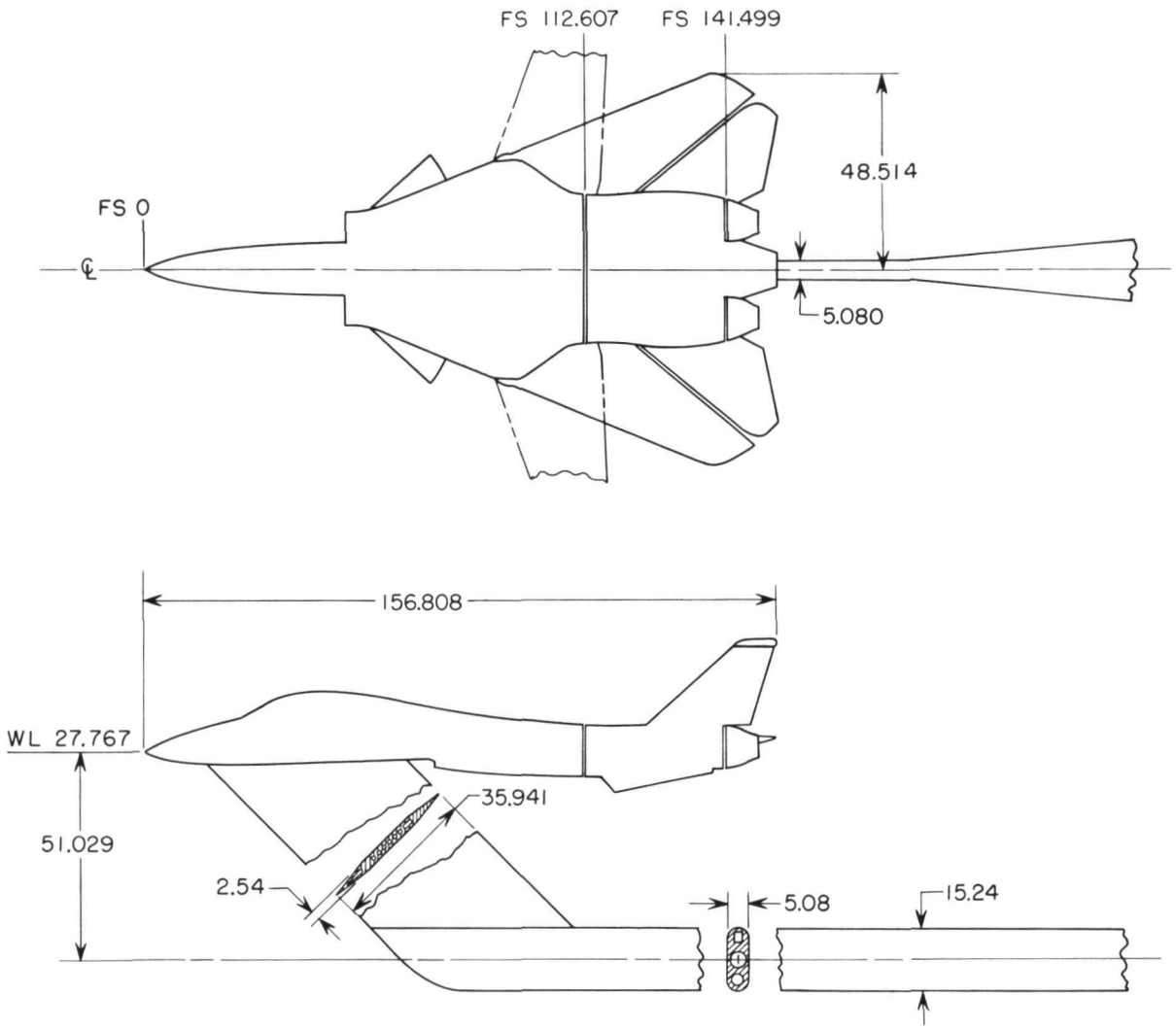

(b) Geometric details of model support.

Figure 2.- Concluded.

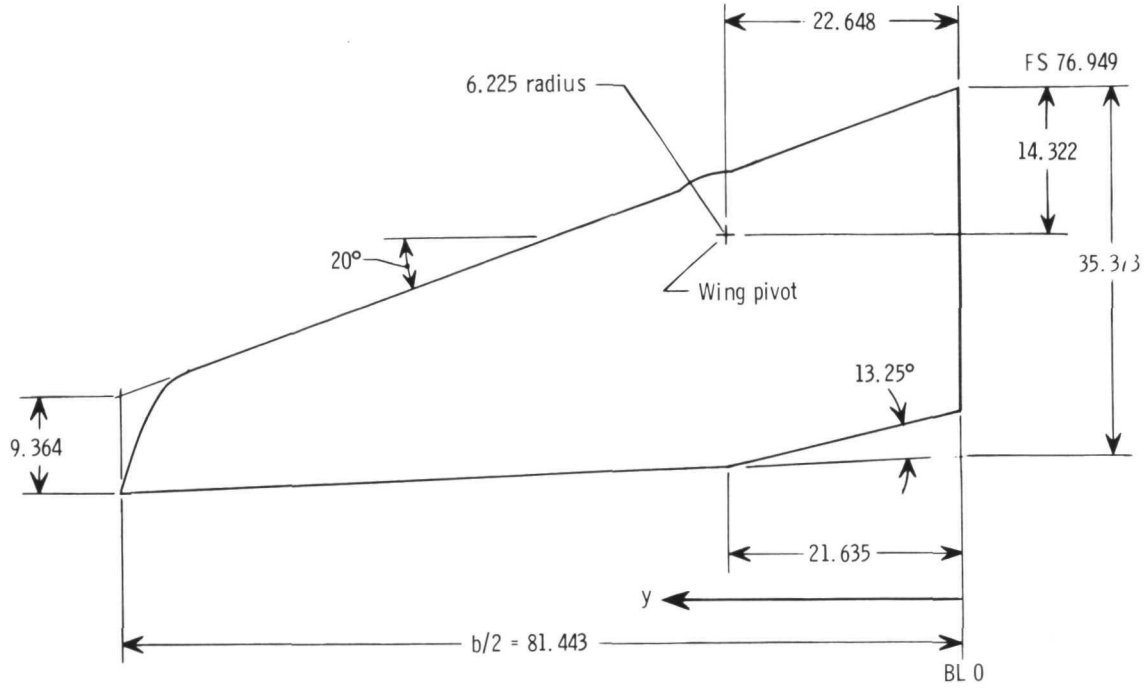

(a) Wing.

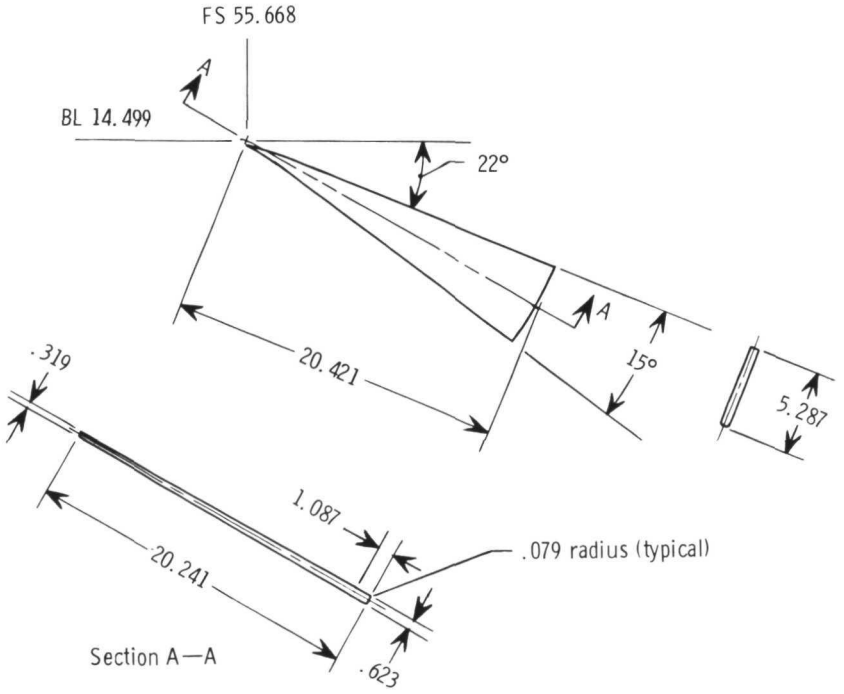

(b) Glove vane.

Figure 3.- Details of model. All dimensions are in centimeters unless otherwise specified.

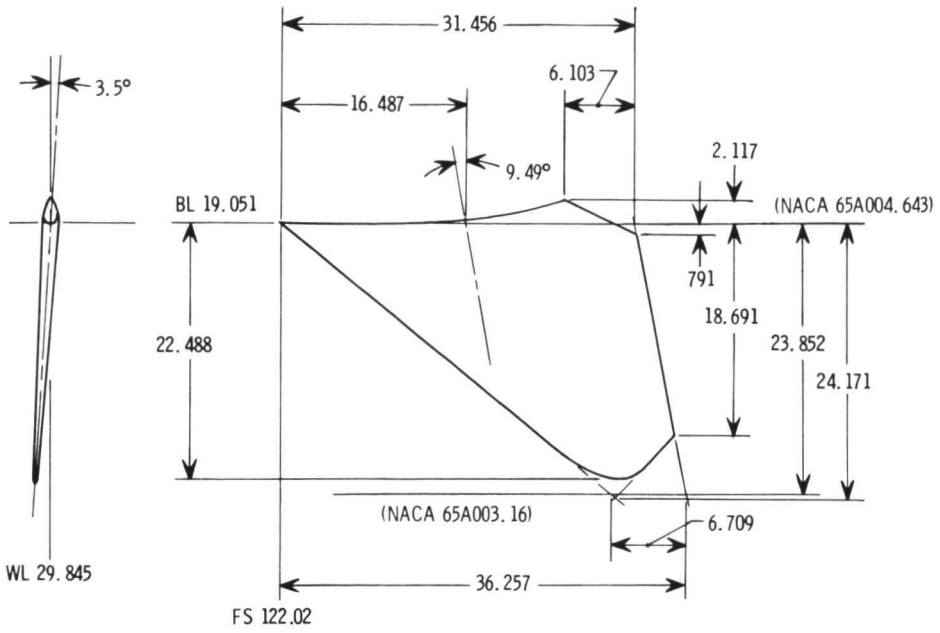

(c) Horizontal tail.

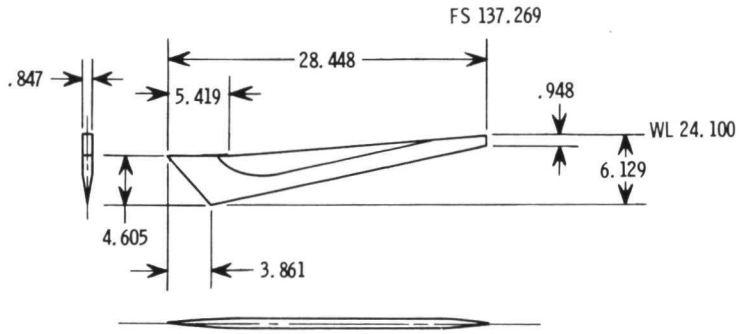

(d) Ventral fin.

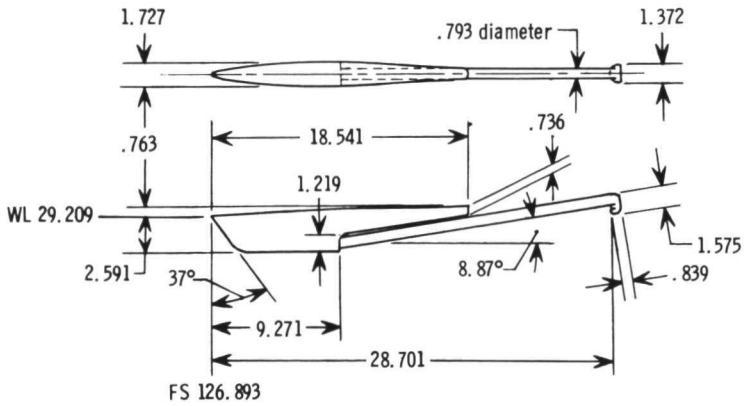

(e) Tail hook and fairing.

Figure 3.- Continued.

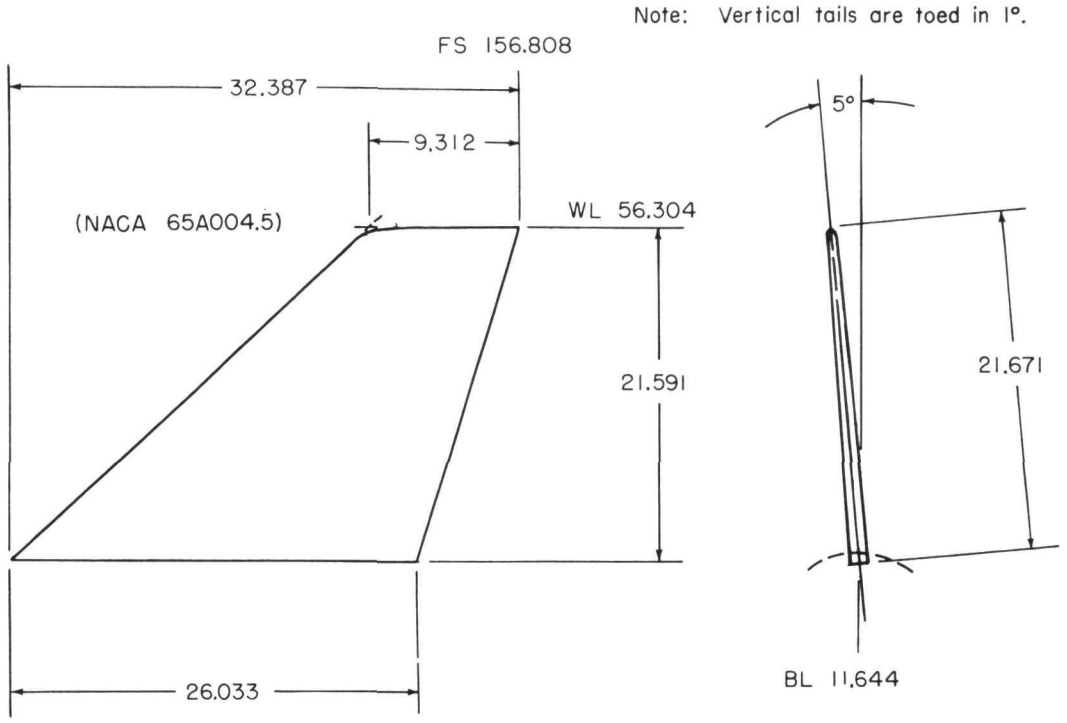

(f) Vertical tails (left shown).

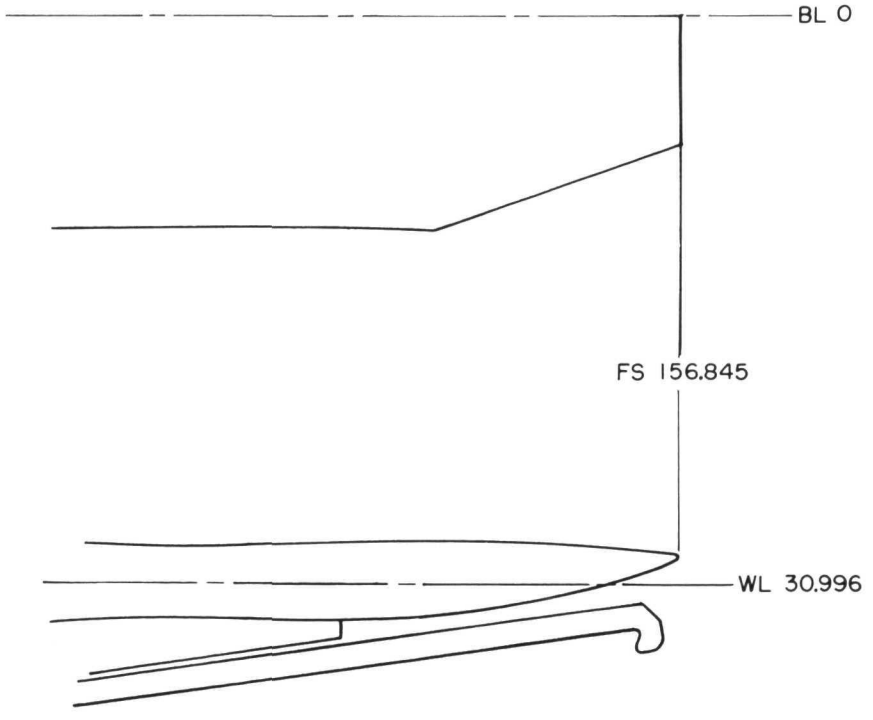

(g) Basic interfairing.

Figure 3.- Continued.

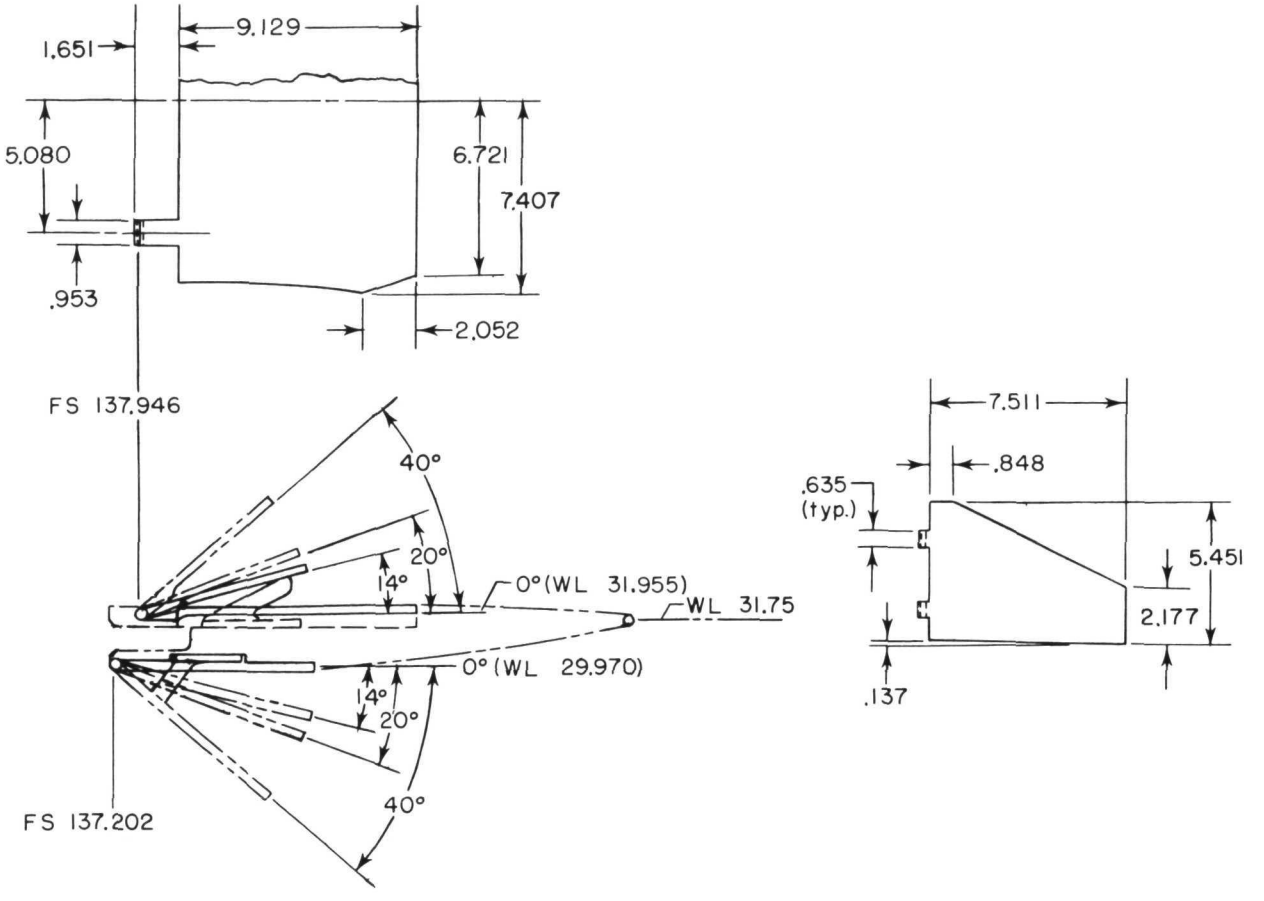

(h) Speed brakes.

Figure 3.- Continued.

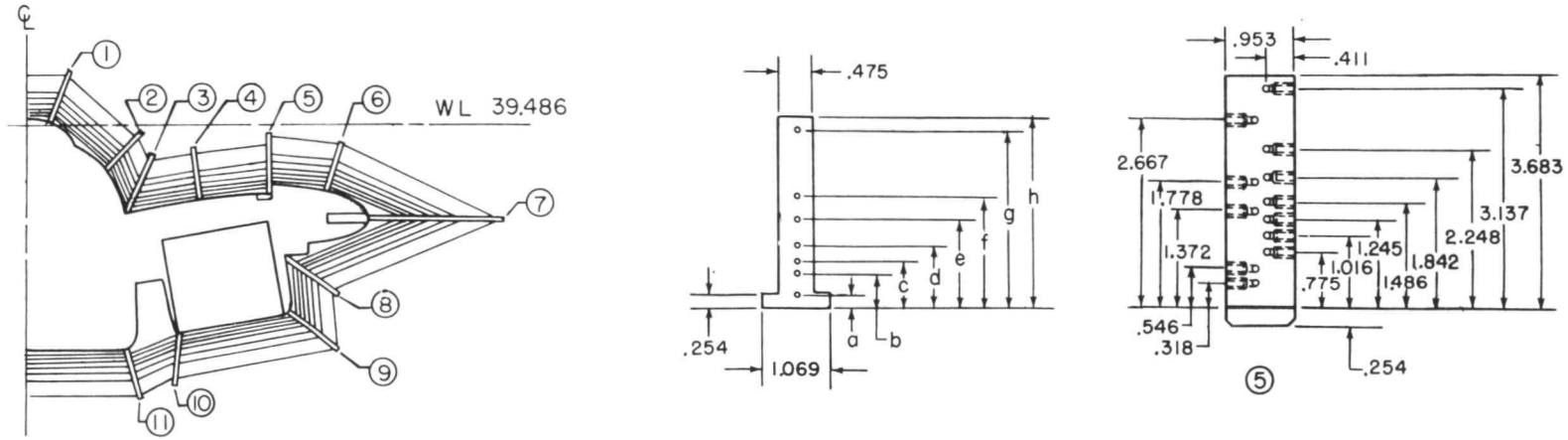

Fence material: Polyester lacing cord V-207, nominal diameter 0.0508.

Dimension								
No.	a	b	c	d	e	f	g	h
1	0.305	0.572	0.800	1.092	1.422	1.880	2.832	3.086
2	.279	.508	.737	.991	1.334	1.753	2.654	2.908
3	.432	.711	1.003	1.346	1.753	2.248	3.353	3.607
4	.229	.457	.686	.940	1.295	1.702	2.591	2.845
6	.305	.572	.787	1.067	1.397	1.829	2.743	2.997
7	1.562	2.210	2.769	3.353	4.293	5.232	7.468	7.722
8	.660	.953	1.245	1.588	2.007	2.477	3.594	3.848
9	.419	.711	1.054	1.308	1.791	2.464	3.581	3.835
10	.229	.457	.686	.991	1.321	1.778	2.692	2.946
11	.318	.559	.787	1.080	1.410	1.854	2.819	3.073

(i) Boundary-layer augmentors ("fences").

Figure 3.- Concluded.

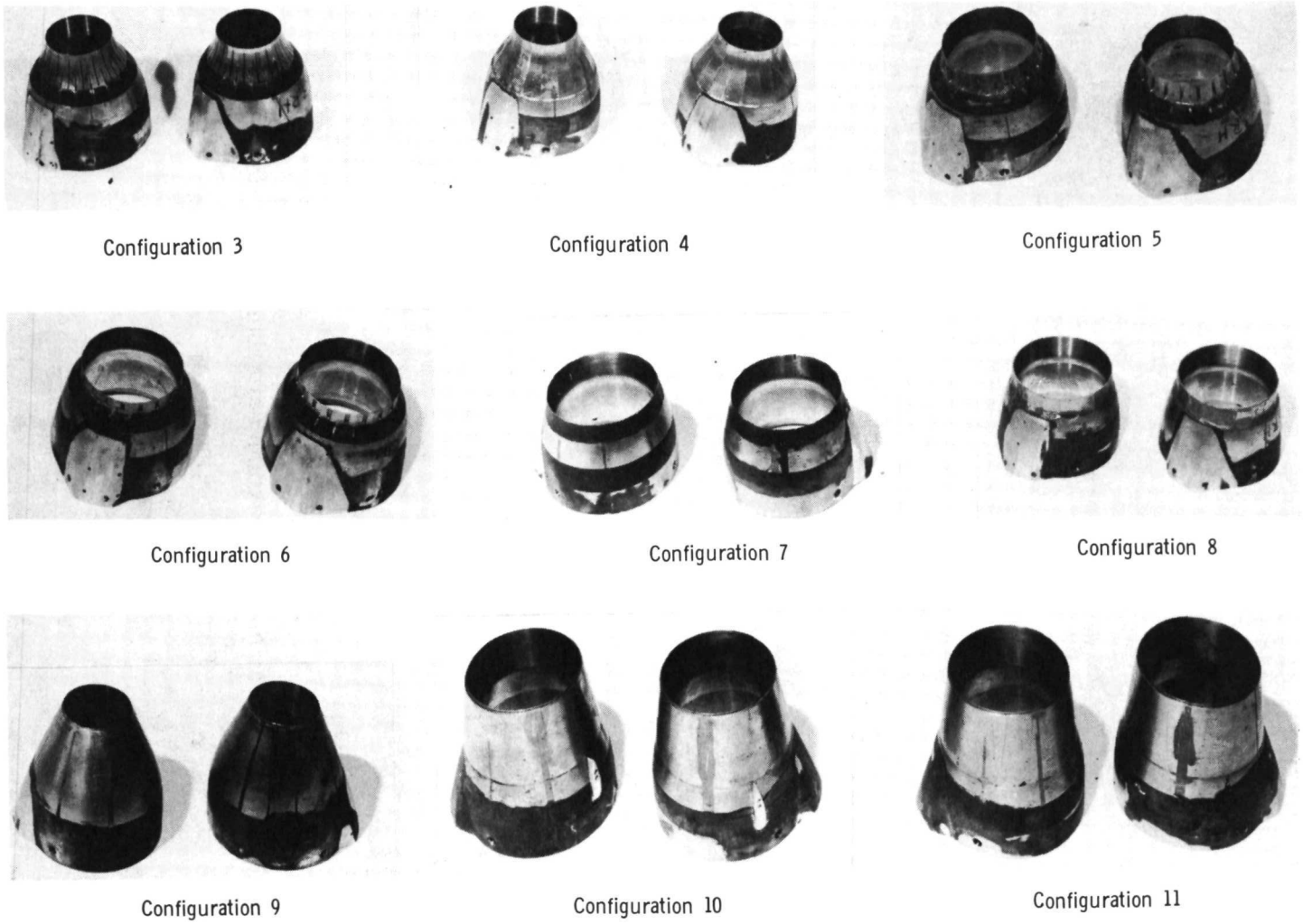

(a) Photographs.

Figure 4.- Photographs and sketches of various nozzle configurations tested. Linear dimensions are in centimeters, angles in degrees.

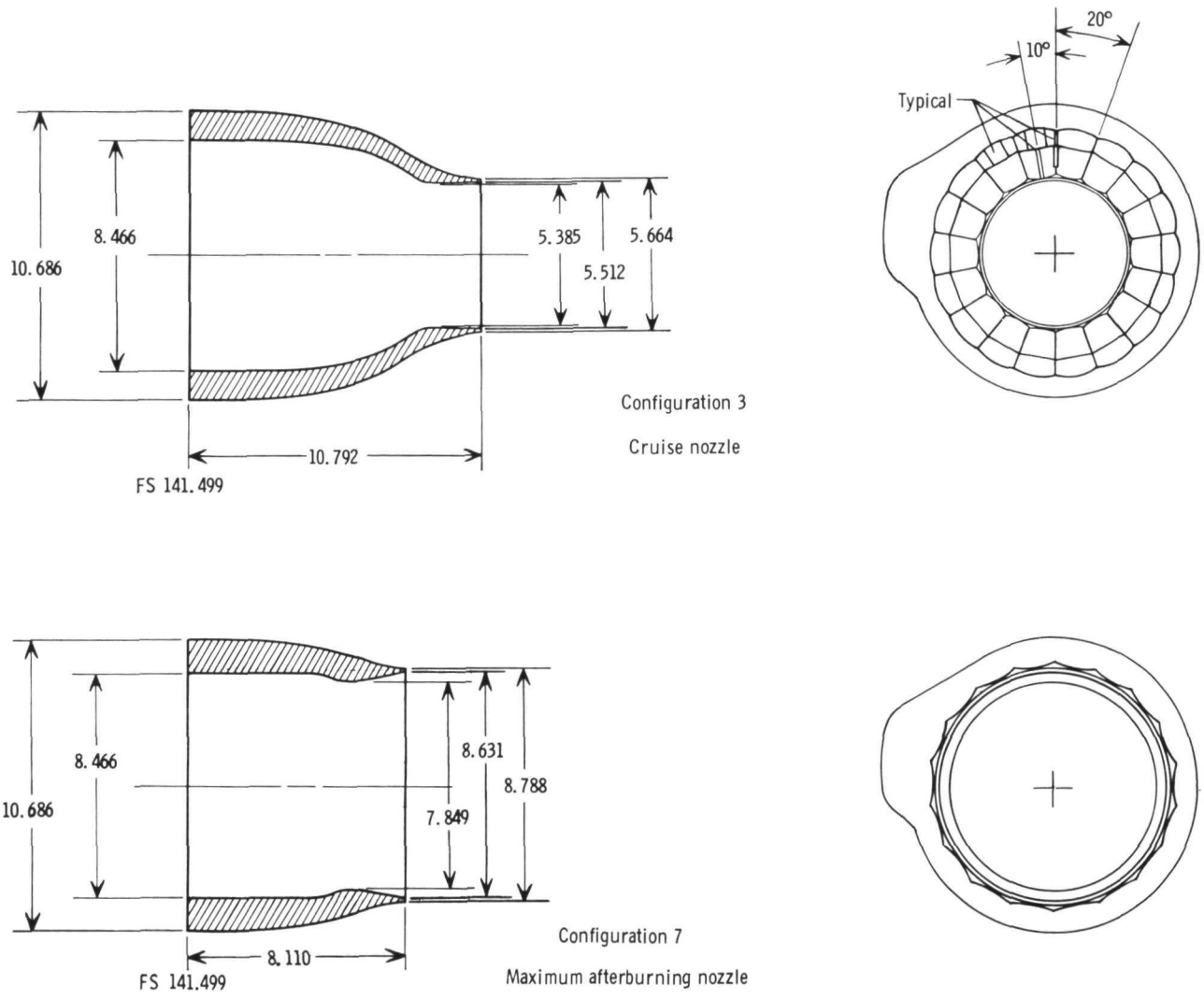

(b) Nozzle type A, cruise and maximum afterburning nozzles.

Figure 4.- Continued.

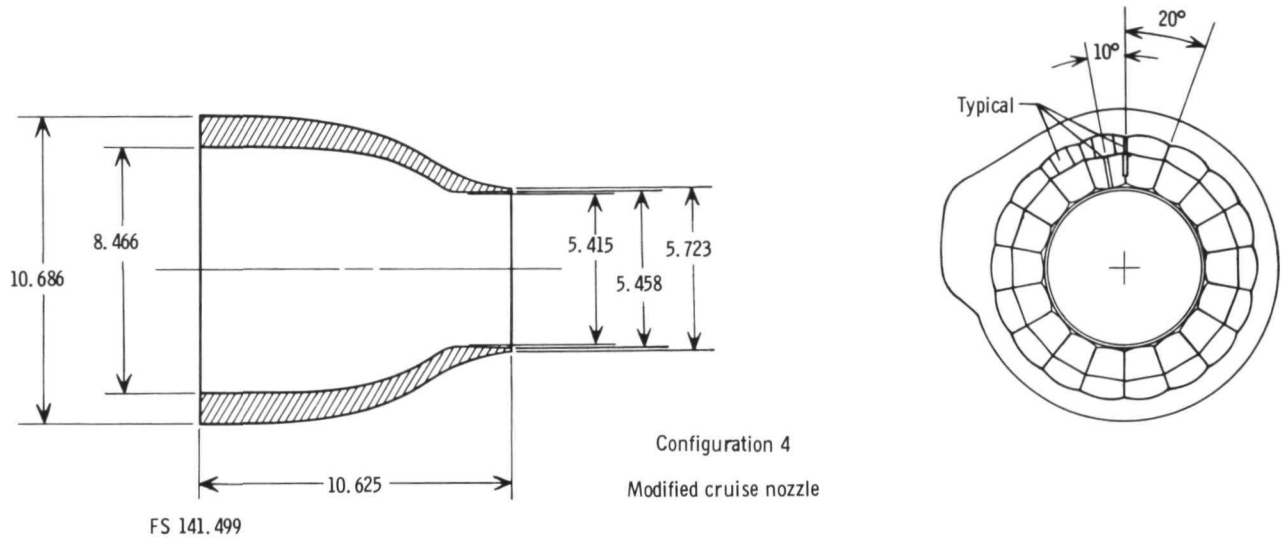

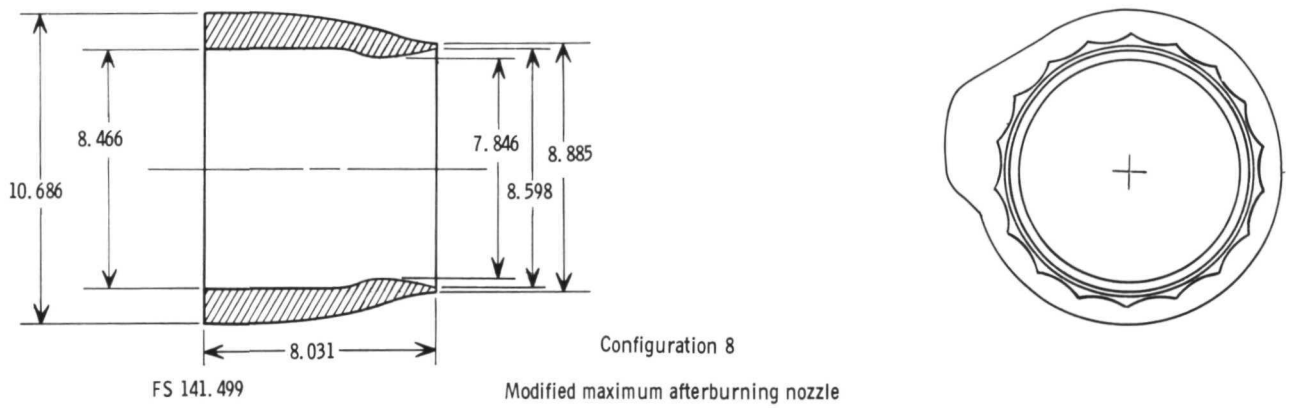

(c) Nozzle type A, modified cruise and modified maximum afterburning nozzle.

Figure 4.- Continued.

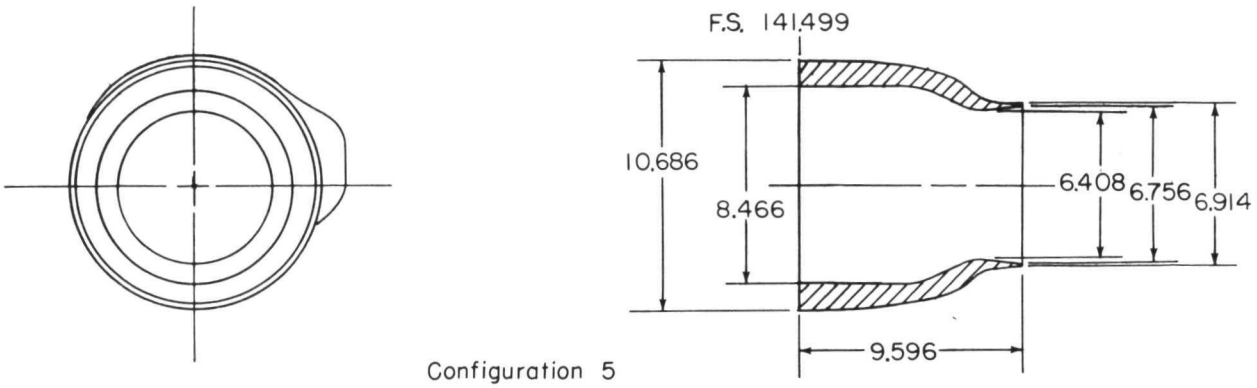

Configuration 5
Low partial afterburning nozzle

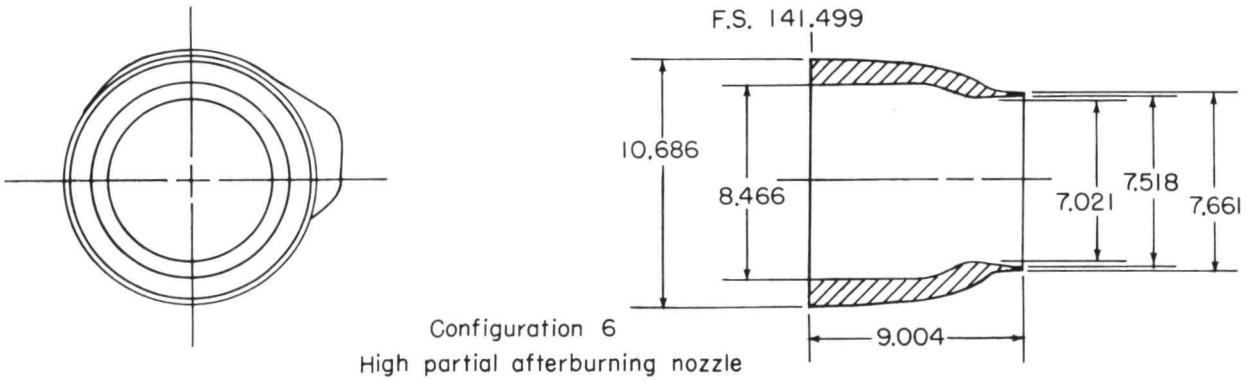

Configuration 6
High partial afterburning nozzle

(d) Nozzle type A, low and high partial afterburning nozzle.

Figure 4.- Continued.

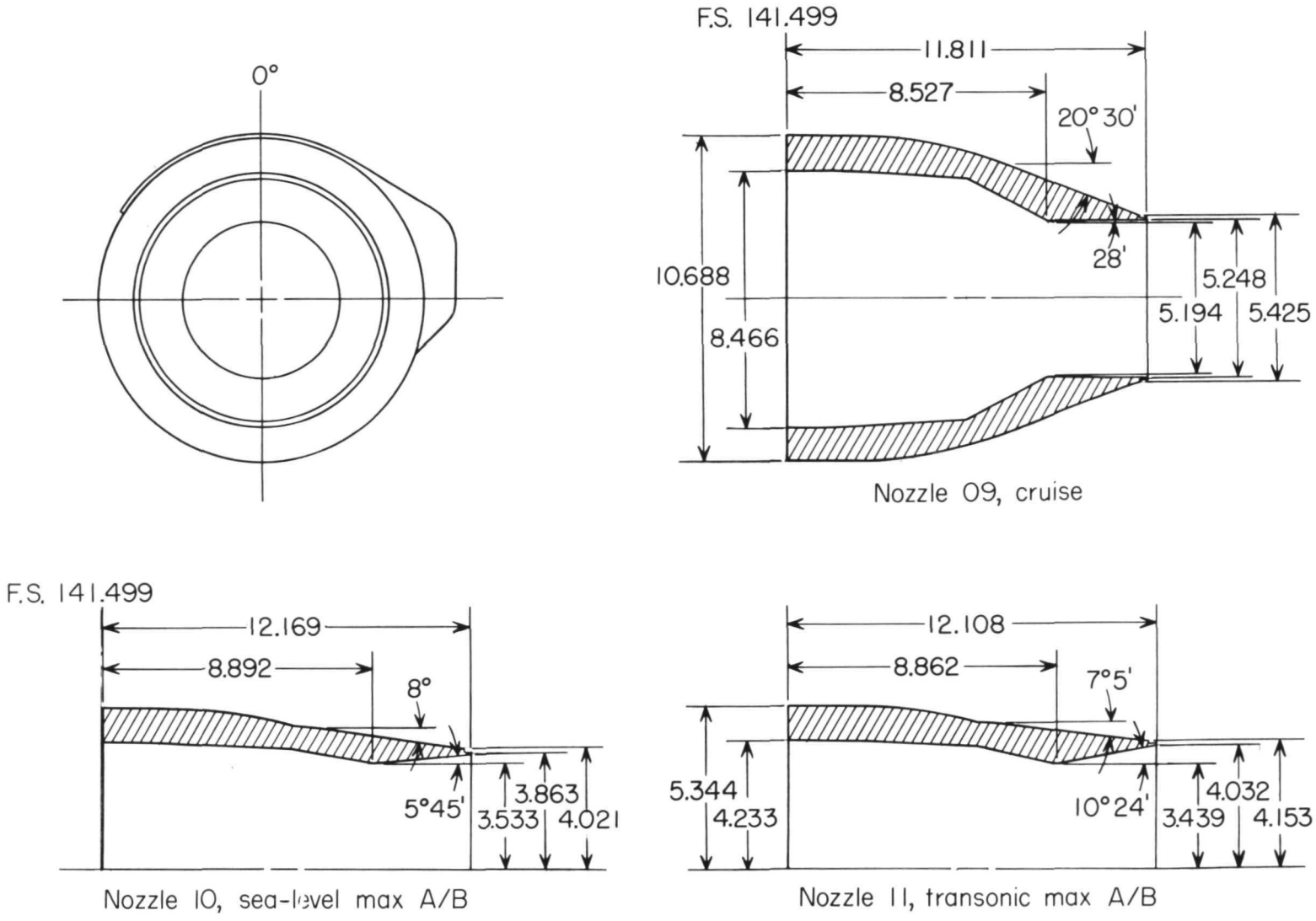

(e) Nozzle type B.

Figure 4.- Concluded.

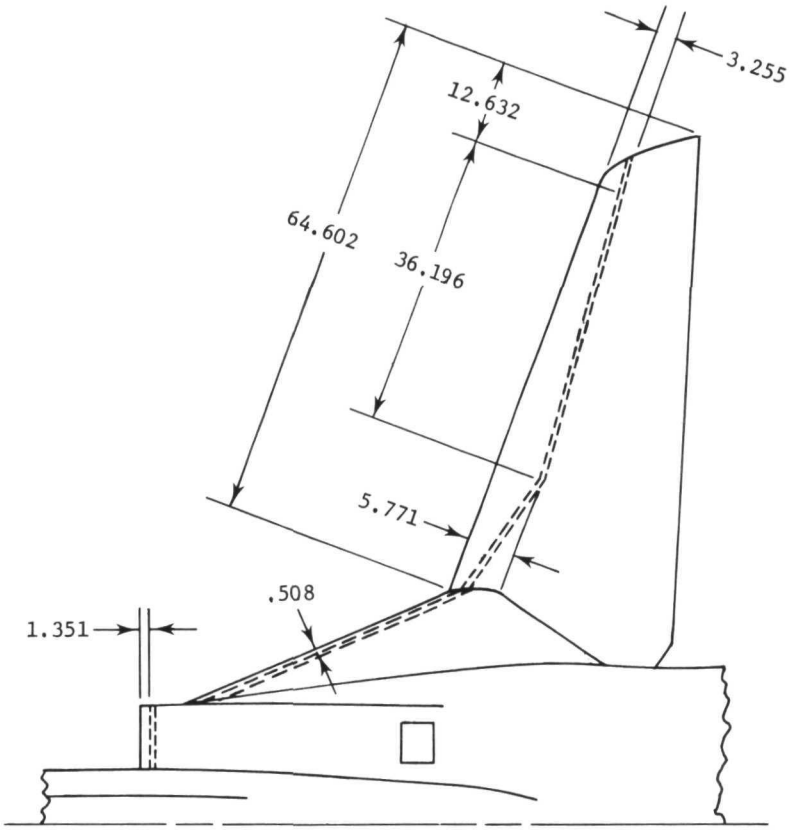

Figure 5.- Sketch showing boundary-layer trip location on wing upper surface for configurations with $\Lambda = 22^{\circ}$. All dimensions are in centimeters.

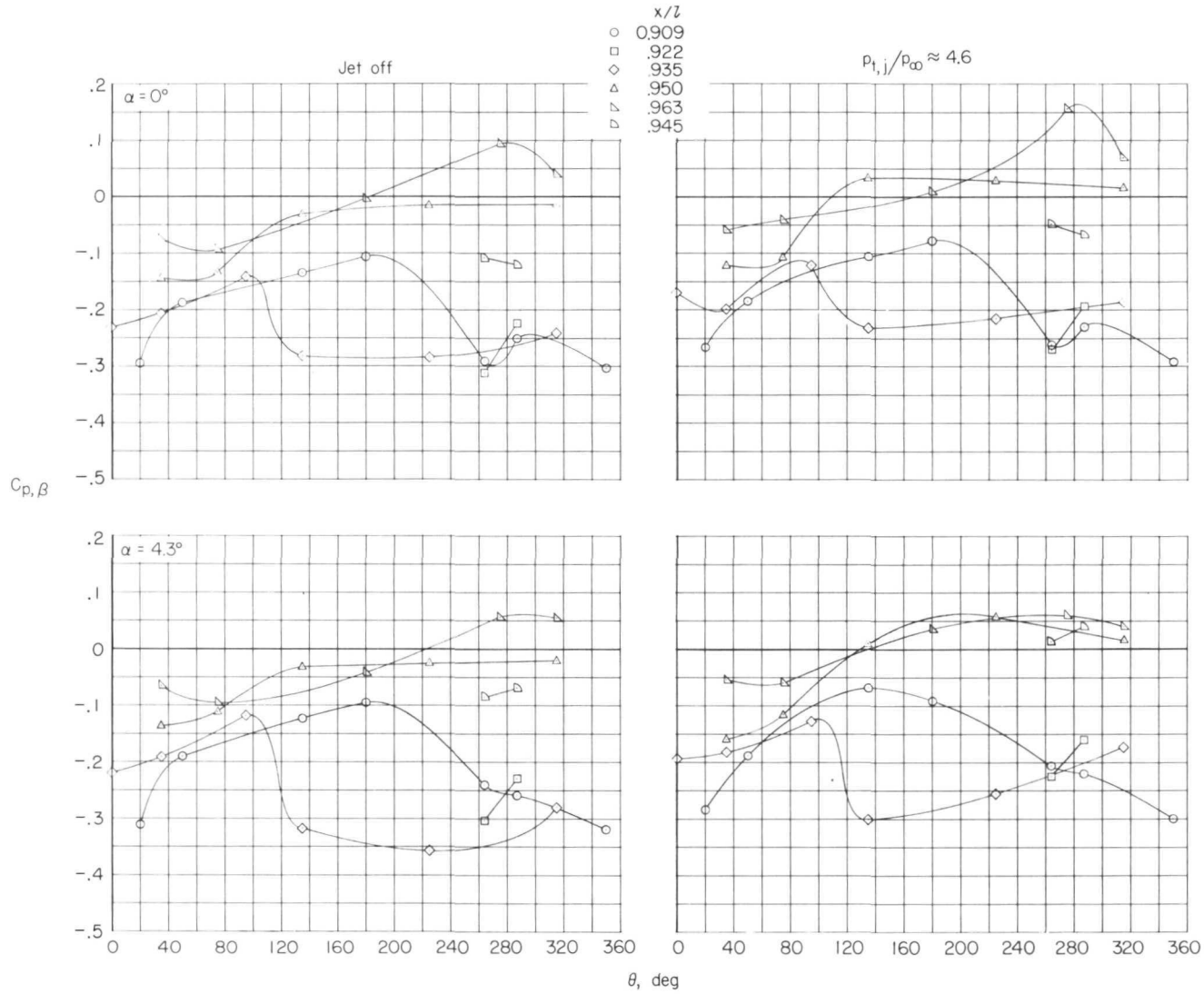

(a) Configuration 3; type A cruise power setting; M = 0.7.

Figure 6.- Typical circumferential distributions of pressure coefficient for the various configurations investigated.

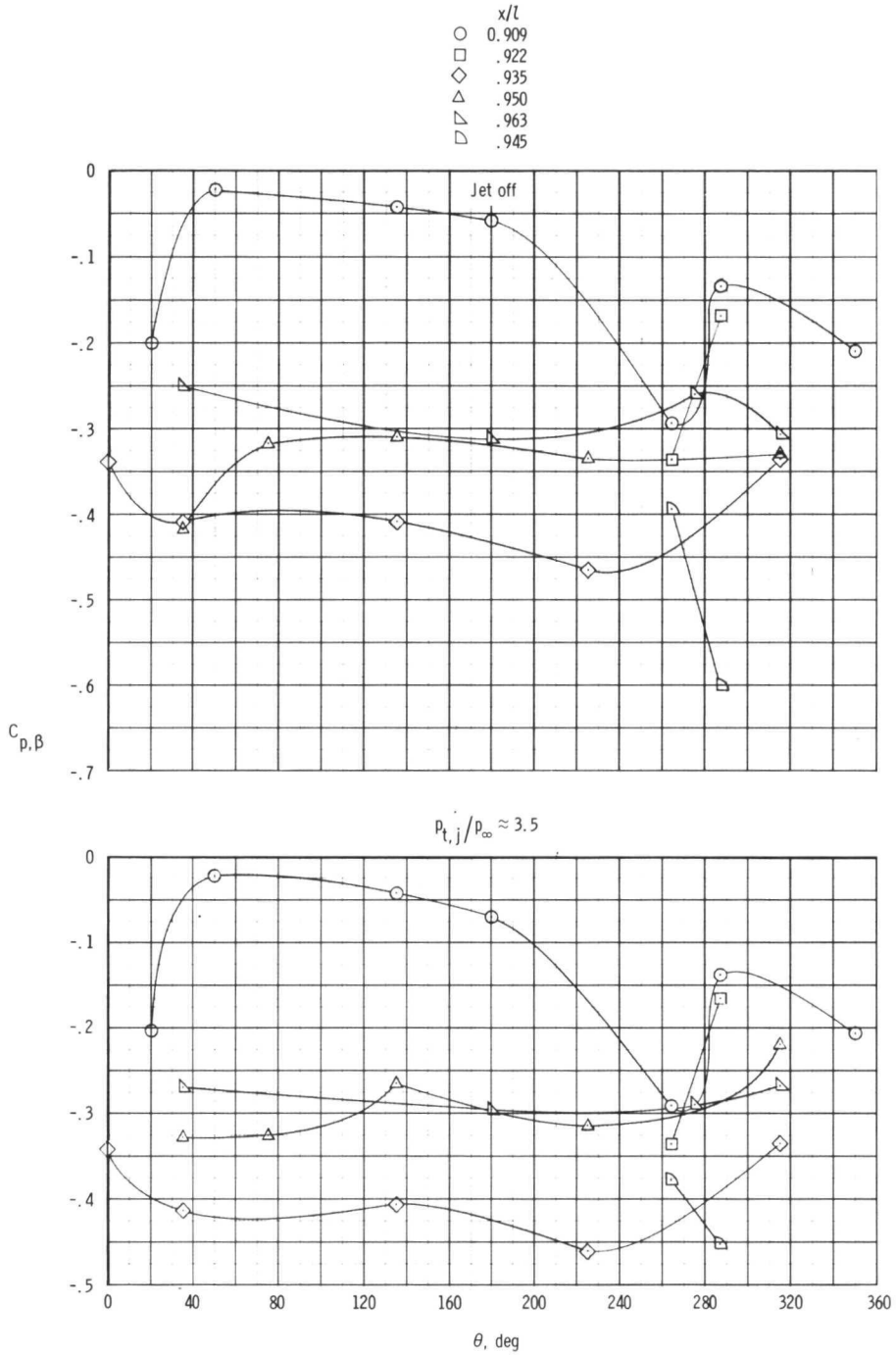

(a) Concluded. M = 1.2; $\alpha = 0^{o}$.

Figure 6.- Continued.

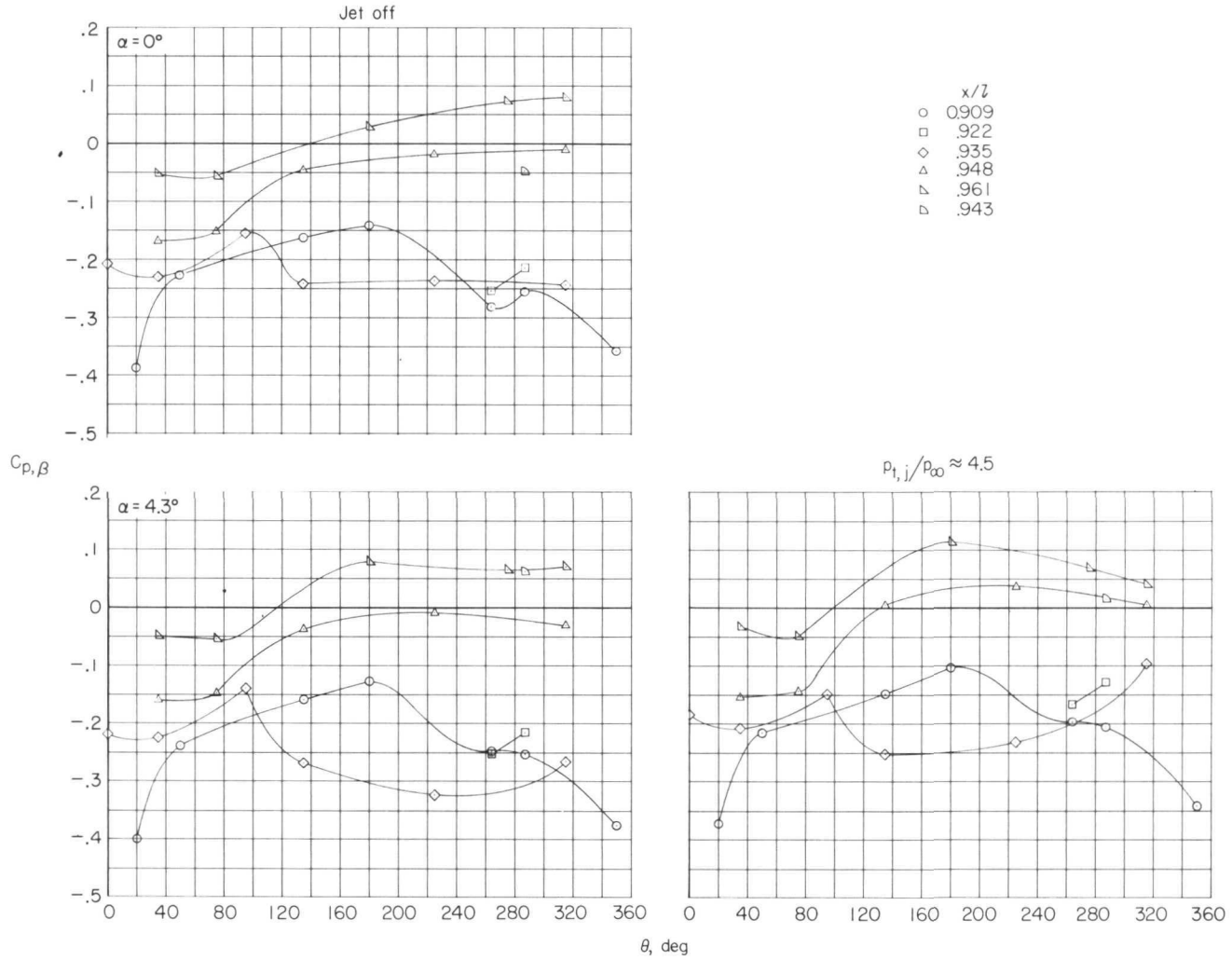

(b) Configuration 4; type A modified cruise power setting; M = 0.7.

Figure 6.- Continued.

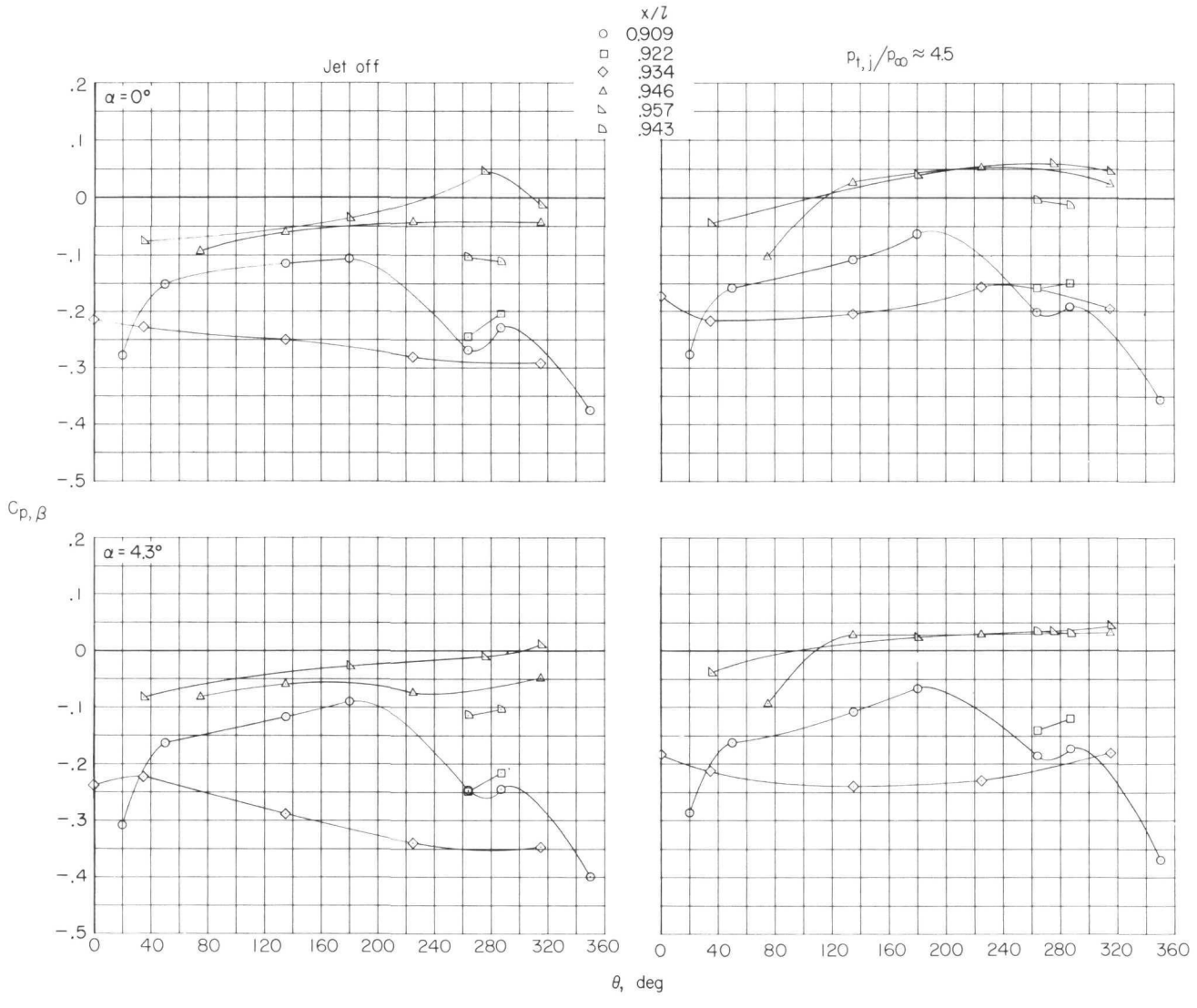

(c) Configuration 5; type A low partial afterburning power setting; M = 0.7.

Figure 6.- Continued.

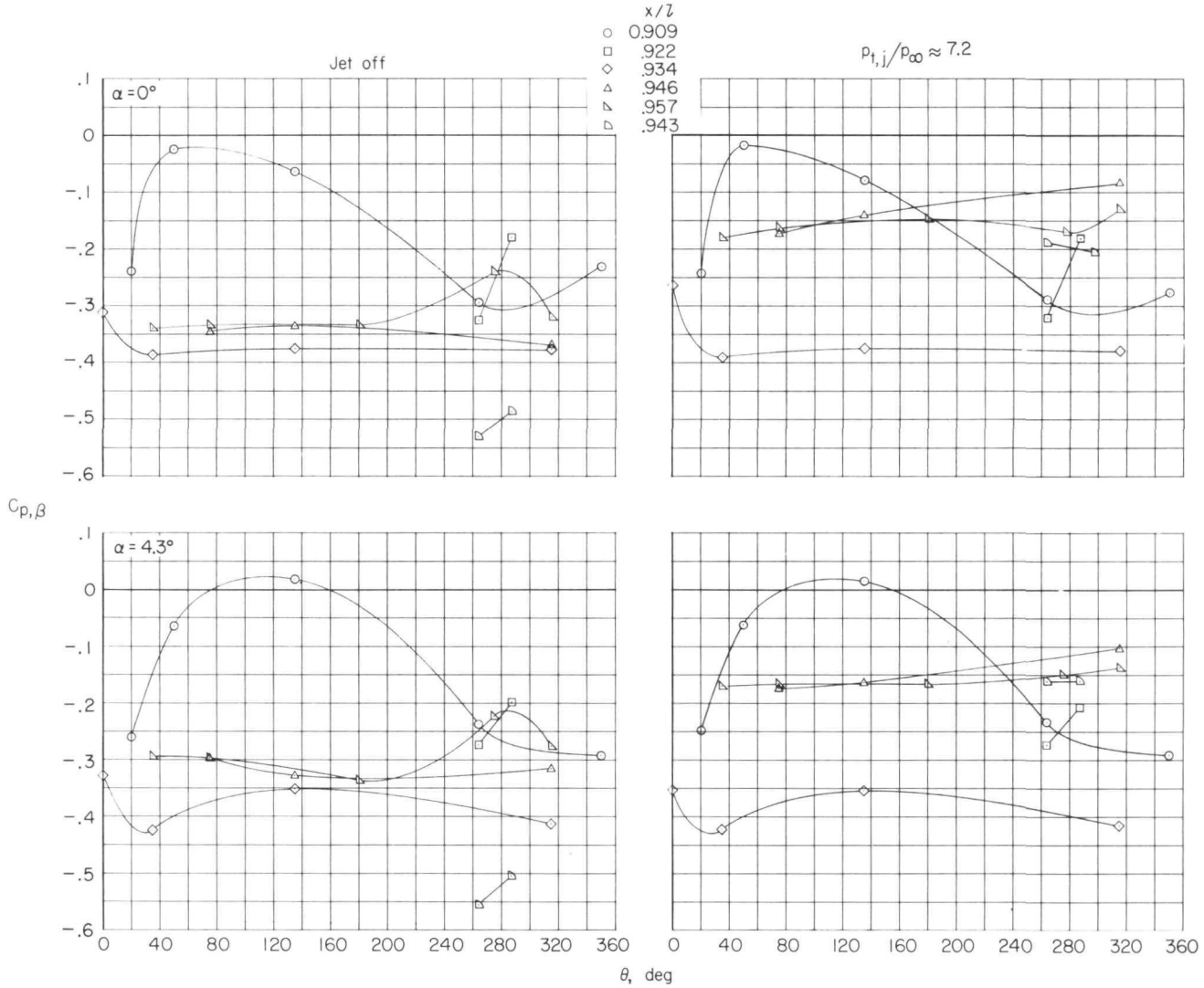

(c) Continued. M = 1.2.

Figure 6.- Continued.

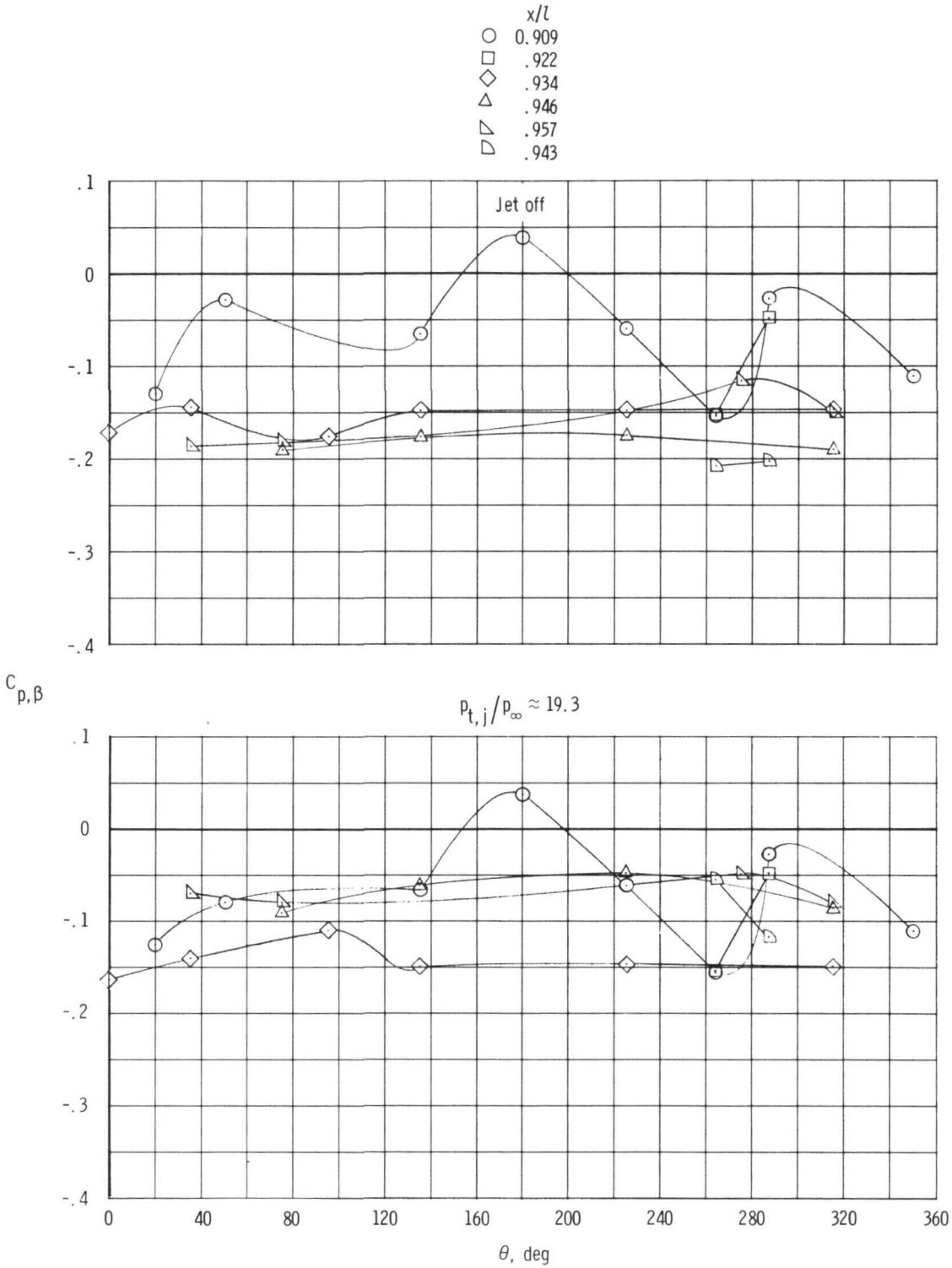

(c) Concluded. M = 2.2; $\alpha = 0^{o}$.

Figure 6.- Continued.

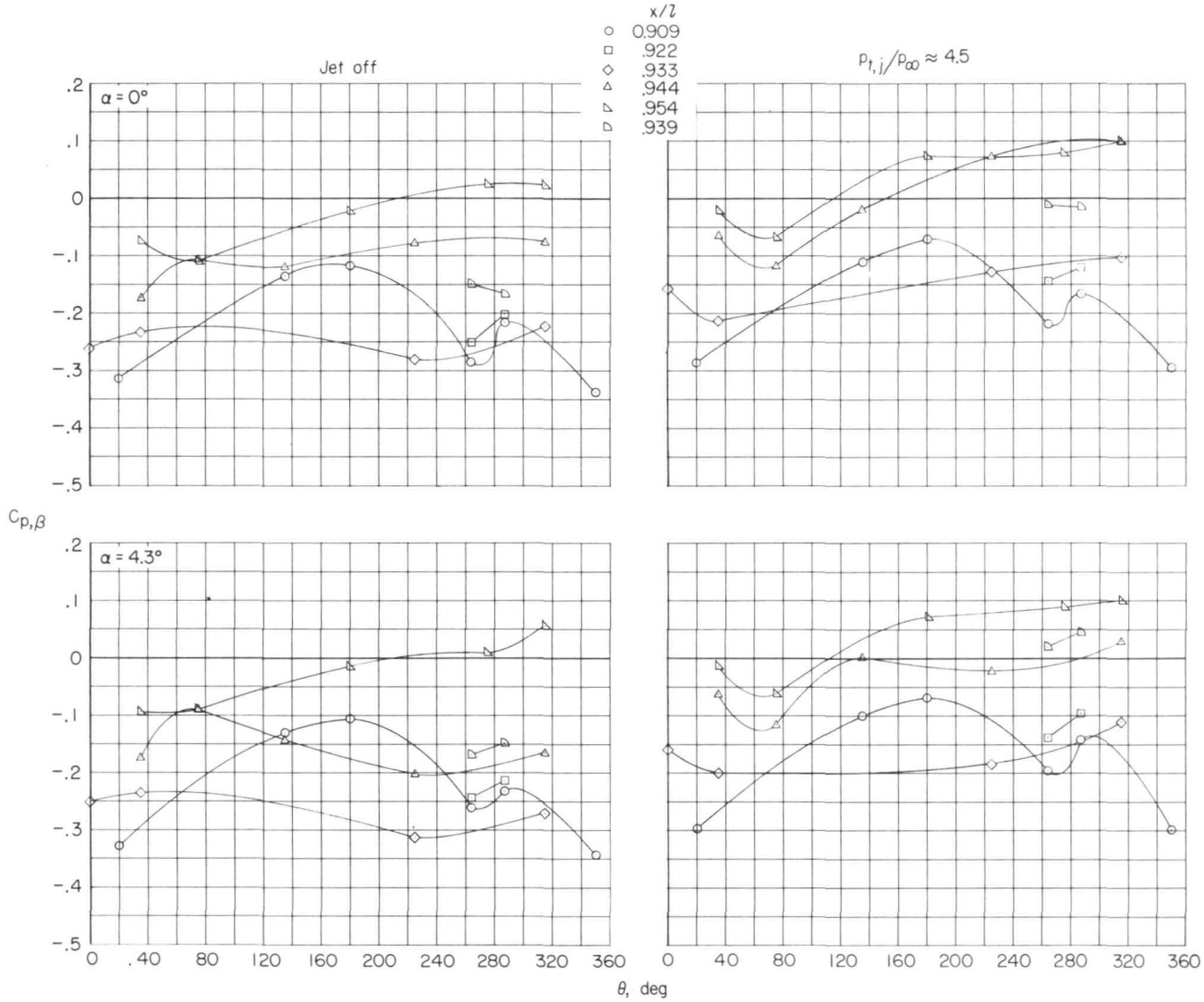

(d) Configuration 6; type A high partial afterburning power setting; M = 0.7.

Figure 6.- Continued.

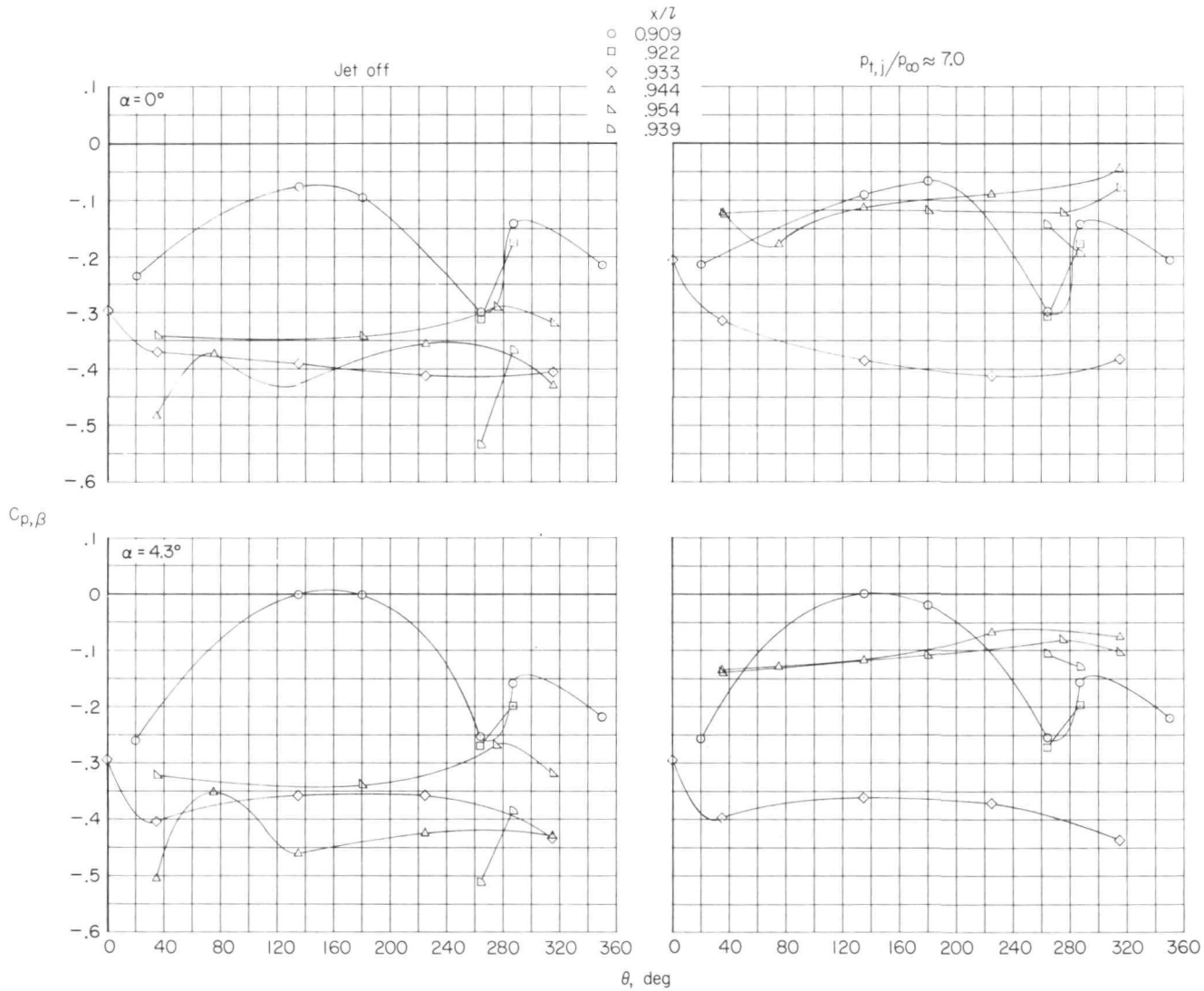

(d) Continued. M = 1.2.

Figure 6.- Continued.

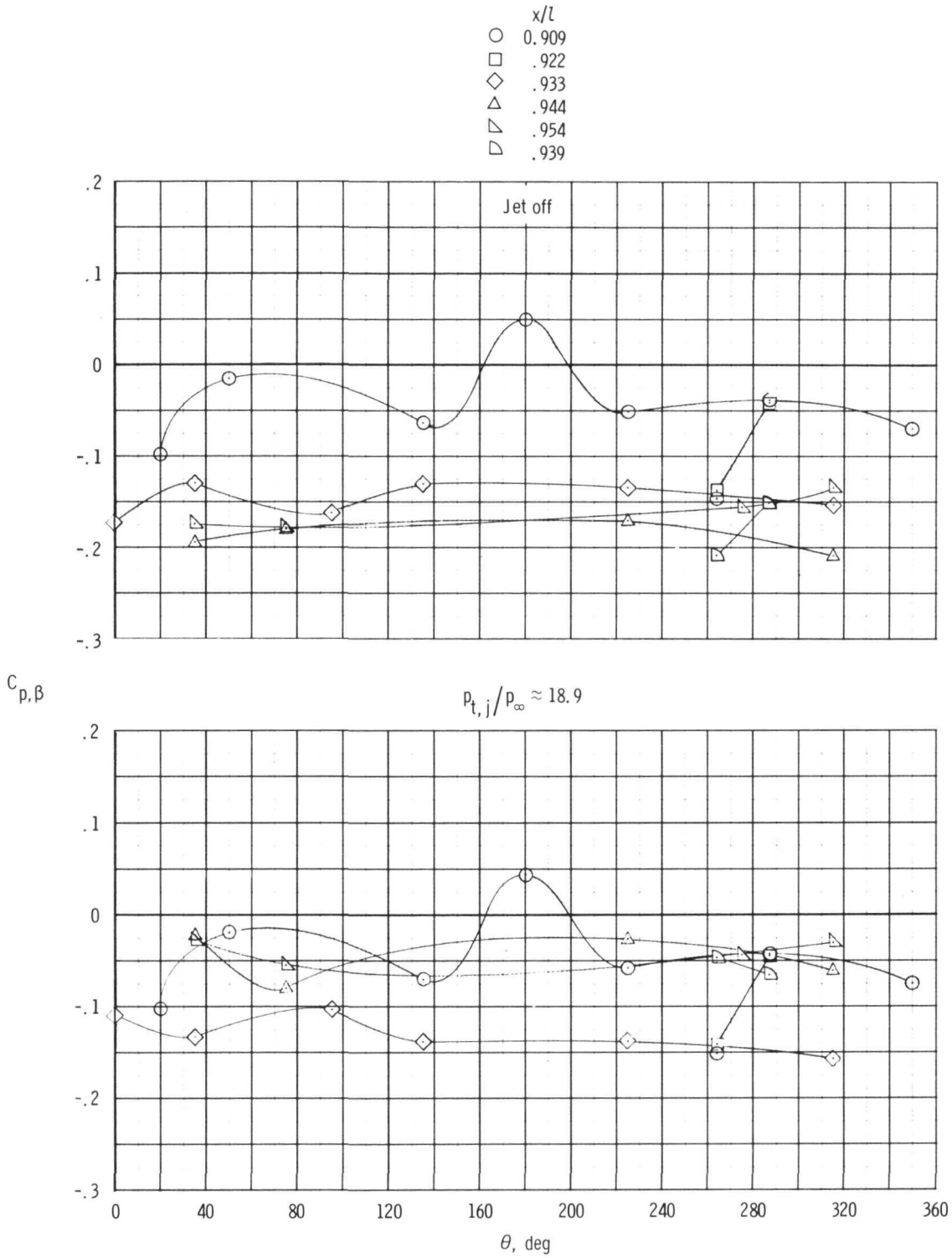

(d) Concluded. M = 2.2; $\alpha = 0^{\circ}$.

Figure 6.- Continued.

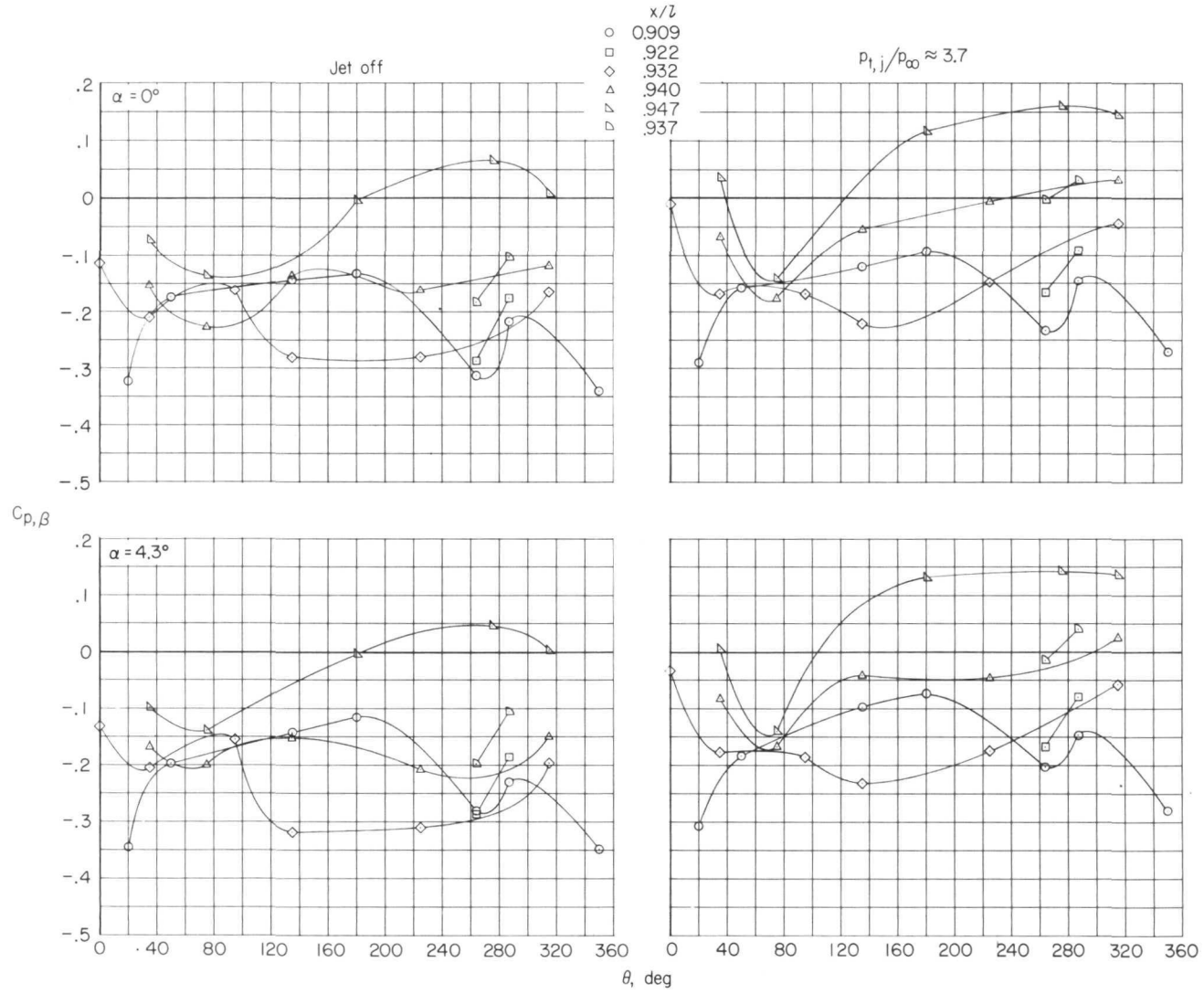

(e) Configuration 7; type A maximum afterburning power setting; M = 0.7.

Figure 6.- Continued.

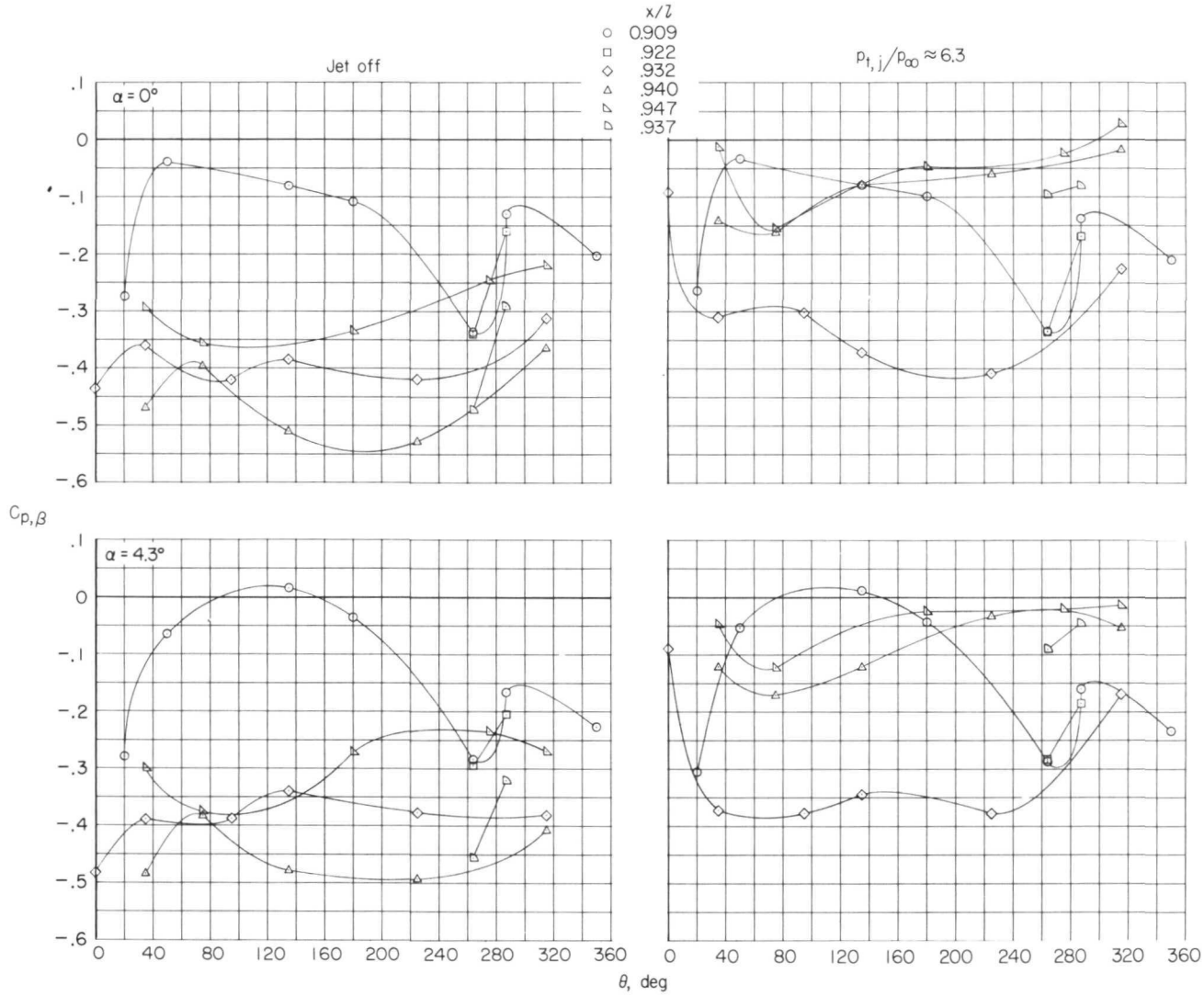

(e) Continued. M = 1.2.

Figure 6.- Continued.

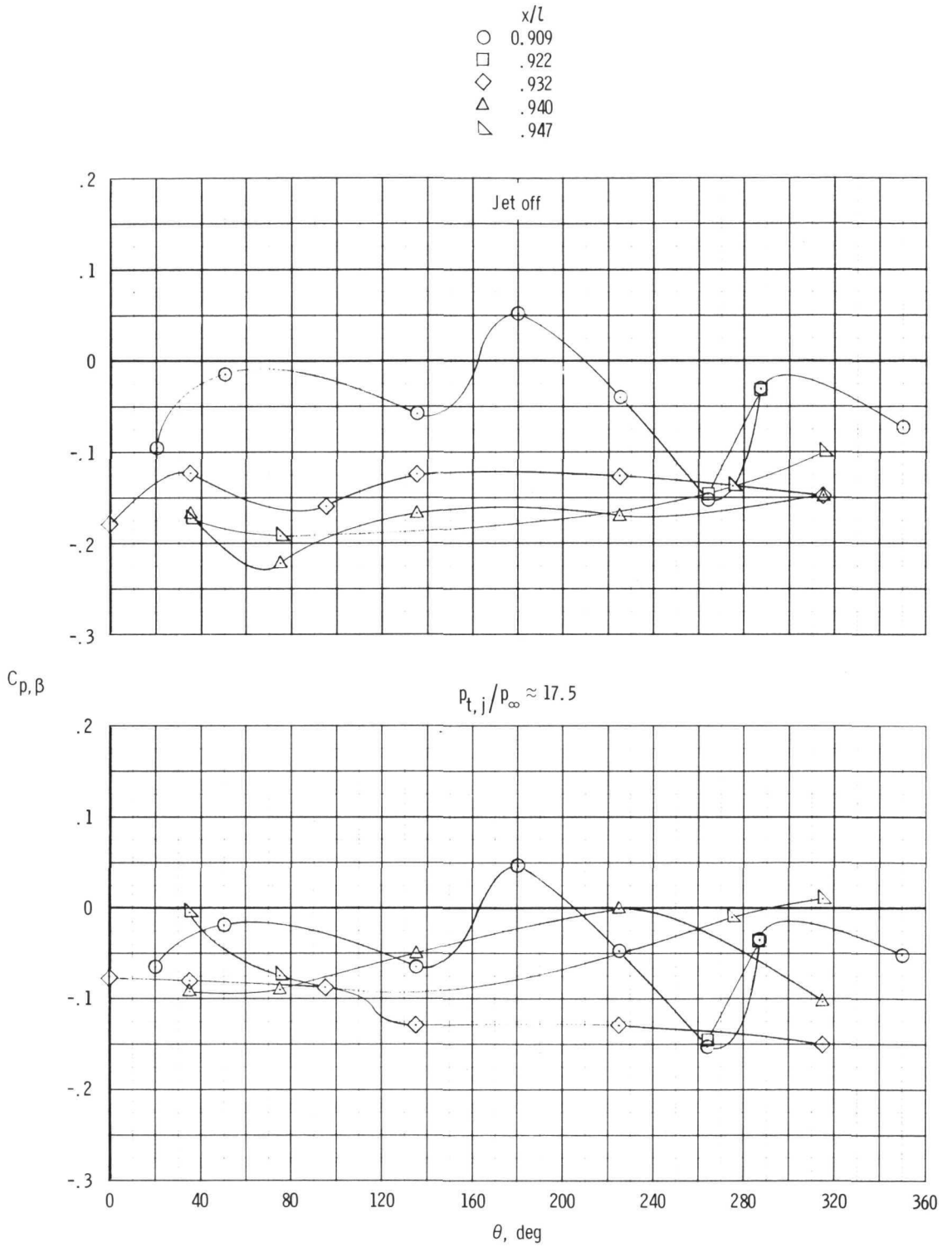

(e) Concluded. M = 2.2; $\alpha = 0^{O}$.

Figure 6.- Continued.

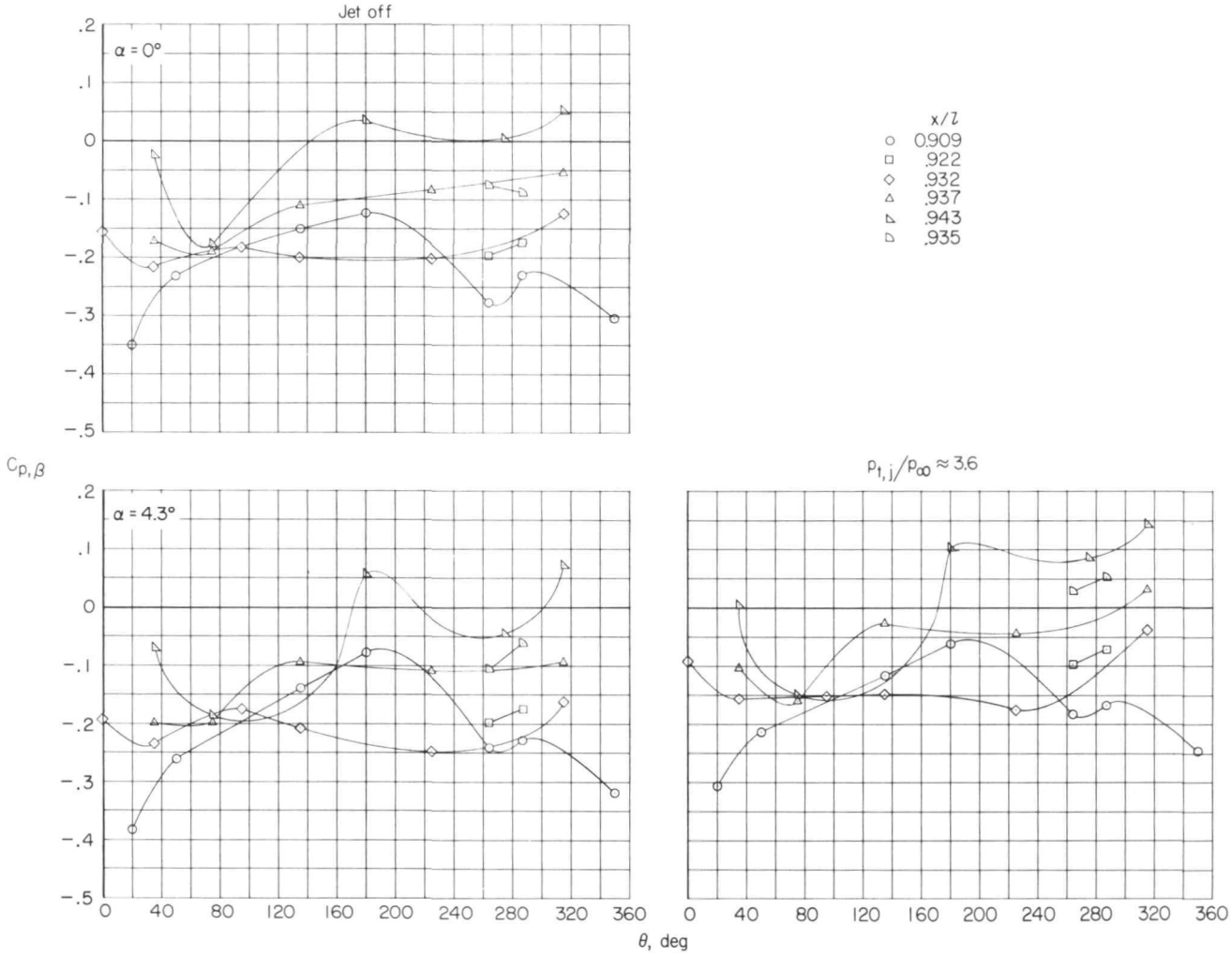

(f) Configuration 8; type A modified maximum afterburning power setting; M = 0.7.

Figure 6.- Continued.

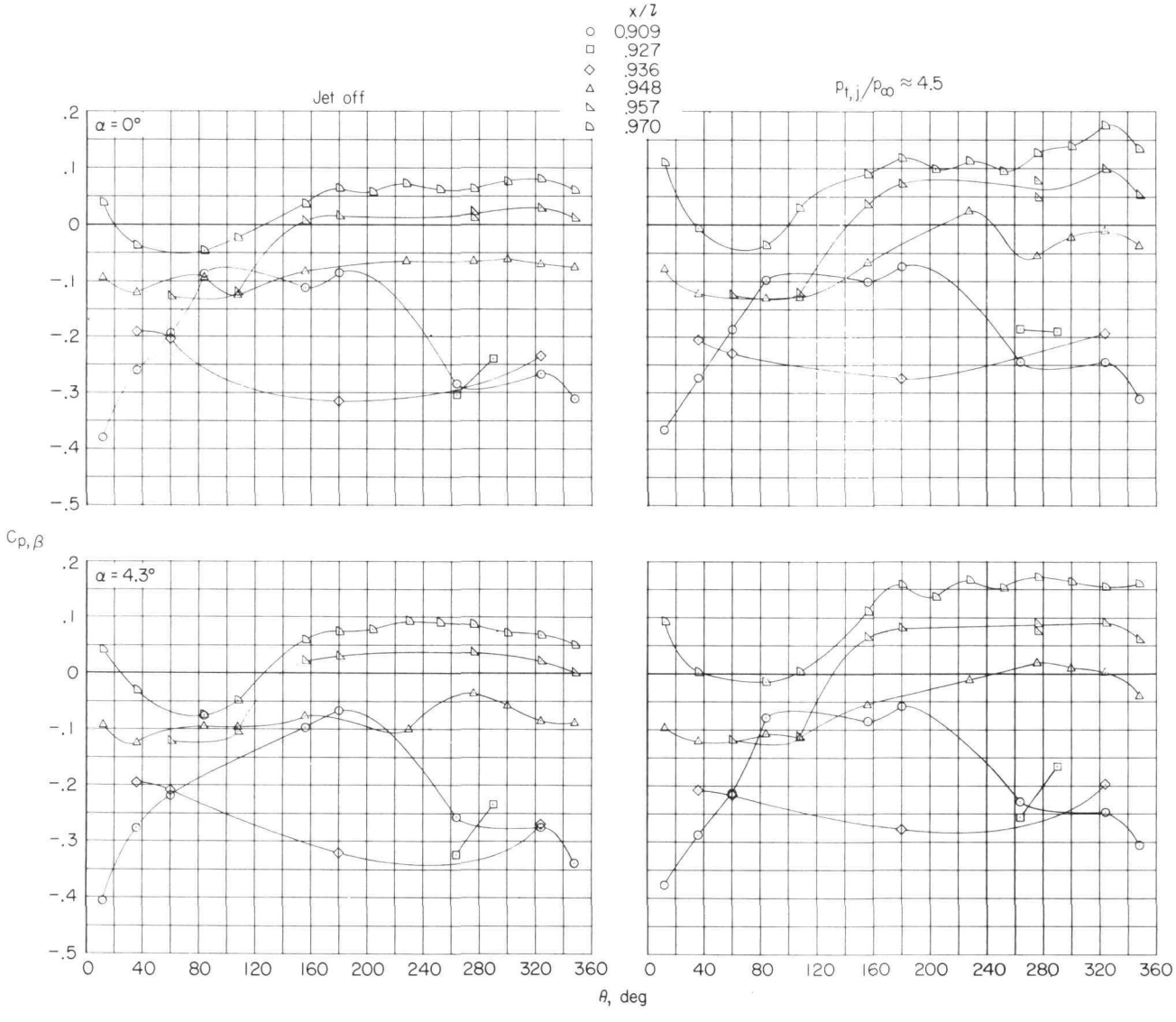

(g) Configuration 9; type B cruise power setting; M = 0.7.

Figure 6.- Continued.

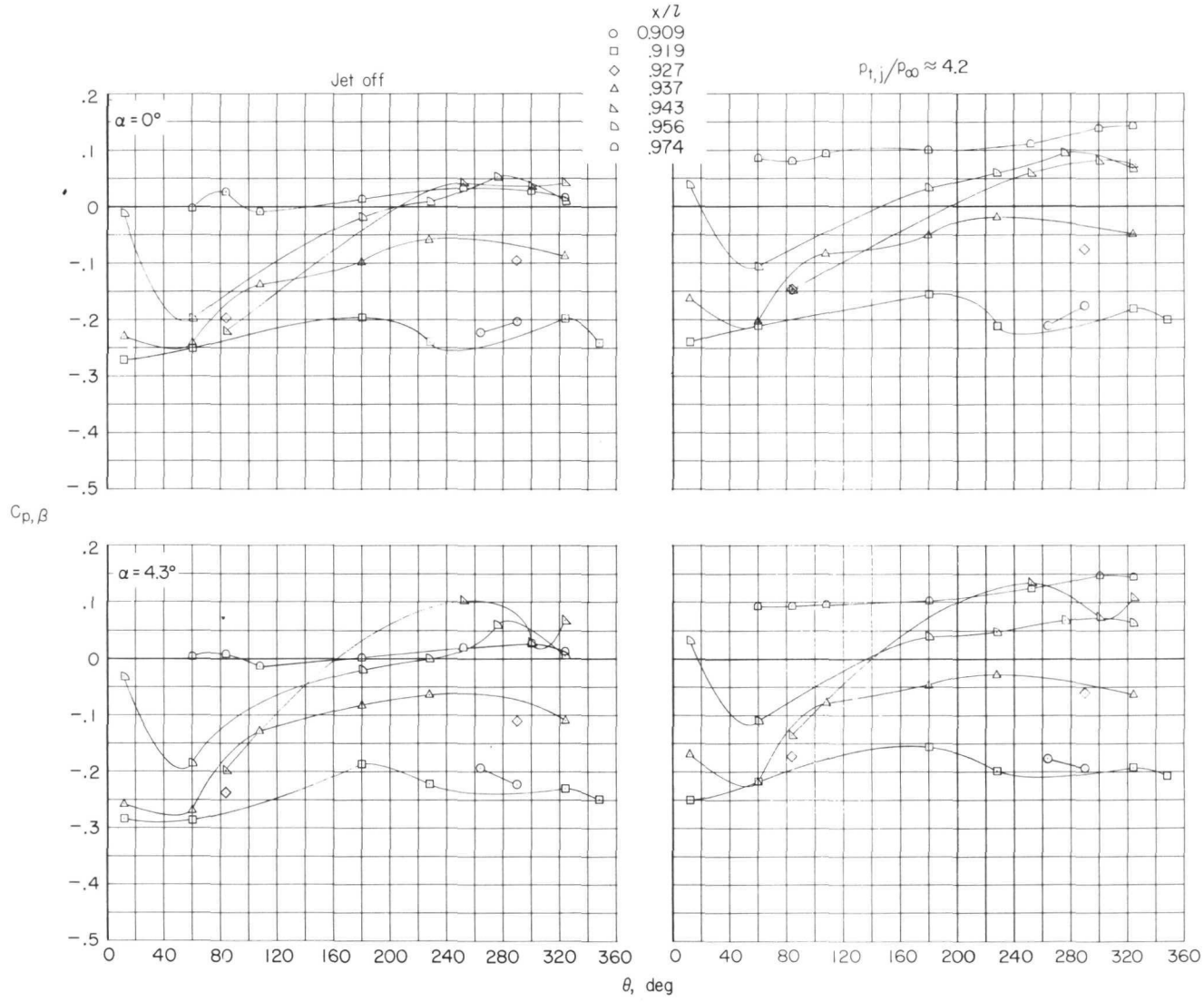

(h) Configuration 10; type B sea level maximum afterburning power setting; M = 0.7.

Figure 6.- Continued.

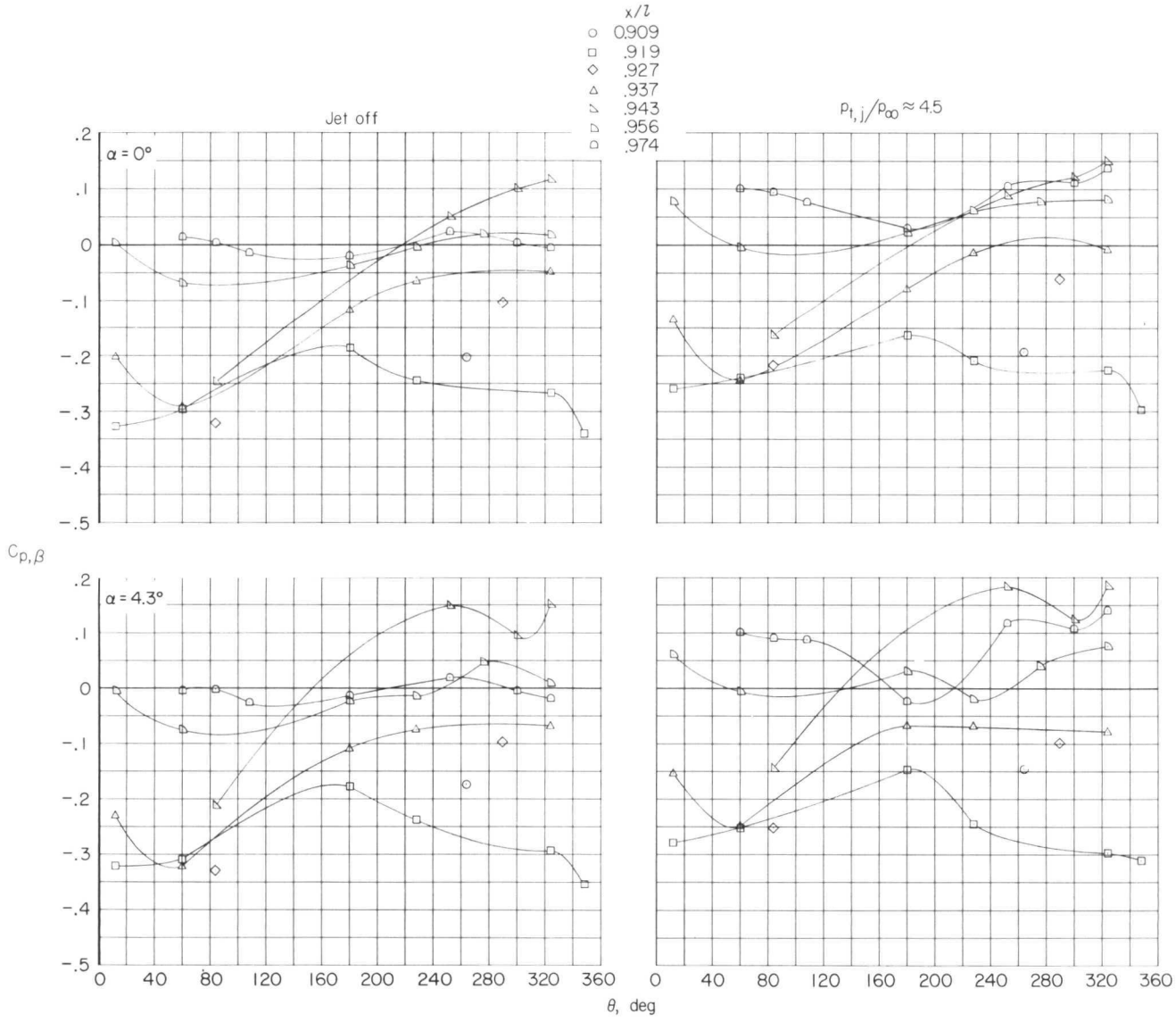

(i) Configuration 11; type B transonic maximum afterburning power setting; M = 0.7.

Figure 6.- Continued.

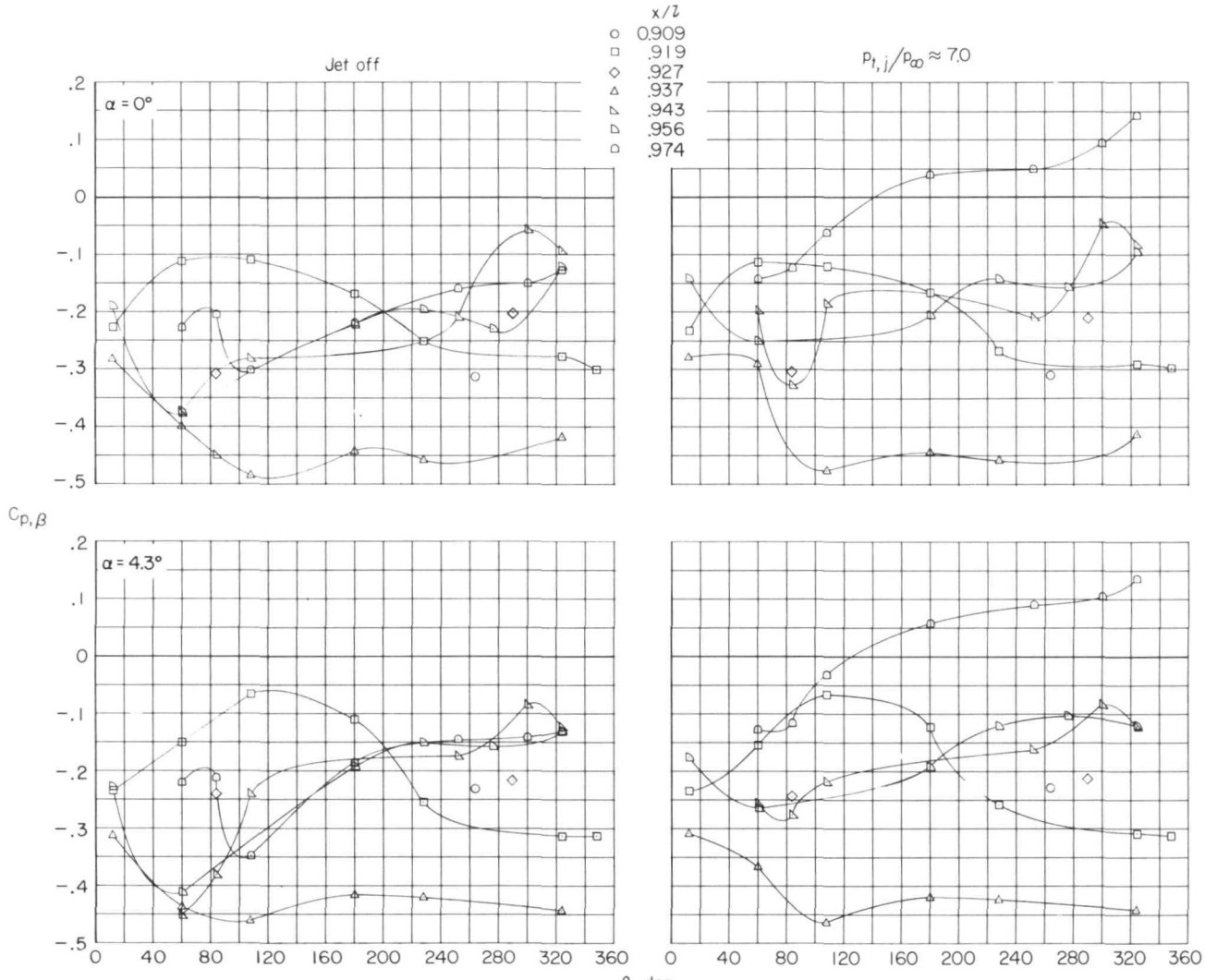

(i) Concluded. M = 1.2.

Figure 6.- Concluded.

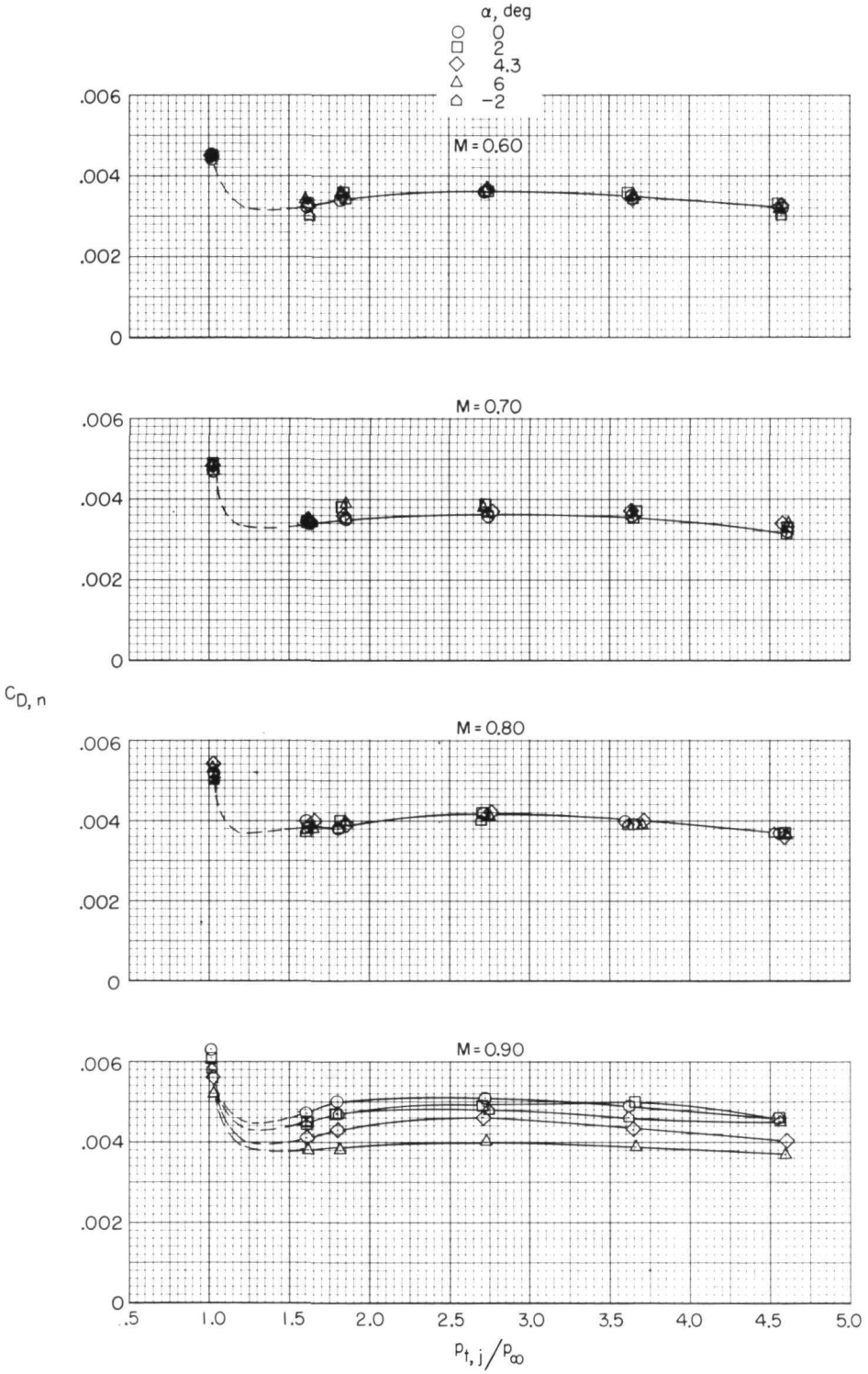

(a) Drag coefficient.

Figure 7.- Effect of jet total-pressure ratio on the nozzle aerodynamic characteristics. Configuration 3 (cruise power setting, nozzle type A).

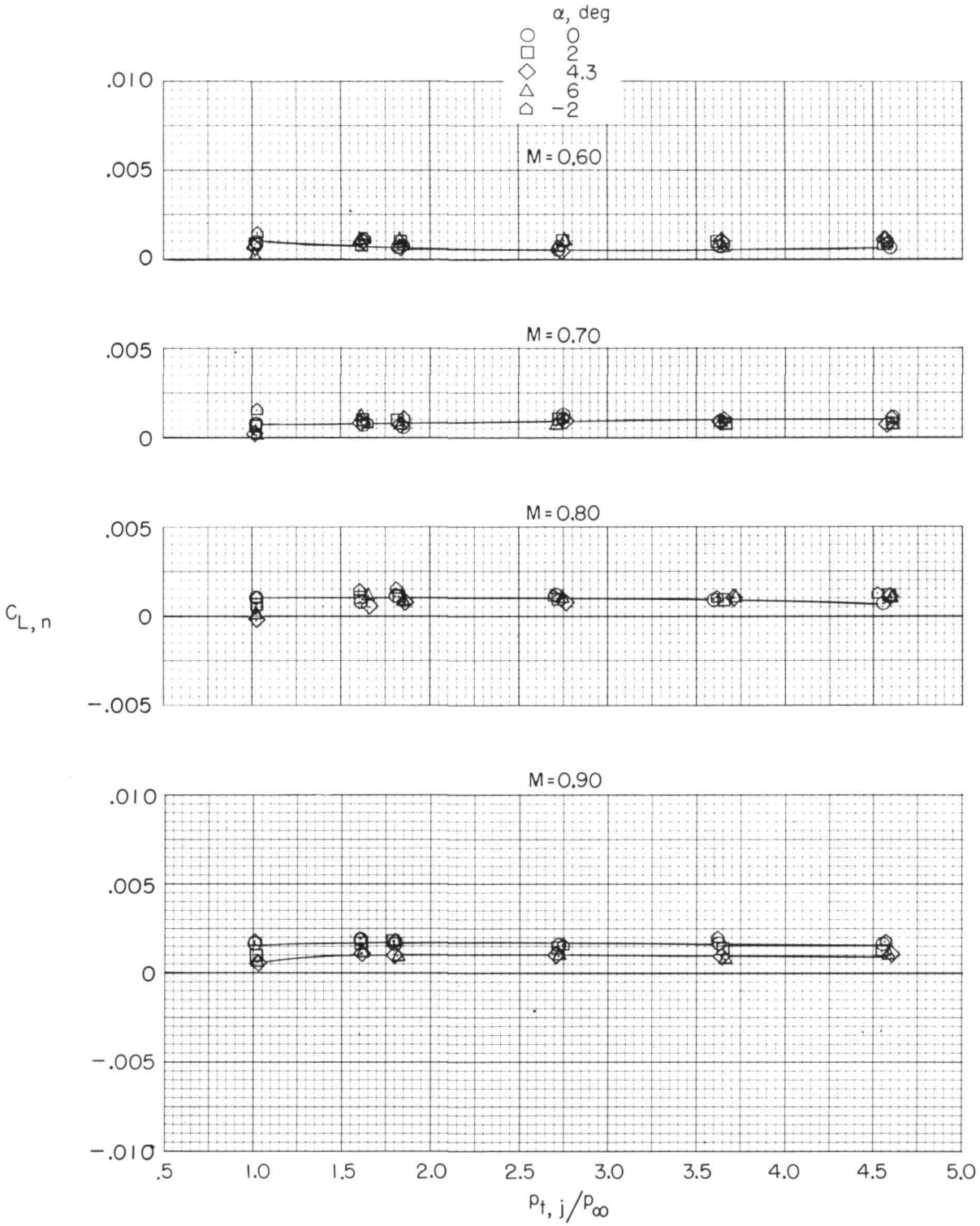

(b) Lift coefficient.

Figure 7.- Continued.

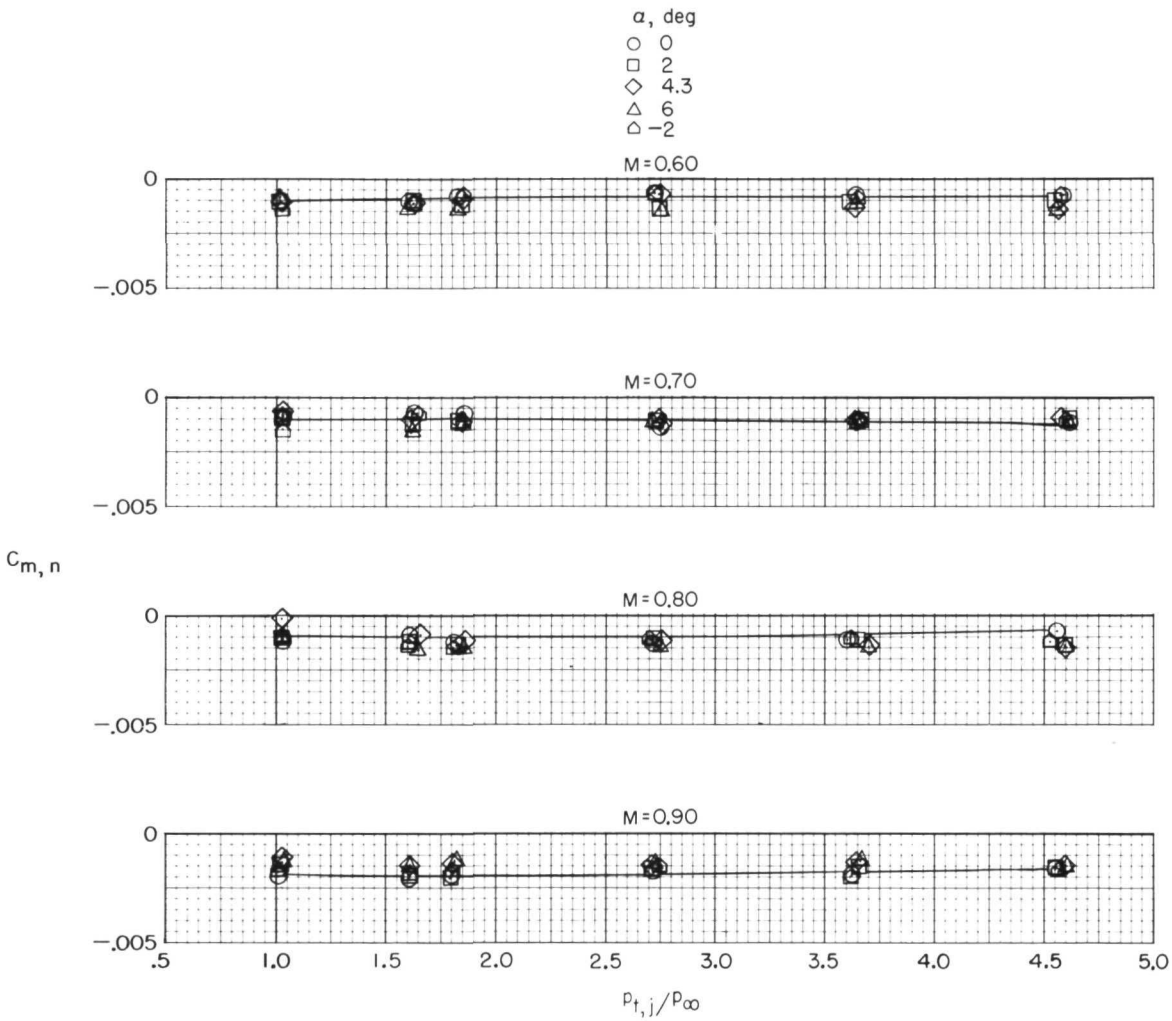

(c) Pitching-moment coefficient.

Figure 7.- Concluded.

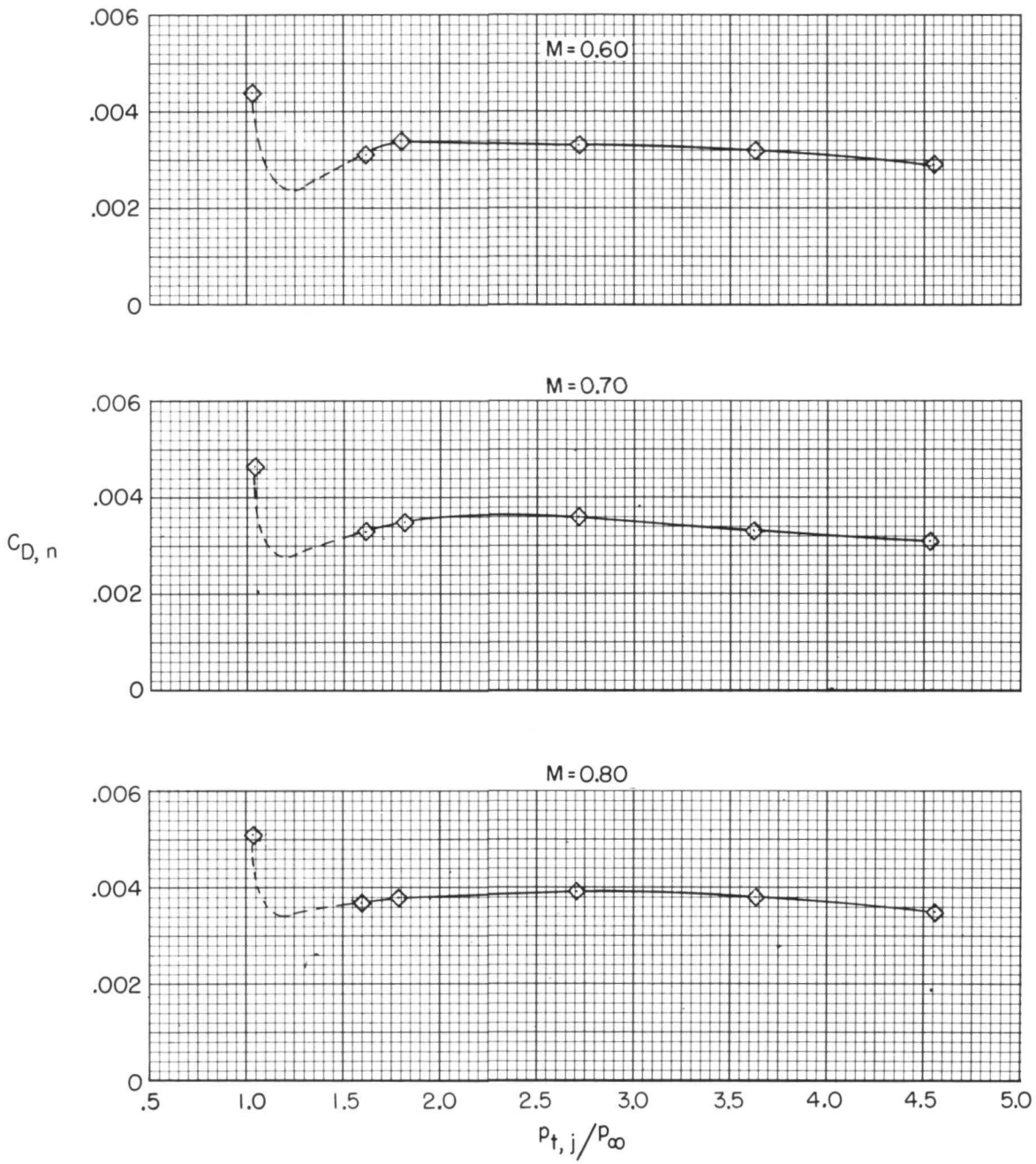

(a) Drag coefficient.

Figure 8.- Effect of jet total-pressure ratio on nozzle aerodynamic characteristics at 4.3^o angle of attack. Configuration 4 (modified cruise power setting, nozzle type A).

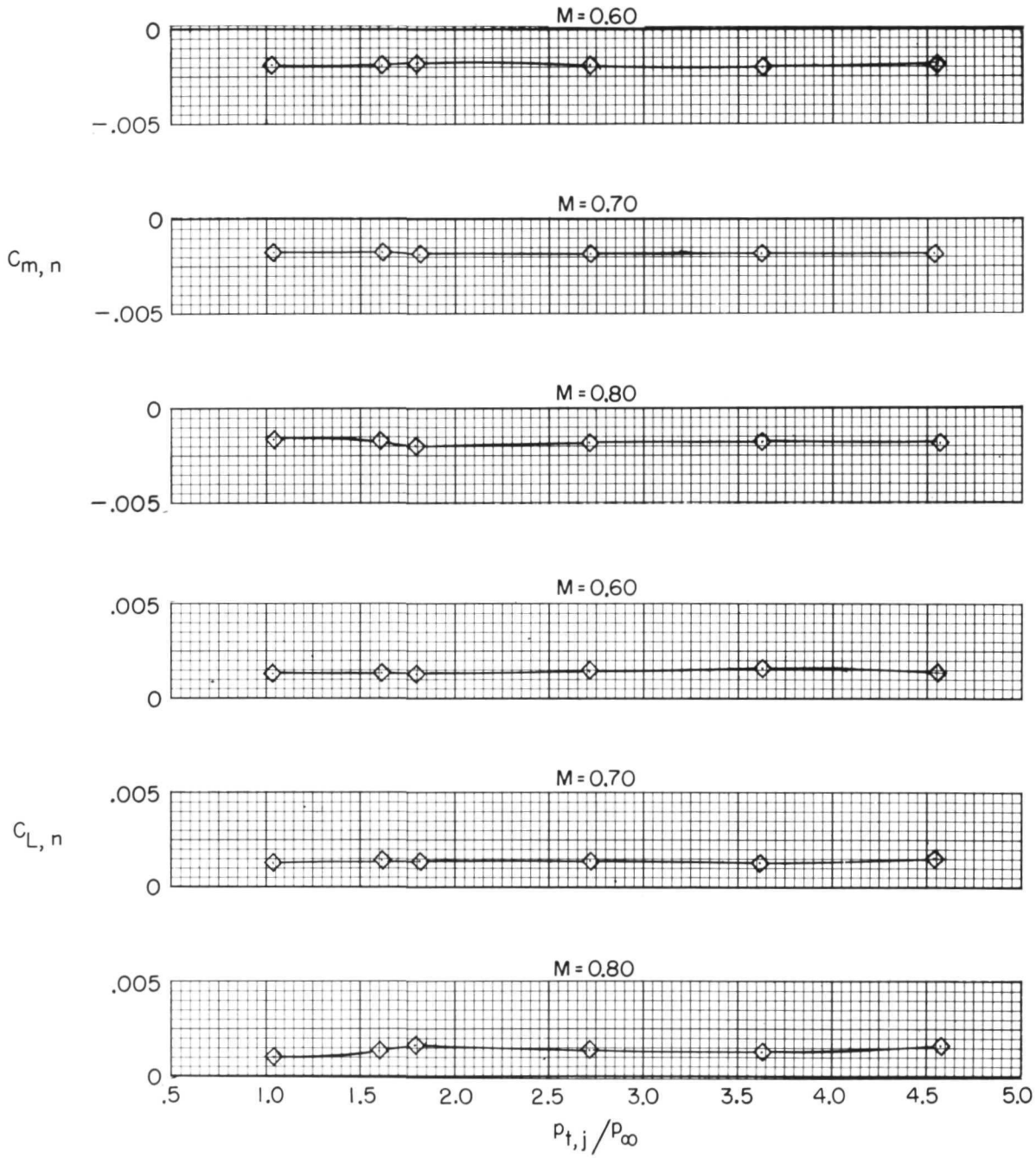

(b) Lift and pitching-moment coefficients.

Figure 8.- Concluded.

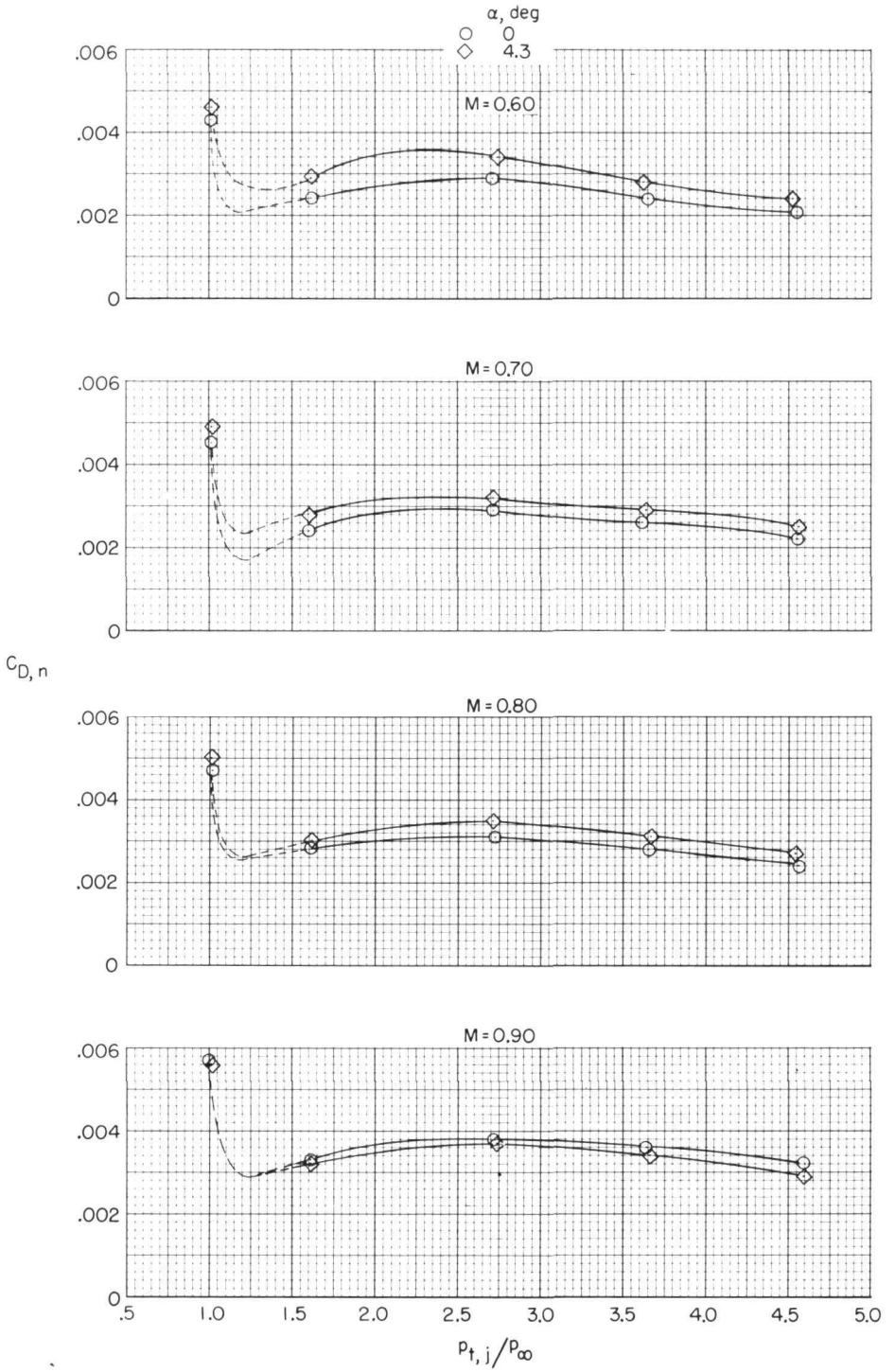

(a) Drag coefficient.

Figure 9.- Effect of jet total-pressure ratio on nozzle aerodynamic characteristics. Configuration 5 (low partial afterburning power setting, nozzle type A).

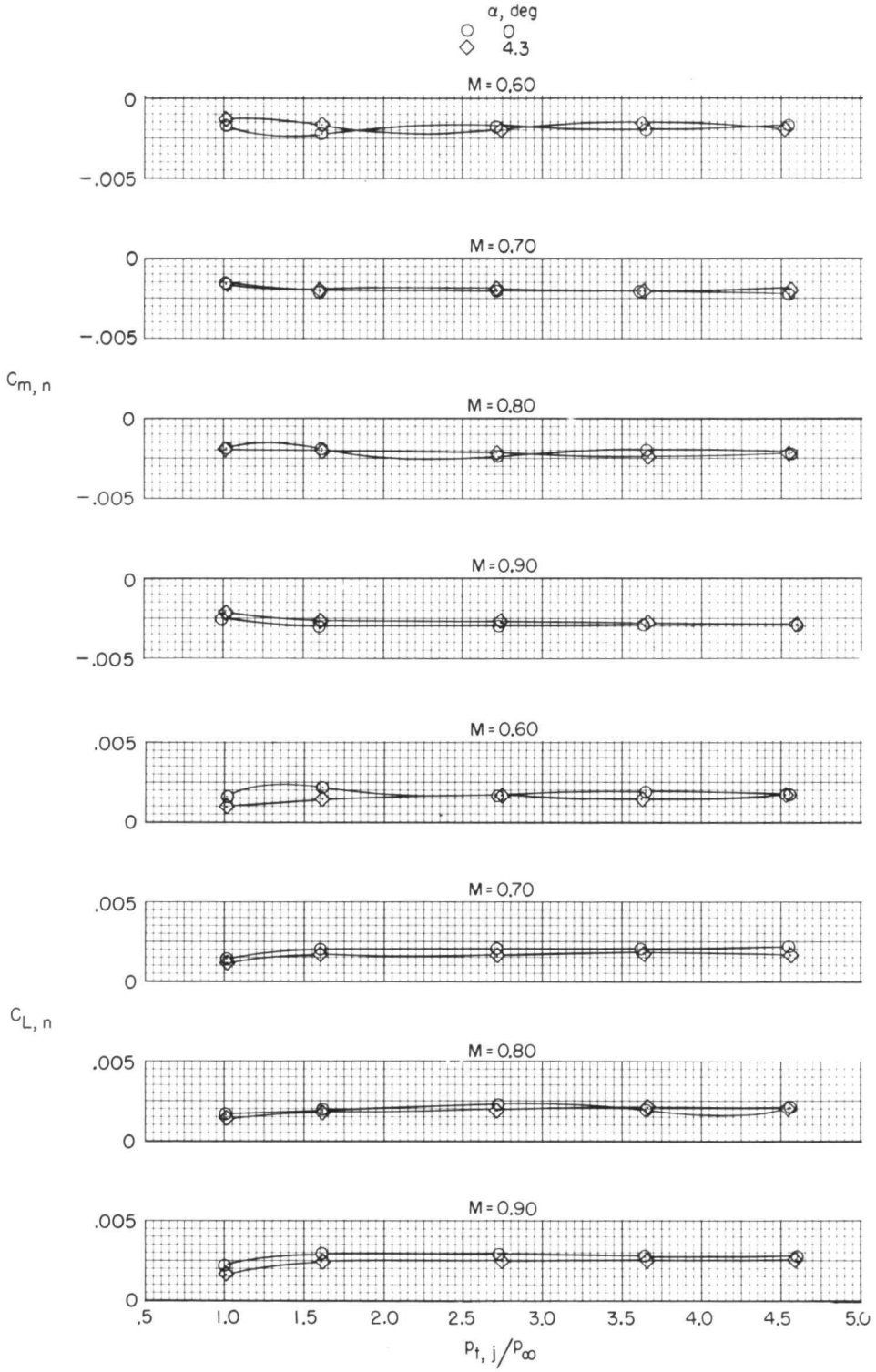

(b) Lift and pitching-moment coefficients.

Figure 9.- Continued.

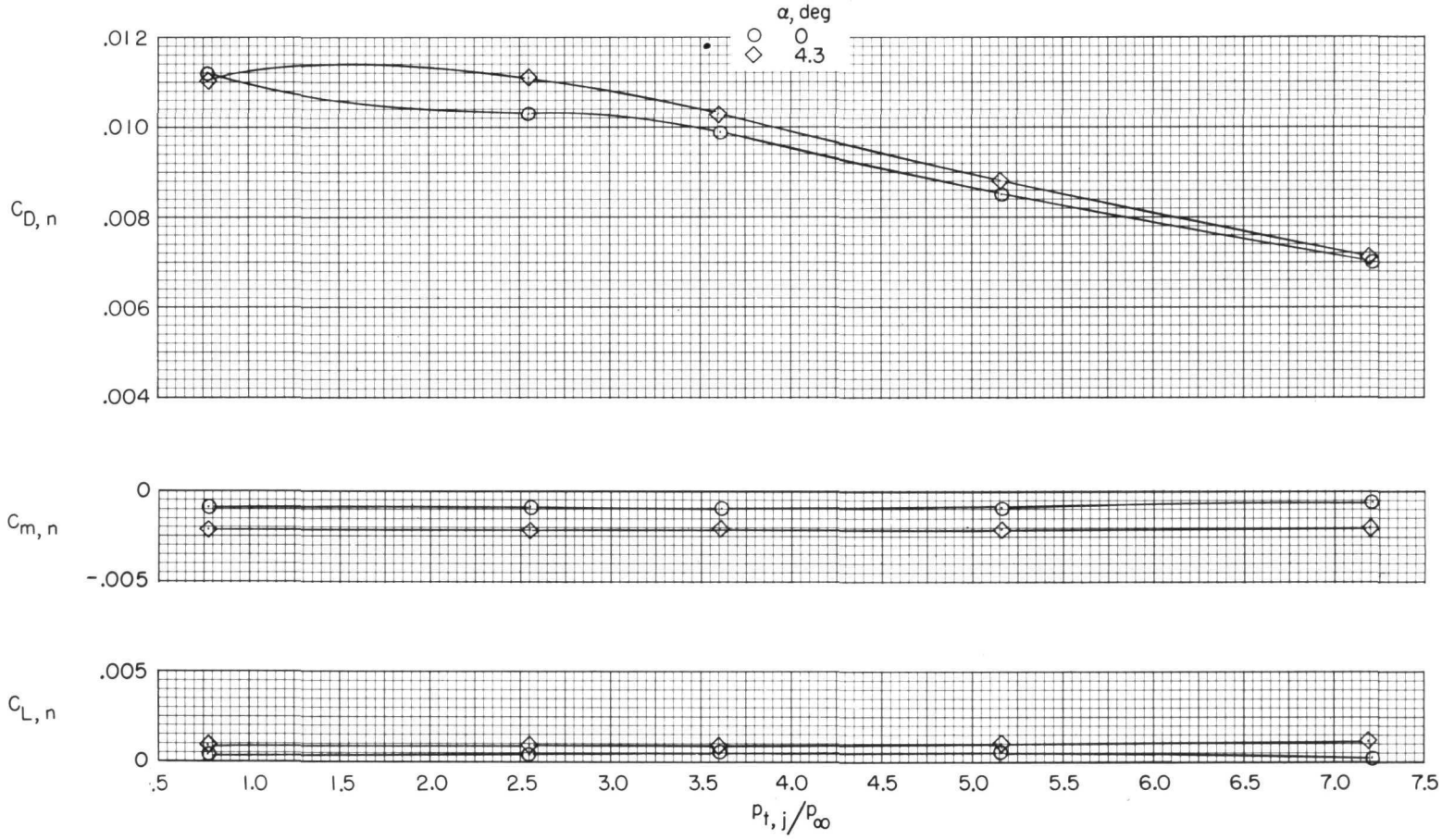

(c) Drag, lift, and pitching-moment coefficients at M = 1.20.

Figure 9.- Continued.

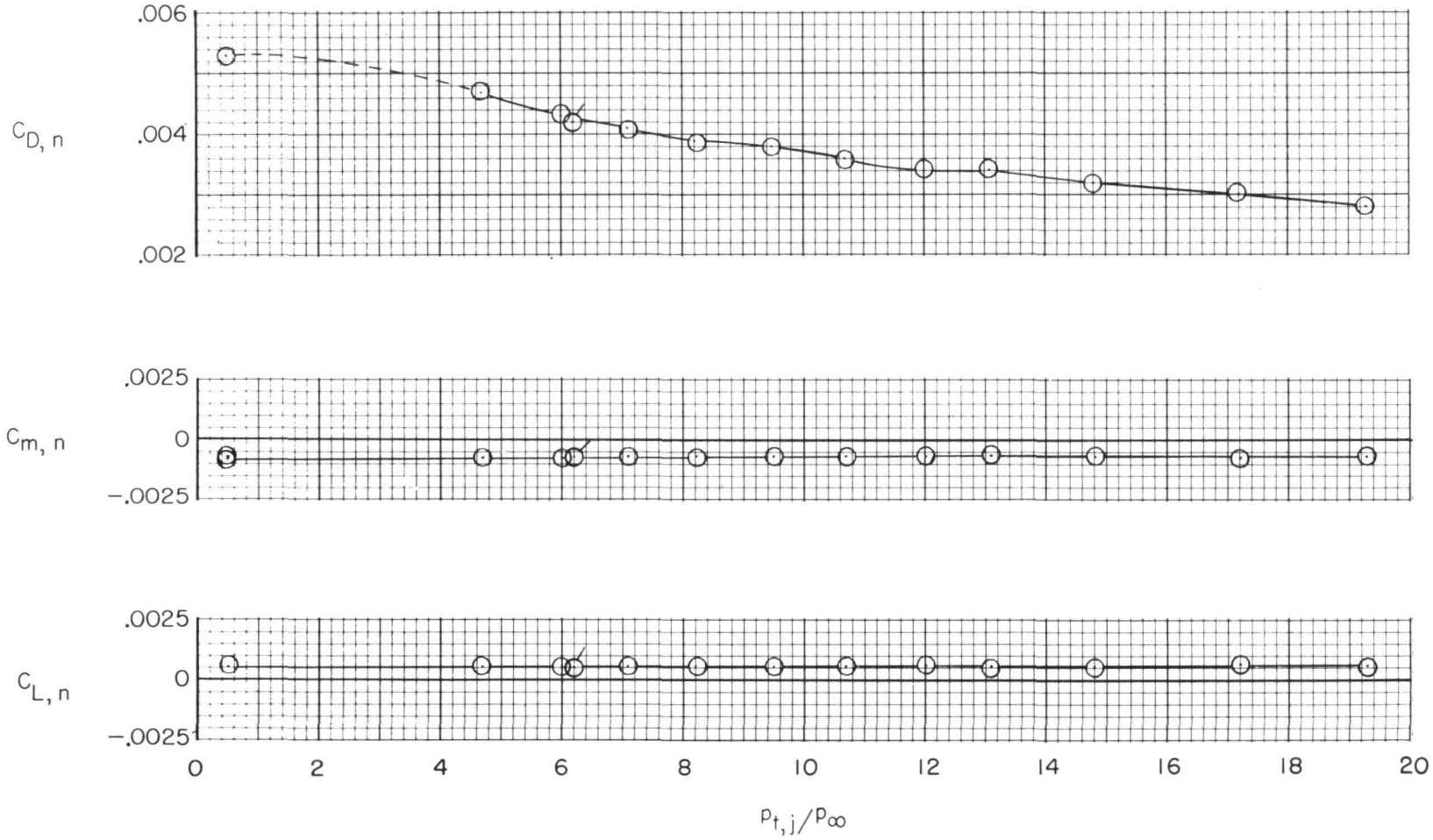

(d) Drag, lift, and pitching-moment coefficients at $M = 2.20$ and $\alpha = 0^{\circ}$. Tick marks indicate flow-through.

Figure 9.- Concluded.

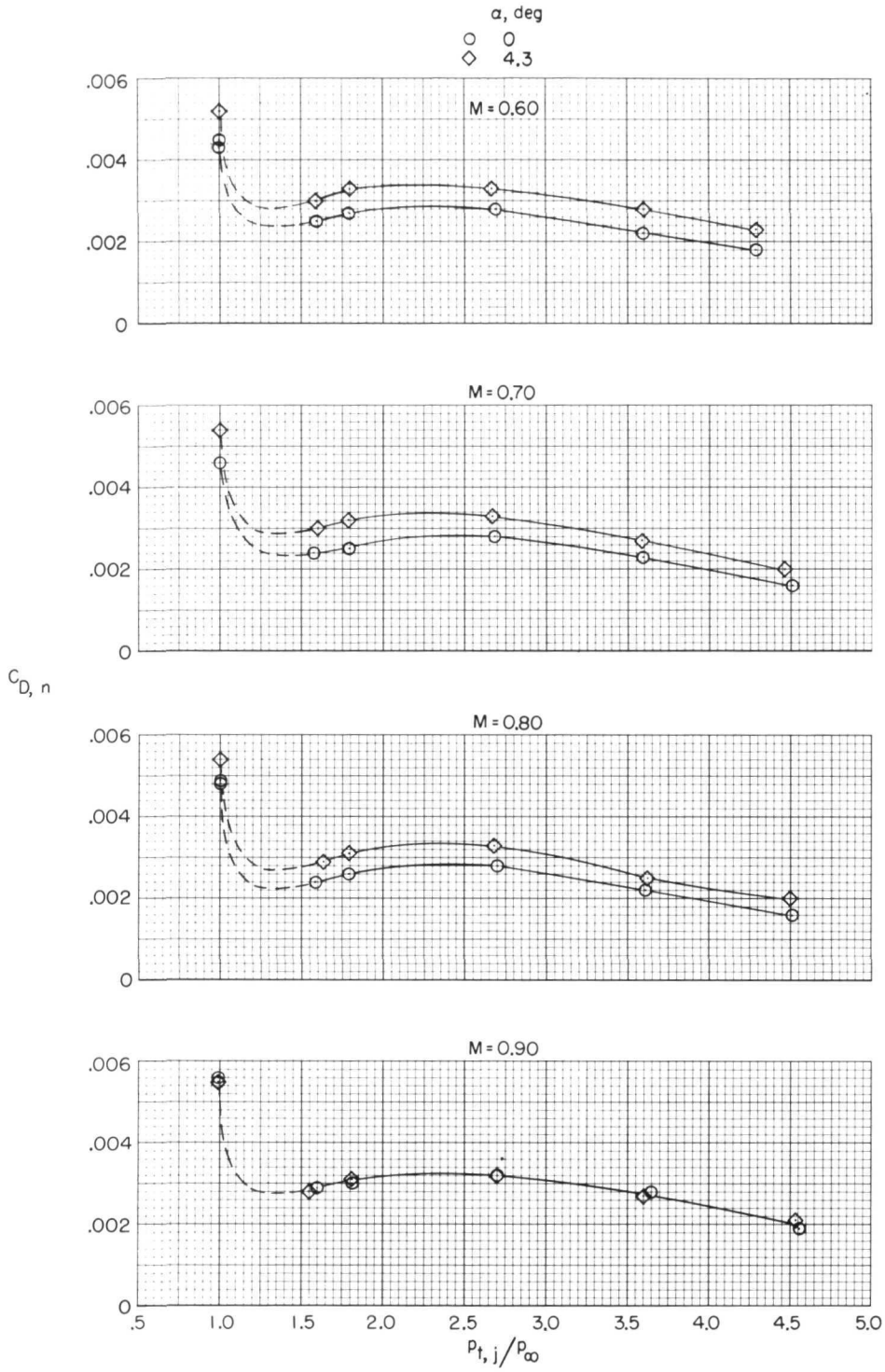

(a) Drag coefficient.

Figure 10.- Effect of jet total-pressure ratio on nozzle aerodynamic characteristics. Configuration 6 (high partial afterburning power setting, nozzle type A).

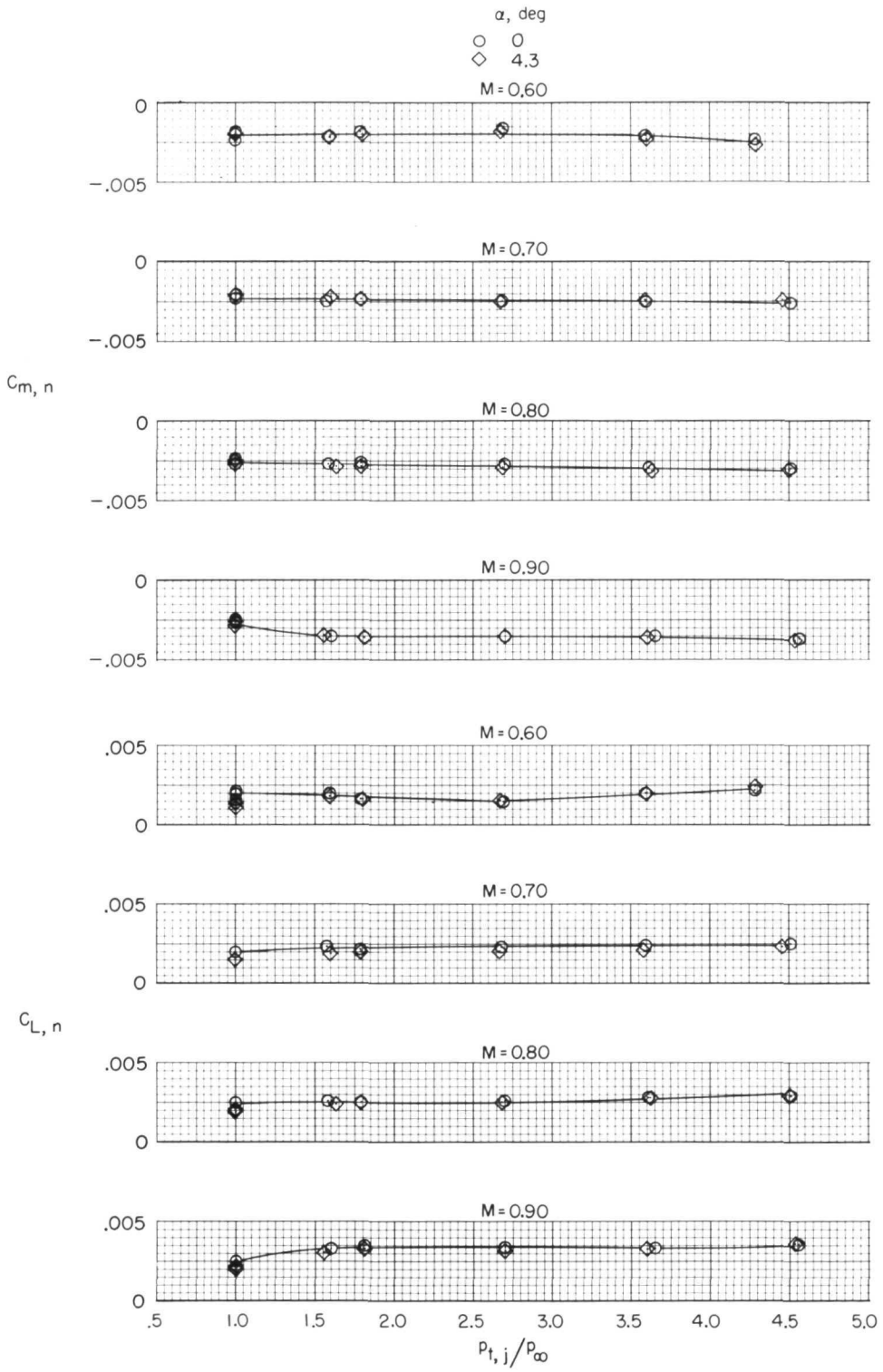

(b) Lift and pitching-moment coefficients.

Figure 10.- Continued.

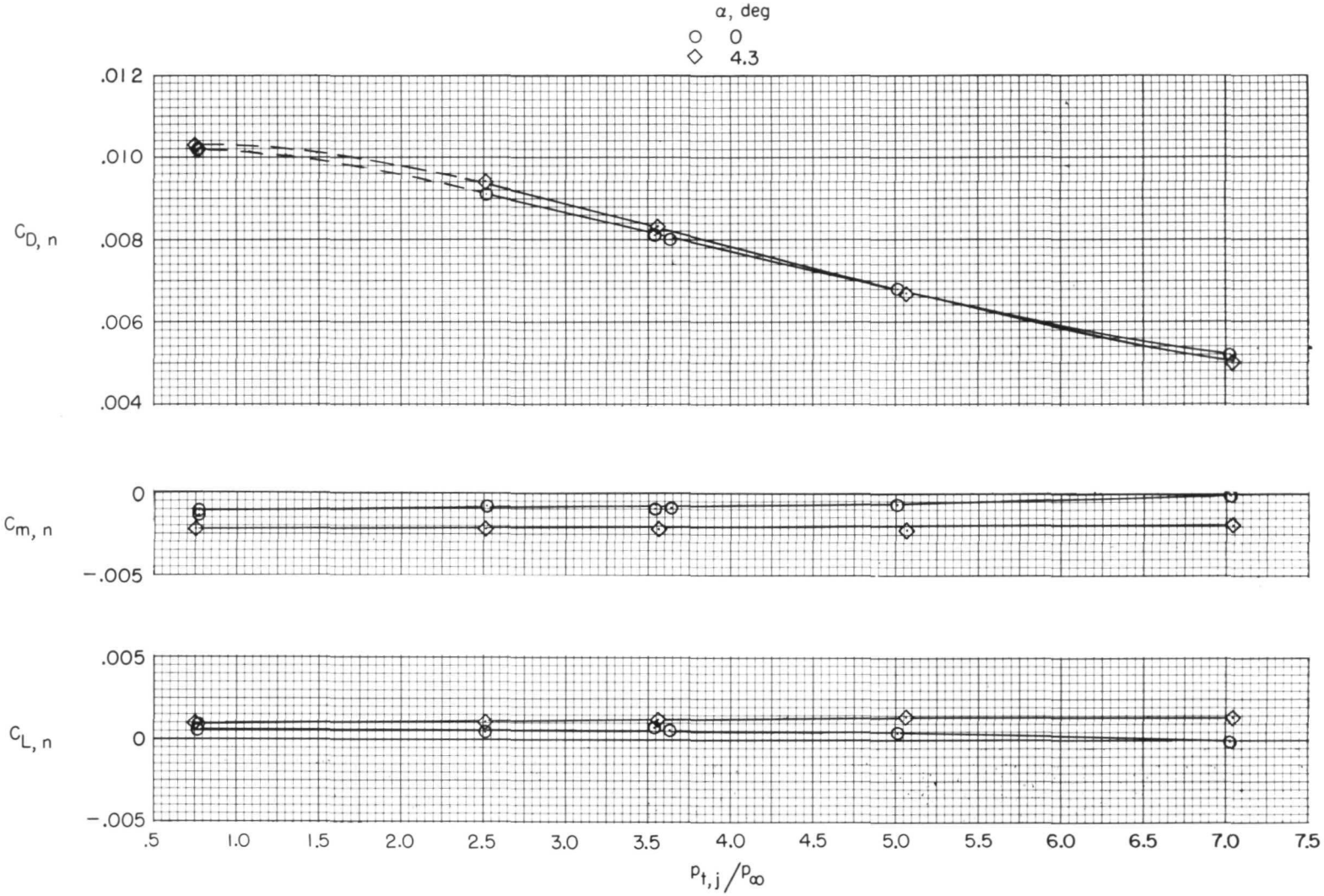

(c) Drag, lift, and pitching-moment coefficients at M = 1.20.

Figure 10.- Continued.

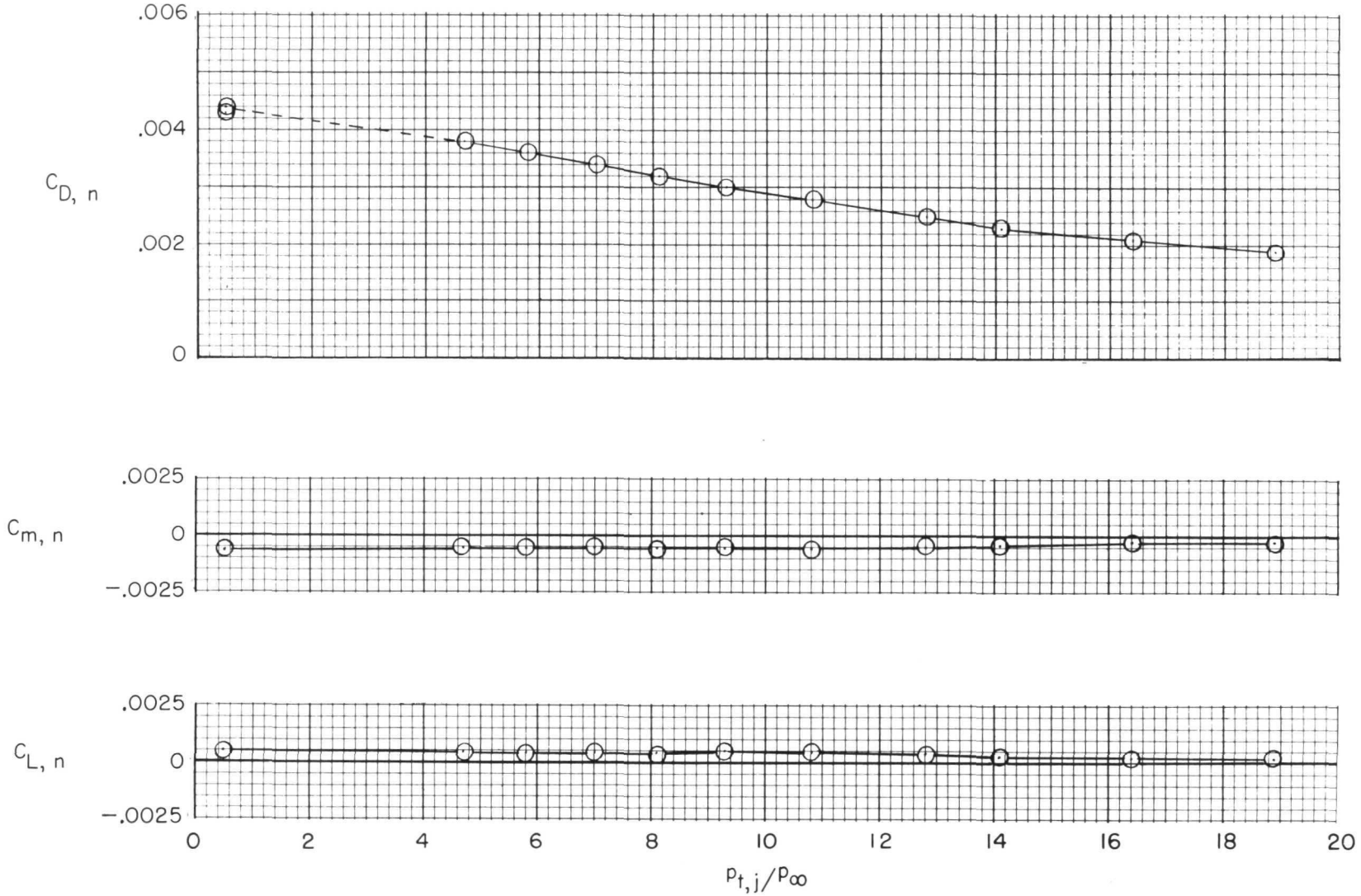

(d) Drag, lift, and pitching-moment coefficients at $M = 2.20$ and $\alpha = 0^o$.

Figure 10.- Concluded.

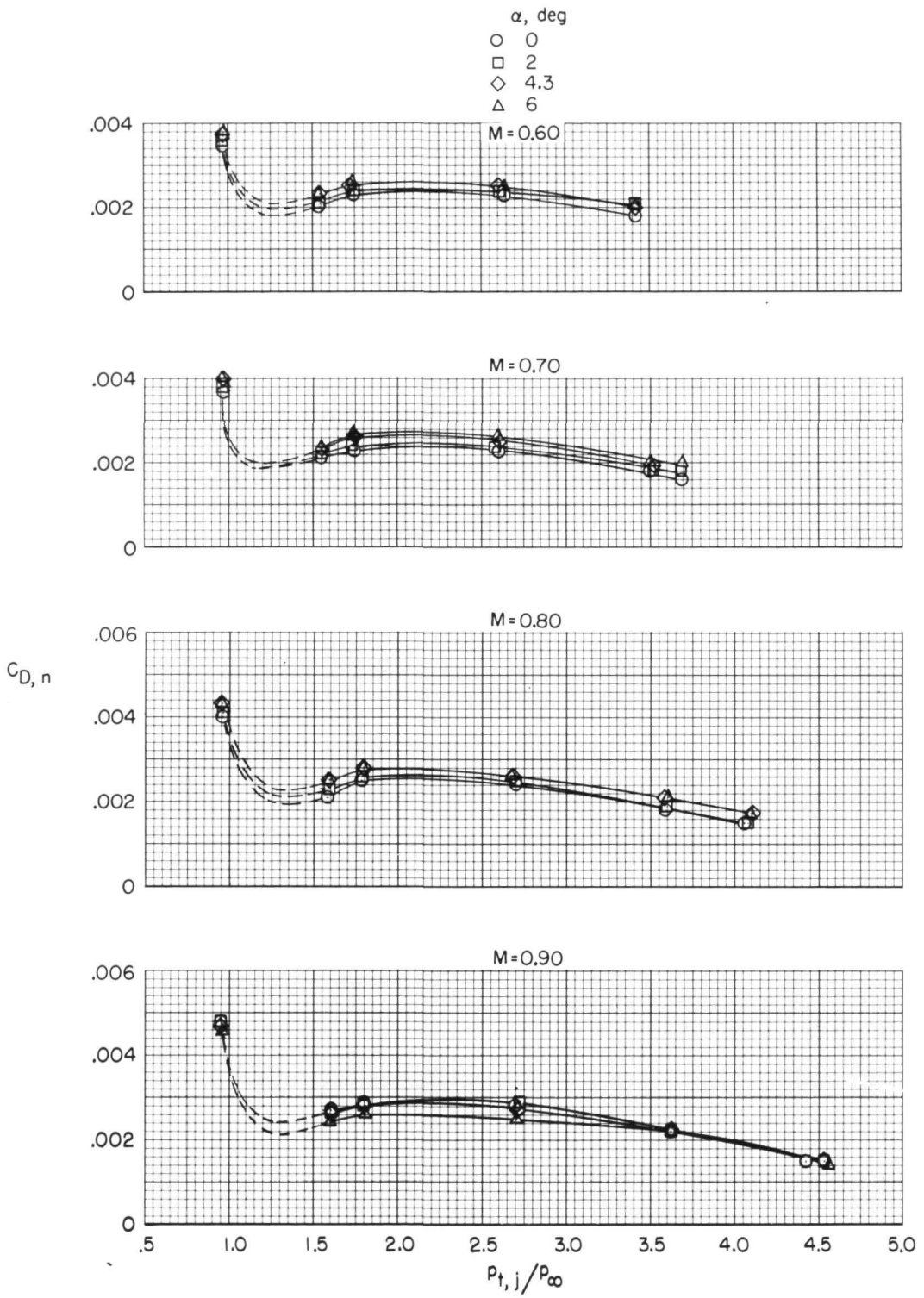

(a) Drag coefficient.

Figure 11.- Effect of jet total-pressure ratio on nozzle aerodynamic characteristics. Configuration 7 (maximum afterburning power setting, nozzle type A).

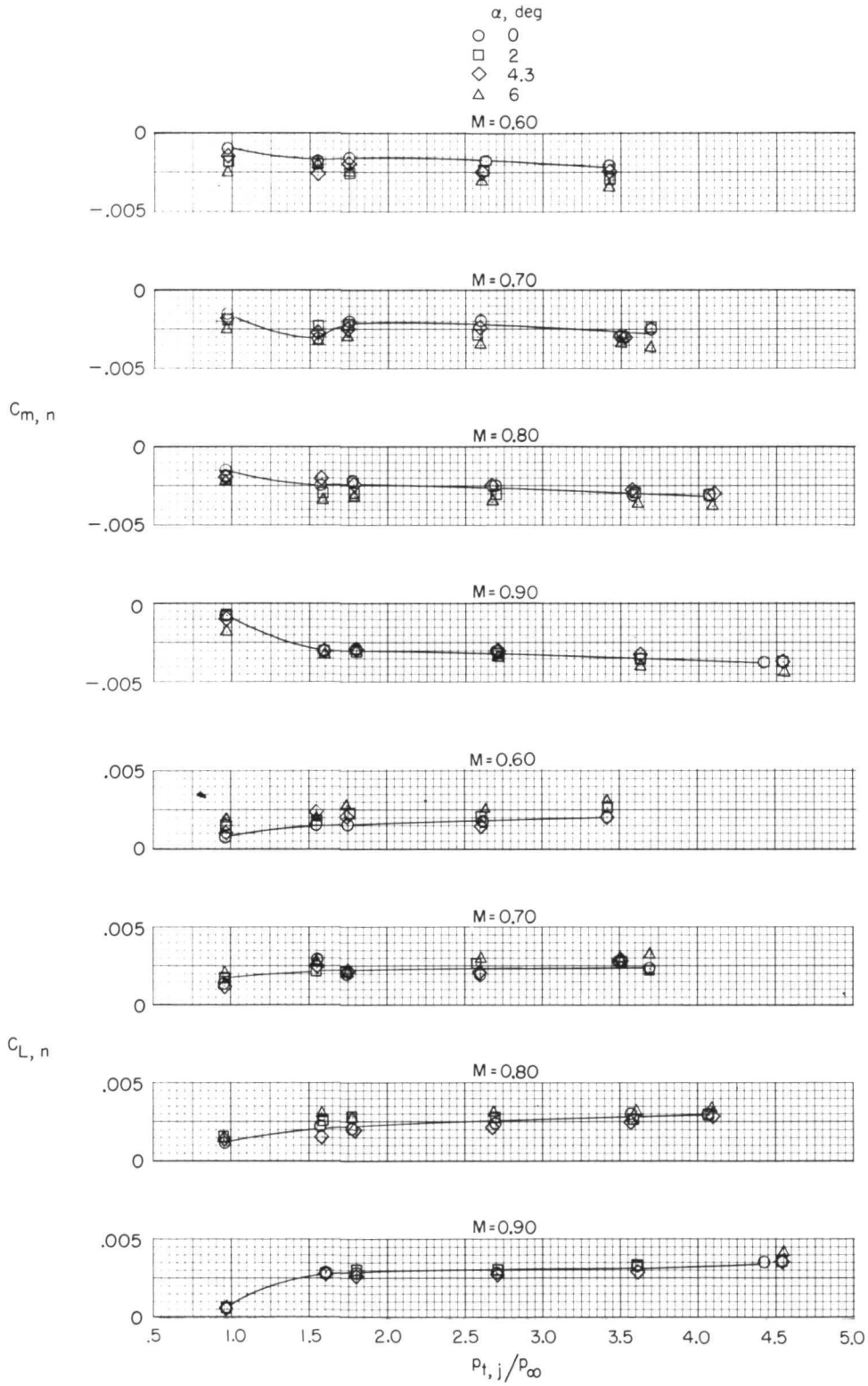

(b) Lift and pitching-moment coefficients.

Figure 11.- Continued.

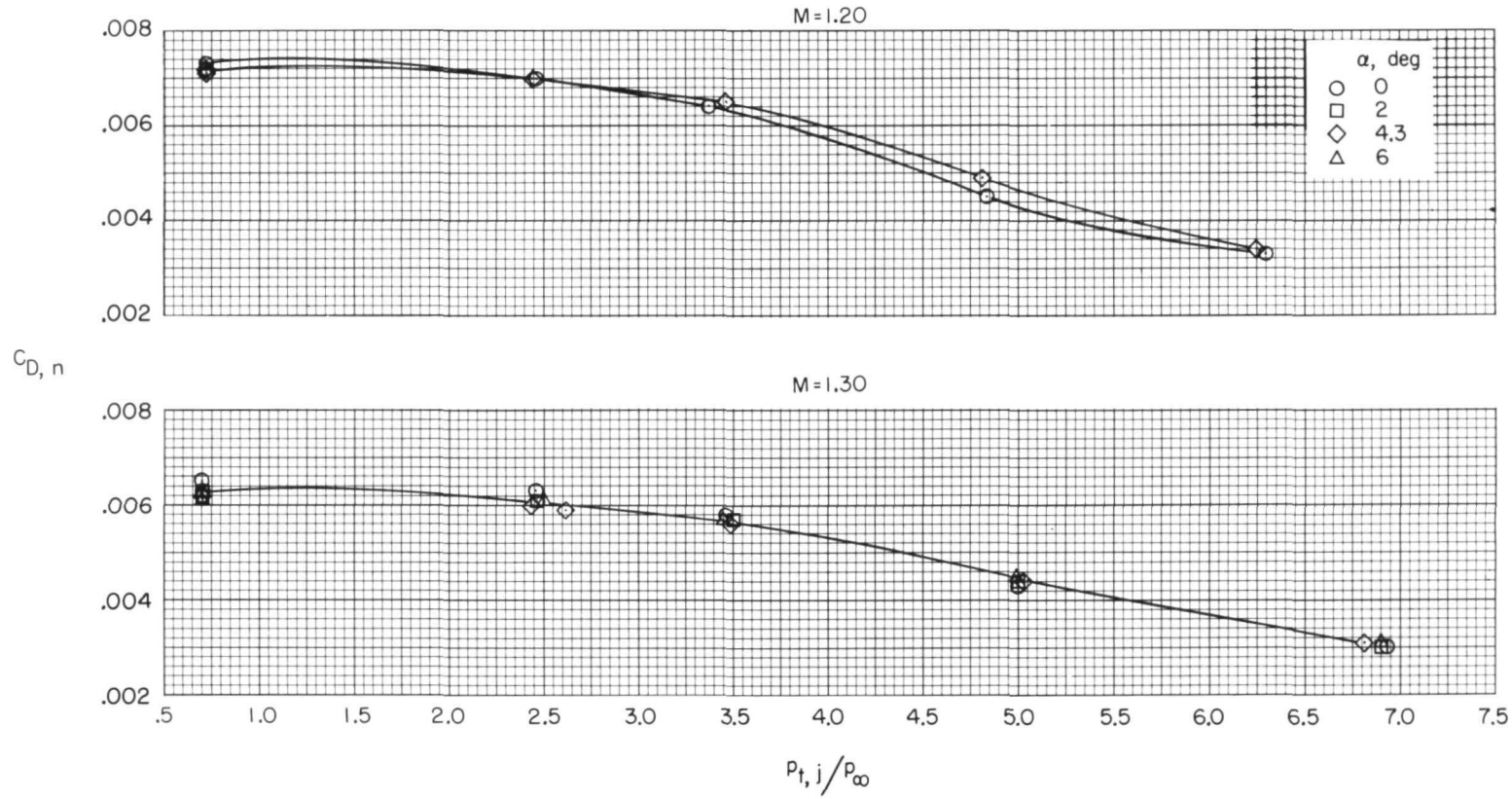

(c) Drag coefficient at M = 1.20 and 1.30.

Figure 11. - Continued.

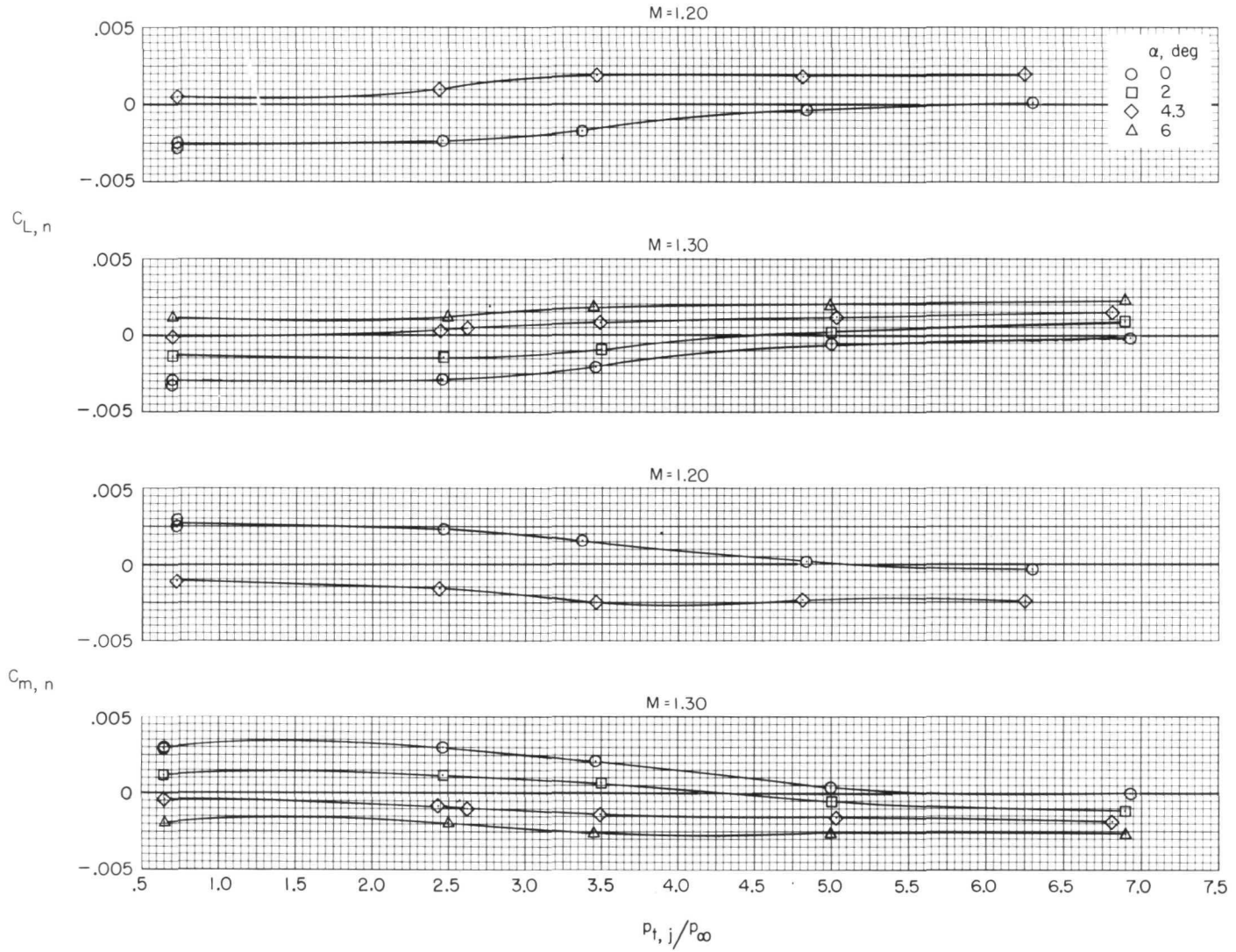

(d) Lift and pitching-moment coefficients at M = 1.20 and 1.30.

Figure 11.- Continued.

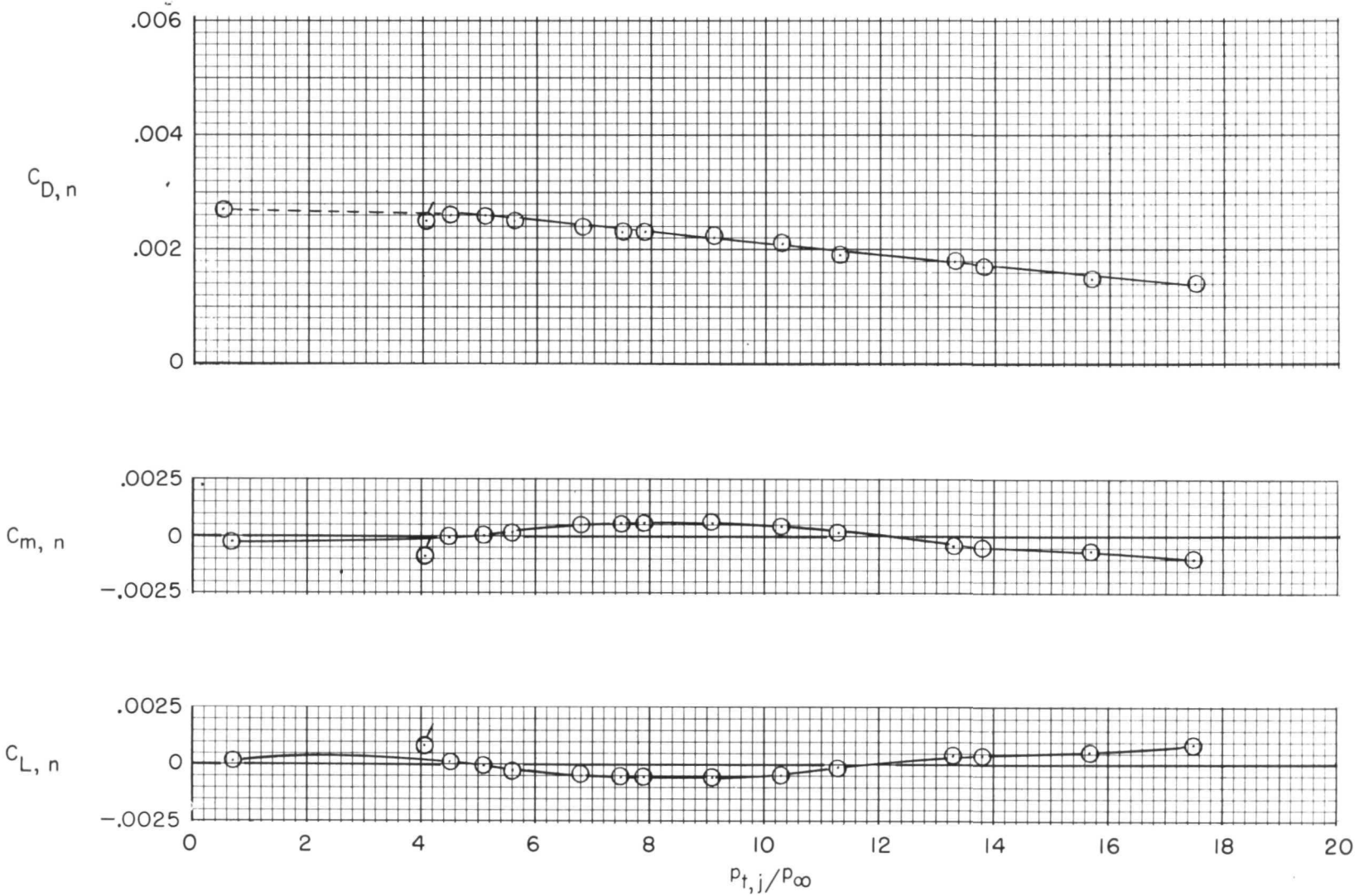

(e) Drag, lift, and pitching-moment coefficients at $M = 2.20$ and $\alpha = 0^{\circ}$. Tick mark indicates flow-through.

Figure 11.- Concluded.

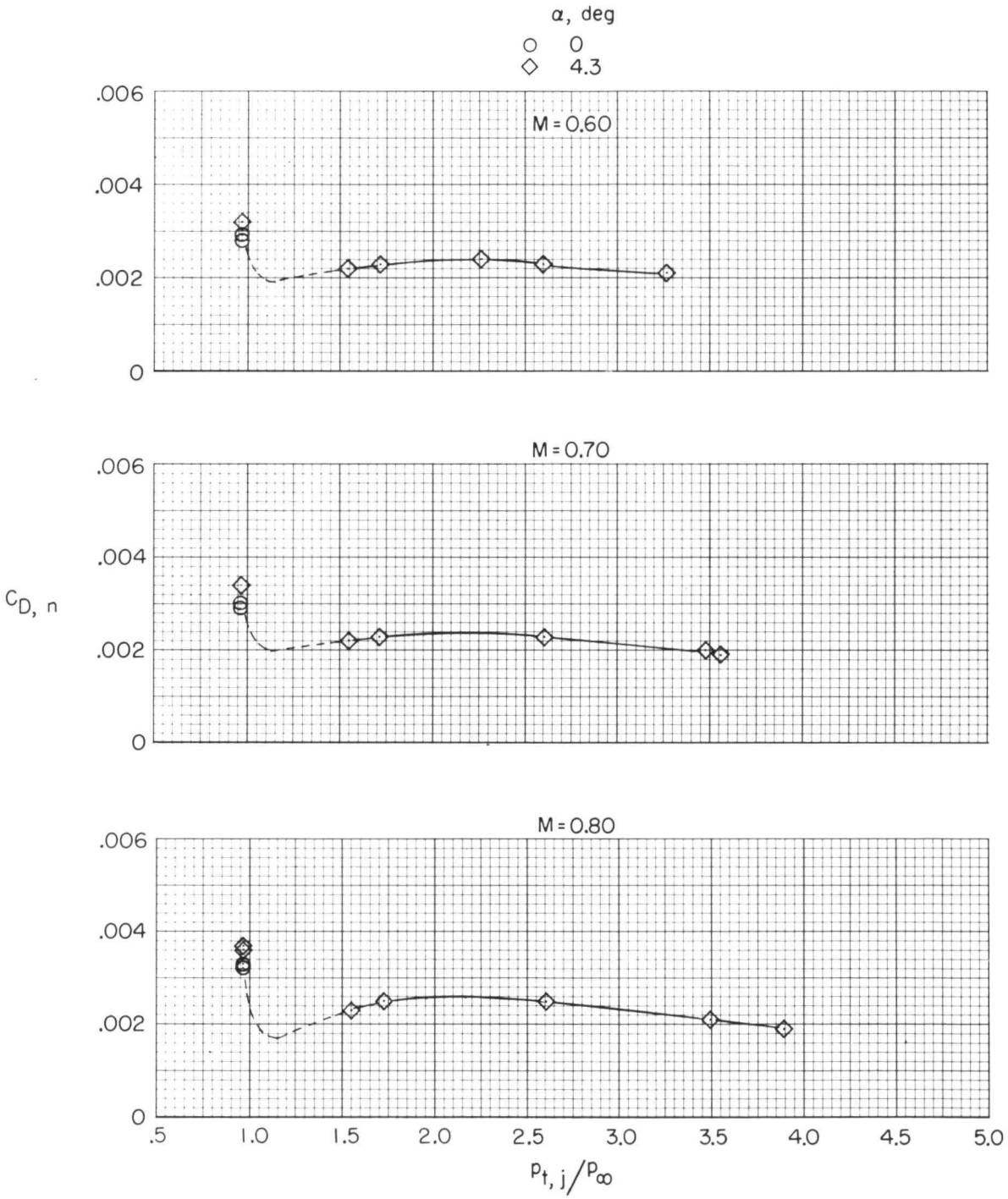

(a) Drag coefficient.

Figure 12.- Effect of jet total-pressure ratio on nozzle aerodynamic characteristics. Configuration 8 (modified maximum afterburning power setting, nozzle type A).

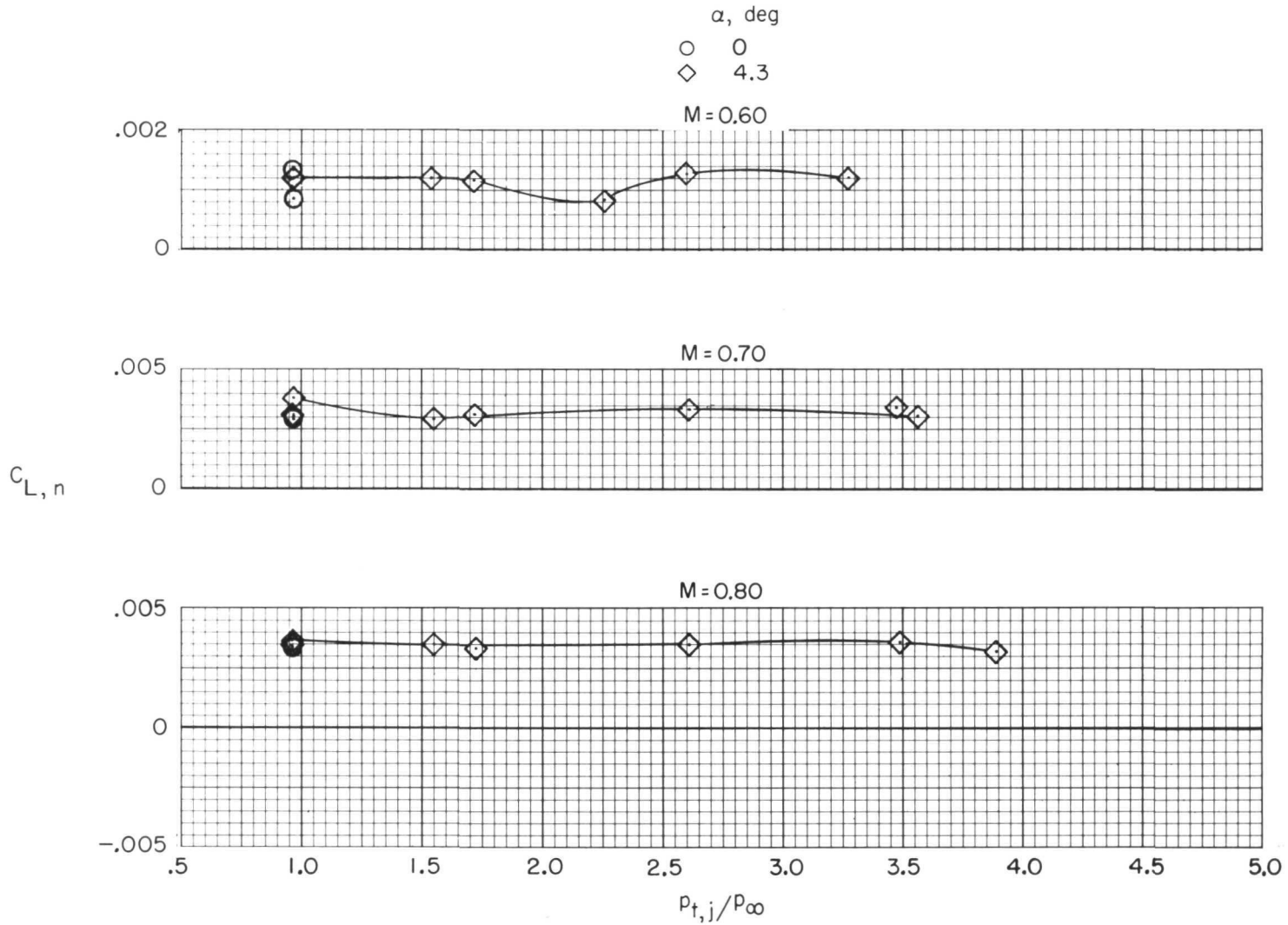

(b) Lift coefficient.

Figure 12. - Continued.

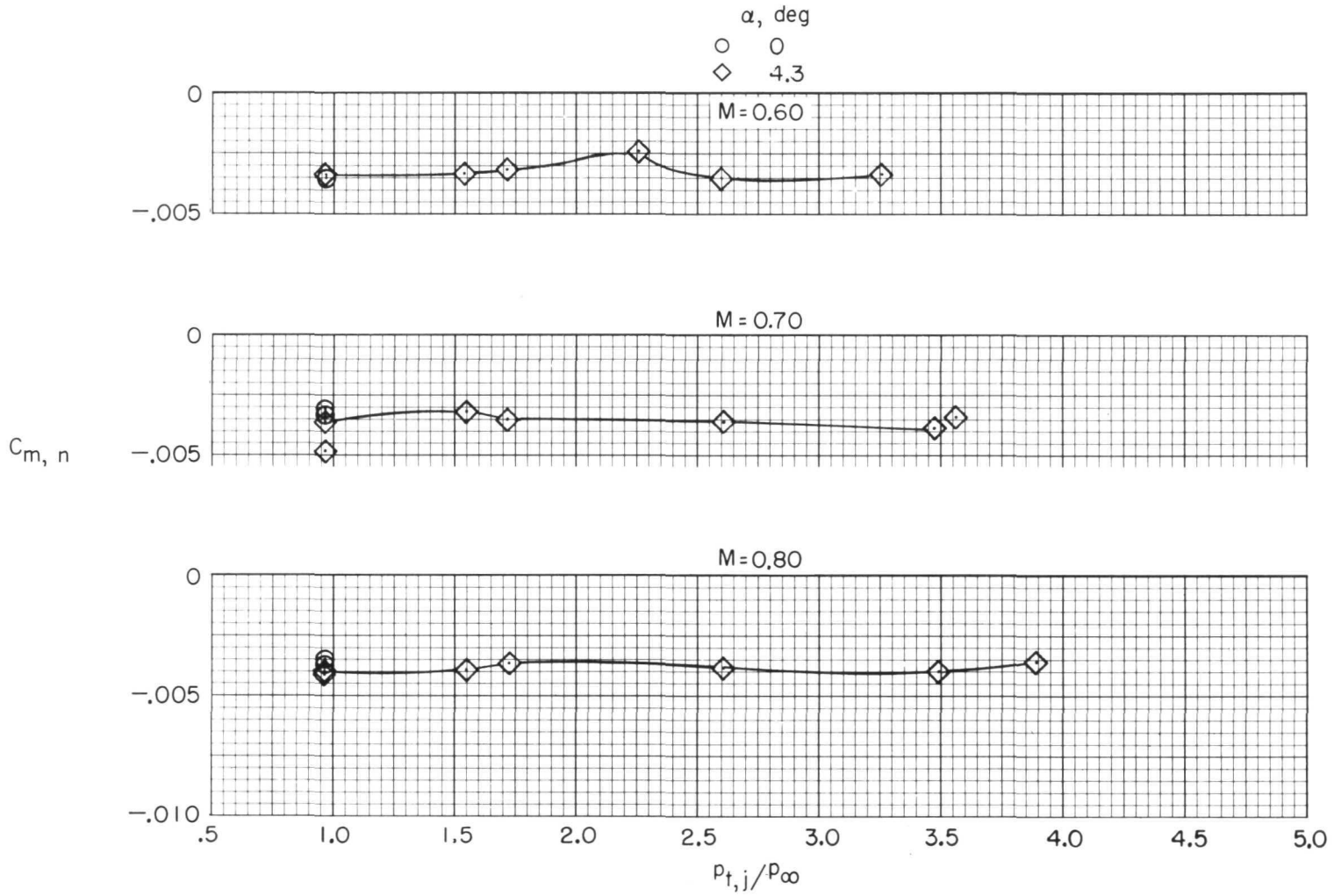

(c) Pitching-moment coefficient.

Figure 12.- Concluded.

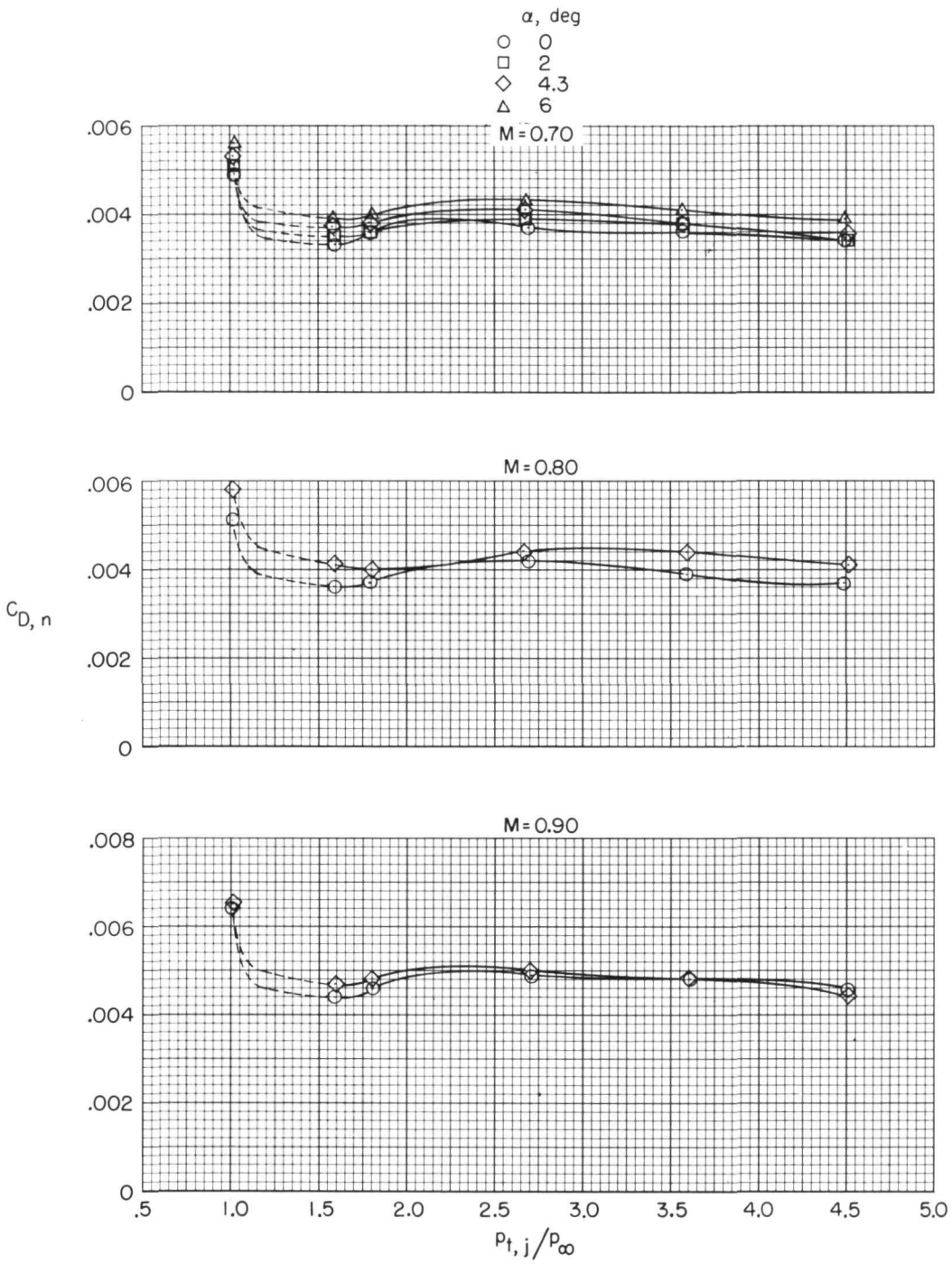

(a) Drag coefficient.

Figure 13.- Effect of jet total-pressure ratio on nozzle aerodynamic characteristics. Configuration 9 (cruise power setting, nozzle type B).

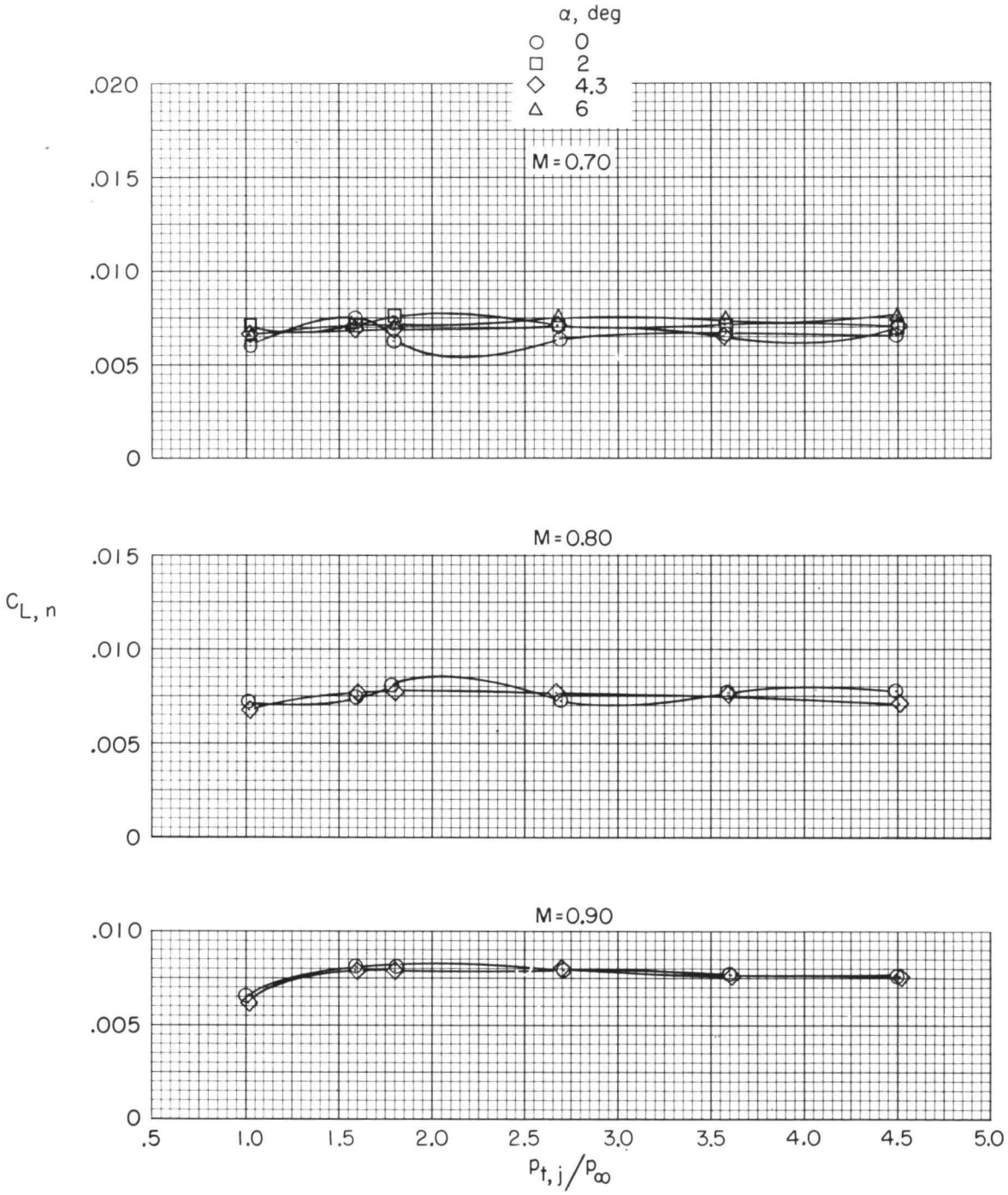

(b) Lift coefficient.

Figure 13.- Continued.

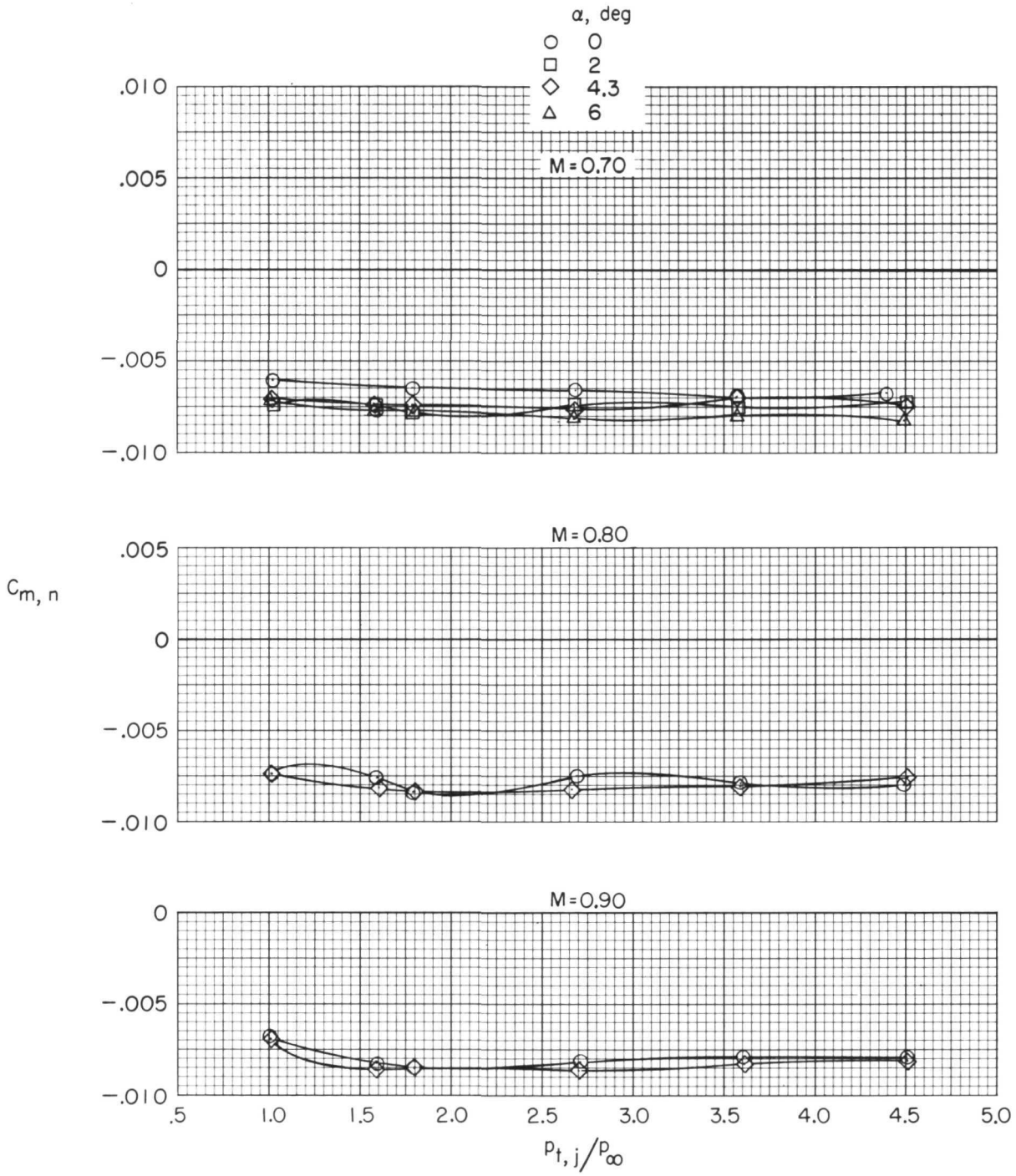

(c) Pitching-moment coefficient.

Figure 13.- Concluded.

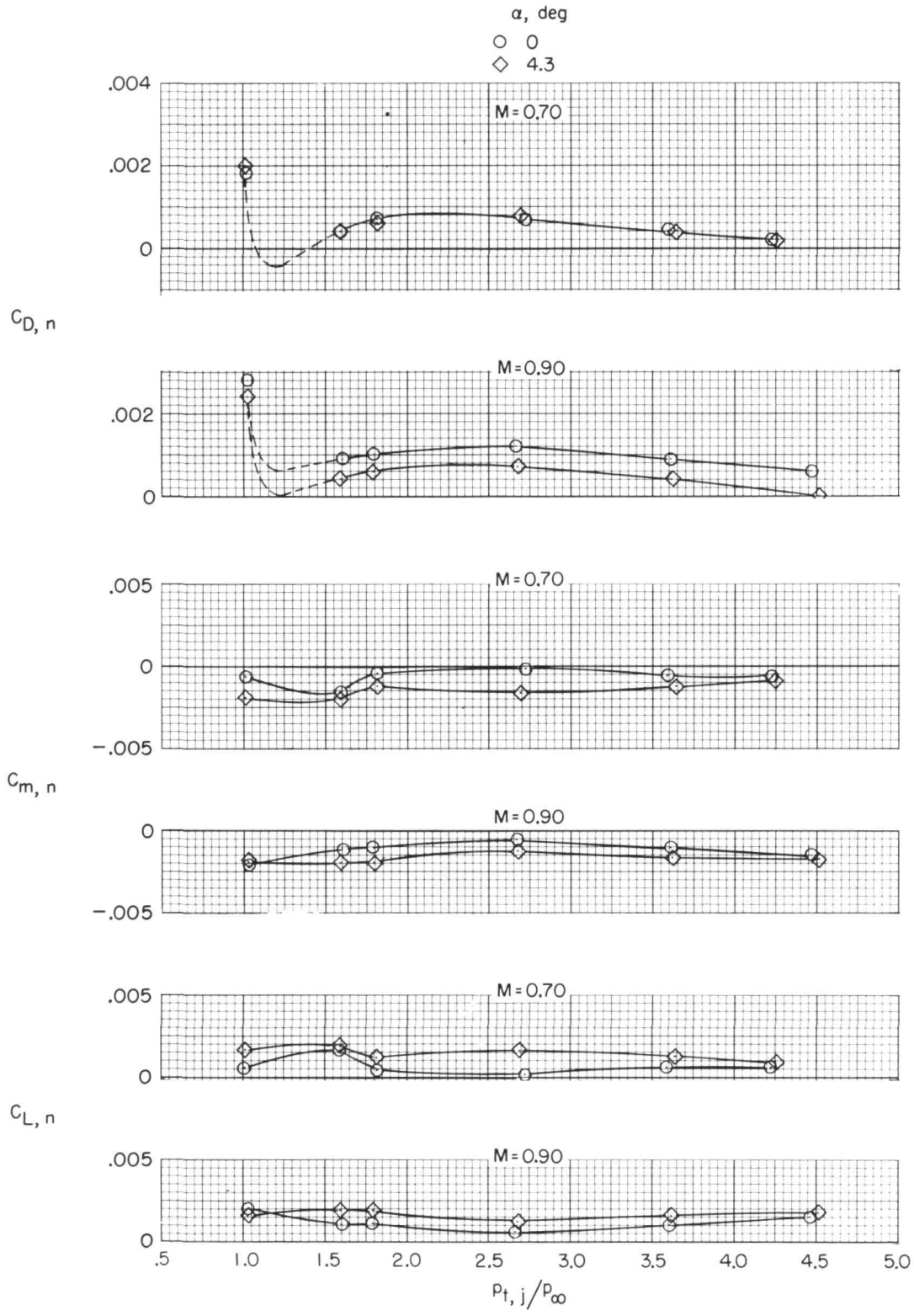

Figure 14.- Effect of jet total-pressure ratio on nozzle aerodynamic characteristics. Configuration 10 (sea level maximum afterburning power setting, nozzle type B).

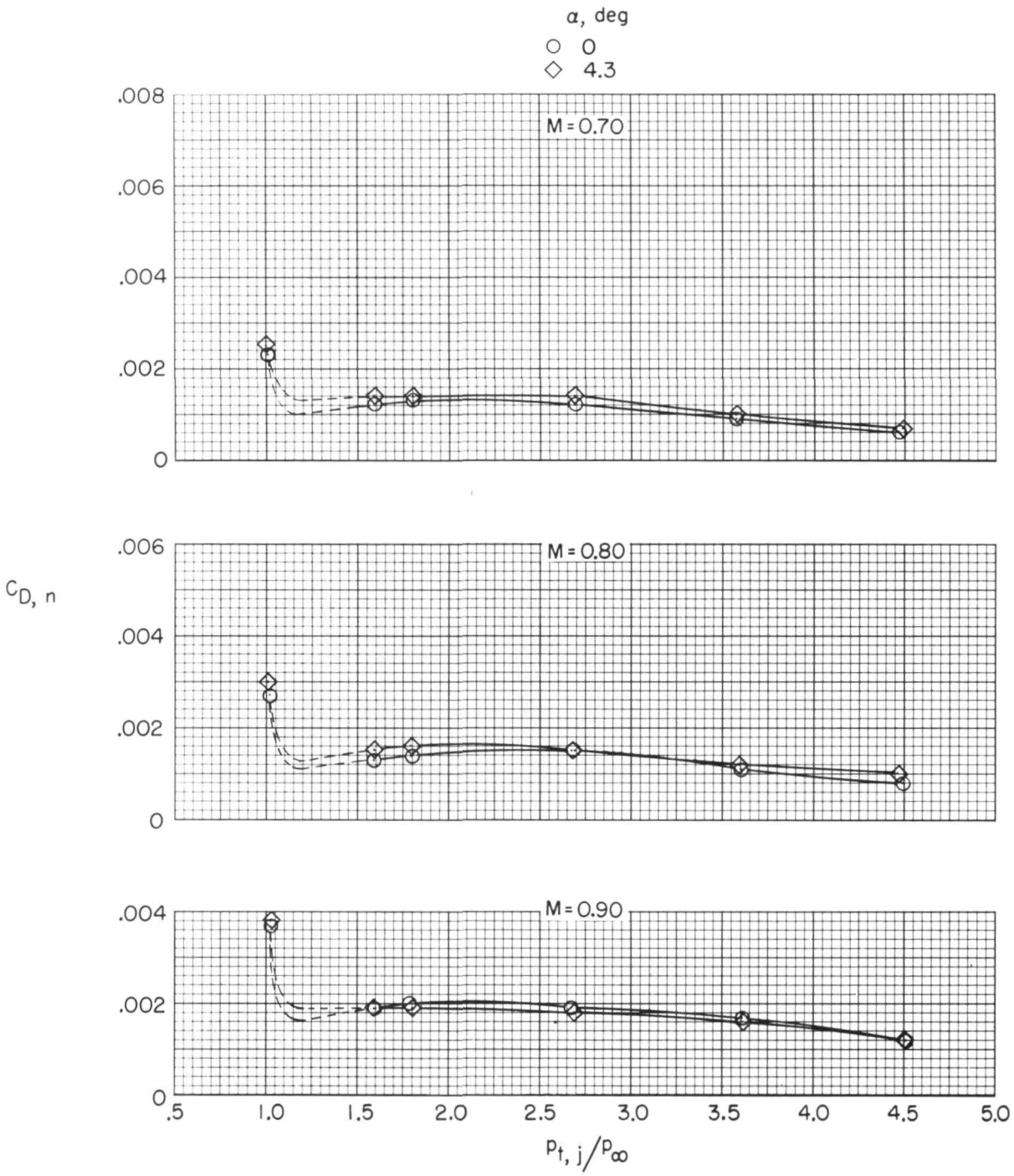

(a) Drag coefficient.

Figure 15.- Effect of jet total-pressure ratio on nozzle aerodynamic characteristics. Configuration 11 (transonic maximum afterburning power setting, nozzle type B).

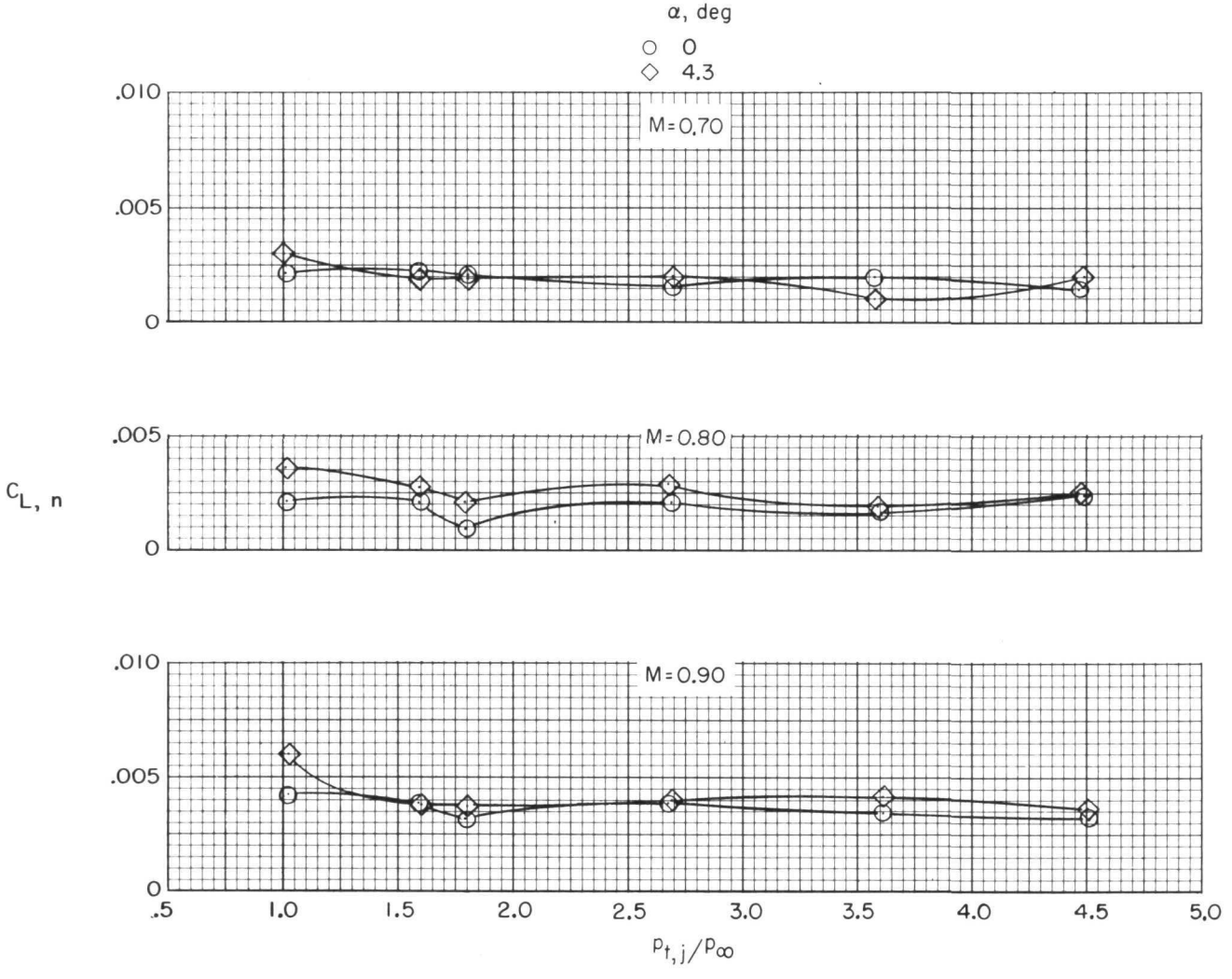

(b) Lift coefficient.

Figure 15.- Continued.

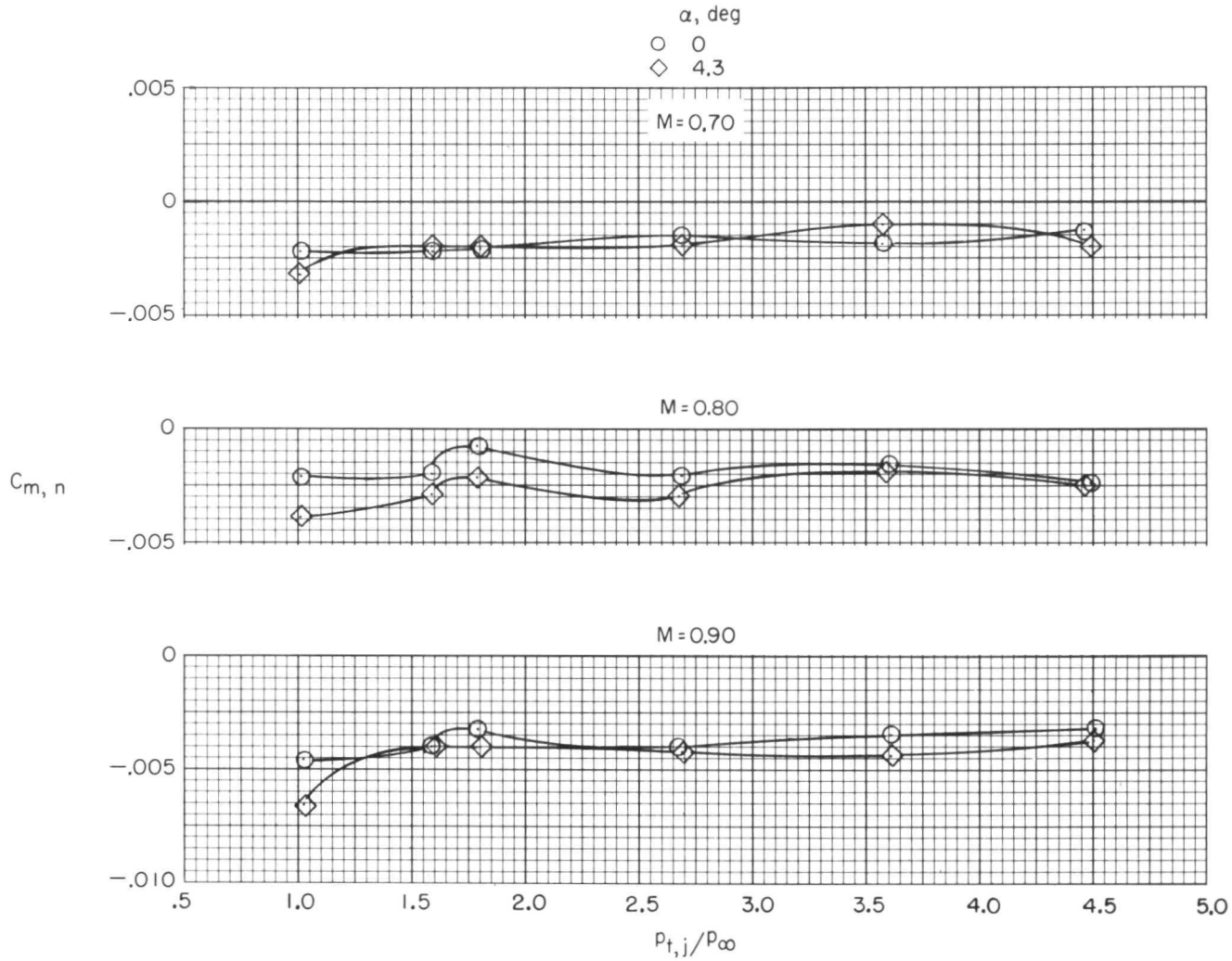

(c) Pitching-moment coefficient.

Figure 15.- Continued.

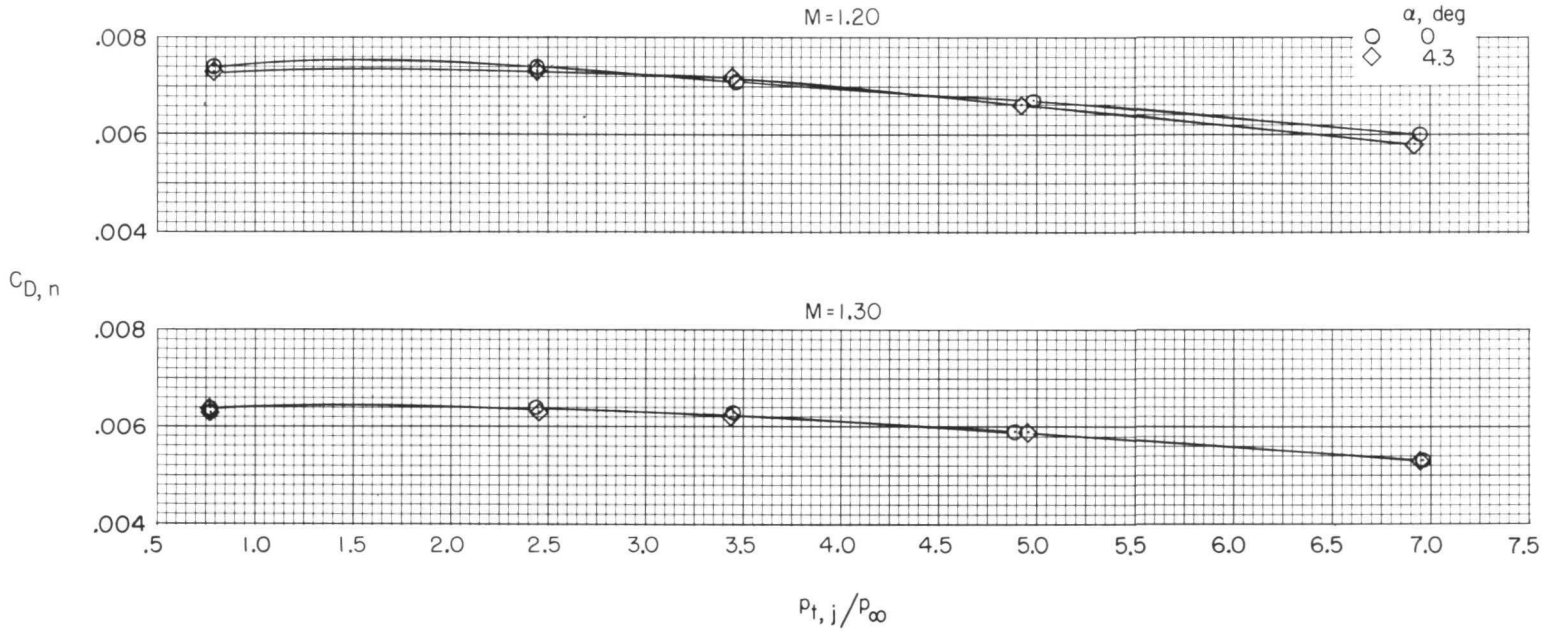

(d) Drag coefficient at M = 1.20 and 1.30.

Figure 15.- Continued.

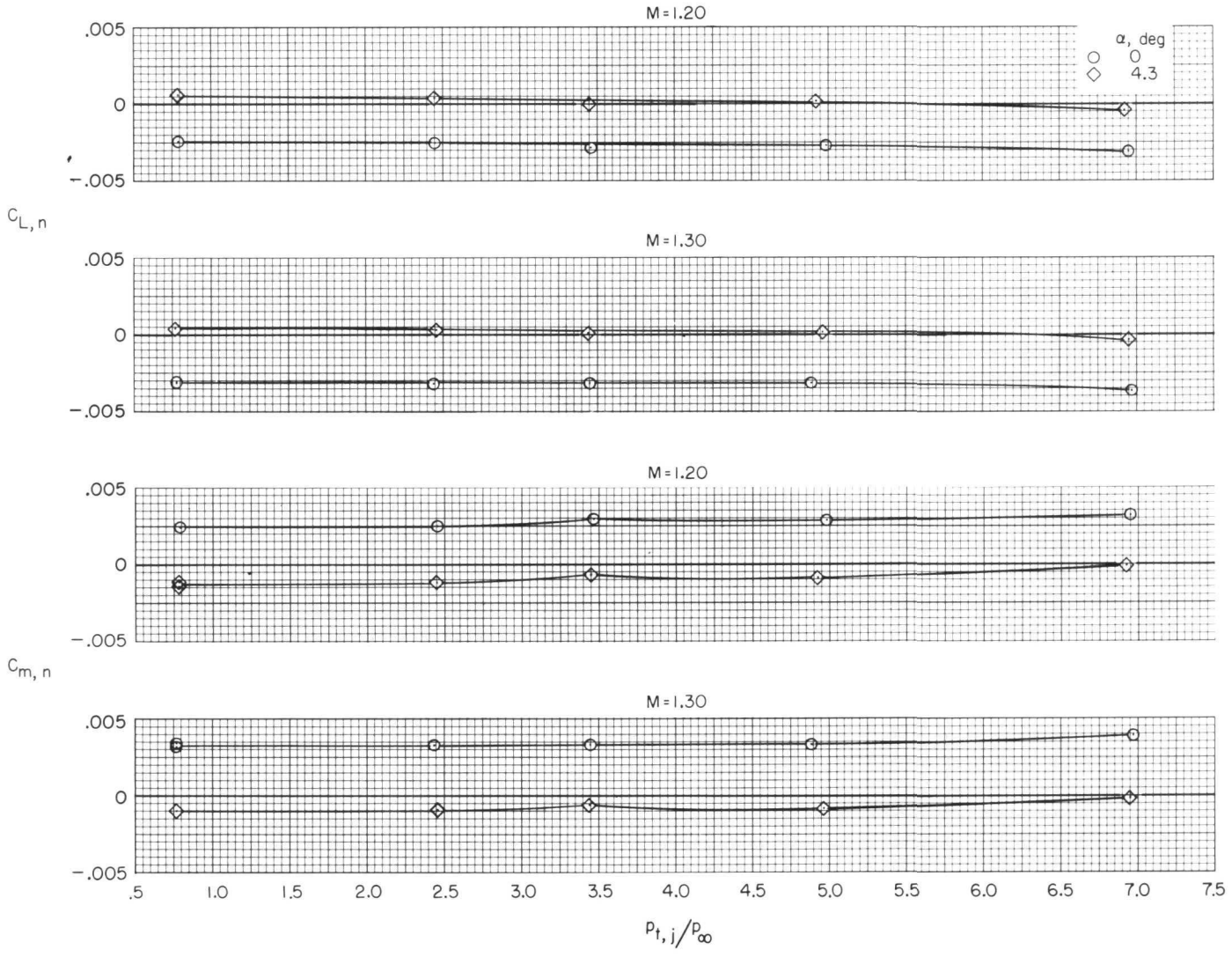

(e) Lift and pitching-moment coefficients at M = 1.20 and 1.30.

Figure 15. - Concluded.

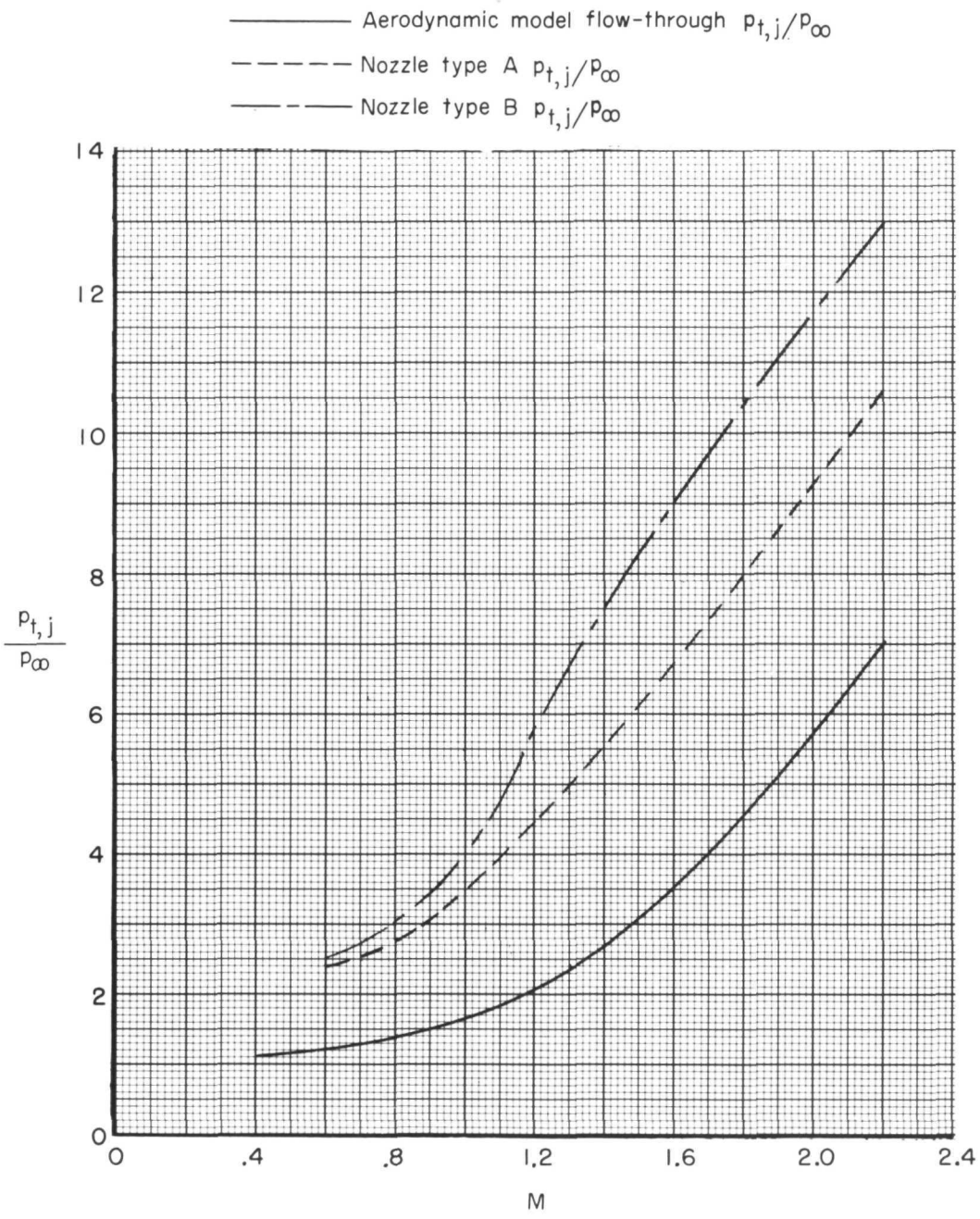

Figure 16.- Typical schedules of aerodynamic-model flow-through and operating jet total-pressure ratio.

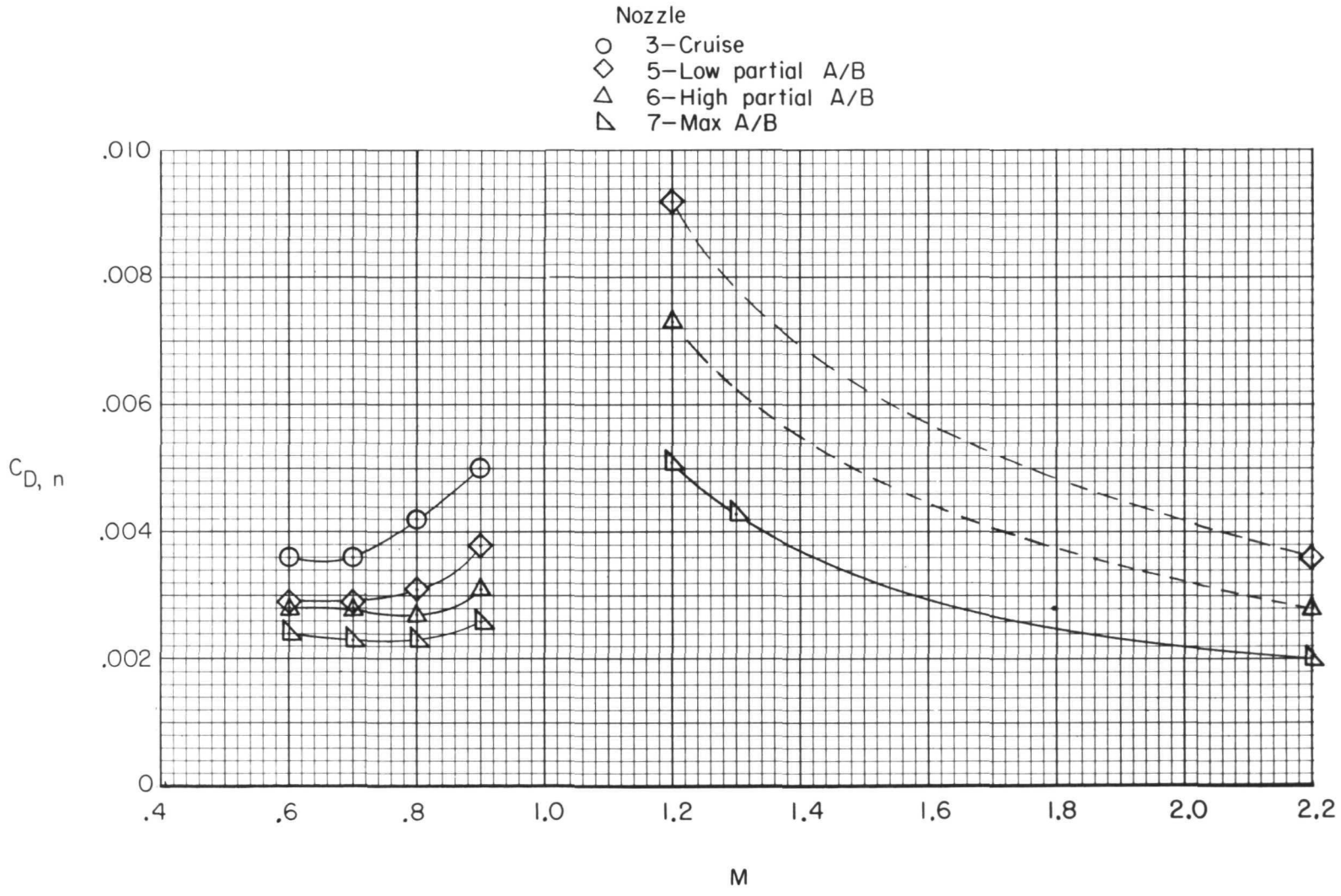

(a) Nozzle type A.

Figure 17.- Cross plots of nozzle drag variation with Mach number at $\alpha = 0^{o}$ for pressure ratio schedules of figure 16. Symbols are from faired data.

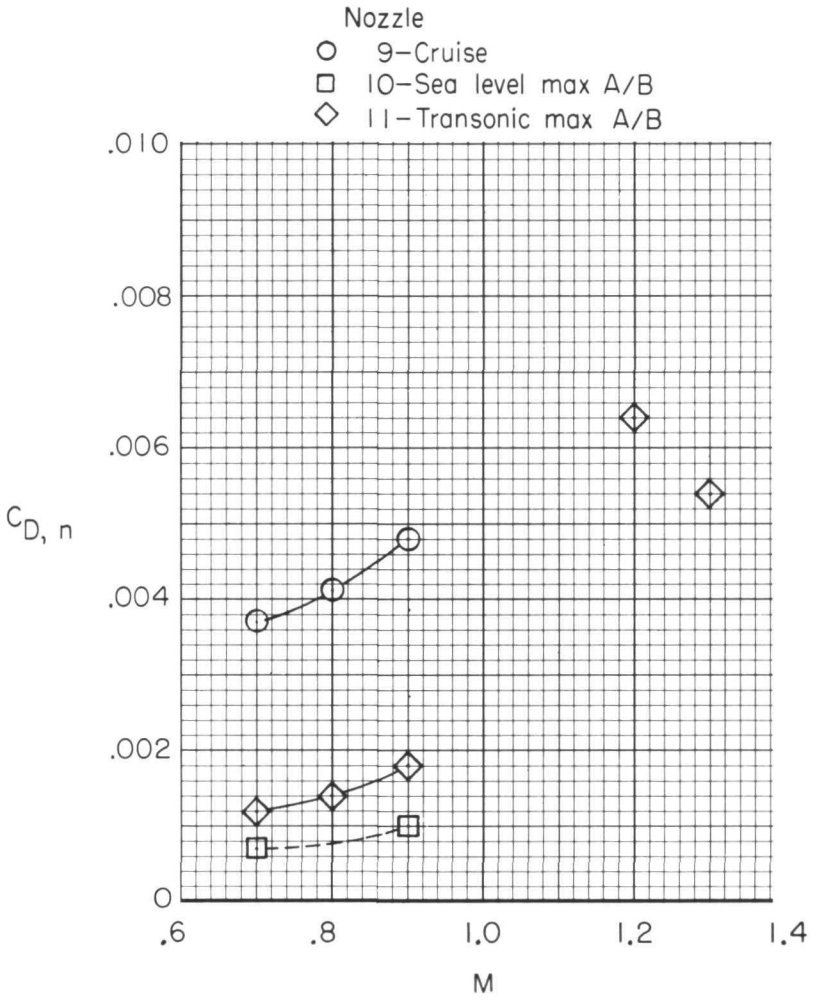

(b) Nozzle type B.

Figure 17.- Concluded.

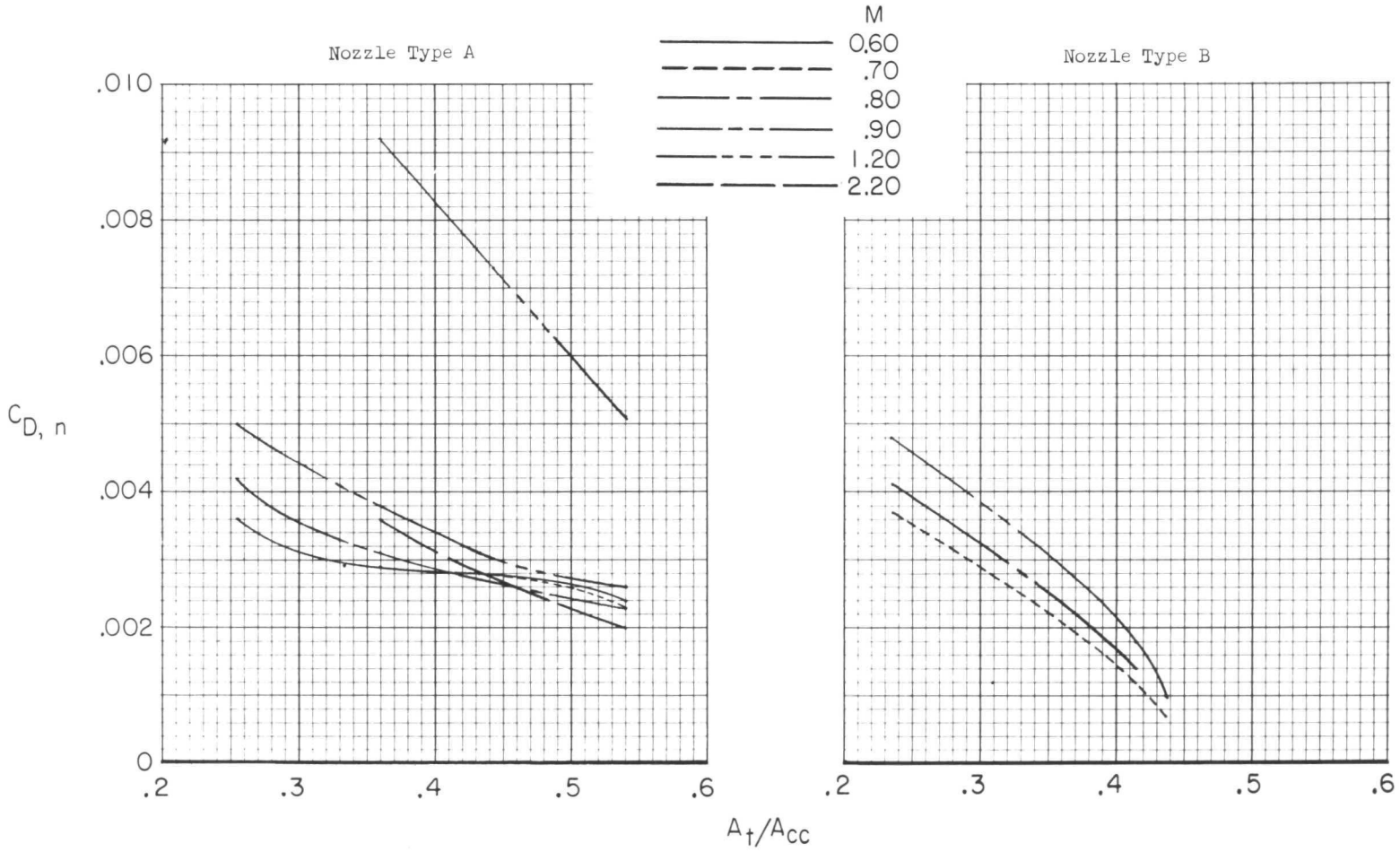

Figure 18.- Cross plot of nozzle drag variation with area ratio at $\alpha = 0^{o}$ for various Mach numbers at pressure ratio schedules of figure 16.

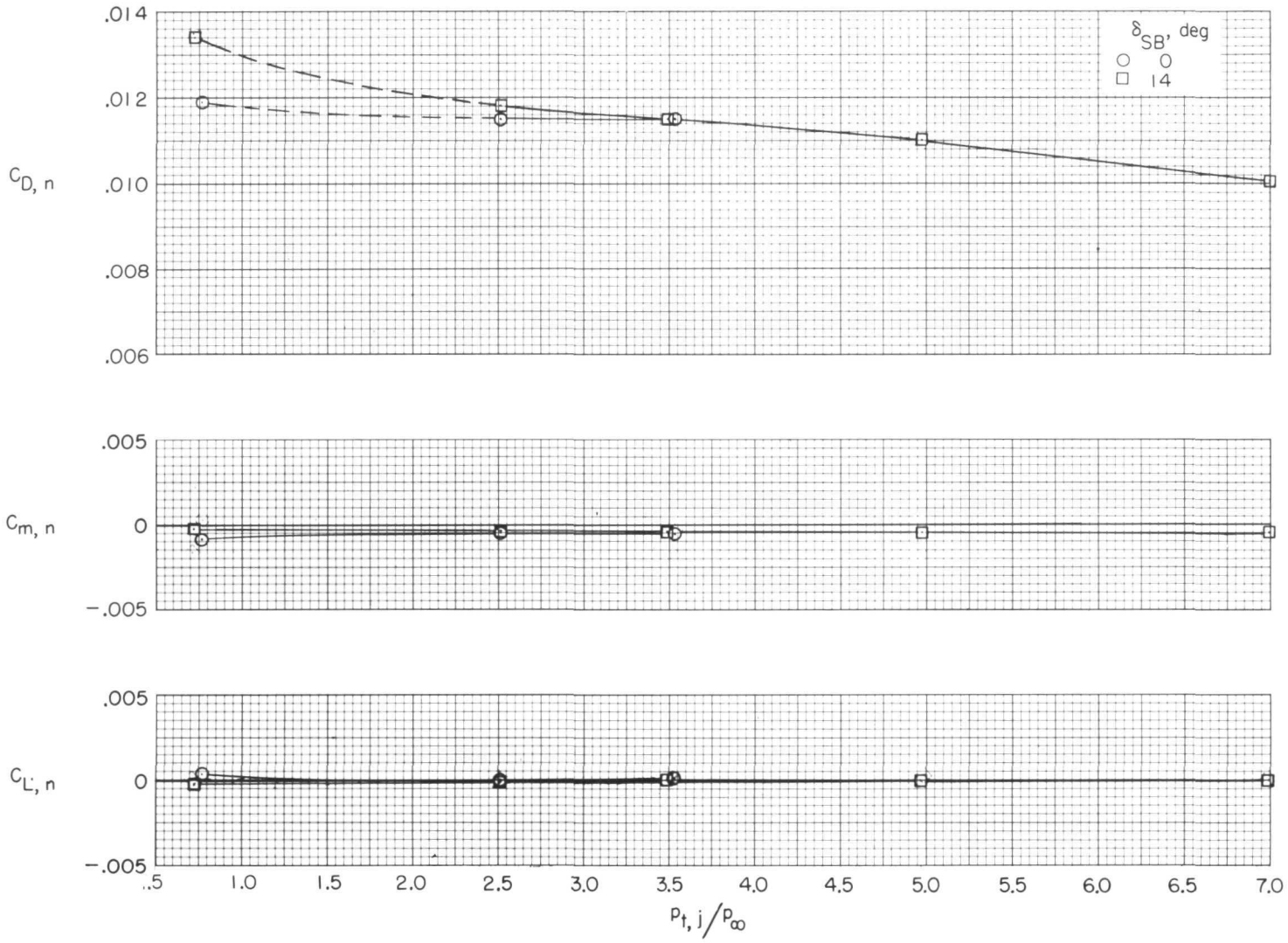

Figure 19.- Effect of speed-brake deflection and jet total-pressure ratio on nozzle aerodynamic characteristics at $M = 1.20$ and $\alpha = 0^{o}$. Configuration 3 (cruise power setting, nozzle type A).

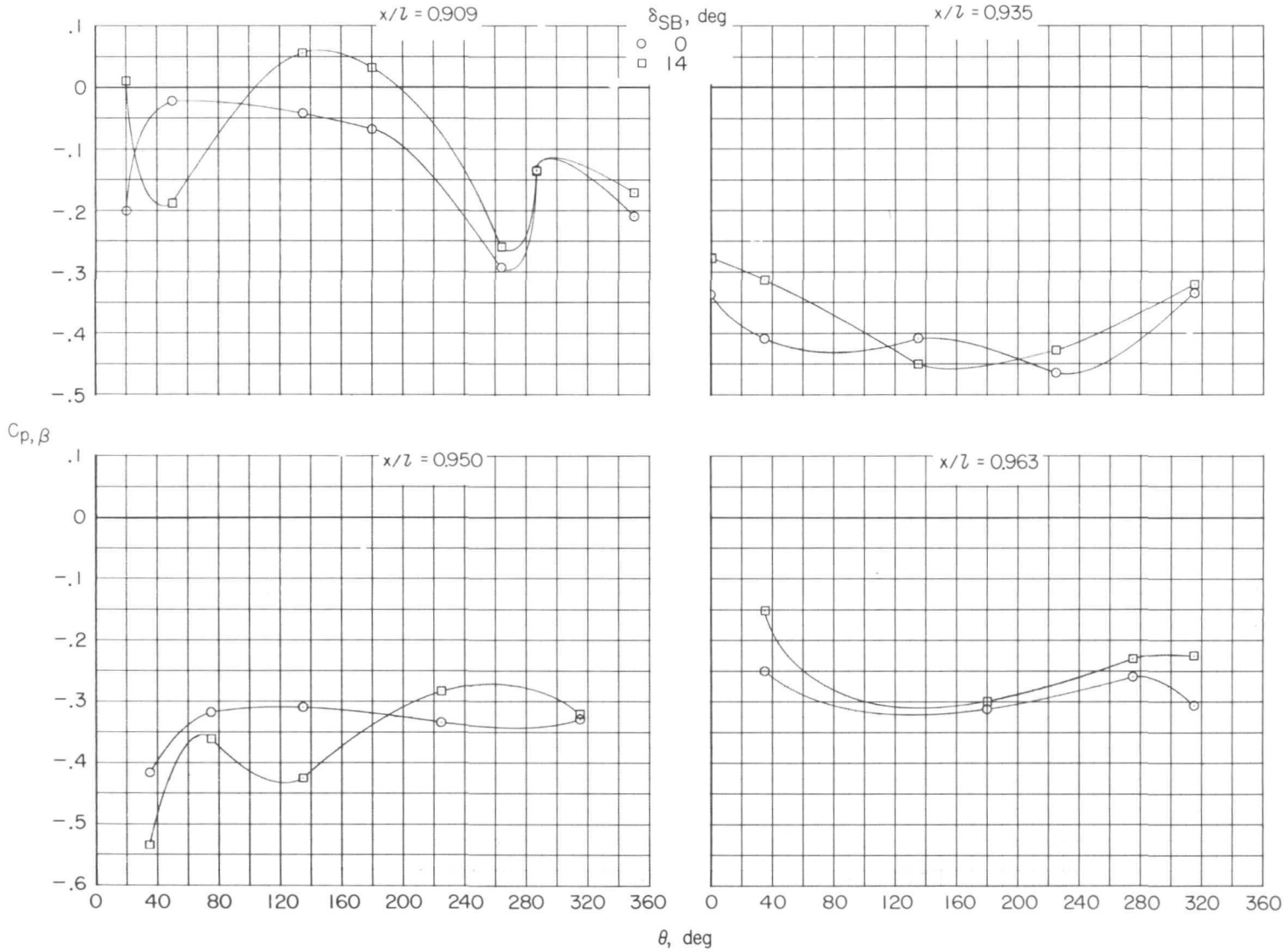

Figure 20.- Effect of speed-brake deflection on circumferential pressure distributions at several x/l stations for configuration 3 nozzles. M = 1.2; $\alpha = 0^{o}$; jet off.

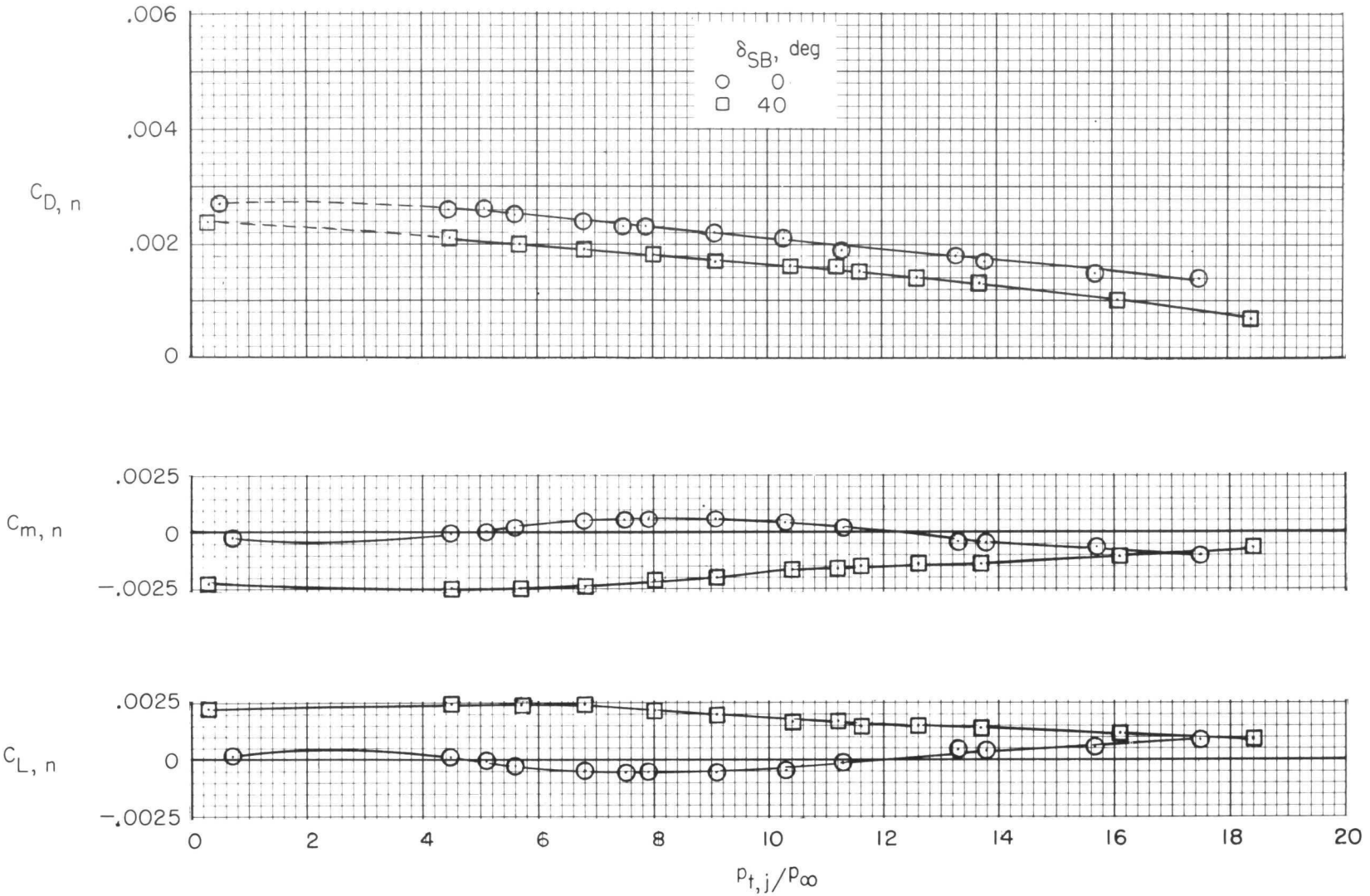

Figure 21.- Effect of speed-brake deflection and jet total-pressure ratio on nozzle aerodynamic characteristics at $M = 2.2$ and $\alpha = 0^{\circ}$. Configuration 7 (maximum afterburning power setting, nozzle type A).

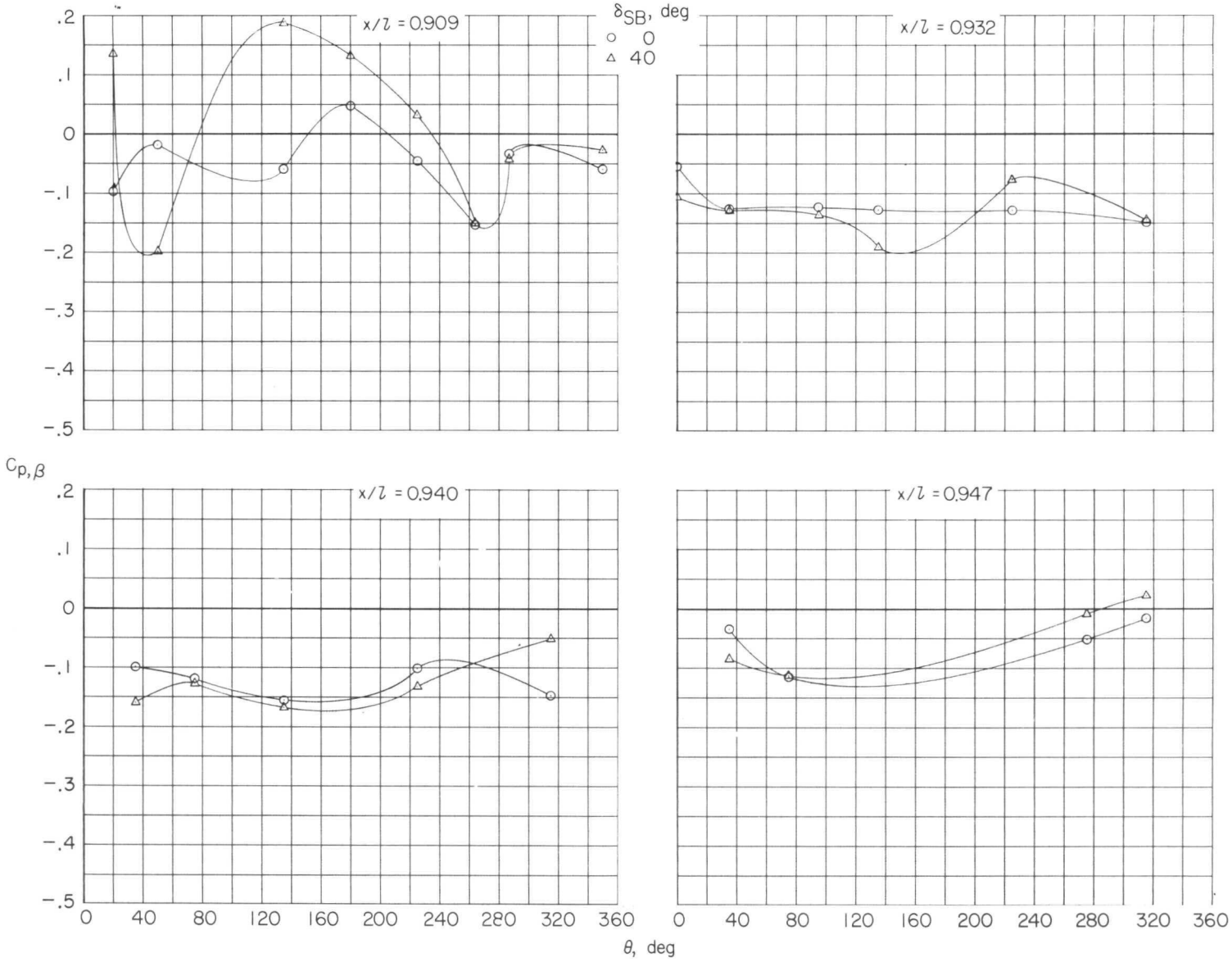

Figure 22.- Effect of speed-brake deflection on circumferential pressure distributions at various x/l stations for configuration 7 nozzles. $M = 2.2$; $\alpha = 0^{o}$; $p_{t,j}/p_{\infty}$.

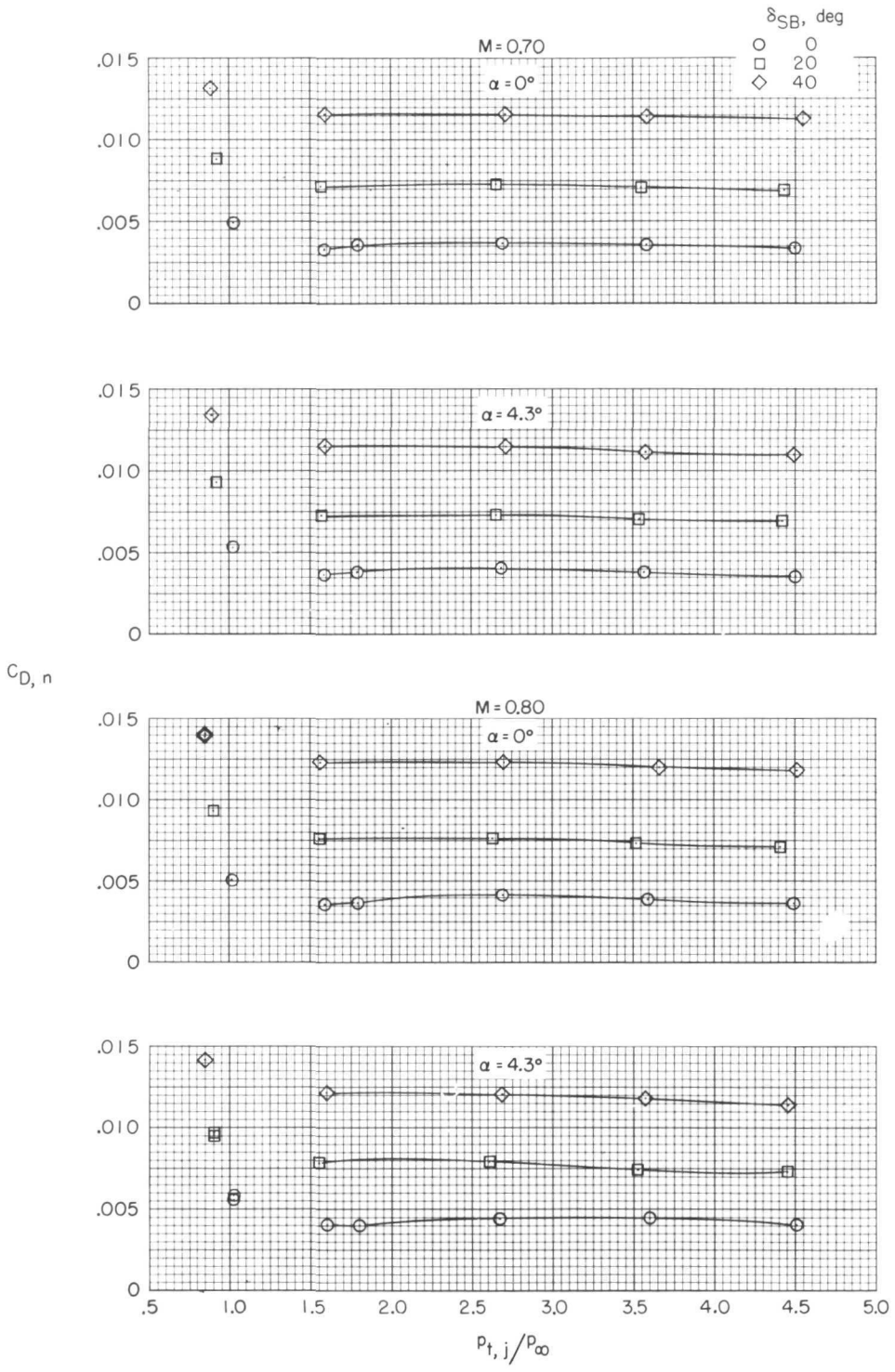

(a) Drag coefficient.

Figure 23.- Effect of speed-brake deflection and jet total-pressure ratio on nozzle aerodynamic characteristics. Configuration 9 (cruise power setting, nozzle type B).

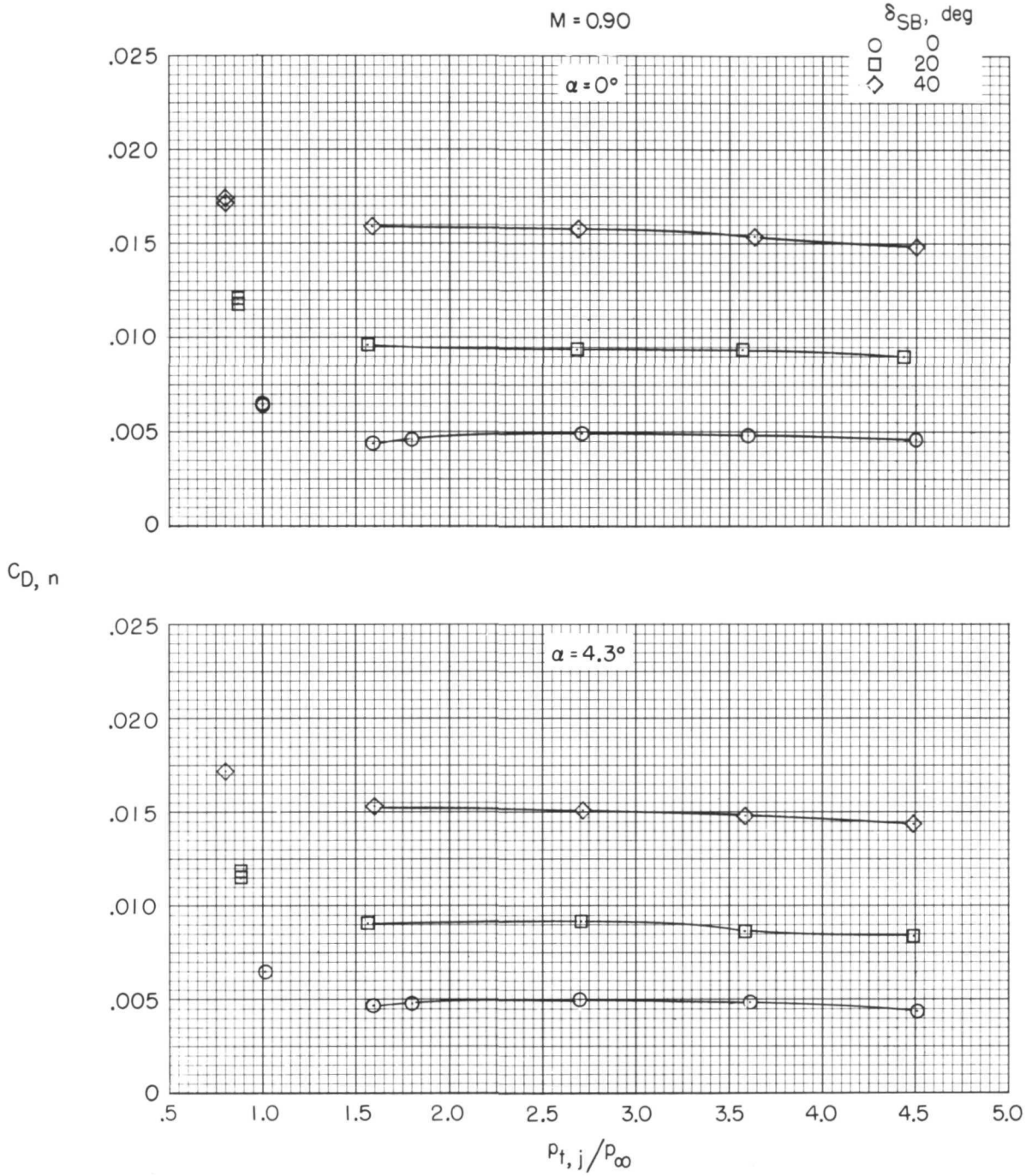

(a) Concluded.

Figure 23.- Continued.

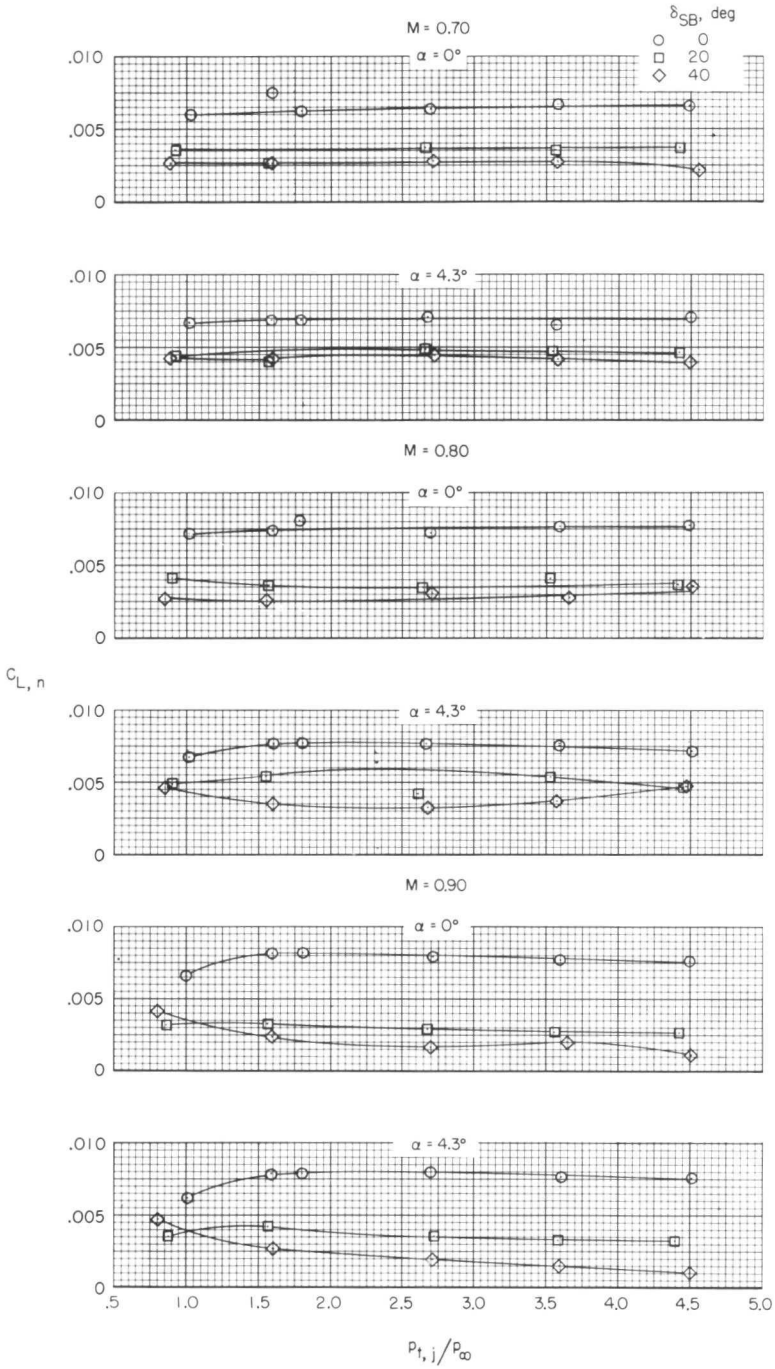

(b) Lift coefficient.

Figure 23.- Continued.

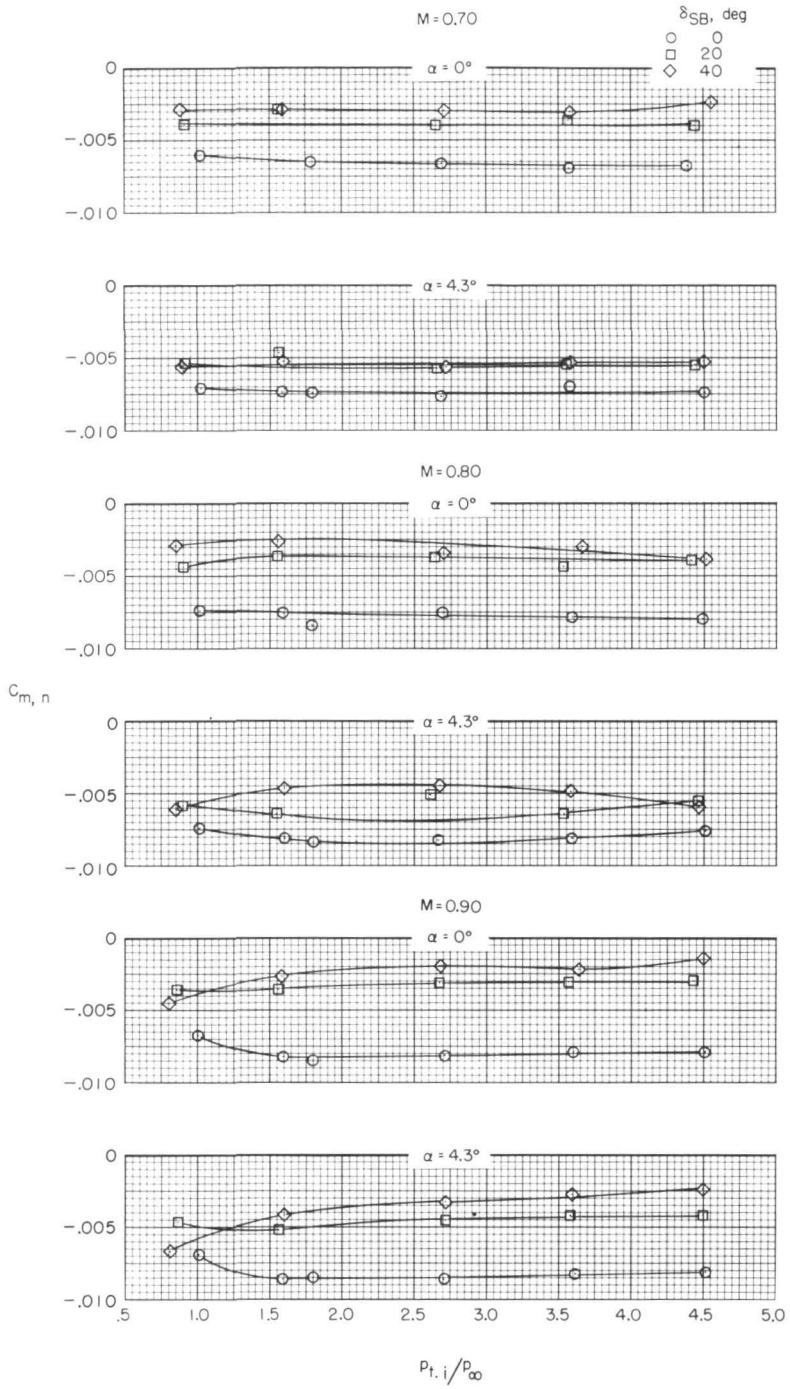

(c) Pitching-moment coefficient.

Figure 23.- Concluded.

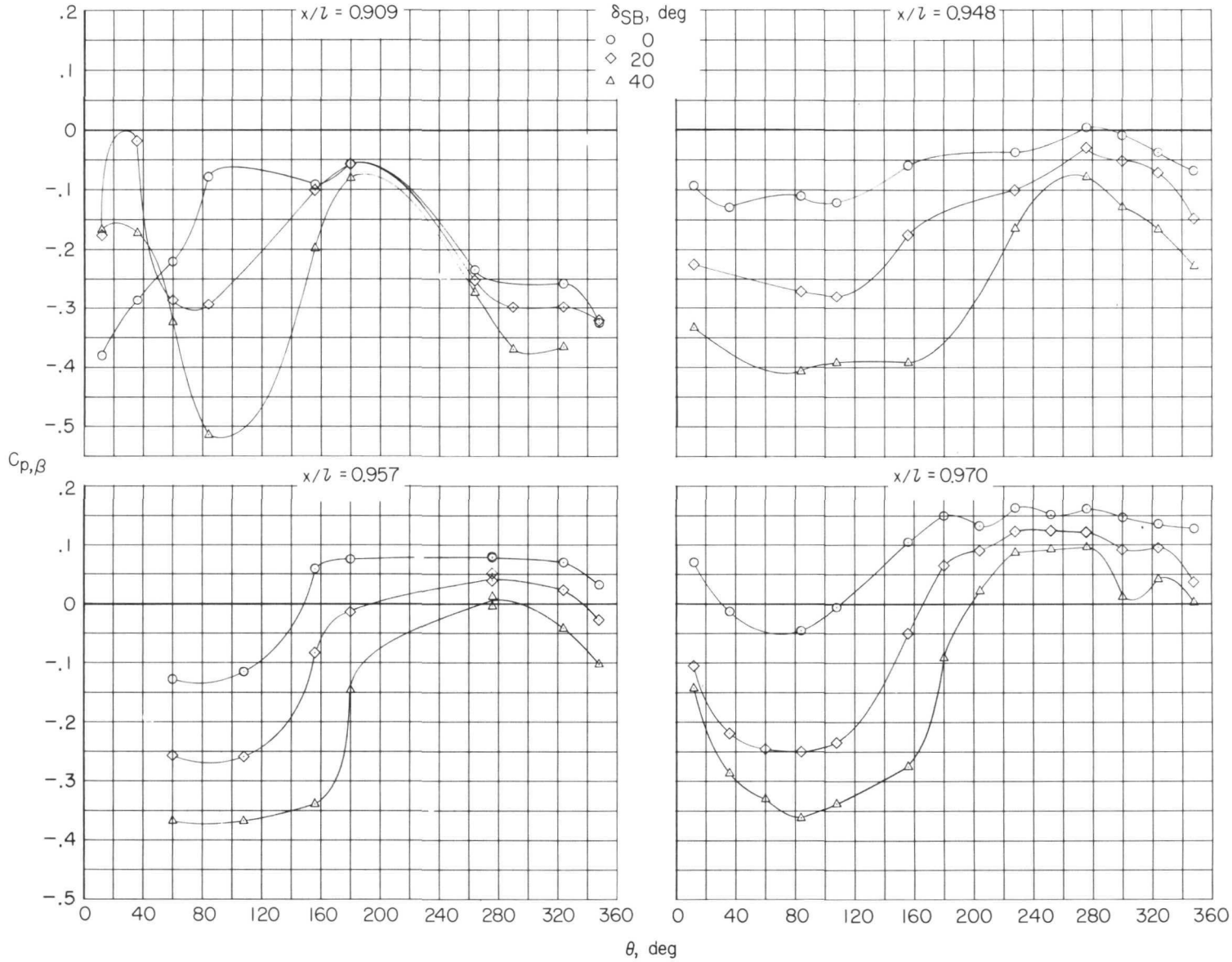

Figure 24.- Effect of speed-brake deflection on circumferential pressure distributions at various x/l stations for configuration 9 nozzles. $M = 0.7$; $\alpha = 4.3^{o}$; $p_{t,j}/p_{\infty} = 2.7$.

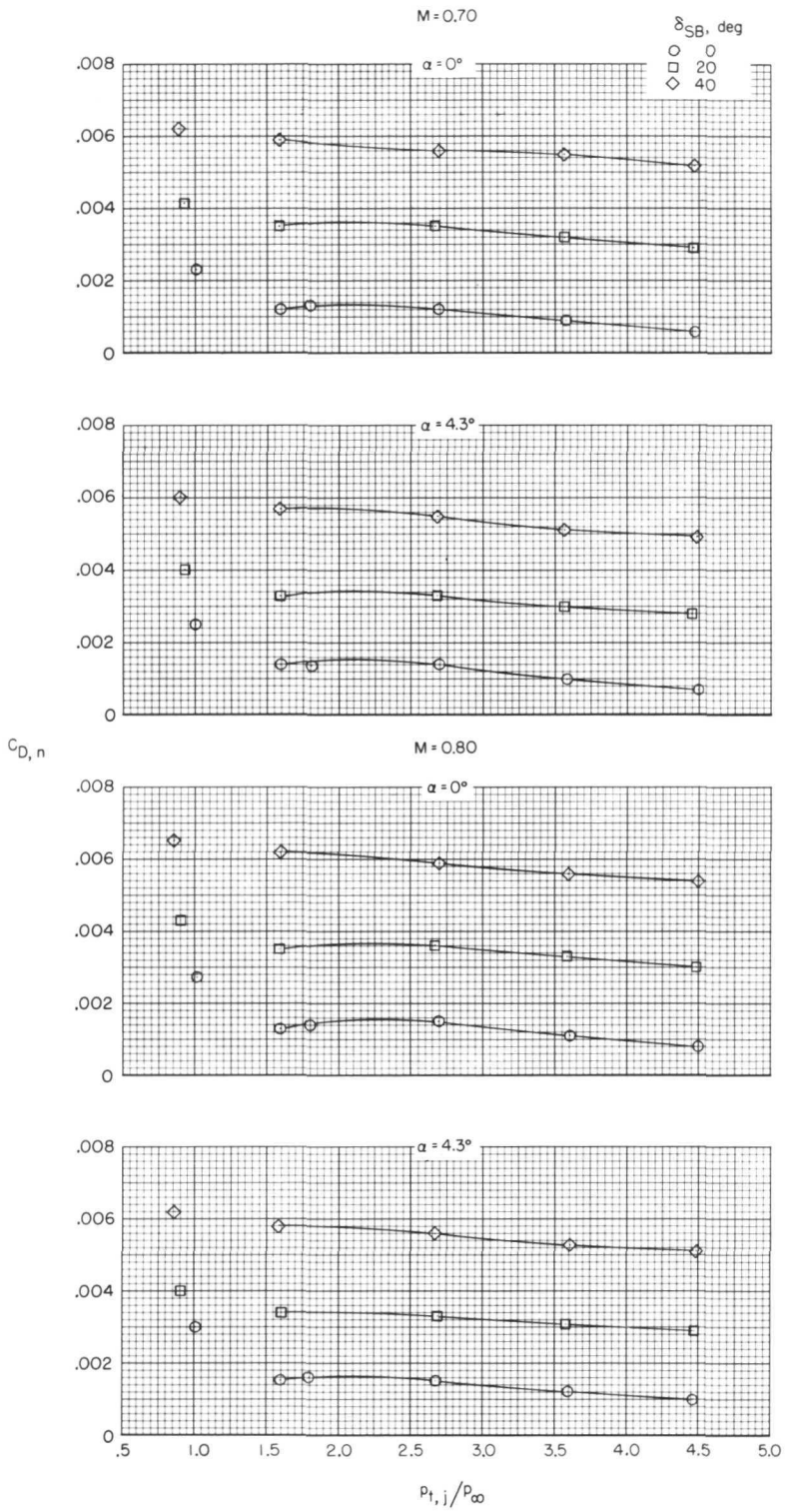

(a) Drag coefficient.

Figure 25.- Effect of speed-brake deflection and jet total-pressure ratio on nozzle aerodynamic characteristics. Configuration 11 (transonic maximum afterburning power setting, nozzle type B).

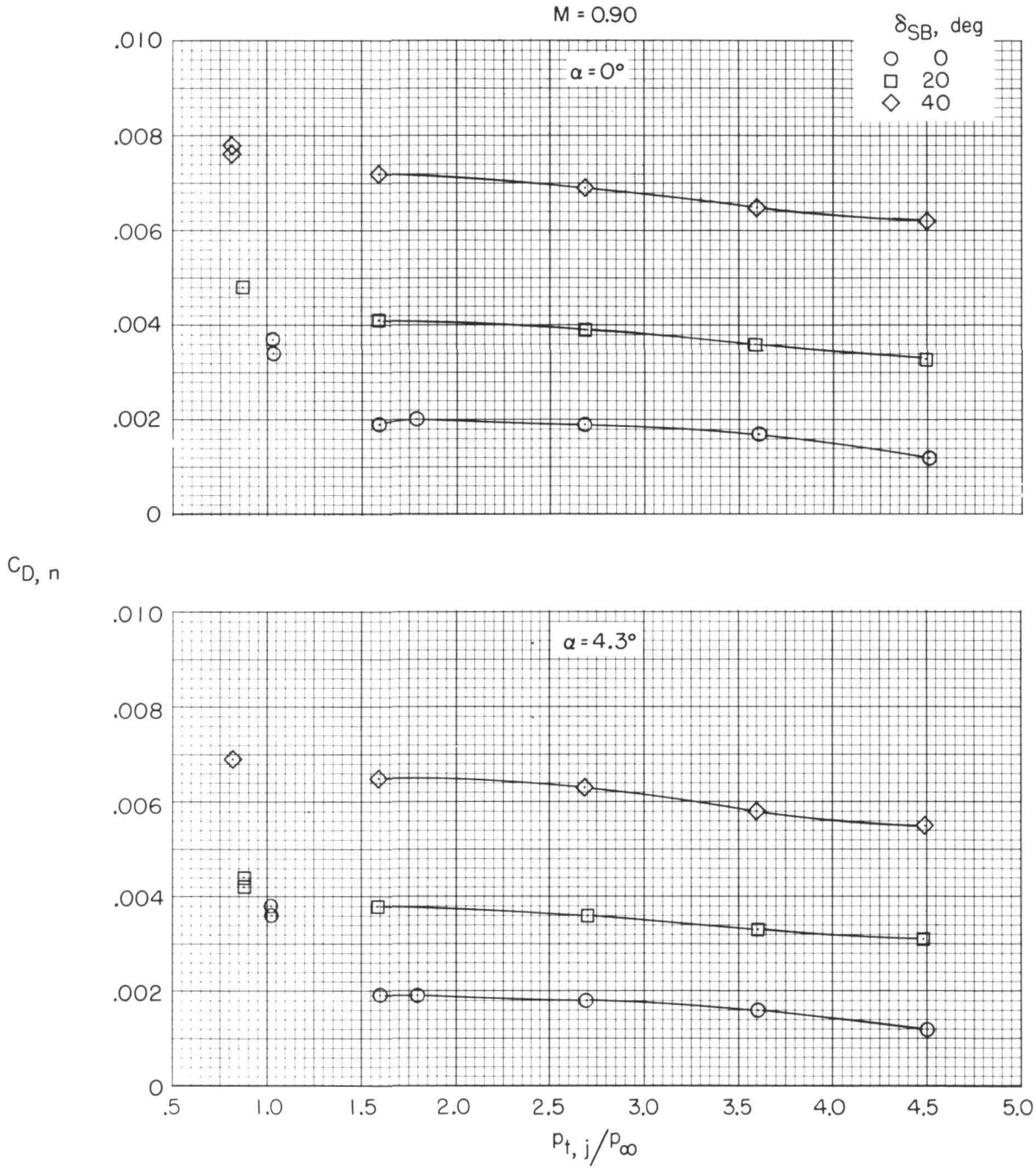

(a) Continued.

Figure 25.- Continued.

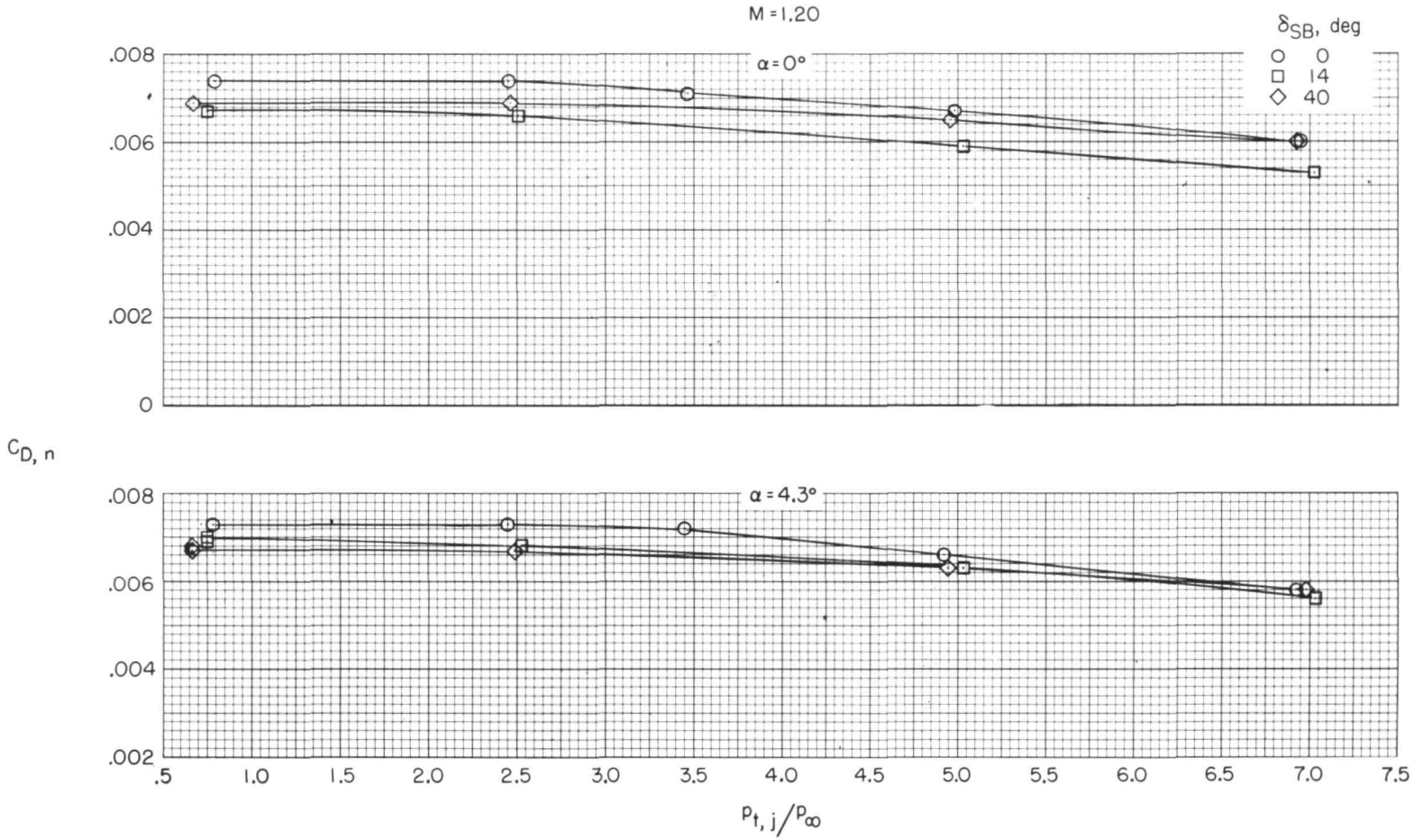

(a) Concluded.

Figure 25.- Continued.

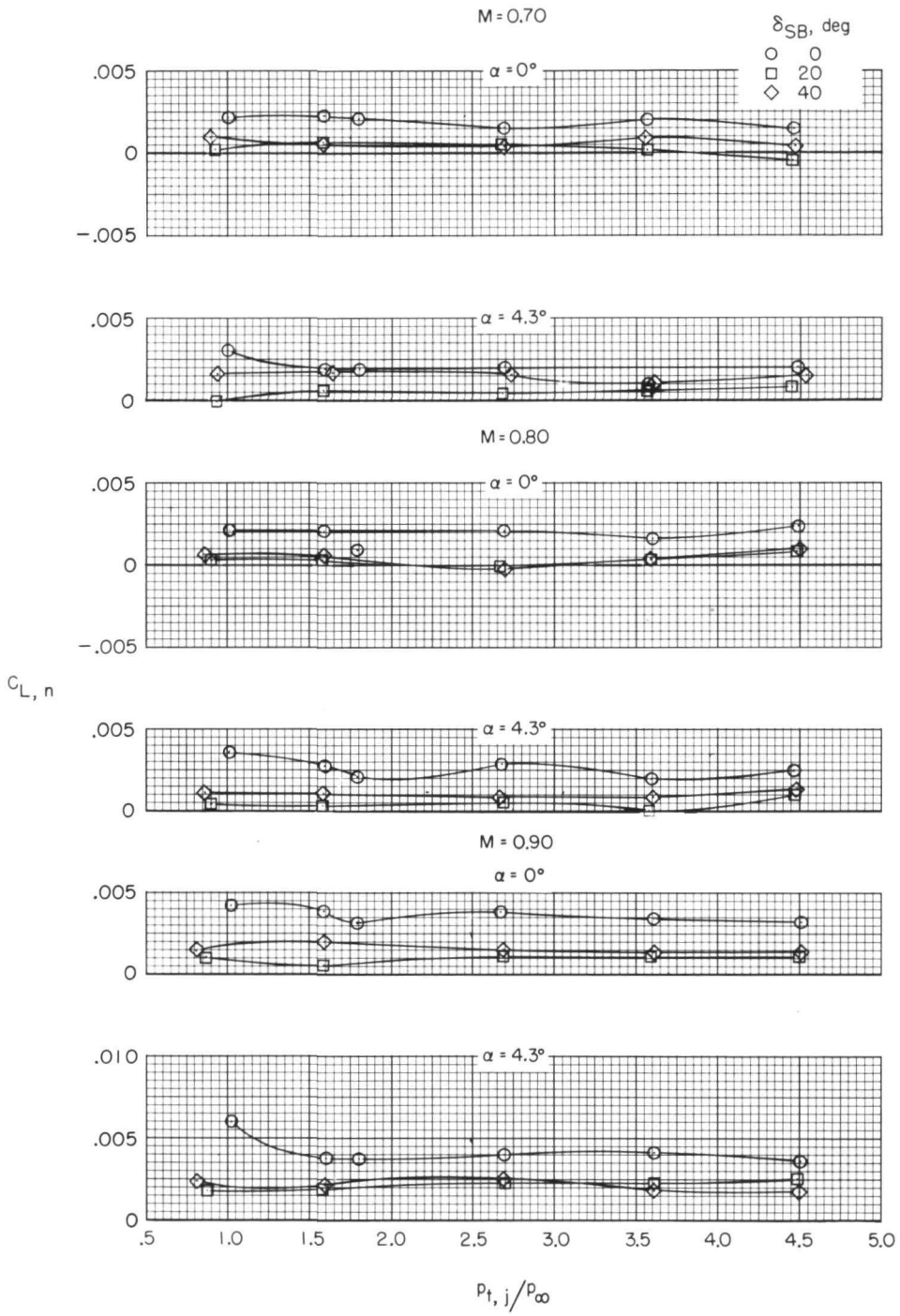

(b) Lift coefficient.

Figure 25.- Continued.

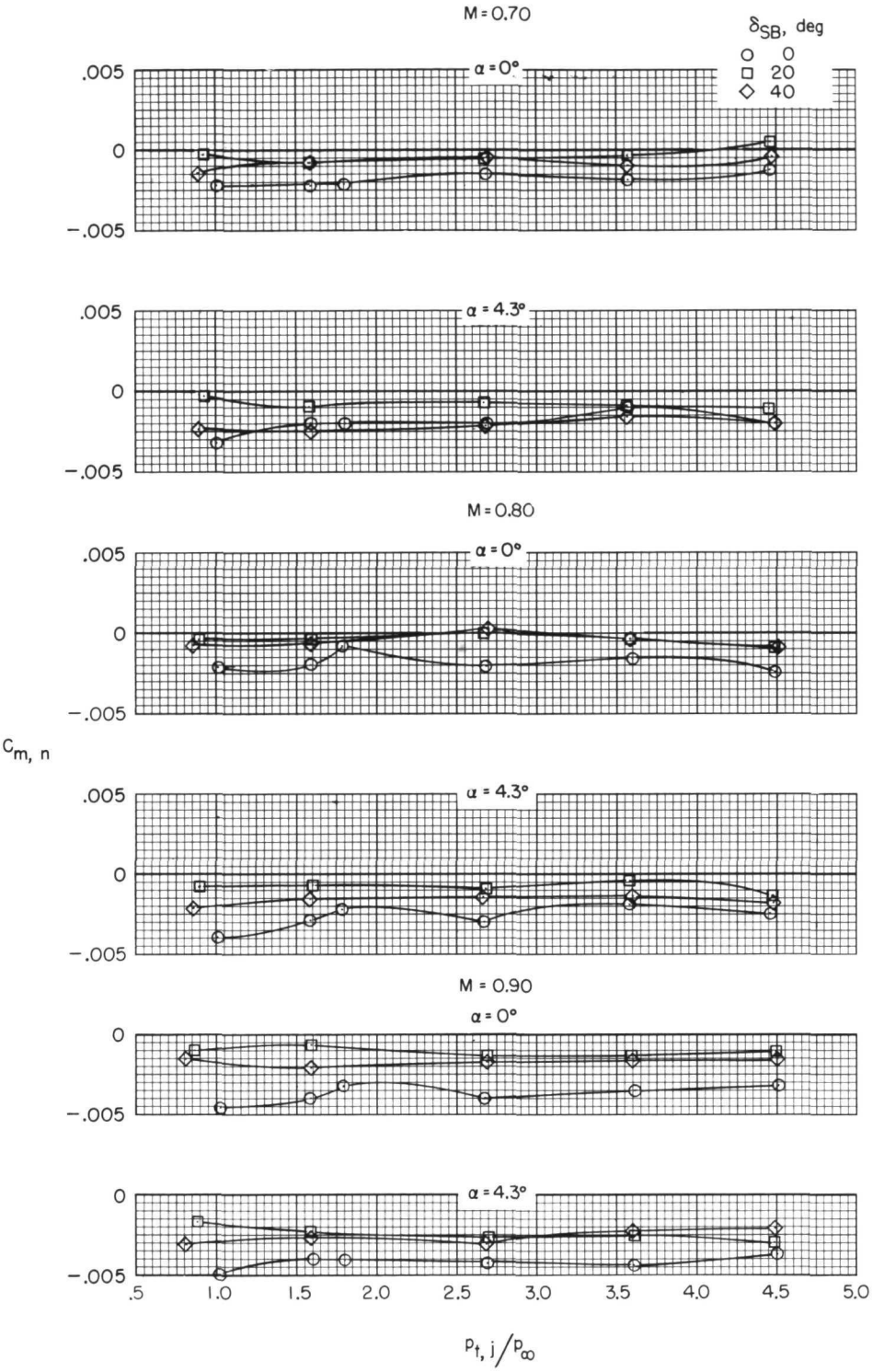

(c) Pitching-moment coefficient.

Figure 25.- Continued.

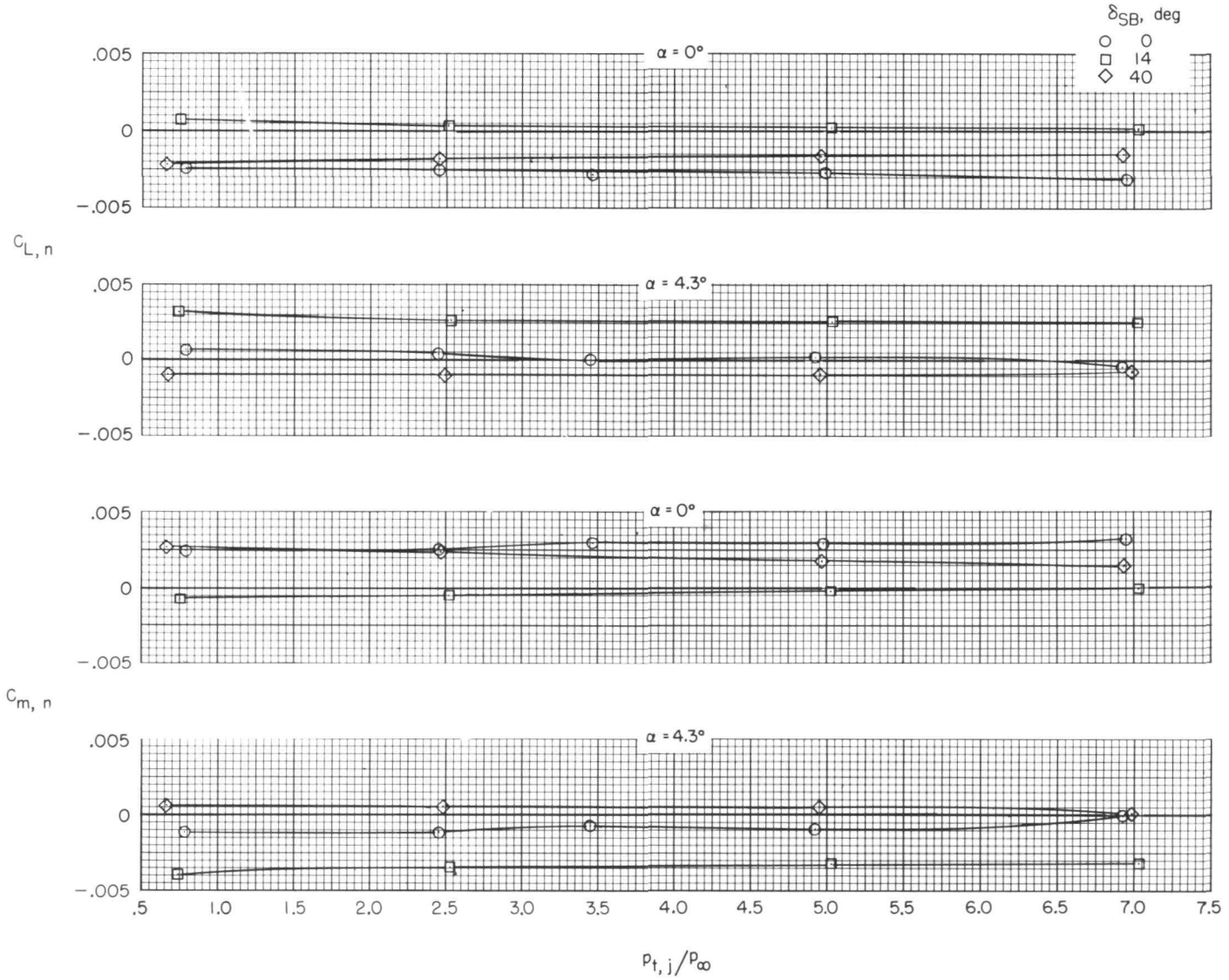

(d) Lift and pitching-moment coefficients at M = 1.20.

Figure 25.- Concluded.

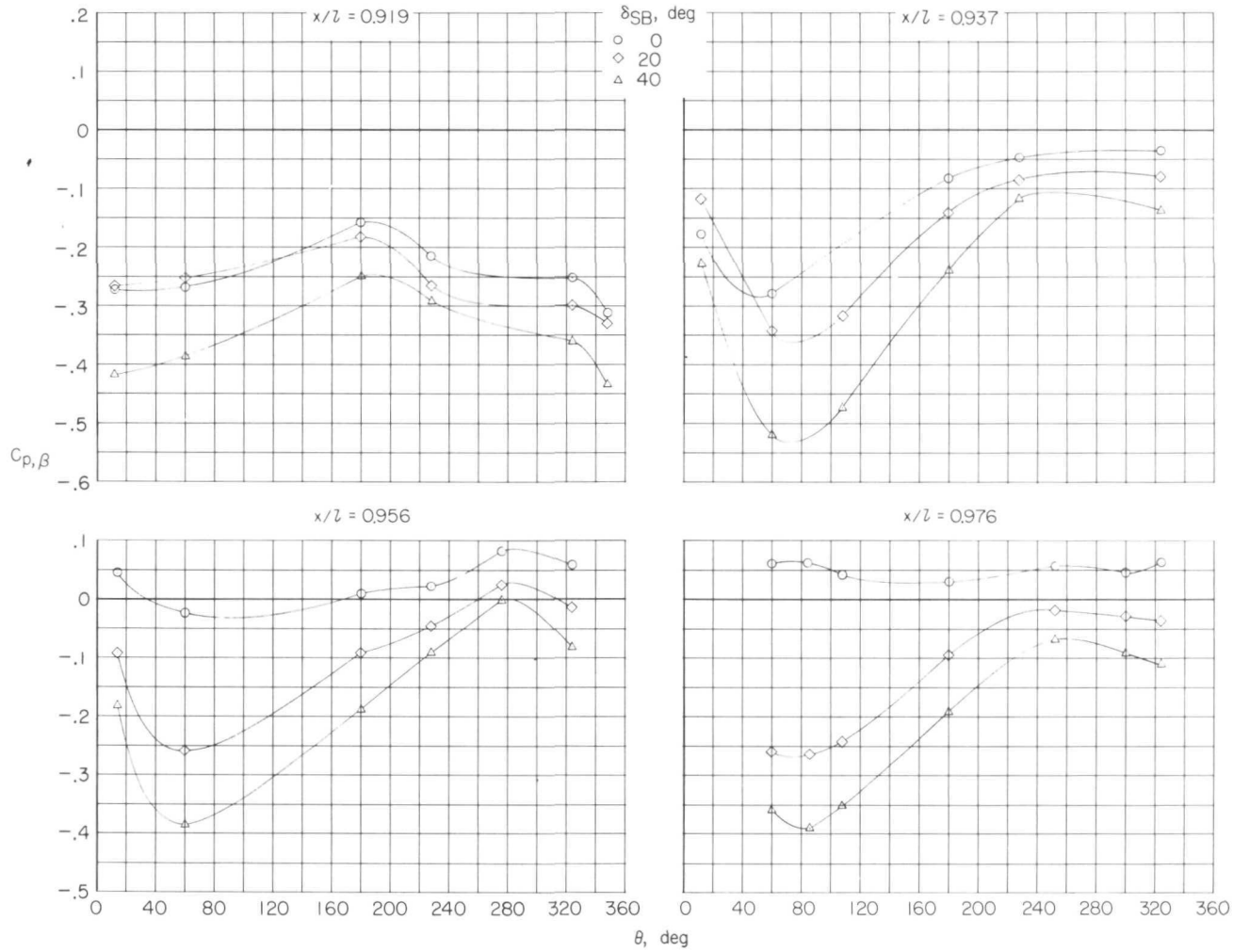

(a) M = 0.7; $\alpha = 4.3^{o}$; $p_{t,j}/p_{\infty} = 2.7$.

Figure 26.- Effect of speed-brake deflection on circumferential distributions of pressure at various x/l stations for configuration 11 nozzles.

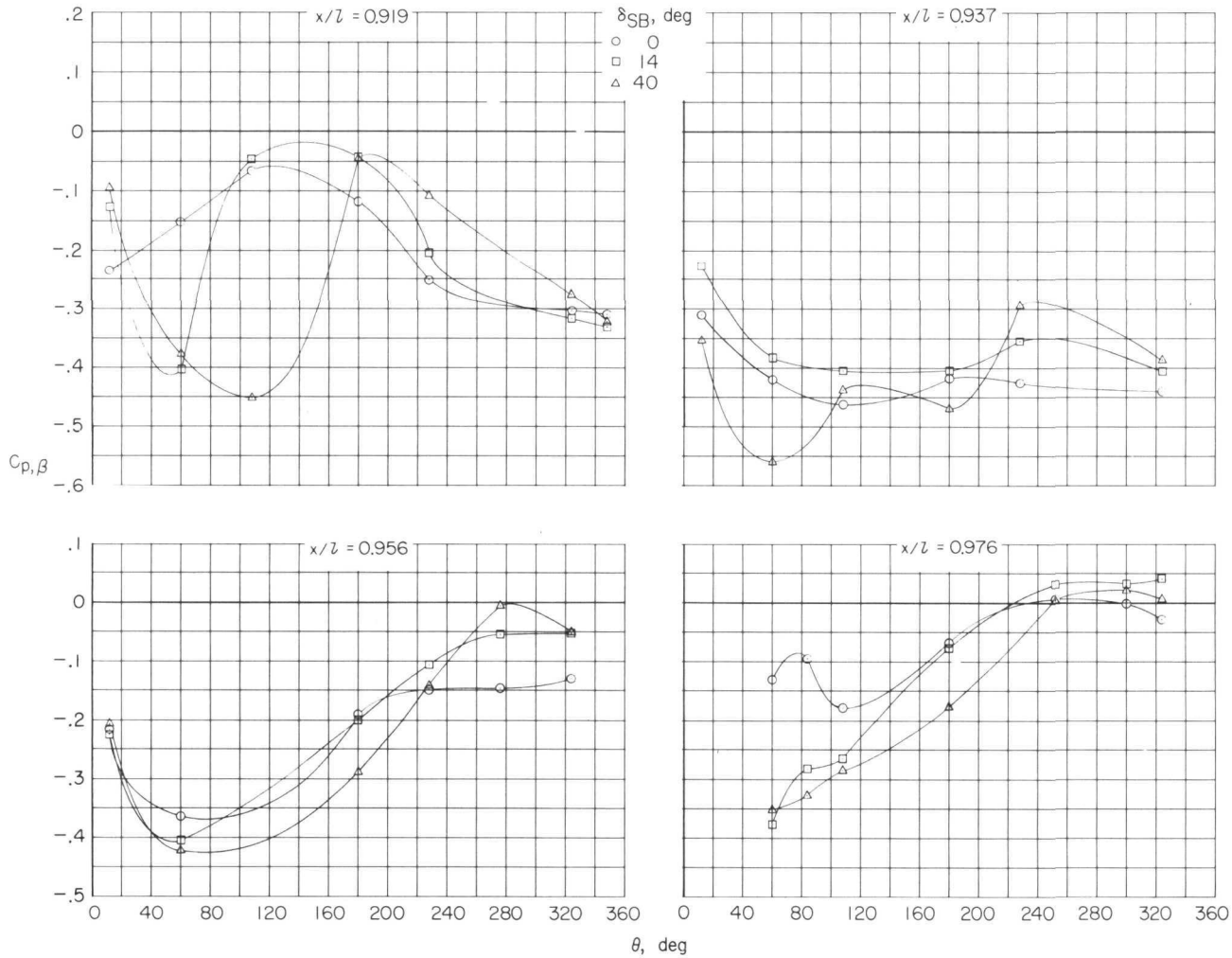

(b) $M = 1.2$; $\alpha = 4.3^{o}$; $p_{t,j}/p_{\infty} = 4.9$.

Figure 26.- Concluded.

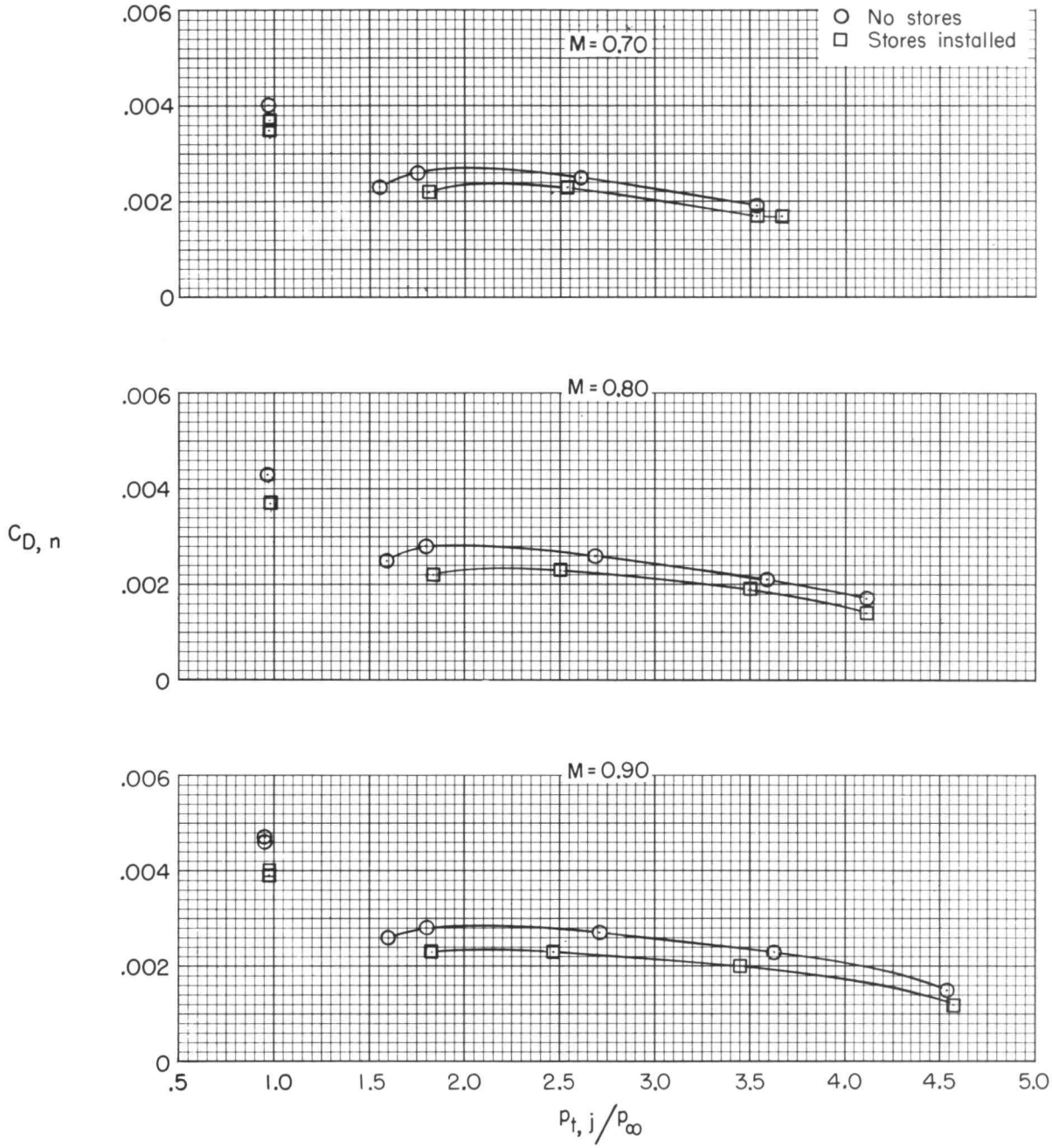

(a) Drag coefficient.

Figure 27.- Effect of store installation and jet total-pressure ratio on nozzle aerodynamic characteristics at $\alpha = 4.3^{\circ}$. Configuration 7 (maximum afterburning power setting, nozzle type A).

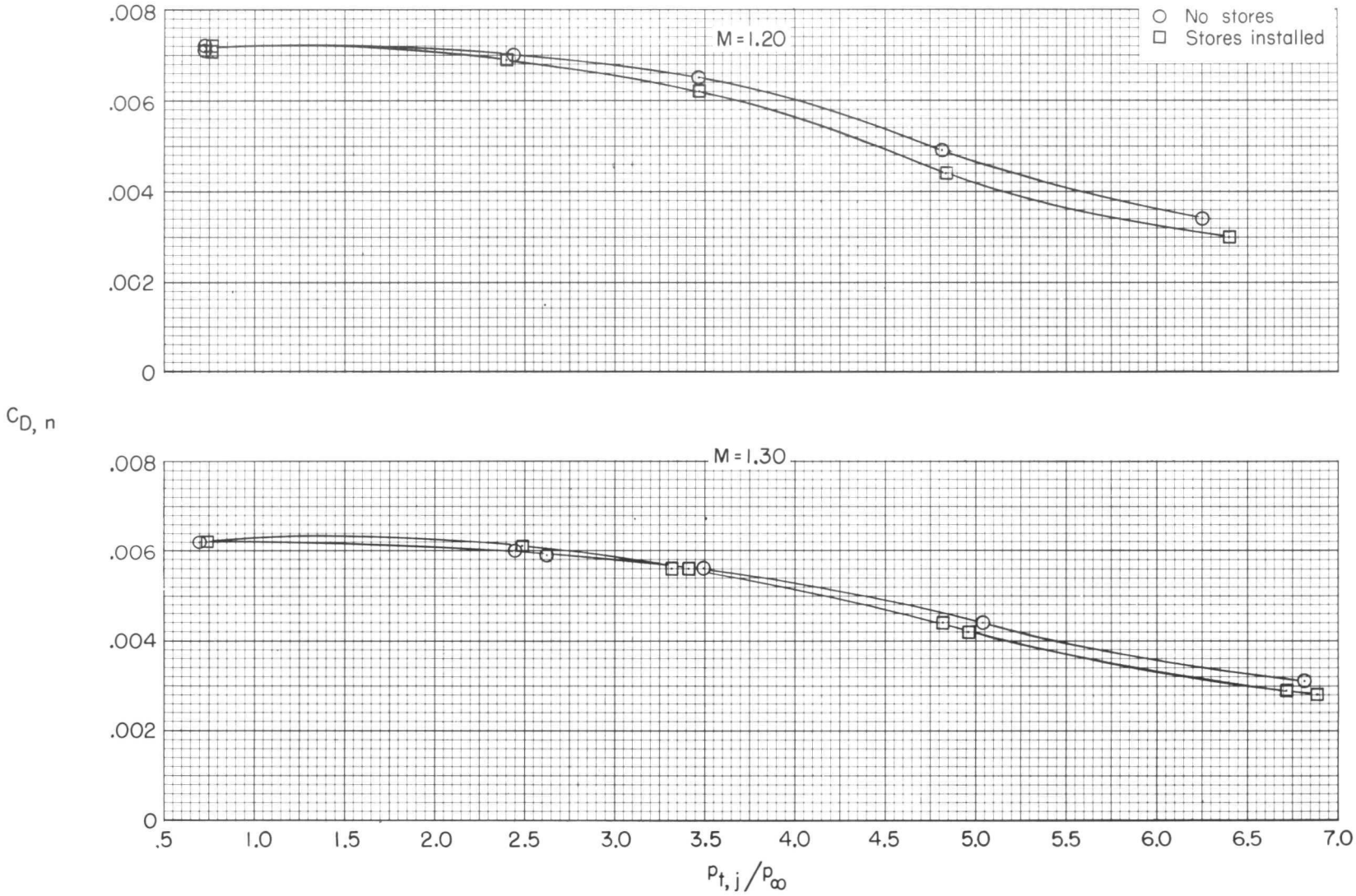

(a) Concluded.

Figure 27.- Continued.

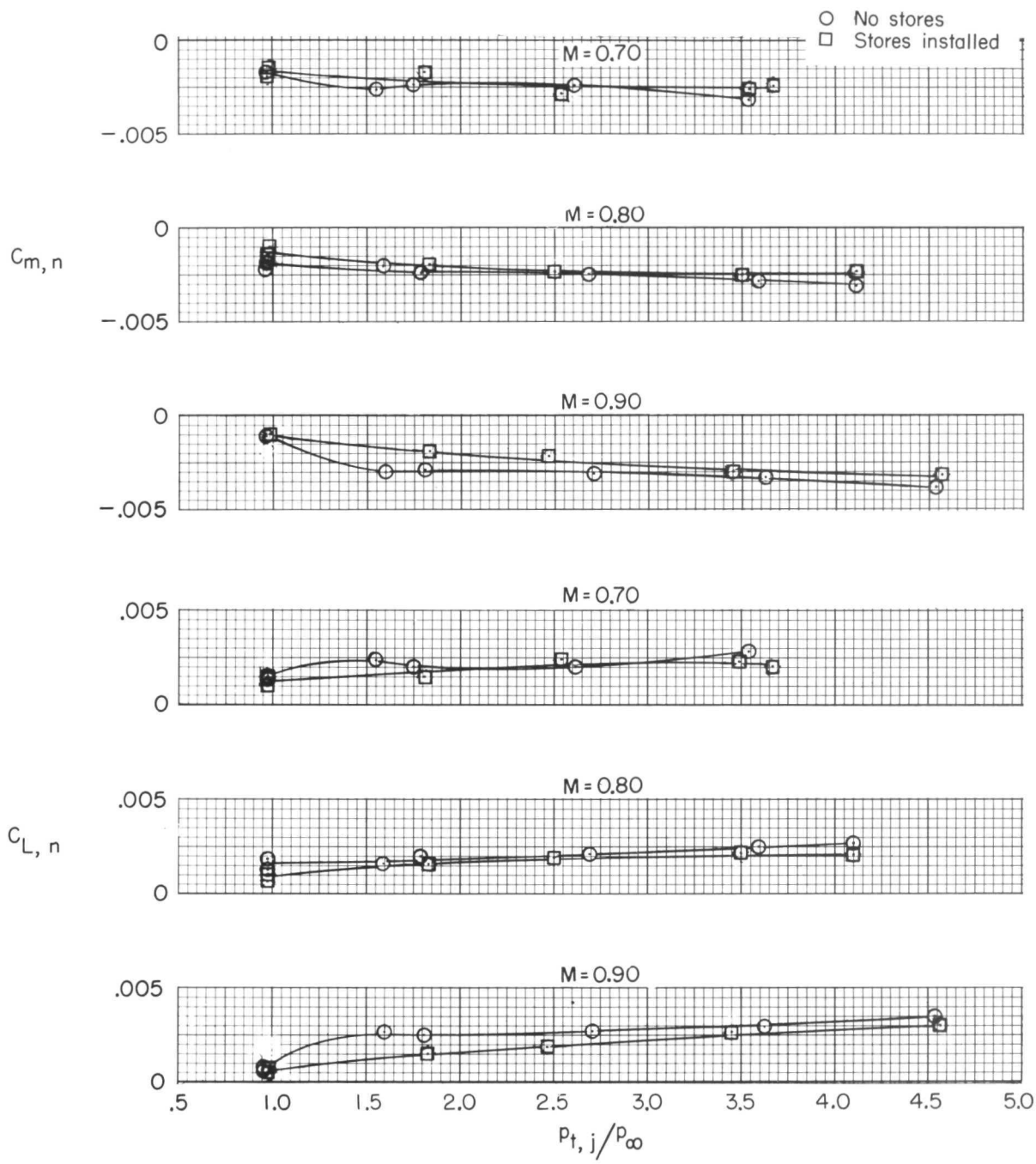

(b) Lift and pitching-moment coefficients.

Figure 27.- Continued.

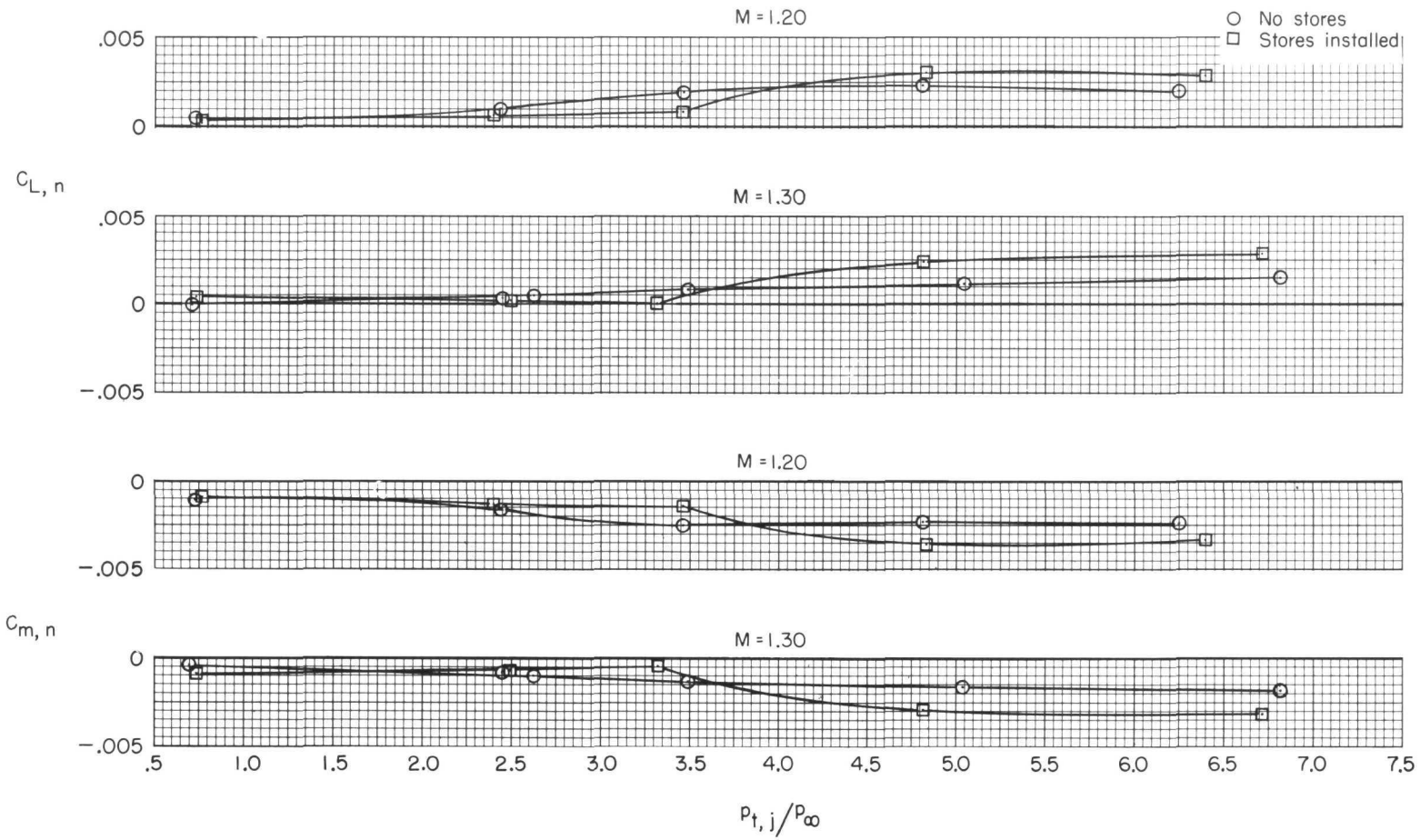

(b) Concluded.

Figure 27.- Concluded.

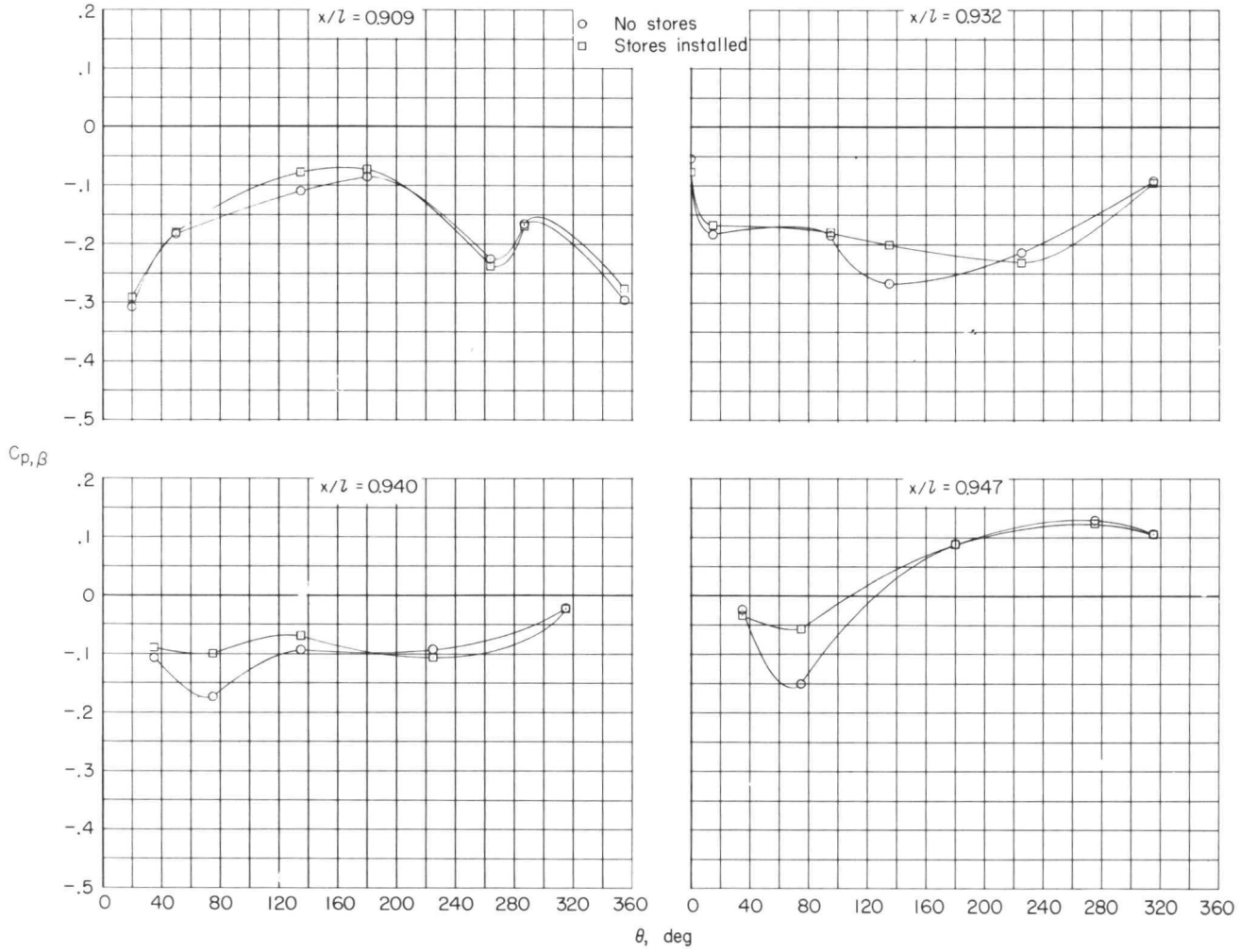

(a) M = 0.7; $\alpha = 4.3^{o}$; $p_{t,j}/p_{\infty} = 2.6$.

Figure 28.- Effect of store installation on circumferential distributions of pressure at various x/l stations for configuration 7 nozzles.

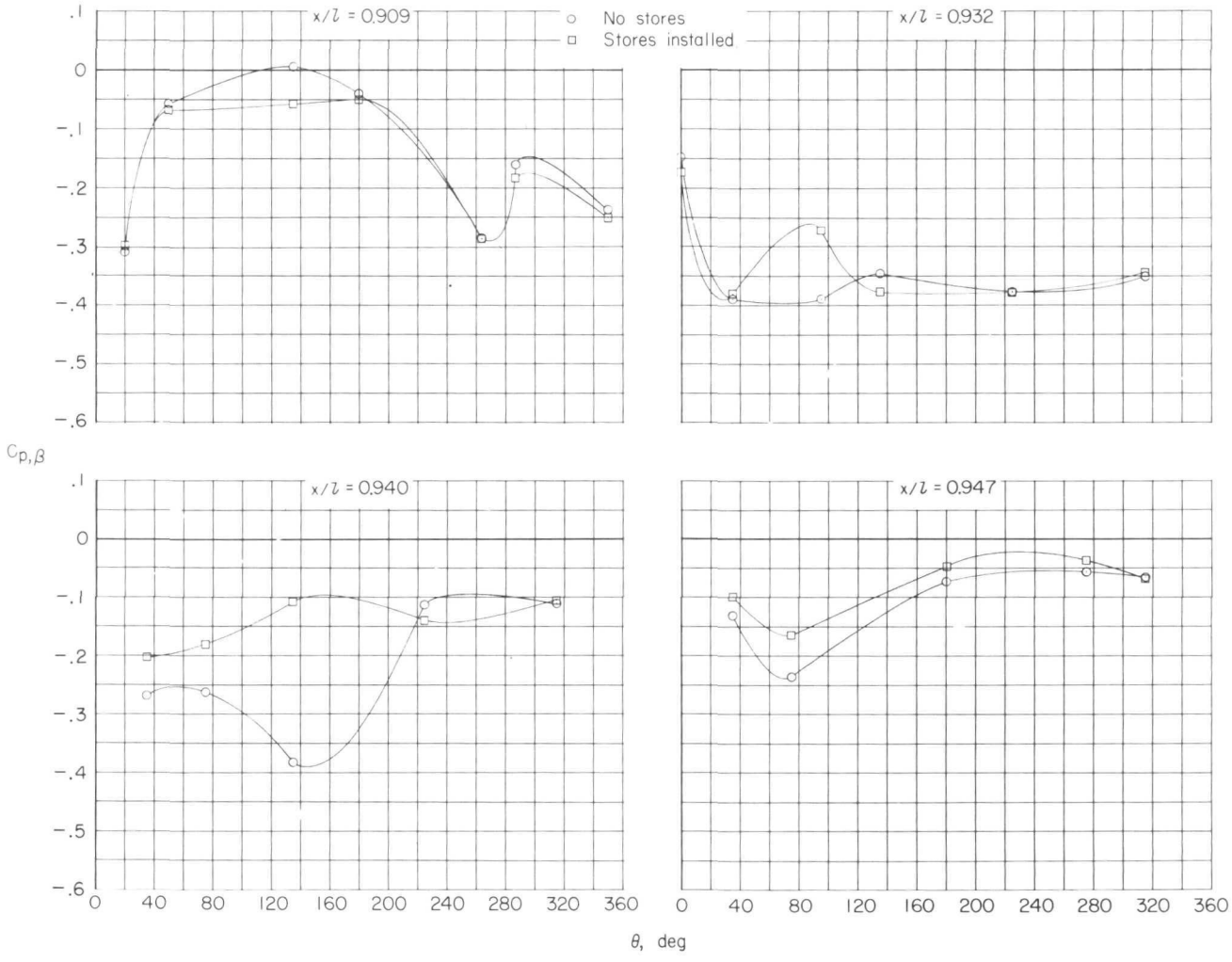

(b) M = 1.2; $\alpha = 4.3^{o}$; $p_{t,j}/p_{\infty} = 4.5$.

Figure 28.- Concluded.

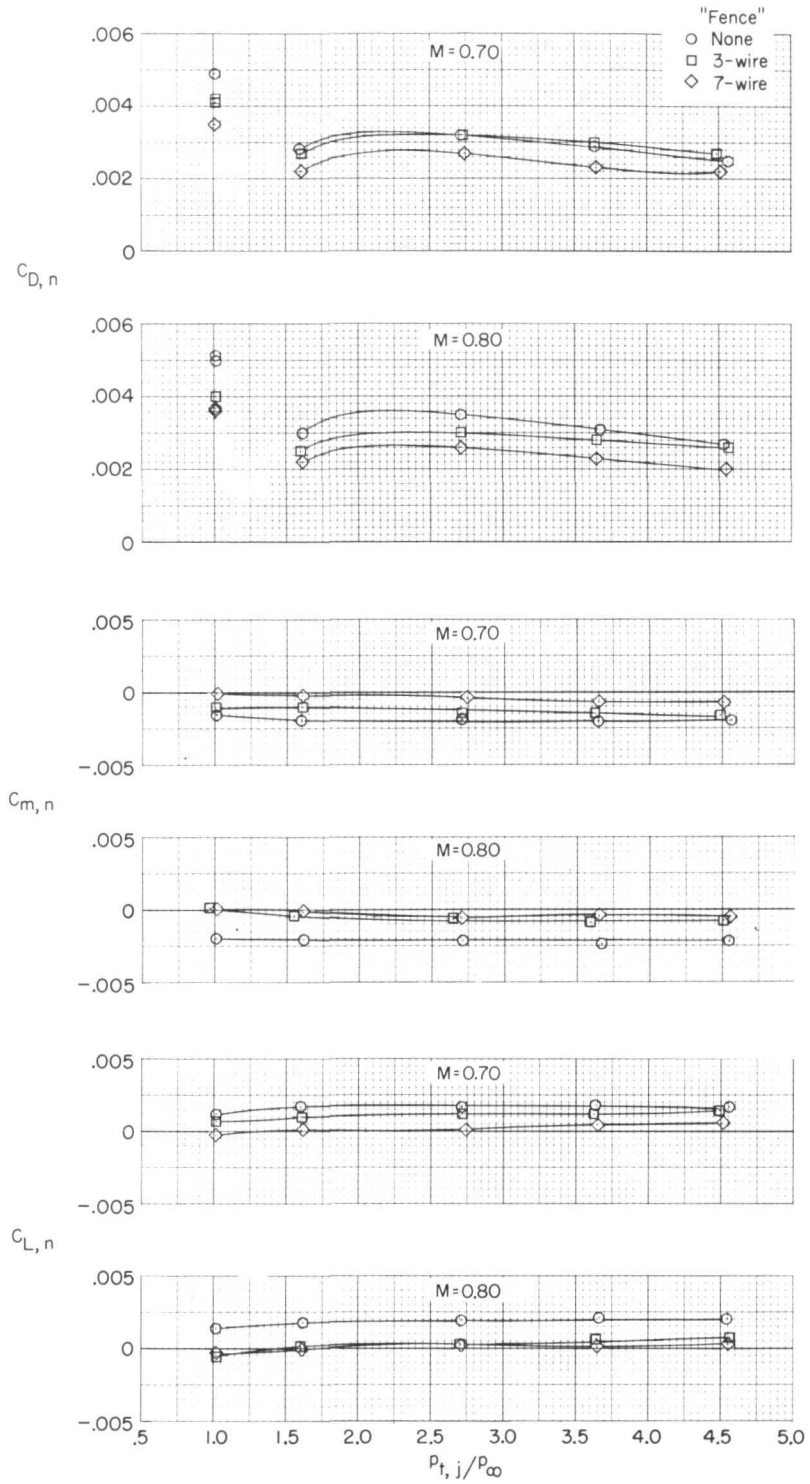

Figure 29.- Effect of boundary-layer modification and jet total-pressure ratio on nozzle aerodynamic characteristics at $\alpha = 4.3^{o}$. Configuration 5 (type A low partial afterburning power setting).

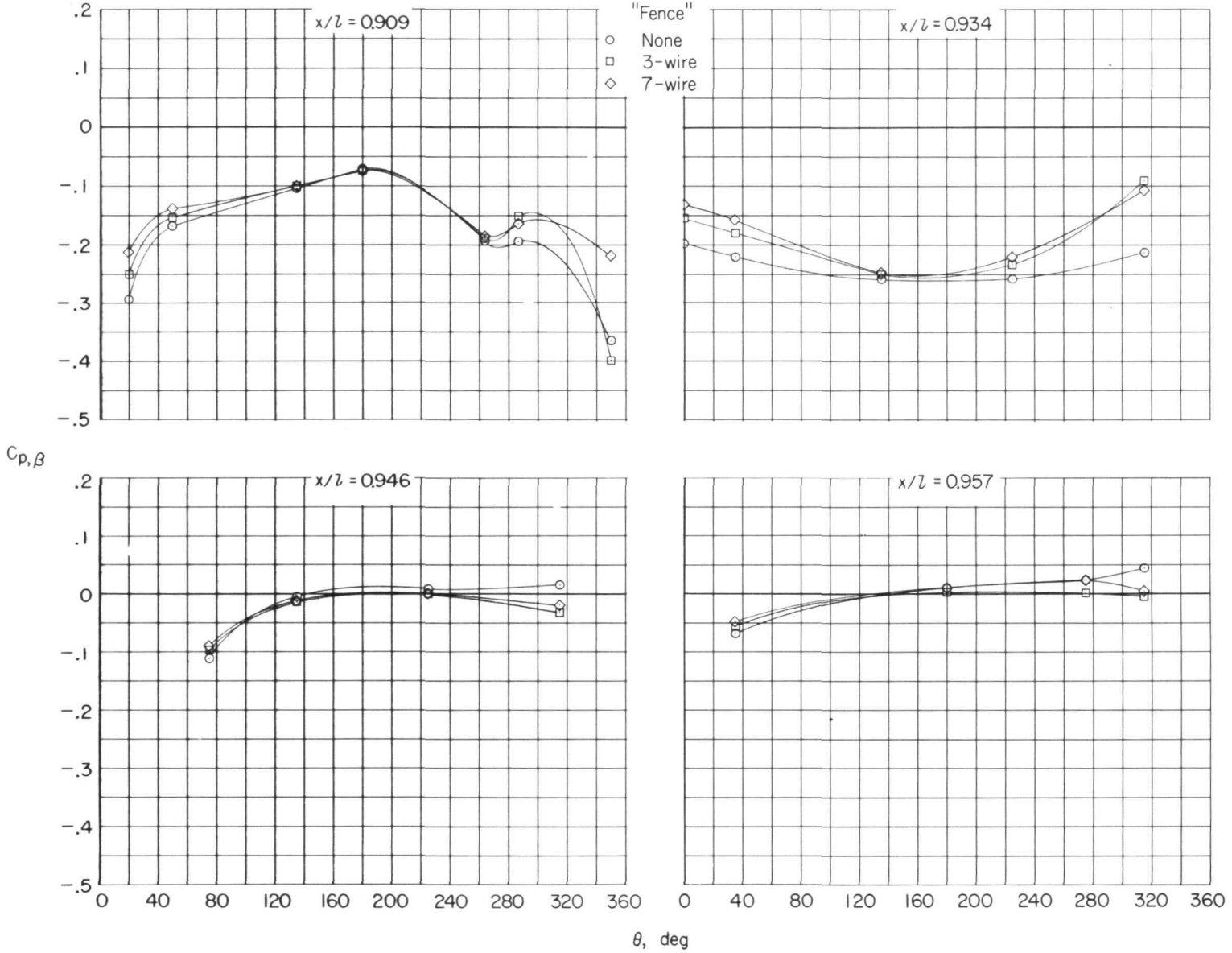

Figure 30.- Effect of boundary-layer modification on circumferential distributions of pressure at various x/l stations for configuration 5 nozzles. M = 0.7; $\alpha = 4.3^{o}$; $p_{t,j}/p_{\infty} = 2.4$.

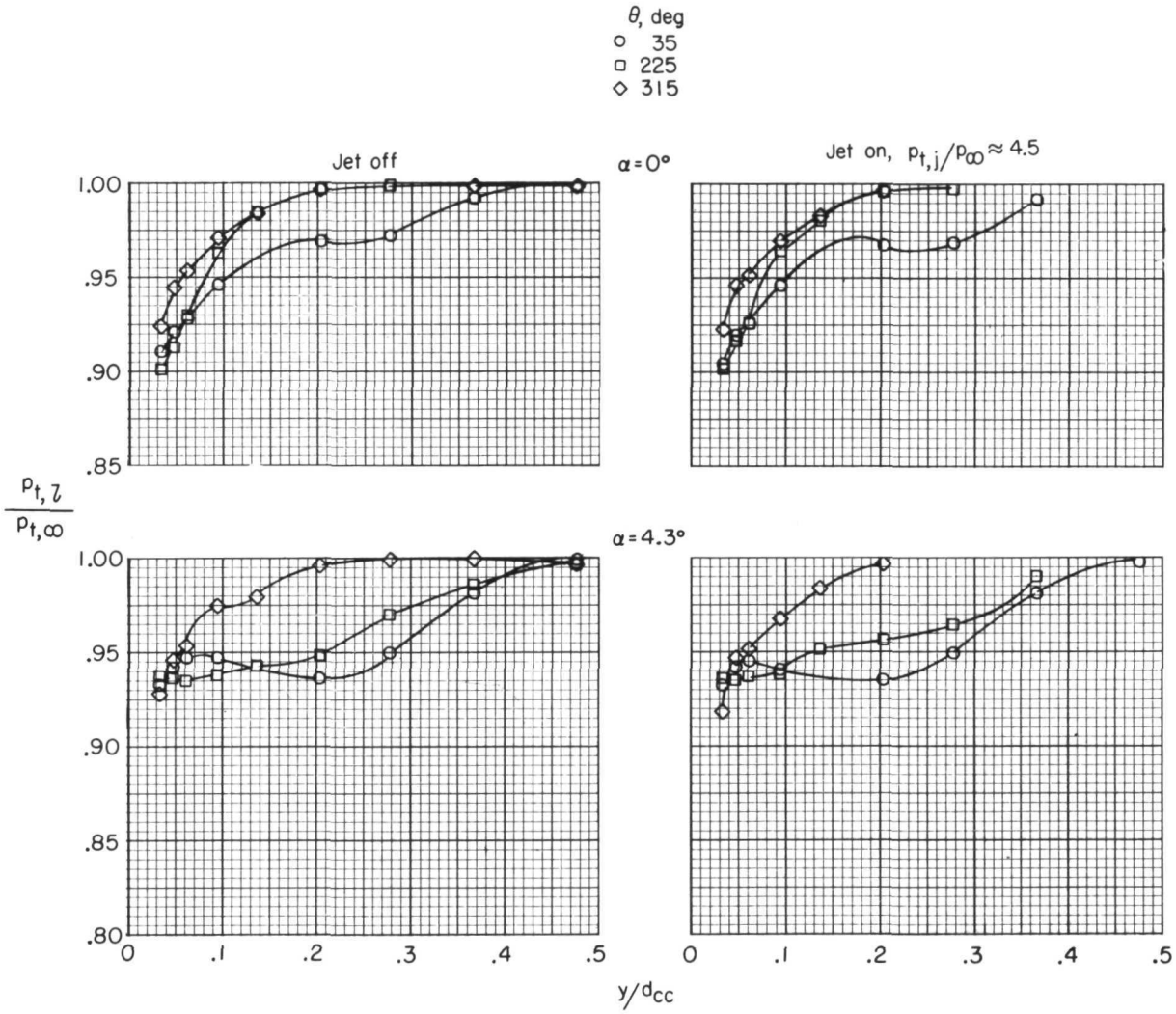

(a) M = 0.6.

Figure 31.- Model boundary-layer profiles obtained at station 141.499 cm with configuration 5 nozzles installed (type A low partial afterburning power setting). No boundary-layer fence.

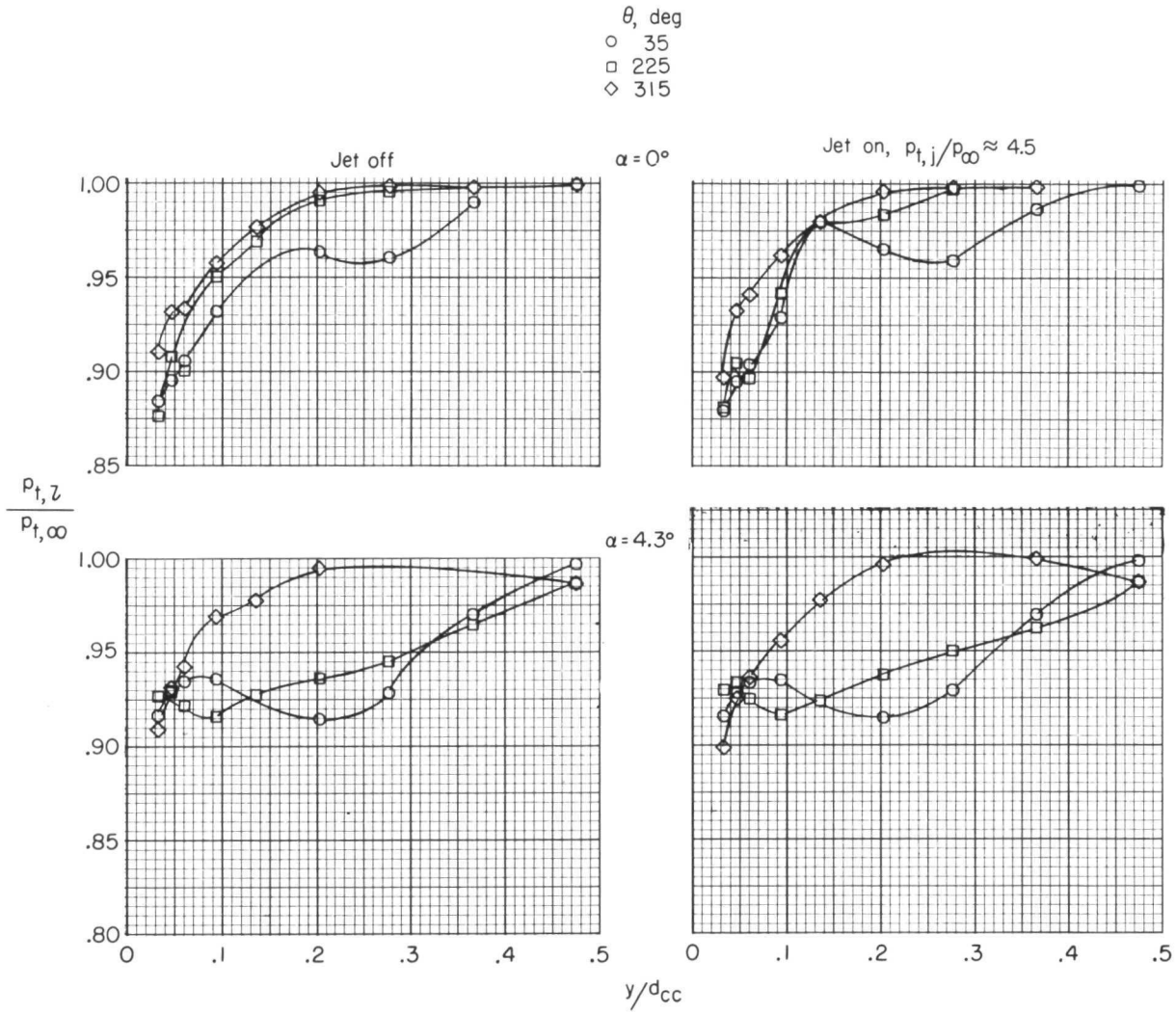

(b) M = 0.7.

Figure 31.- Continued.

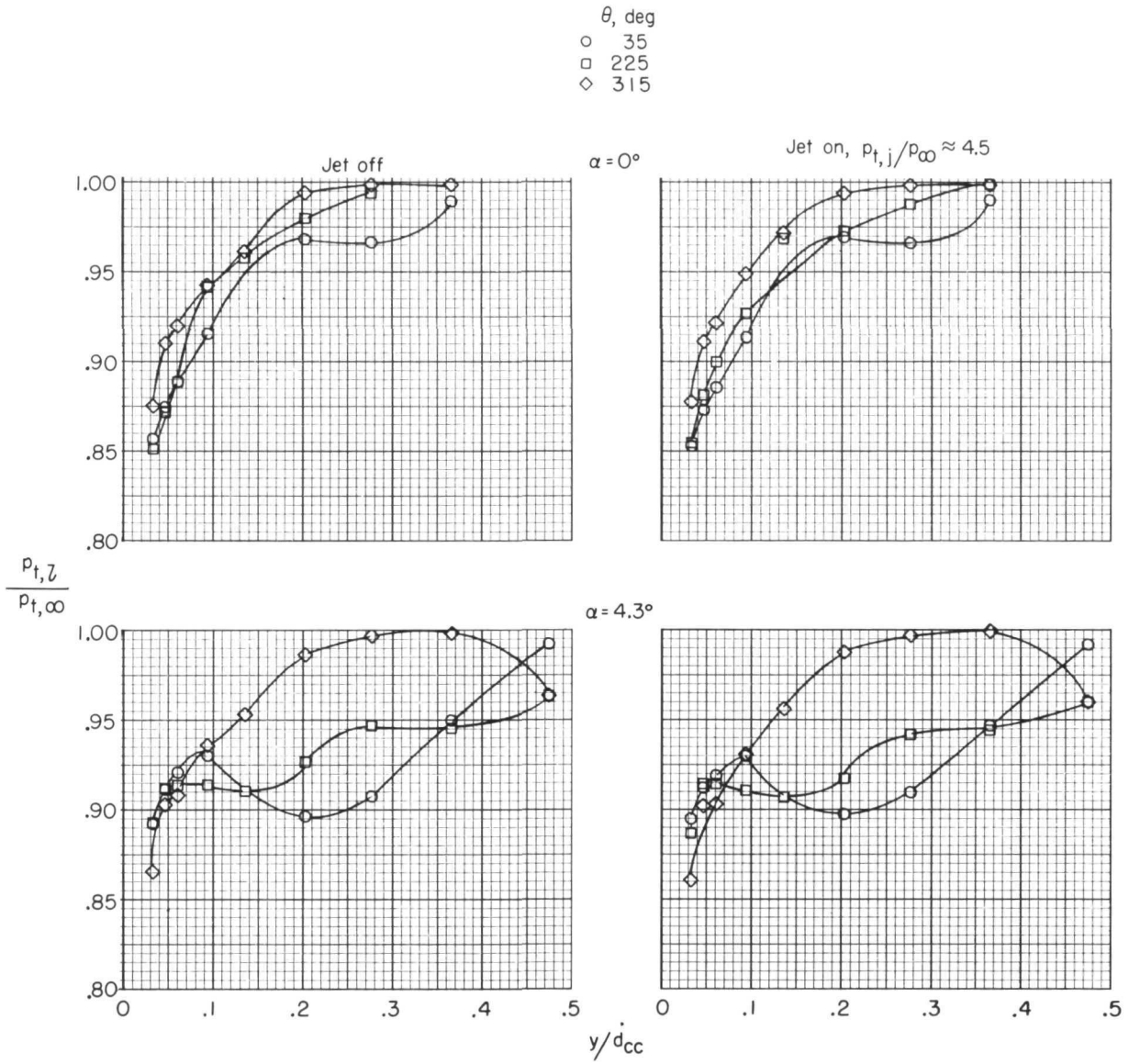

(c) M = 0.8.

Figure 31.- Continued.

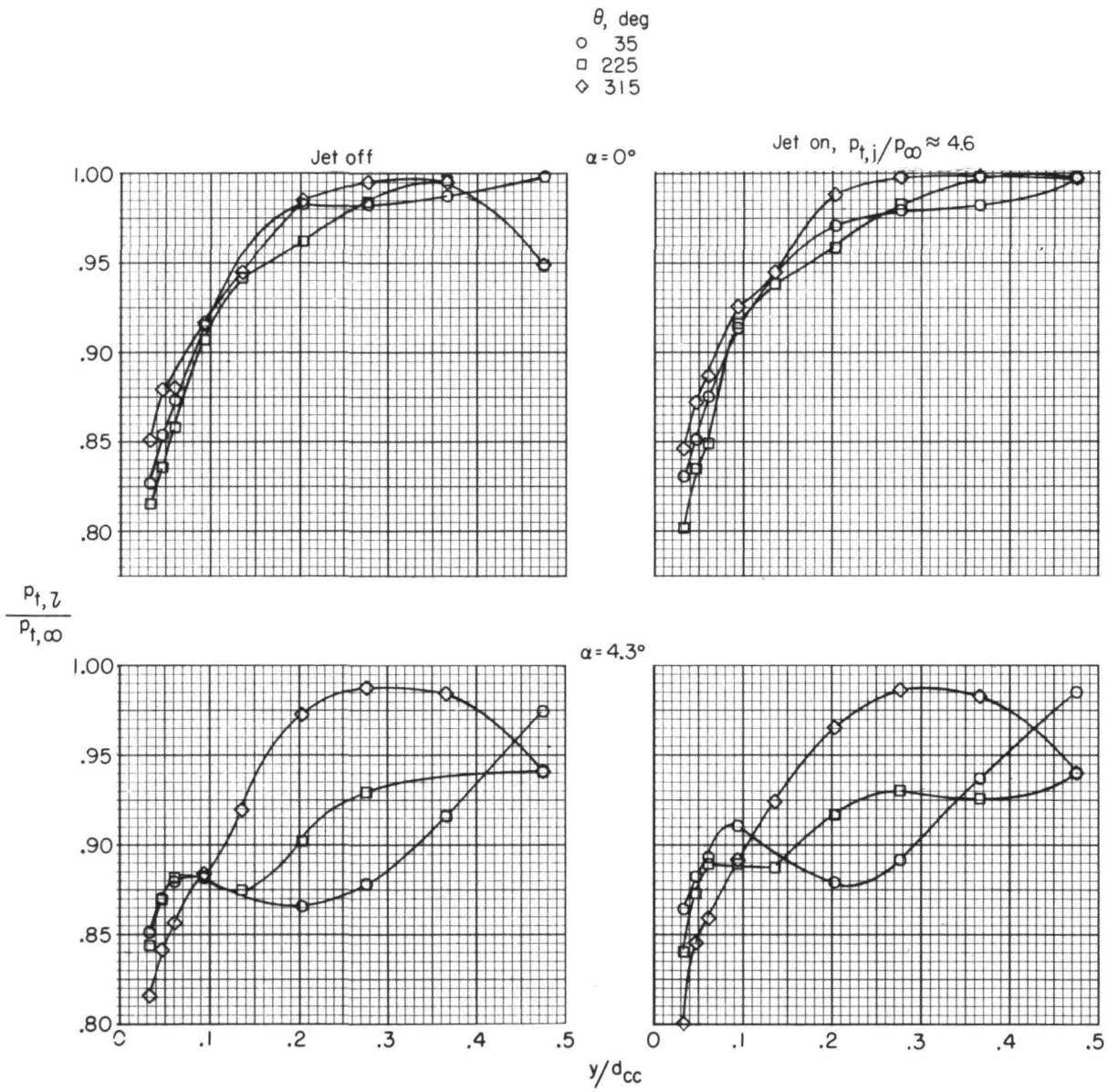

(d) M = 0.9.

Figure 31.- Continued.

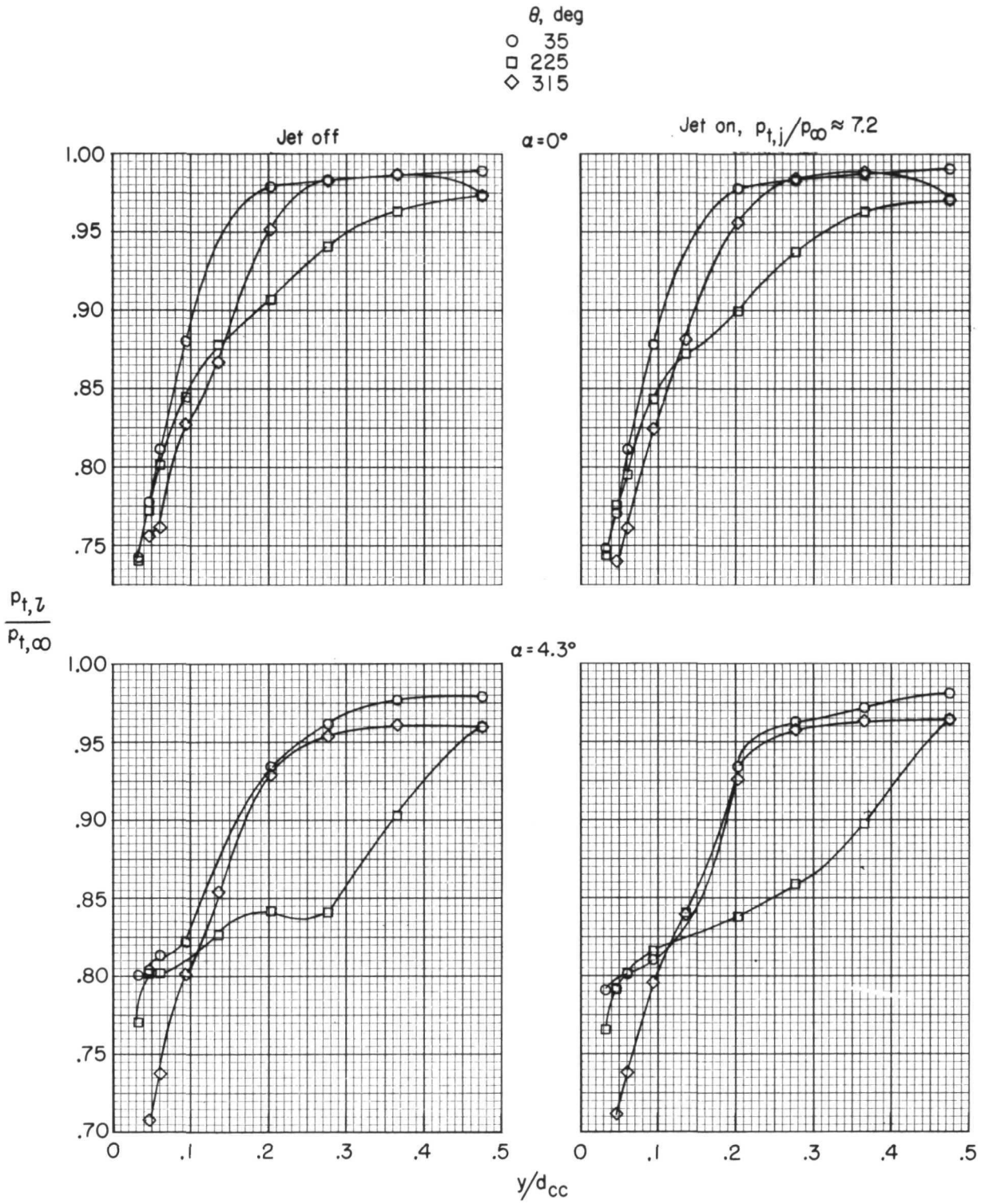

(e) M = 1.2.

Figure 31.- Concluded.

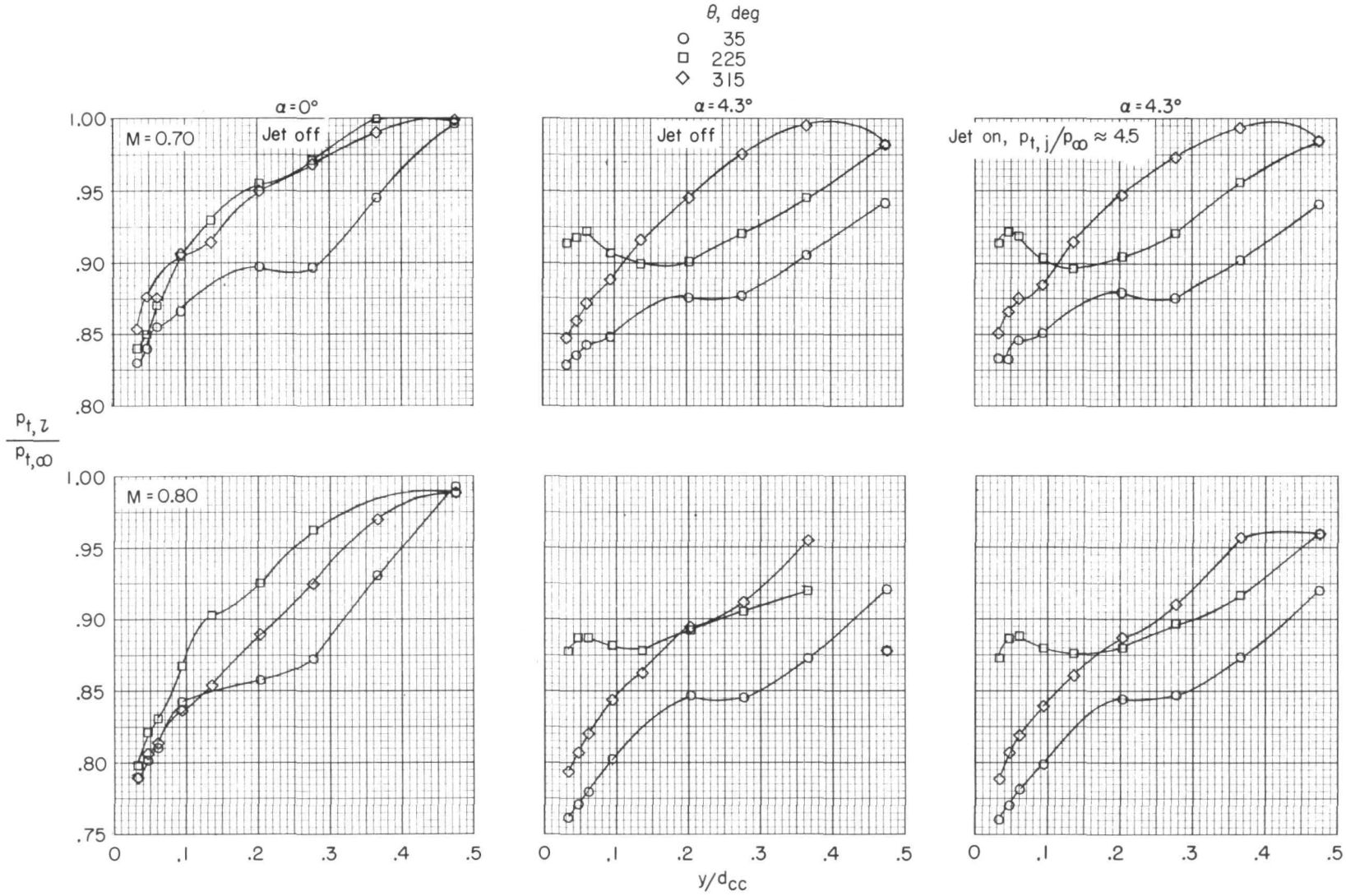

Figure 32.- Model boundary-layer profiles obtained at station 141.499 cm with configuration 5 nozzles installed (type A low partial afterburning power setting). Boundary layer thickened by installation of a 3-wire fence.

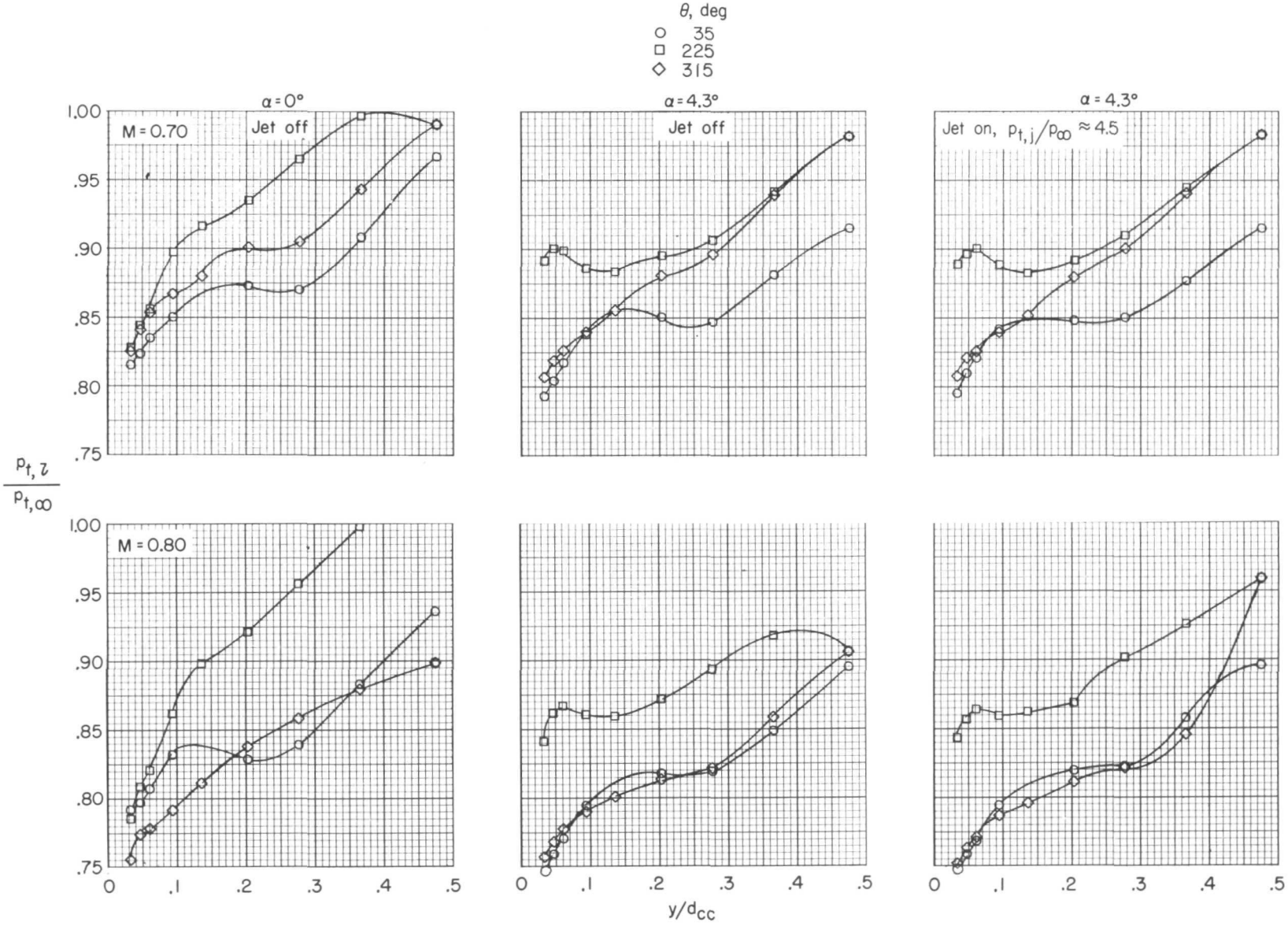

Figure 33.- Model boundary-layer profiles obtained at station 141.499 cm with configuration 5 nozzles installed (type A low partial afterburning power setting). Boundary layer thickened by installation of a 7-wire fence.

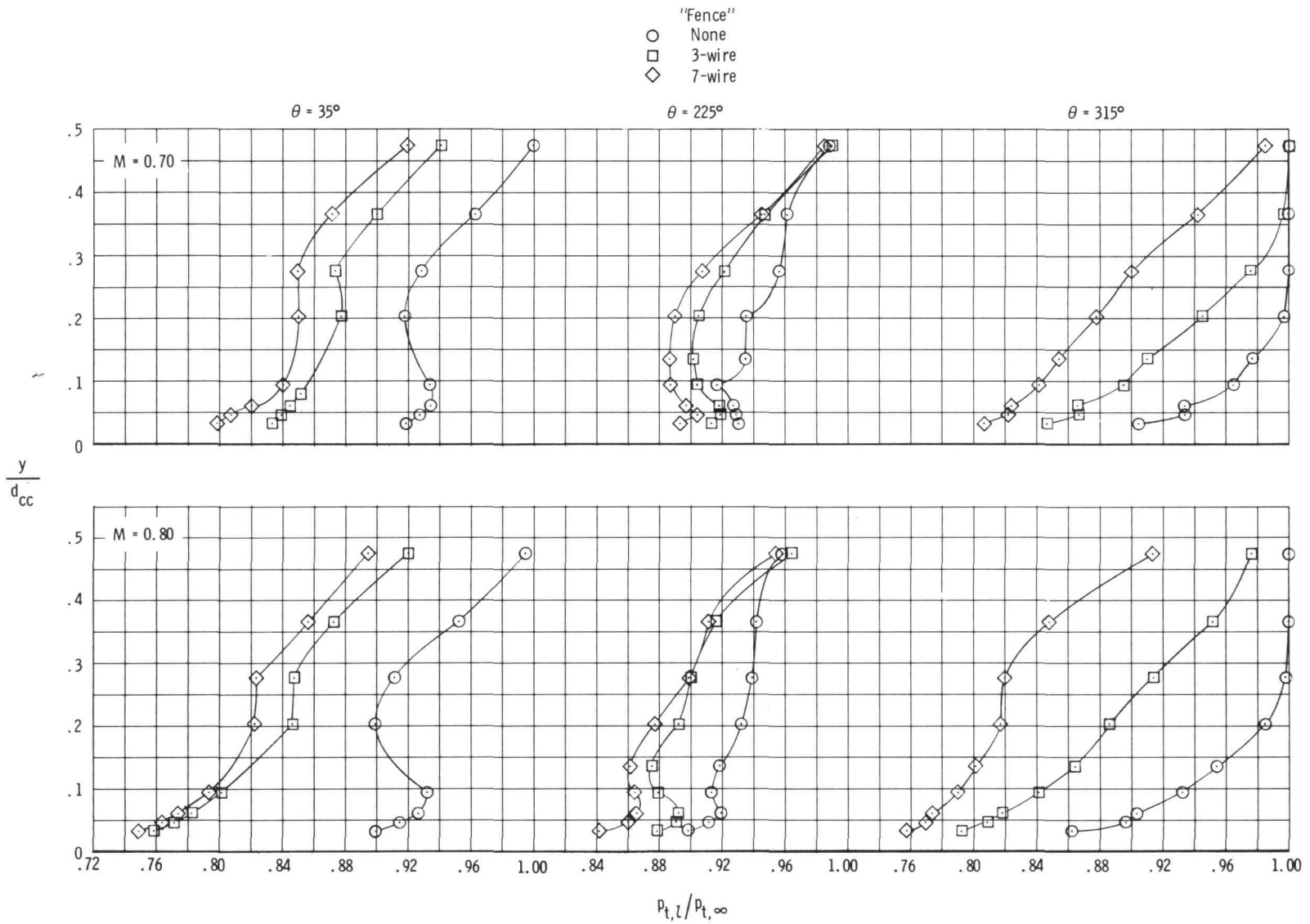

Figure 34.- Comparison of unmodified boundary-layer profiles on model at station 141.499 cm with boundary-layer profiles modified by "fences." $\alpha = 4.3^{o}$; $p_{t,j}\ p_{\infty} = 2.7$.

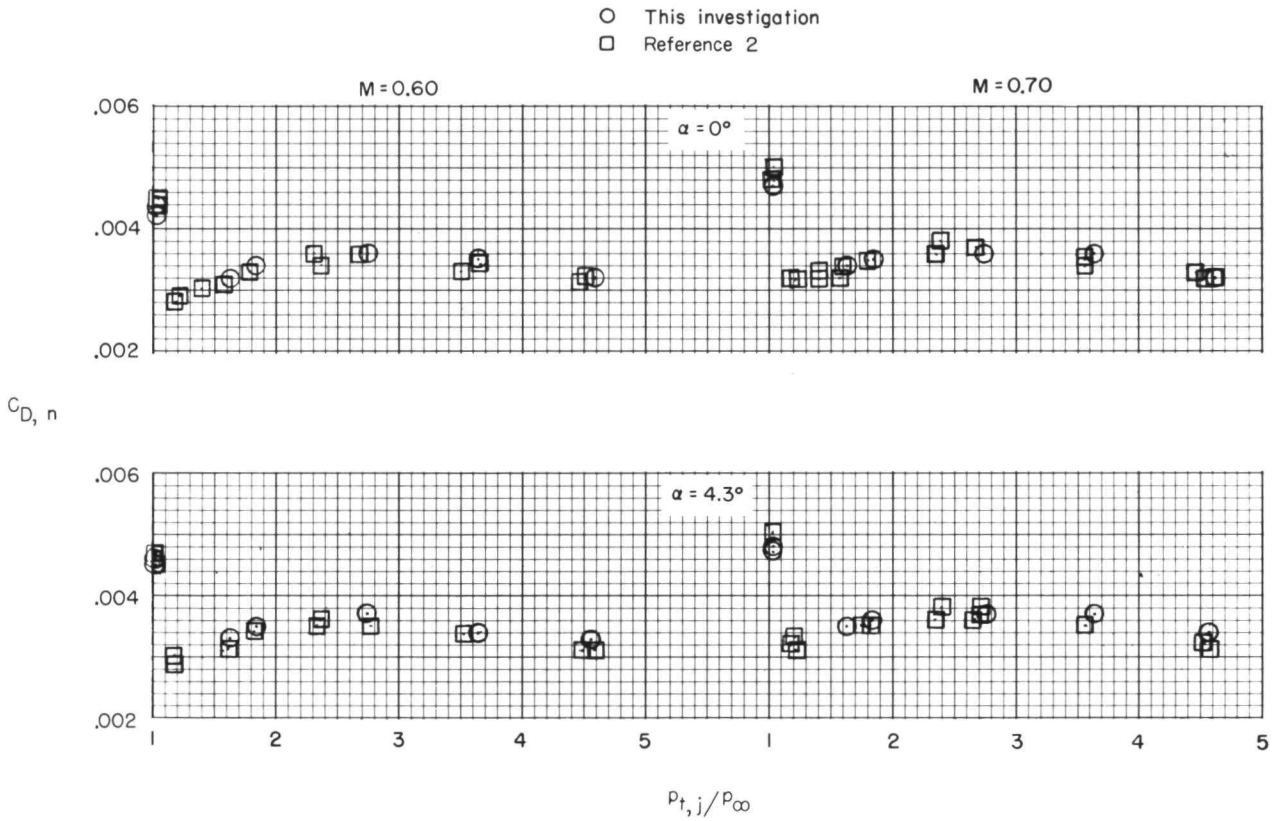

(a) Configuration 3.

Figure 35.- Comparison of nozzle drag data obtained from this investigation with that from reference 2.

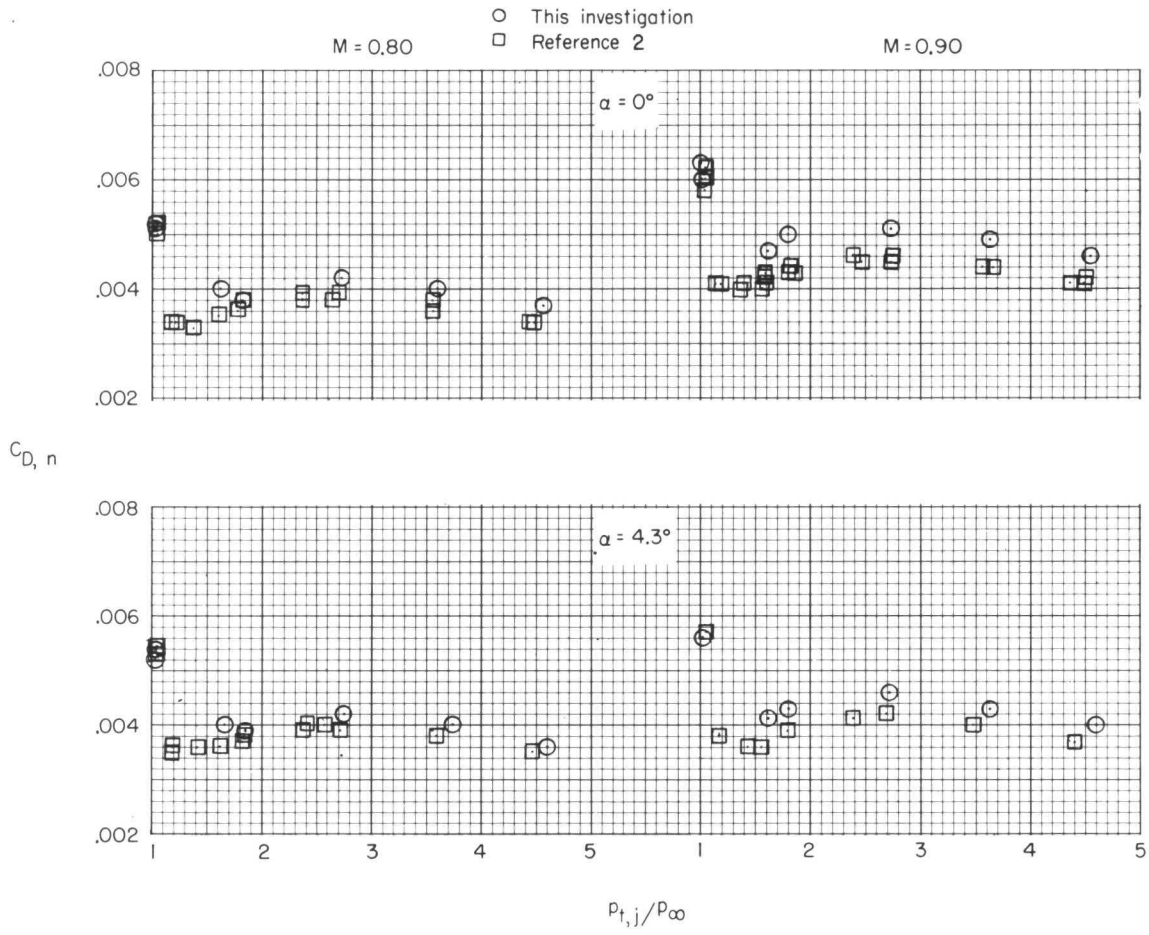

(a) Concluded.

Figure 35. - Continued.

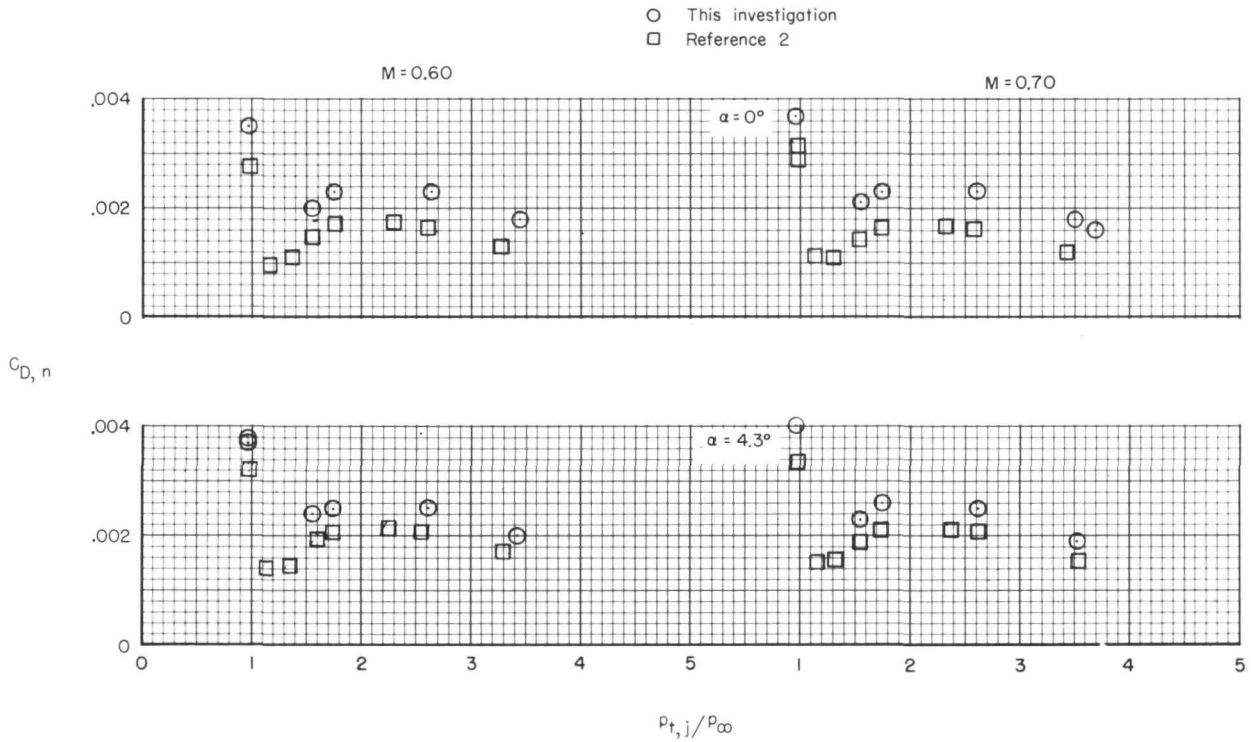

(b) Configuration 7.

Figure 35.- Continued.

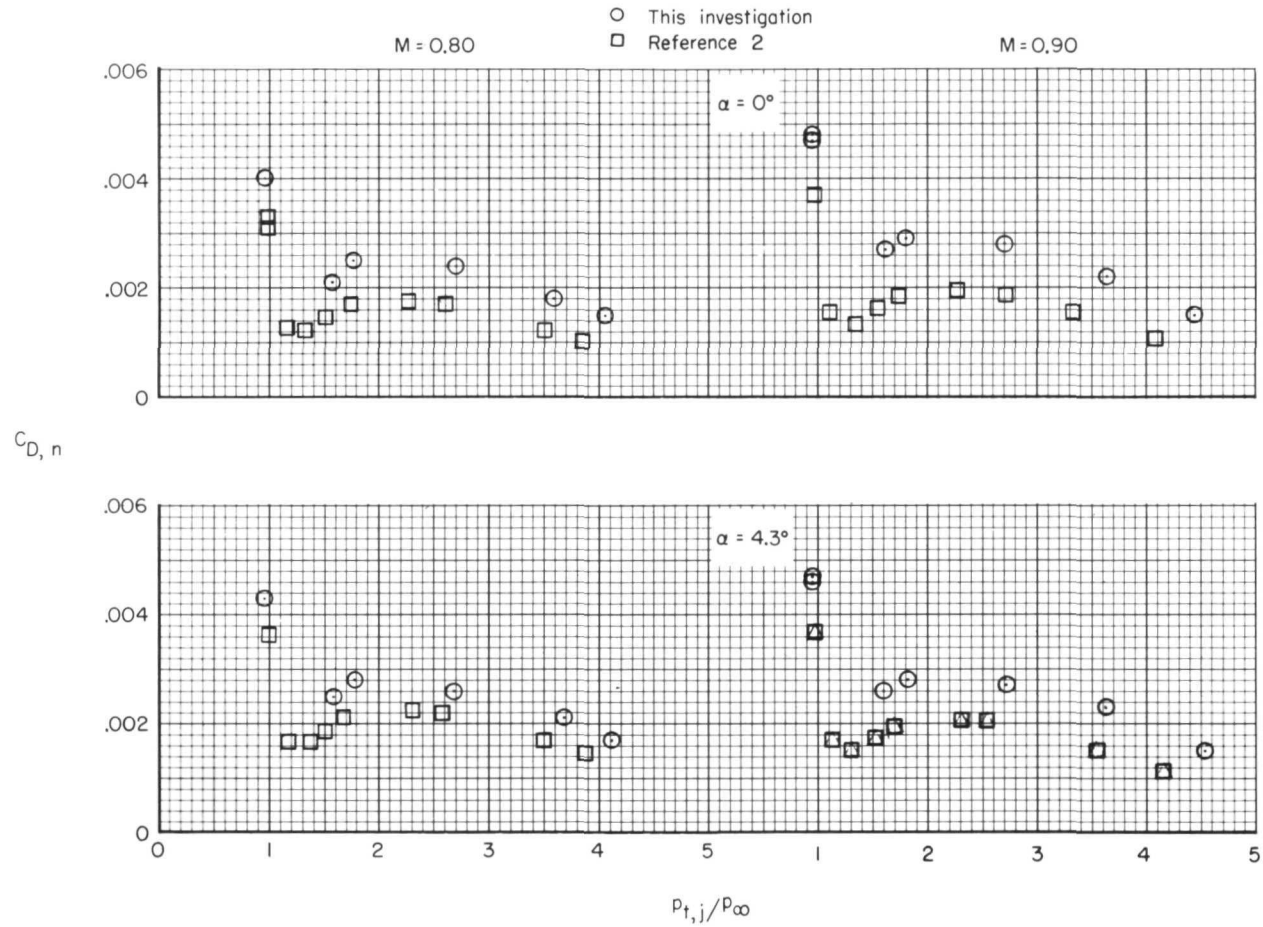

(b) Continued.

Figure 35.- Continued.

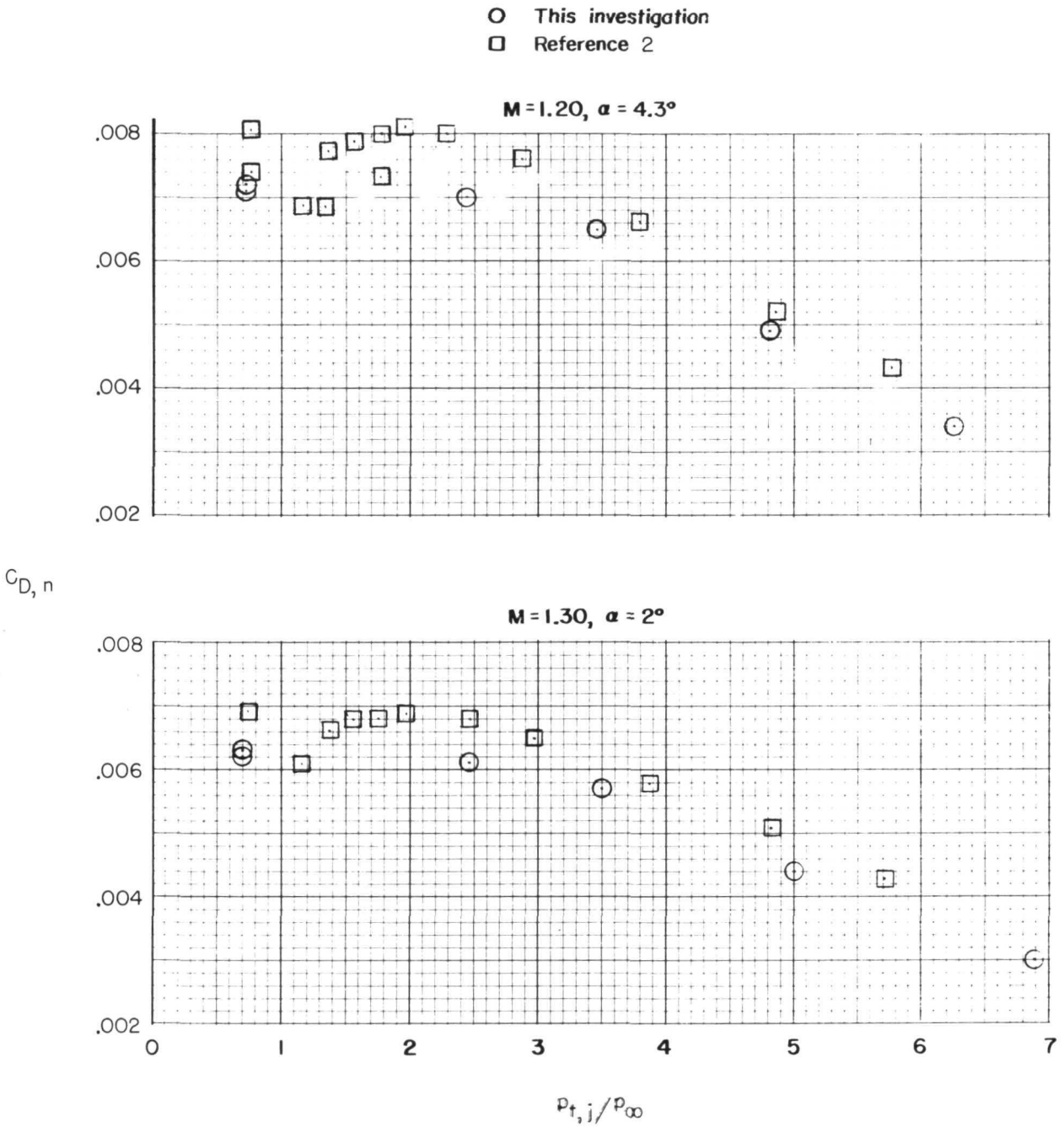

(b) Continued.

Figure 35.- Continued.

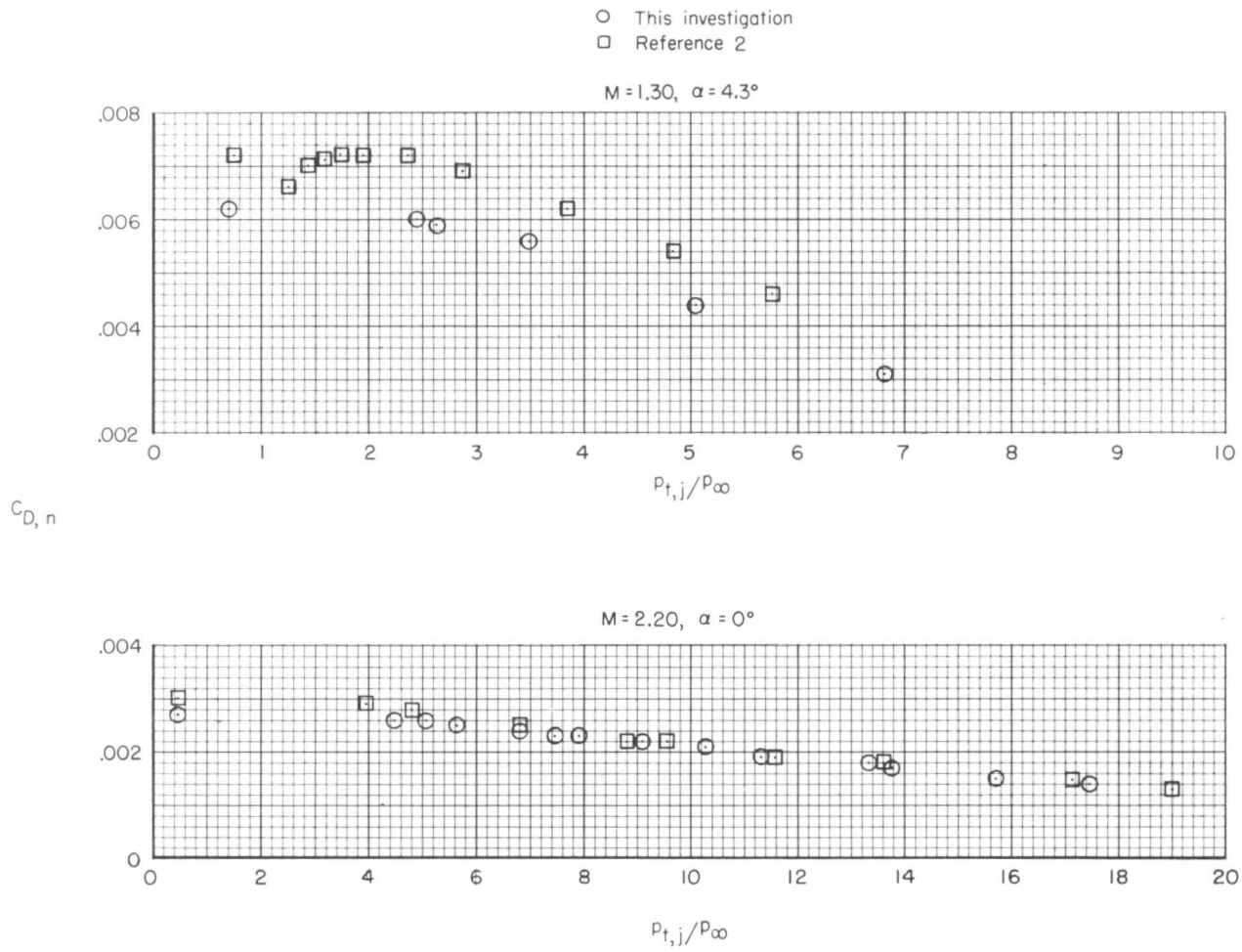

(b) Concluded.

Figure 35. - Continued.

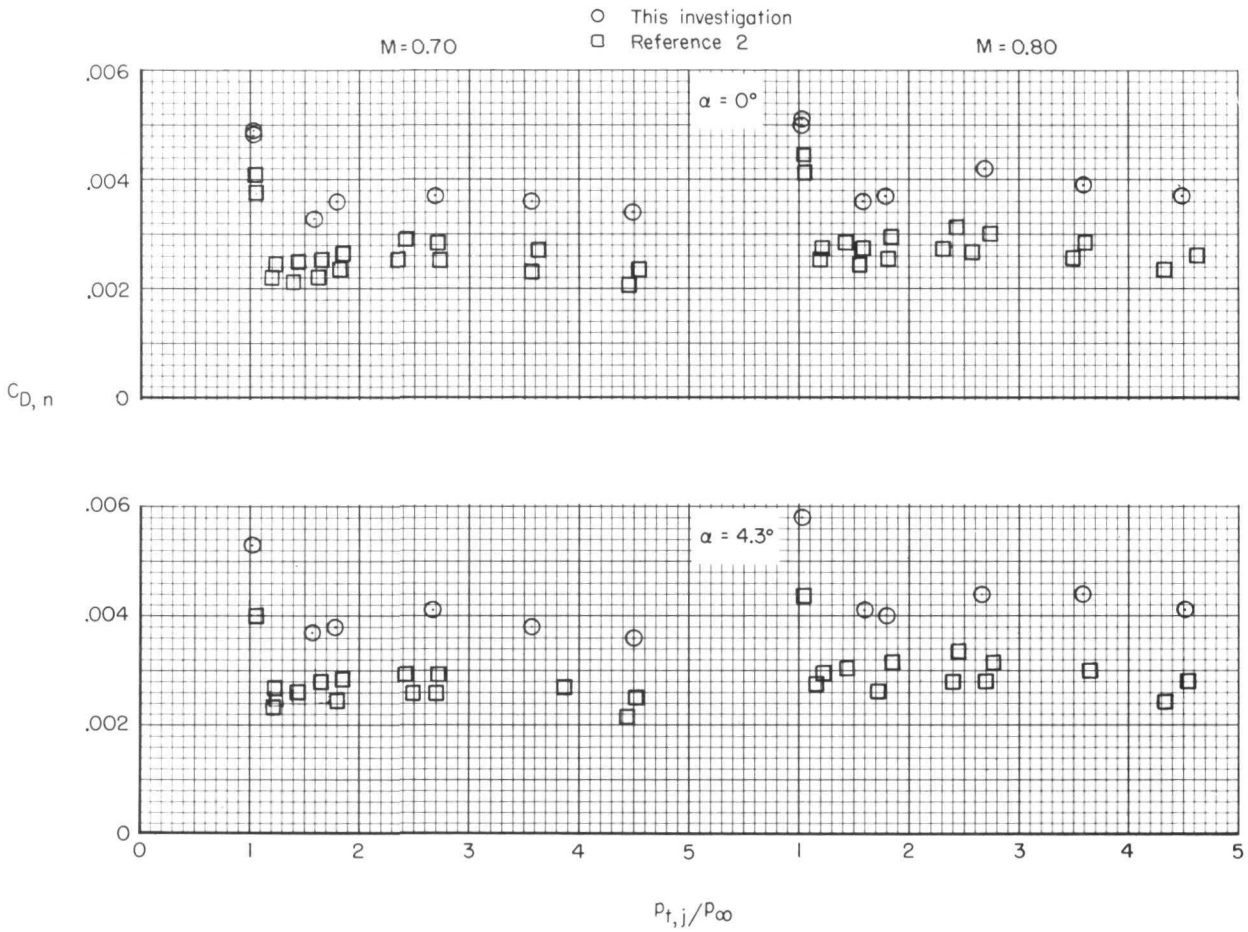

(c) Configuration 9.

Figure 35.- Continued.

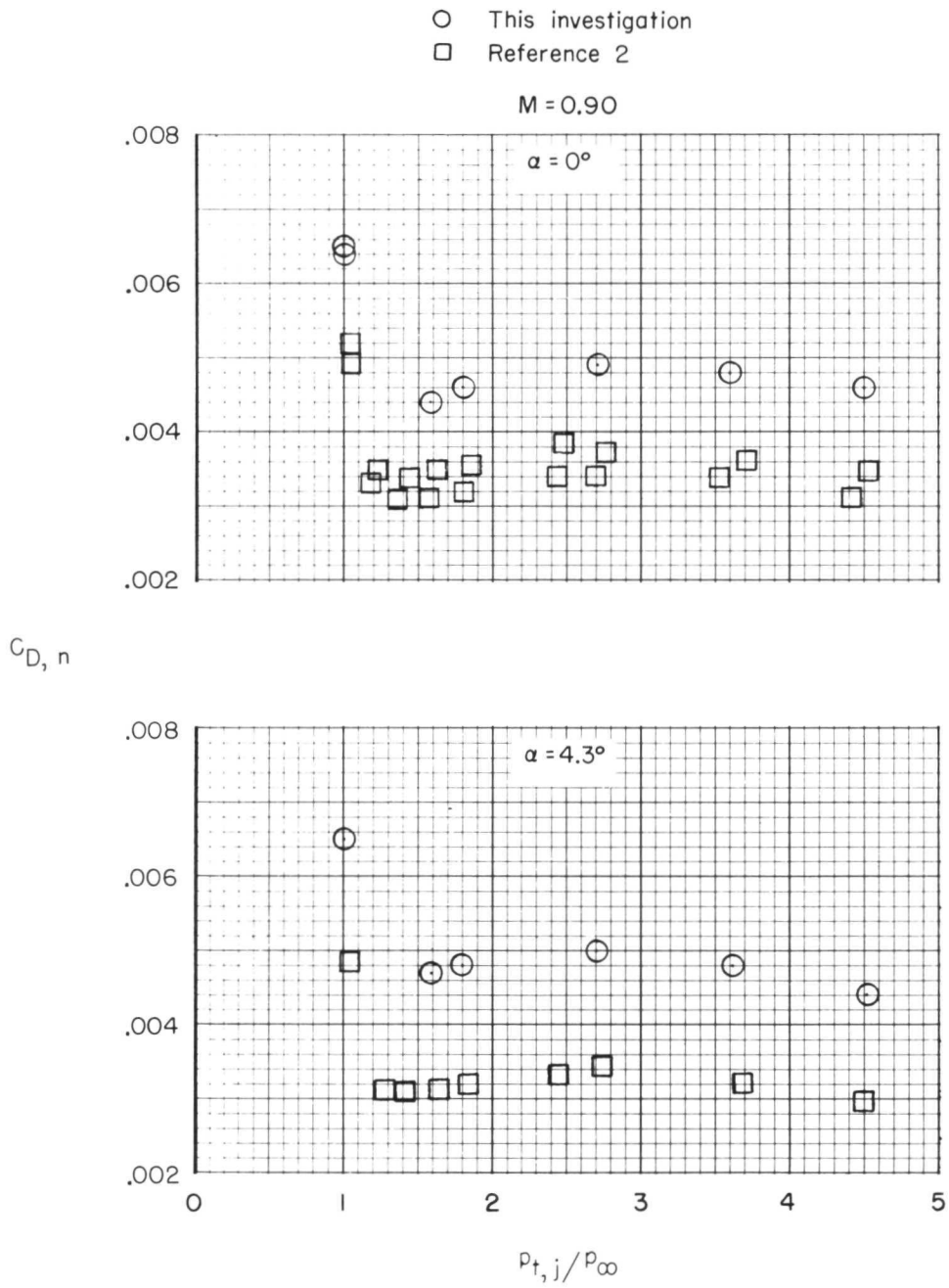

(c) Concluded.

Figure 35.- Continued.

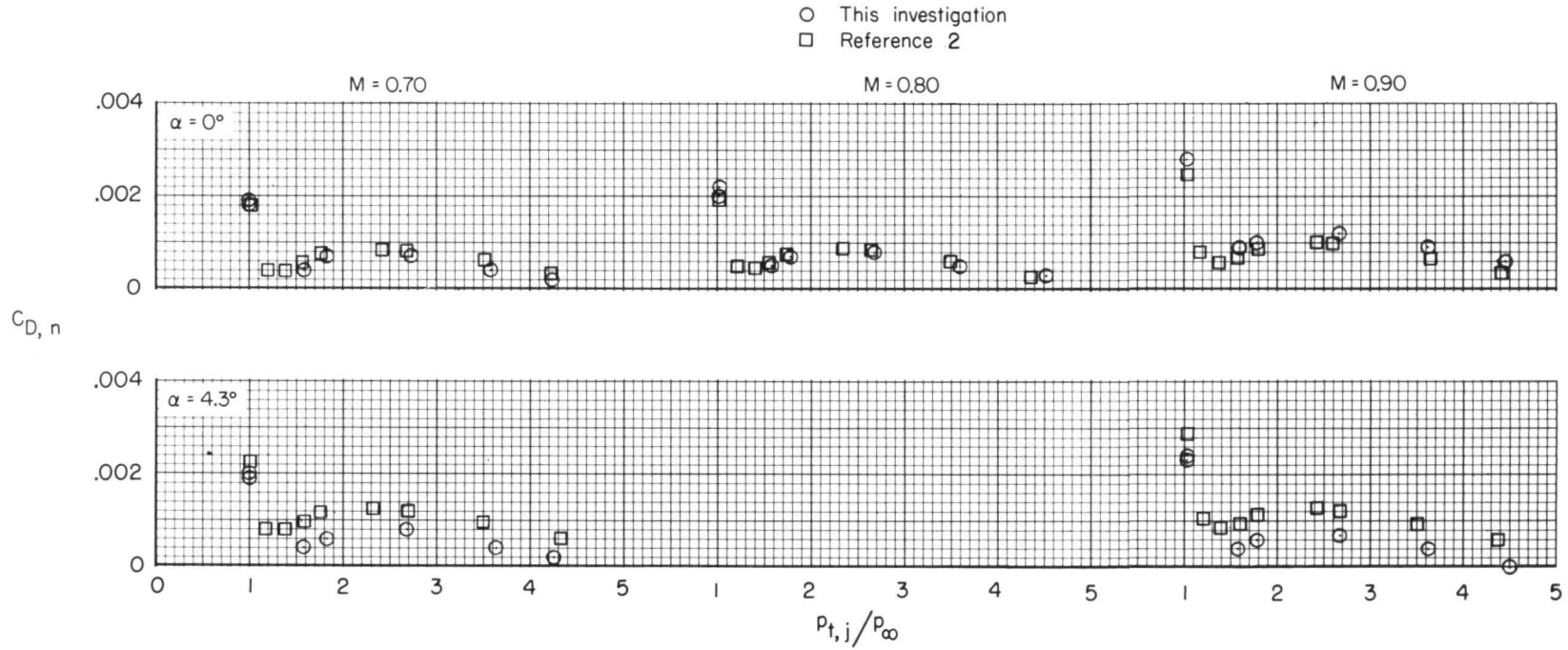

(d) Configuration 10.

Figure 35.- Continued.

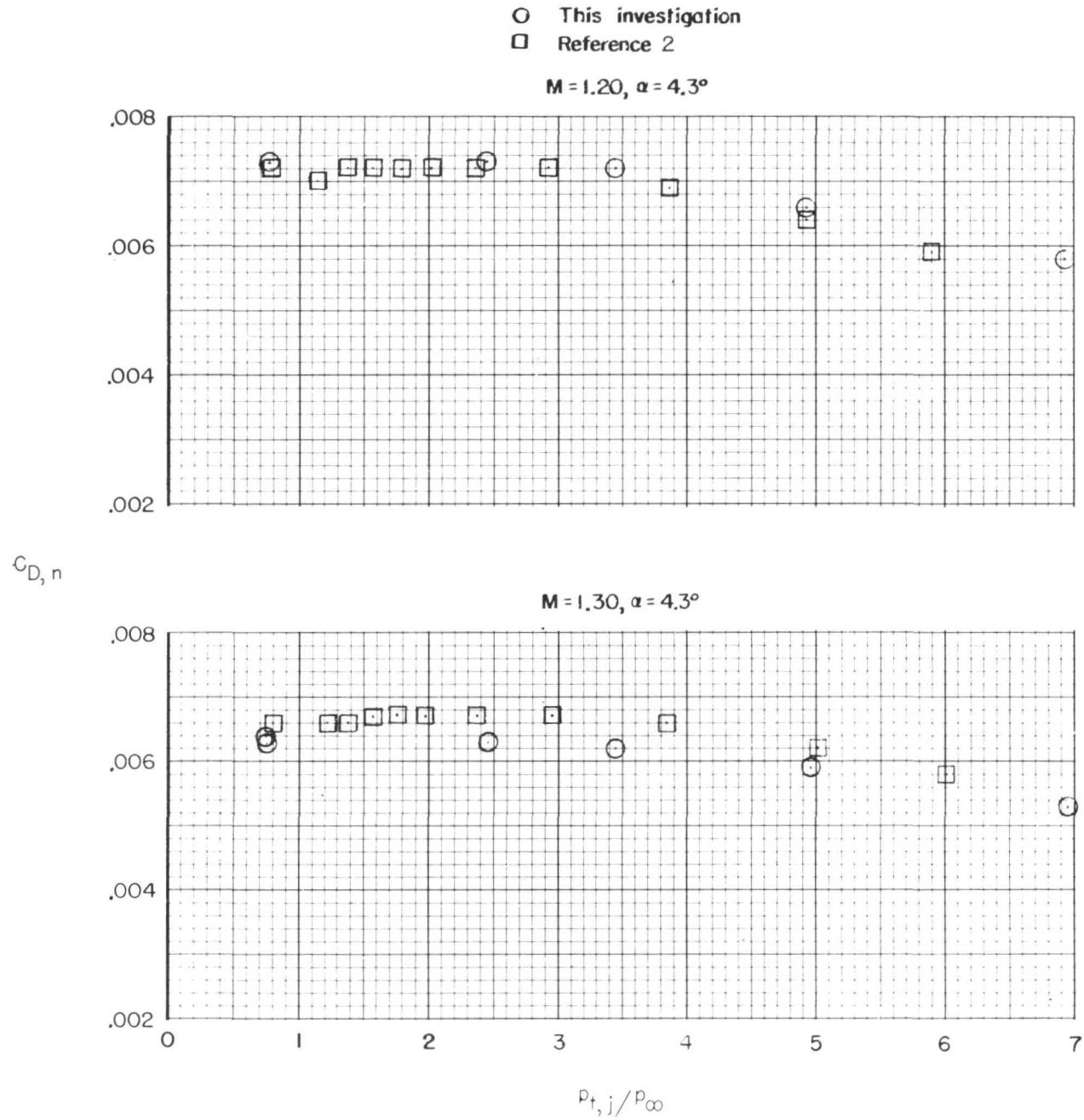

(e) Configuration 11.

Figure 35.- Concluded.

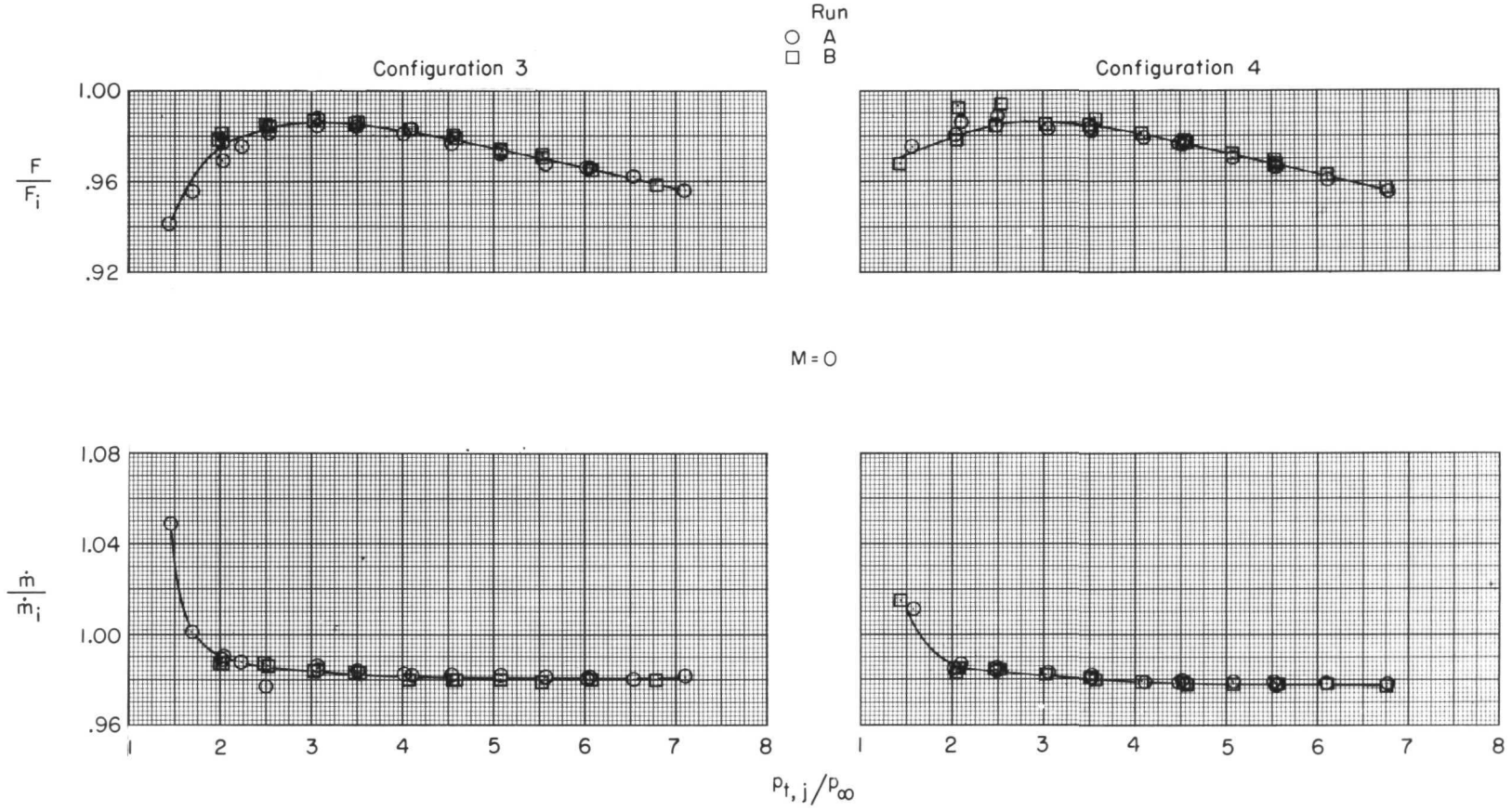

(a) Configurations 3 and 4.

Figure 36.- Effect of jet total-pressure ratio on the static thrust and mass-flow ratio for the various configurations tested.

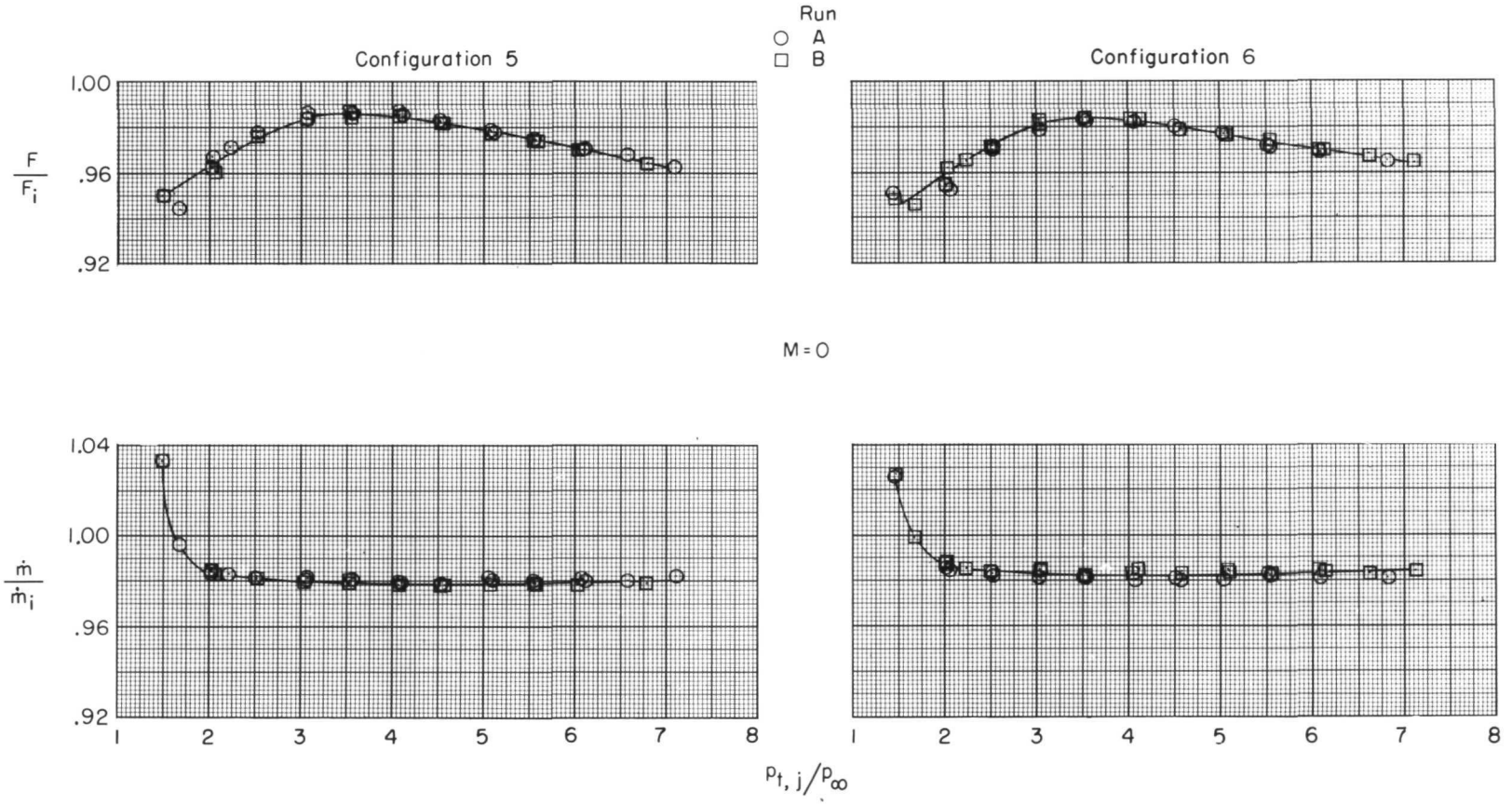

(b) Configurations 5 and 6.

Figure 36.- Continued.

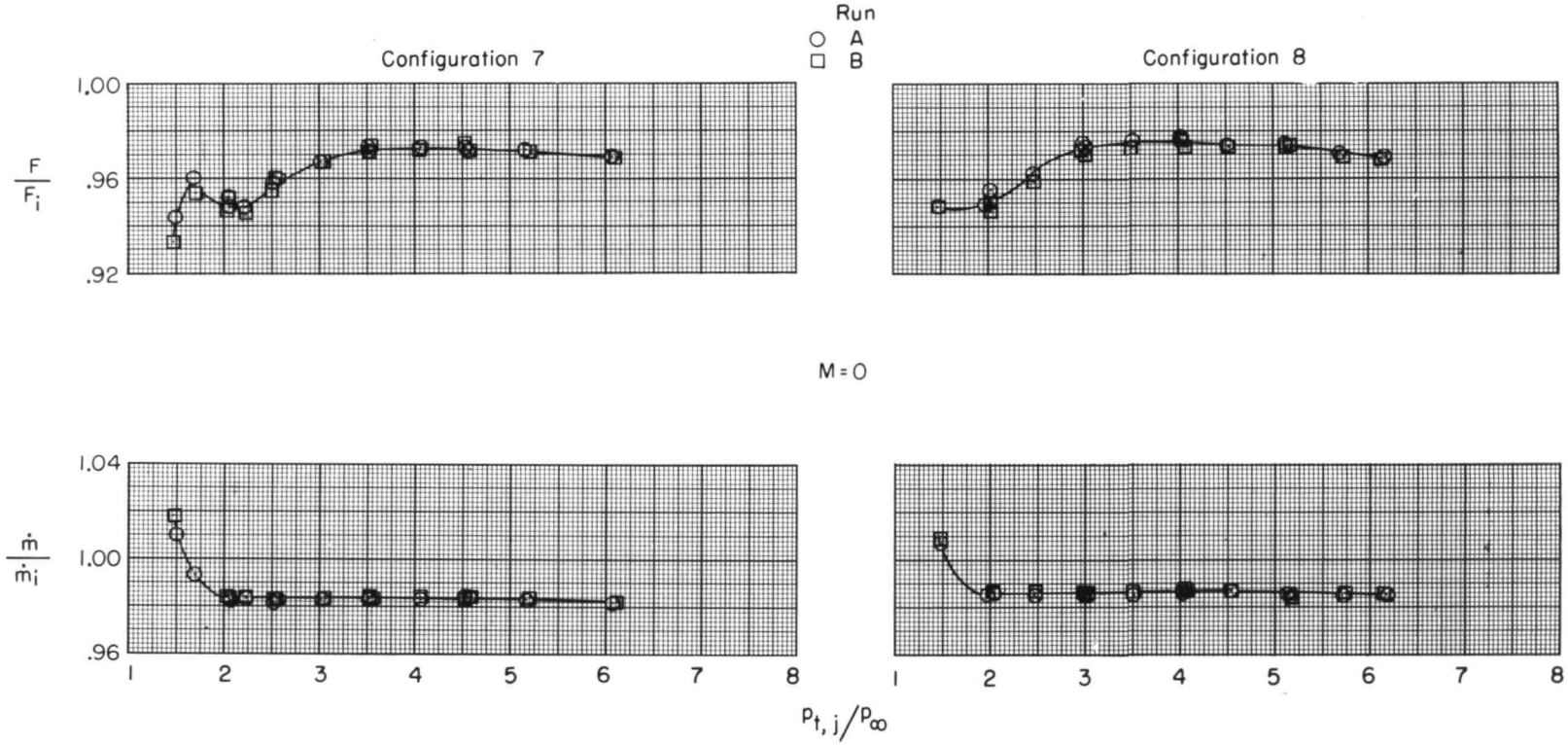

(c) Configurations 7 and 8.

Figure 36.- Continued.

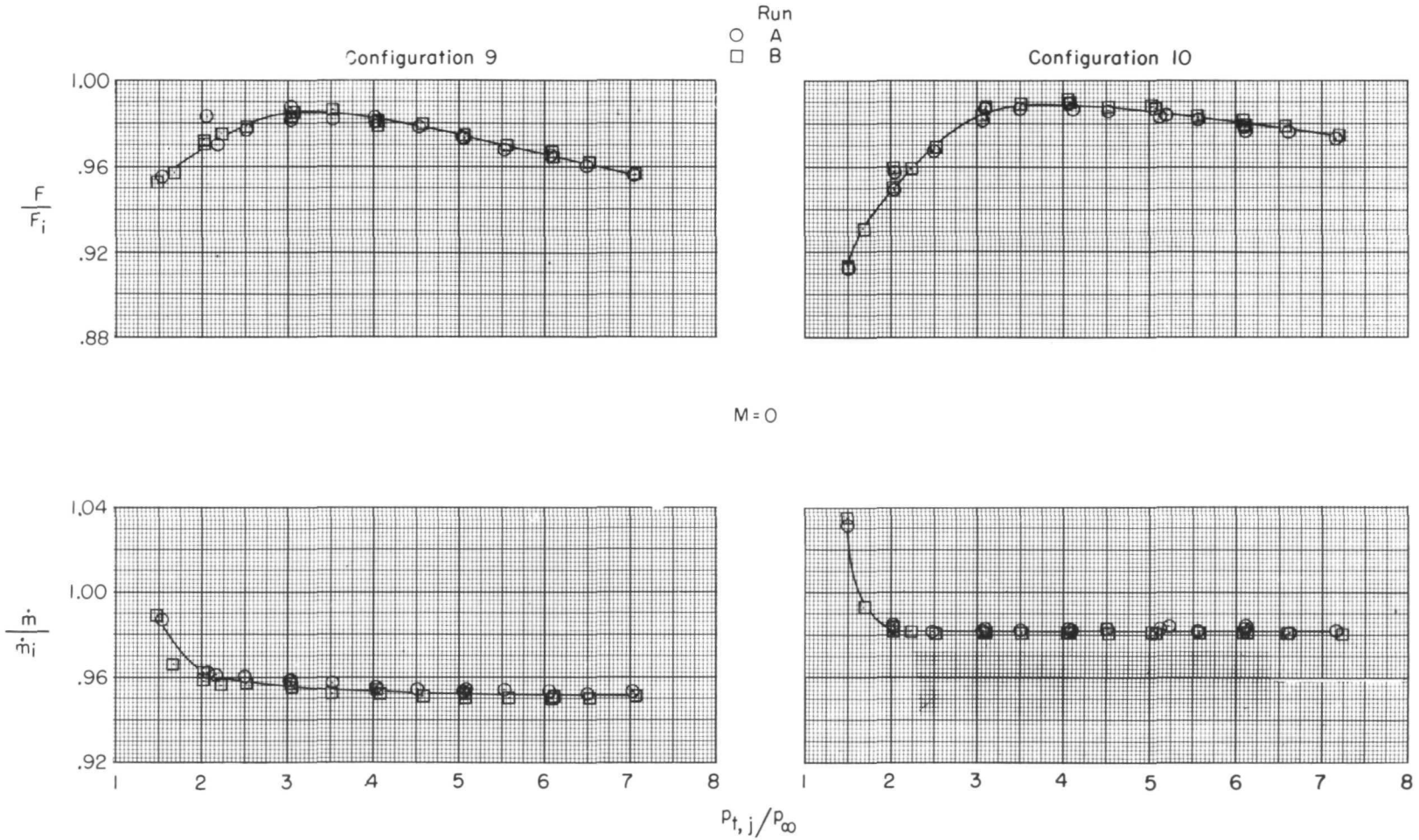

(d) Configurations 9 and 10.

Figure 36.- Continued.

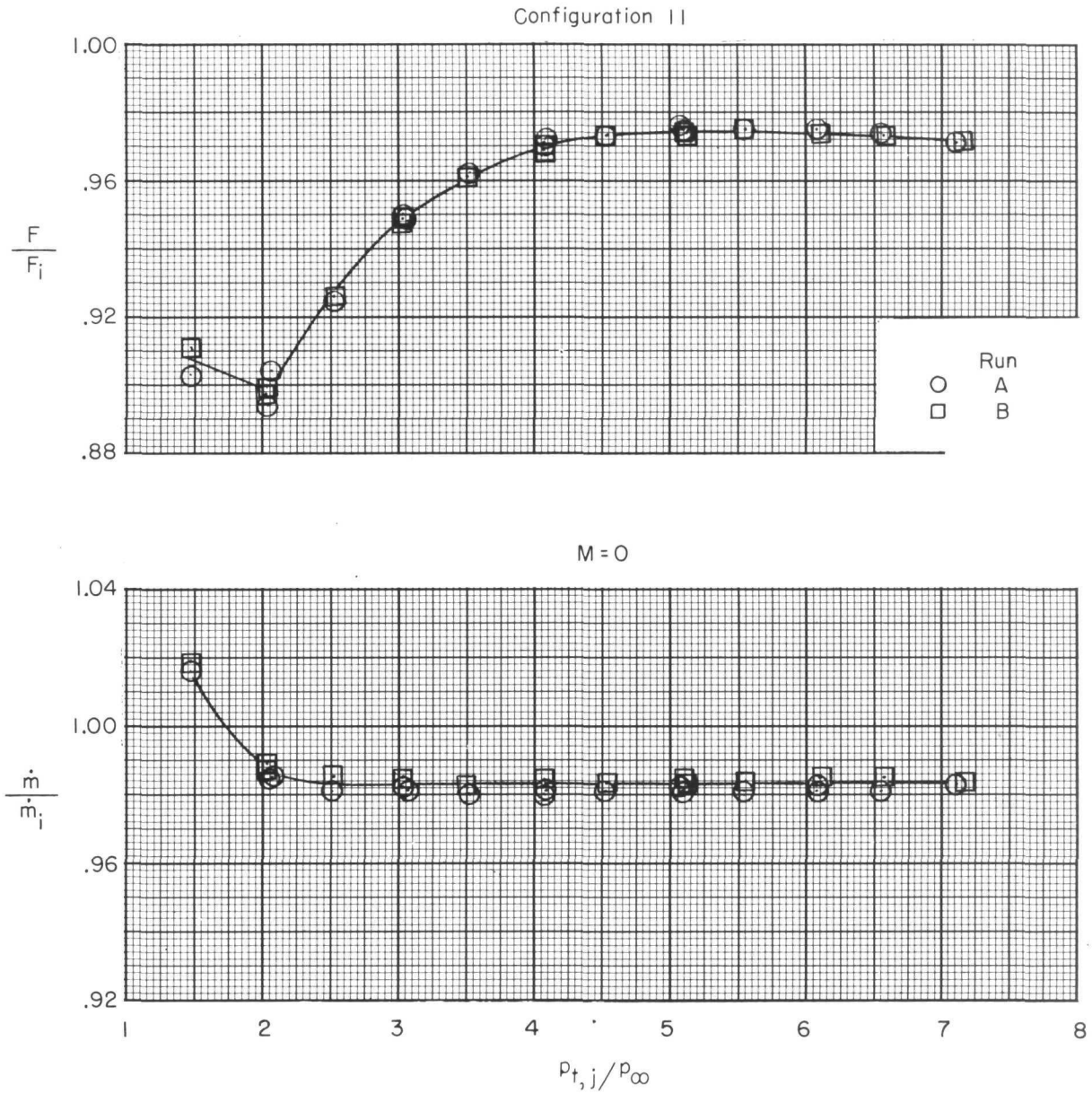

(e) Configuration 11.

Figure 36.- Concluded.

NATIONAL AERONAUTICS AND SPACE ADMINISTRATION
WASHINGTON, D.C. 20546

OFFICIAL BUSINESS
PENALTY FOR PRIVATE USE $300

SPECIAL FOURTH-CLASS RATE BOOK

POSTAGE AND FEES PAID
NATIONAL AERONAUTICS AND SPACE ADMINISTRATION
451

U.S.MAIL

POSTMASTER: If Undeliverable (Section 158 Postal Manual) Do Not Return

"The aeronautical and space activities of the United States shall be conducted so as to contribute . . . to the expansion of human knowledge of phenomena in the atmosphere and space. The Administration shall provide for the widest practicable and appropriate dissemination of information concerning its activities and the results thereof."

—NATIONAL AERONAUTICS AND SPACE ACT OF 1958

NASA SCIENTIFIC AND TECHNICAL PUBLICATIONS

TECHNICAL REPORTS: Scientific and technical information considered important, complete, and a lasting contribution to existing knowledge.

TECHNICAL NOTES: Information less broad in scope but nevertheless of importance as a contribution to existing knowledge.

TECHNICAL MEMORANDUMS: Information receiving limited distribution because of preliminary data, security classification, or other reasons. Also includes conference proceedings with either limited or unlimited distribution.

CONTRACTOR REPORTS: Scientific and technical information generated under a NASA contract or grant and considered an important contribution to existing knowledge.

TECHNICAL TRANSLATIONS: Information published in a foreign language considered to merit NASA distribution in English.

SPECIAL PUBLICATIONS: Information derived from or of value to NASA activities. Publications include final reports of major projects, monographs, data compilations, handbooks, sourcebooks, and special bibliographies.

TECHNOLOGY UTILIZATION PUBLICATIONS: Information on technology used by NASA that may be of particular interest in commercial and other non-aerospace applications. Publications include Tech Briefs, Technology Utilization Reports and Technology Surveys.

Details on the availability of these publications may be obtained from:

SCIENTIFIC AND TECHNICAL INFORMATION OFFICE

NATIONAL AERONAUTICS AND SPACE ADMINISTRATION

Washington, D.C. 20546